

AD _____

GRANT NUMBER: DAMD17-93-J-3014

TITLE: Early Detection of Breast Cancer on Mammograms Using:
Perceptual Feedback, Computer Processed Images and Ultrasound

PRINCIPAL INVESTIGATOR: Peter Bloch, Ph.D.

CONTRACTING ORGANIZATION: University of Pennsylvania
Philadelphia, Pennsylvania 19104-3246

REPORT DATE: January 1996

TYPE OF REPORT: Annual

PREPARED FOR: Commander
U.S. Army Medical Research and Materiel Command
Fort Detrick, Frederick, Maryland 21702-5012

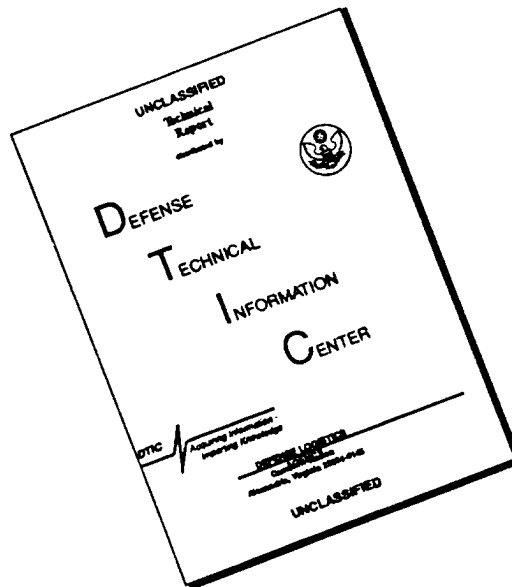
DISTRIBUTION STATEMENT: Approved for public release;
distribution unlimited

The views, opinions and/or findings contained in this report are those of the author(s) and should not be construed as an official Department of the Army position, policy or decision unless so designated by other documentation.

19960508 075

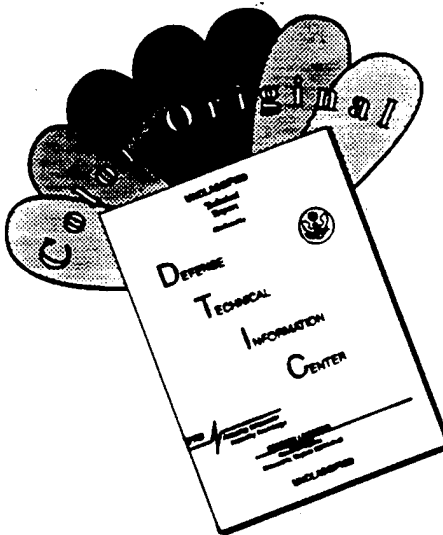
DTIC QUALITY INSPECTION 1

DISCLAIMER NOTICE



THIS DOCUMENT IS BEST QUALITY AVAILABLE. THE COPY FURNISHED TO DTIC CONTAINED A SIGNIFICANT NUMBER OF PAGES WHICH DO NOT REPRODUCE LEGIBLY.

DISCLAIMER NOTICE



THIS DOCUMENT IS BEST QUALITY AVAILABLE. THE COPY FURNISHED TO DTIC CONTAINED A SIGNIFICANT NUMBER OF COLOR PAGES WHICH DO NOT REPRODUCE LEGIBLY ON BLACK AND WHITE MICROFICHE.

REPORT DOCUMENTATION PAGE			Form Approved OMB No. 0704-0188	
Public reporting burden for this collection of information is estimated to average 1 hour per response, including the time for reviewing instructions, searching existing data sources, gathering and maintaining the data needed, and completing and reviewing the collection of information. Send comments regarding this burden estimate or any other aspect of this collection of information, including suggestions for reducing this burden, to Washington Headquarters Services, Directorate for Information Operations and Reports, 1215 Jefferson Davis Highway, Suite 1204, Arlington, VA 22202-4302, and to the Office of Management and Budget, Paperwork Reduction Project (0704-0188), Washington, DC 20503.				
1. AGENCY USE ONLY (Leave blank)		2. REPORT DATE January 1996		3. REPORT TYPE AND DATES COVERED Annual (31 Dec 94 - 30 Dec 95)
4. TITLE AND SUBTITLE Early Detection of Breast Cancer on Mammograms Using: Perceptual Feedback, Computer Processed Images and Ultrasound			5. FUNDING NUMBERS DAMD17-93-J-3014	
6. AUTHOR(S) Peter Bloch, Ph.D.				
7. PERFORMING ORGANIZATION NAME(S) AND ADDRESS(ES) University of Pennsylvania Philadelphia, Pennsylvania 19104-3246			8. PERFORMING ORGANIZATION REPORT NUMBER	
9. SPONSORING/MONITORING AGENCY NAME(S) AND ADDRESS(ES) U.S. Army Medical Research and Materiel Command Fort Detrick Frederick, Maryland 21702-5012			10. SPONSORING/MONITORING AGENCY REPORT NUMBER	
11. SUPPLEMENTARY NOTES				
12a. DISTRIBUTION/AVAILABILITY STATEMENT Approved for public release; distribution unlimited			12b. DISTRIBUTION CODE	
13. ABSTRACT (Maximum 200 words) Several approaches for improving the detection of small tumors in the breast were explored. These included; (1) Perceptual feedback to decrease errors in missing tumors that are actually visible on the initial screening mammogram. The observers head-eye-position was recorded while viewing mammograms. It was found that false negative decisions in identifying a lesion was associated with prolong dwell time. Visual feedback, obtained by placing a small circle on the image surrounding the suspicious region (as predicted by the gaze duration), enhanced the detectability of masses. (2) Computer processing of screening mammograms for detection of clusters of microcalcifications and parenchyma patterns associated with developing lesions. Preserving the high spatial resolution and wide latitude in the digitized mammogram was found important for computer aided detection of subtle microcalcifications. Elevated mammography density has been associated with an increased risk of developing breast cancer. An algorithm was developed to perform quantification of the elevated parenchyma density on digitized mammograms. (3) High resolution ultrasound. The ultrasound distortion in the female breast image was identified and compensating algorithm developed to reduce the distortions. Design consideration was performed for two dimensional large acoustic transducers for high resolution breast imaging. The analysis indicates that using a 2D array would significantly increase the resolution of ultrasound mammography.				
14. SUBJECT TERMS Breast cancer, breast cancer detection, biofeedback, ultrasound, image processing			15. NUMBER OF PAGES 160	
			16. PRICE CODE	
17. SECURITY CLASSIFICATION OF REPORT Unclassified	18. SECURITY CLASSIFICATION OF THIS PAGE Unclassified	19. SECURITY CLASSIFICATION OF ABSTRACT Unclassified	20. LIMITATION OF ABSTRACT Unlimited	

GENERAL INSTRUCTIONS FOR COMPLETION OF 200

The Report Documentation Page (RDP) is used in announcing and cataloging reports. It is important that this information be consistent with the rest of the report, particularly the cover and title page. Instructions for filling in each block of the form follow. It is important to *stay within the lines* to meet optical scanning requirements.

Block 1. Agency Use Only (Leave blank).

Block 2. Report Date. Full publication date including day, month, and year, if available (e.g. 1 Jan 88). Must cite at least the year.

Block 3. Type of Report and Dates Covered. State whether report is interim, final, etc. If applicable, enter inclusive report dates (e.g. 10 Jun 87 - 30 Jun 88).

Block 4. Title and Subtitle. A title is taken from the part of the report that provides the most meaningful and complete information. When a report is prepared in more than one volume, repeat the primary title, add volume number, and include subtitle for the specific volume. On classified documents enter the title classification in parentheses.

Block 5. Funding Numbers. To include contract and grant numbers; may include program element number(s), project number(s), task number(s), and work unit number(s). Use the following labels:

C - Contract	PR - Project
G - Grant	TA - Task
PE - Program Element	WU - Work Unit
	Accession No.

Block 6. Author(s). Name(s) of person(s) responsible for writing the report, performing the research, or credited with the content of the report. If editor or compiler, this should follow the name(s).

Block 7. Performing Organization Name(s) and Address(es). Self-explanatory.

Block 8. Performing Organization Report Number. Enter the unique alphanumeric report number(s) assigned by the organization performing the report.

Block 9. Sponsoring/Monitoring Agency Name(s) and Address(es). Self-explanatory.

Block 10. Sponsoring/Monitoring Agency Report Number. (If known)

Block 11. Supplementary Notes. Enter information not included elsewhere such as: Prepared in cooperation with...; Trans. of...; To be published in.... When a report is revised, include a statement whether the new report supersedes or supplements the older report.

Block 12a. Distribution/Availability Statement. Denotes public availability or limitations. Cite any availability to the public. Enter additional limitations or special markings in all capitals (e.g. NOFORN, REL, ITAR).

DDP - See DDP 1230.24, "Distribution Statements on Technical Documents."

DDP - See authorities.

NASA - See Handbook NHB 2200.2.

NTIS - Leave blank.

Block 12b. Distribution Code

DDP - Leave blank.

DDP - Enter DDP distribution categories from the Standard Distribution for Unclassified Scientific and Technical Reports.

NASA - Leave blank.

NTIS - Leave blank.

Block 13. Abstract. Include a brief (maximum 200 words) factual summary of the most significant information contained in the report.

Block 14. Subject Terms. Keywords or phrases identifying major subjects in the report.

Block 15. Page Count. Enter the total number of pages.

Block 16. Price Code. Enter appropriate price code (NAPS 6-77).

Blocks 17-19. Security Classifications. Self-explanatory. Enter U.S. Security Classification in accordance with U.S. Security Regulations (i.e., UNCLASSIFIED). If from countries designated information, stamp classification on the top and bottom of this page.

Block 20. Limitations of Abstract. This block must be completed to assign a limitation to the abstract. Enter either UL (unlimited) or SAR (summary report). An entry in this block is necessary if the abstract is to be limited. If blank, the abstract is assumed to be unlimited.

FOREWORD

Opinions, interpretations, conclusions and recommendations are those of the author and are not necessarily endorsed by the US Army.

N/A Where copyrighted material is quoted, permission has been obtained to use such material.

N/A Where material from documents designated for limited distribution is quoted, permission has been obtained to use the material.

PB Citations of commercial organizations and trade names in this report do not constitute an official Department of Army endorsement or approval of the products or services of these organizations.

N/A In conducting research using animals, the investigator(s) adhered to the "Guide for the Care and Use of Laboratory Animals," prepared by the Committee on Care and Use of Laboratory Animals of the Institute of Laboratory Resources, National Research Council (NIH Publication No. 86-23, Revised 1985).

PB For the protection of human subjects, the investigator(s) adhered to policies of applicable Federal Law 45 CFR 46.

N/A In conducting research utilizing recombinant DNA technology, the investigator(s) adhered to current guidelines promulgated by the National Institutes of Health.

N/A In the conduct of research utilizing recombinant DNA, the investigator(s) adhered to the NIH Guidelines for Research Involving Recombinant DNA Molecules.

N/A In the conduct of research involving hazardous organisms, the investigator(s) adhered to the CDC-NIH Guide for Biosafety in Microbiological and Biomedical Laboratories.

Peter Blank 1/31/96
PI - Signature Date

TABLE OF CONTENTS

Early Detection of Breast Cancer on Mammograms Using: Perceptual Feedback, Computer Processed Images and Ultrasound Peter Bloch, Ph.D., Principal Investigator

	<u>Page Numbers</u>
Front Cover.....	1
SF298.....	2
Foreword.....	3
Table of Contents.....	4
Introduction of Report.....	5-6
 <u>Project 1a: Perceptual Feedback as an Aid to the Early Detection of Cancer on Mammograms</u>	
Introduction.....	7
Progress Report.....	7-10
Summary.....	10
Publications and Abstracts.....	10
References.....	10-11
 <u>Project 1b: Digital Image Processing of Mammography Films</u>	
Introduction.....	12-13
Body.....	13-25
Summary and Accomplishments.....	26
Literature Cited.....	27-28
 <u>Project 1c: High Resolution Ultrasound Mammography</u>	
Introduction.....	29
Summary of Achievements.....	29-32
Conclusions.....	32
Publications.....	32
References.....	32-33
Appendices.....	A-H

Early Detection of Breast Cancer on Mammograms Perceptual Feedback, Computer Processed Images and Ultrasound

Grant # DAMD 17-93-J-3014

Principal Investigator: Peter Bloch, Ph.D.

Clinical data indicates that early detection of breast cancer results in significantly higher success rates in the treatment of the disease. Ten year disease free survival greater than 95 percent are achieved with modern treatment when the breast lesions are detected less than <1 cm in diameter. The goal of this project was to improve the detection of small non-palpable lesions. Three methods for improvement in the detection of small lesions were explored in this study. These include:

Project 1A: Perceptual Feedback as an Aid to the Early Detection of Cancer on Mammograms,

Project 1B: Digital Image Processing of Mammograms, and

Project 1C: High Resolution Ultrasound Mammography.

In summary the major accomplishments include:

- An extensive database of high and low resolution digitized clinical mammograms was established that consists of 87 mammographic examination (two films per study ; a cranial-caudal and a oblique view). The clinical database has pathology confirmed abnormal lesions (34 microcalcifications, 28 masses) and 24 normals. This extensive database was required to test the efficacy of improving detection of lesions on mammograms both by perceptual feedback (project 1A) and computer image processing and feature extraction (project 1B).

- Hardware and software was developed for the computer display of high resolution digitized mammograms

- Elevated mammographic density has been associated in clinical studies with an increased risk of developing breast cancer. Techniques were developed and tested to quantify the fibroglandular tissue automatically from digitized mammograms.

- Algorithms were developed for extracting clusters of microcalcification from the high resolution digitized mammograms

- Hardware and software was developed for recording of eye-position of observers while reading mammograms

- It was found that false-negative decisions in reading mammograms was associated with prolonged visual dwell time. This information was feedback

to the observer (by placing a bold circle around the suspicious site on the image) which resulted in improved detection of masses.

- Two-dimensional ultrasound breast data was obtained and analyzed.
- Ultrasonic distortion in the female breast was identified in the 2D dataset including: (1) phase, (2) incoherent scatter and (3) multipath interference.
- Contrast resolution in breast ultrasound imaging was shown to be significantly restored using a phase deaberration algorithm
- Time-delay type compensation algorithms were developed and found to minimize the scattered energy significantly (15 dB)
- Significant progress was made in recognizing true targets from false ones caused by ultrasound interference. We demonstrated that the image of true targets remains in the same position and changes little in size or shape when imaged from different array locations.
- Design consideration were performed for 2D large acoustic transducers for high resolution breast imaging. The analysis indicated that the ultrawideband property of a 2D array would be more desirable than the conventional narrowband array. This would result in fewer array elements and much lower side band scattered energy .

The achievements on these projects are presented in this final report.

Grant # DAMD17-93-J-3014

Project 1A: Perceptual Feedback as an Aid to the Early Detection of Cancer on Mammograms.

Project Director Harold L. Kundel, M.D.

INTRODUCTION: RESEARCH OBJECTIVES

About 15% of tumors that are actually visible are missed on the initial reading of screening mammograms [Bird et al. 1992]. These misses are considered to be perceptual errors. Eye-position recordings made during the search for tumors on chest radiograms and mammograms have been used to classify perceptual errors into those due to incomplete scanning (15%), failure of the feature recognition mechanism (15%) and incorrect decisions (70%). Decision errors are associated with prolonged visual dwell on the tumor site in the image [Kundel et al. 1989]. Two observations have been made using chest radiograms. First, when sites that receive prolonged visual dwell during primary reading are identified and marked by circling, immediate re-evaluation results in an improvement in accuracy [Kundel, et al., 1990]. Second, circling a tumor site increases the readers ability to detect a tumor [Krupinski et al., 1993].

This project will extend the observations made on chest radiograms to mammograms. The following methodology is being followed. (1) Develop a computer display for mammograms that matches the grayscale properties of the display to the contrast discrimination function of the observer's eye. (2) Interface a head-eye-position recording system to the display. (3) Develop and digitize a set of mammograms with barely visible visual cues for tumor. (4) In a case-control study, compare detection performance with and without eye-position feedback.

PROGRESS REPORT:

Evaluation of the Performance of the Mammogram Display Station

The mammography display station has been implemented using a SUN SPARC 10, Dome video controller boards and two, Tektronix GMA 201 monitors. The active display area is 26 x 26 cm with a pixel matrix of 2048 x 2048 x 8. The images are stored in a 16 bit buffer that is reduced in size (2048 x 2048 pixels) and driving intensity (8 bit) for display. The images can be viewed in reduced size, natural size, and magnified. Reduction is sometimes necessary to fit an entire breast image into the window. Magnification is limited by the available pixels in the display buffer. No pixel replicating is permitted. The monitor gray scale has been perceptually linearized [Blume et al., 1993]. The portion of the intensity range that is displayed over the 8 bit display range is determined by adjusting the intensity window width and window center.

The display was tested using a set of 87 mammograms assembled by Dr. Orel. The set consisted of 34 cases with validated microcalcifications without masses, 28 cases with validated masses without microcalcifications and 25 case matched, control images. The matching of controls is by age, sex, and major incidental image features. The validity

of the normal images was determined by stability of the image findings for at least two years prior to the test mammogram. The images were digitized with two digitizers. Digitizer A (Lumisys) had a nominal scanning spot size of 100 microns and produced a 2030 x 2540 x 12 bit image from a 20 x 25 cm mammogram. Digitizer B (DBA) had a nominal scanning spot size of 43 microns and produced a 5075 x 6350 x 16 bit image from a 20 x 25 cm mammogram. The images were read by three experienced mammographers on film, and on the display station. The readers responses were recorded using a 5 level rating scale format which consistent with the receiver operating characteristic (ROC) analysis. The data were analyzed using ROCFIT [Metz,1986] and the area under the ROC curve Az determined for the detection of masses and calcification and for the classification of masses and calcification as benign or malignant. The results of the original test (R1) and a replication of the test (R2) made after a lapse of six months are shown in the Table 1.

Table 1. The performance of three readers given as the area under the ROC curve, Mean (St.Dev.).

		Detection		Classification	
		Calc'n	Mass	Calc'n	Mass
Film	(R1)	.98 (.02)	.95 (.03)	.82 (.06)	.77 (.08)
Scanner A	(R1)	.91 (.04)	.92 (.04)	.76 (.09)	.75 (.09)
	(R2)	.91 (.05)	.87 (.07)	.85 (.07)	.63 (.15)
Scanner B	(R1)	.91 (.07)	.93 (.04)	.62 (.10)	.76 (.10)
	(R2)	.87 (.09)	.90 (.05)	.75 (.10)	.75 (.10)

The data indicate that the digitizer-display combination degrades the detection of microcalcifications (The difference of .07 is significant , $p < .05$) but not the detection of masses. Classification shows more variation (.62 to .85 for calcification and .63 to .76 for masses) but is not affected by digitization and soft copy display. This sample could not show a difference between digitizer. The limitation may be in the display.

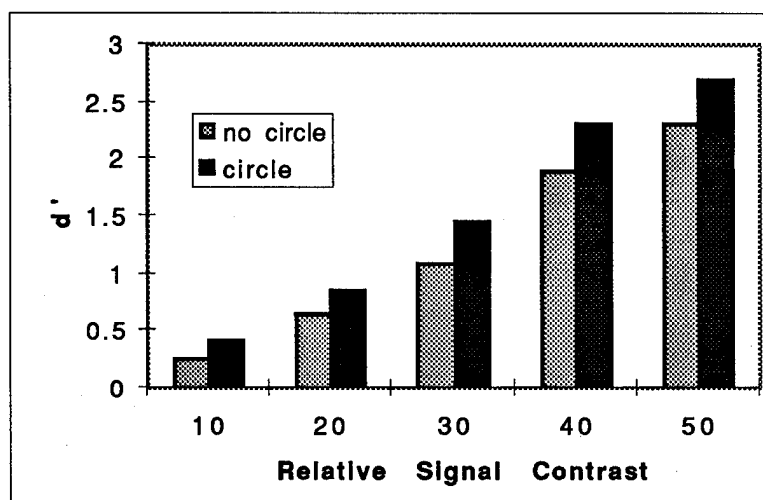
Confirmation that Gaze Duration Predicts the Location of Tumors by Eye-position Recording During Search

The Applied Science Laboratories (ASL) eye and head position monitor has been used to record the eye-position of 3 mammographers during the search for tumors. We have confirmed the observation that false-negative decisions are associated with prolonged visual dwell time. (This also has been confirmed independently by Krupinski and Nodine [1994].) The ASL eye and head tracker has an accuracy of .5 degrees (.5 cm at 57 cm viewing distance) and a precision of .3 degrees. This means that 95% of x,y coordinates are within .3 degrees of the recorded value (precision) and that 95% of the recorded values are within .5 degrees of the location of the fixation. This level of precision and accuracy is adequate for identifying image sites that receive long visual dwell.

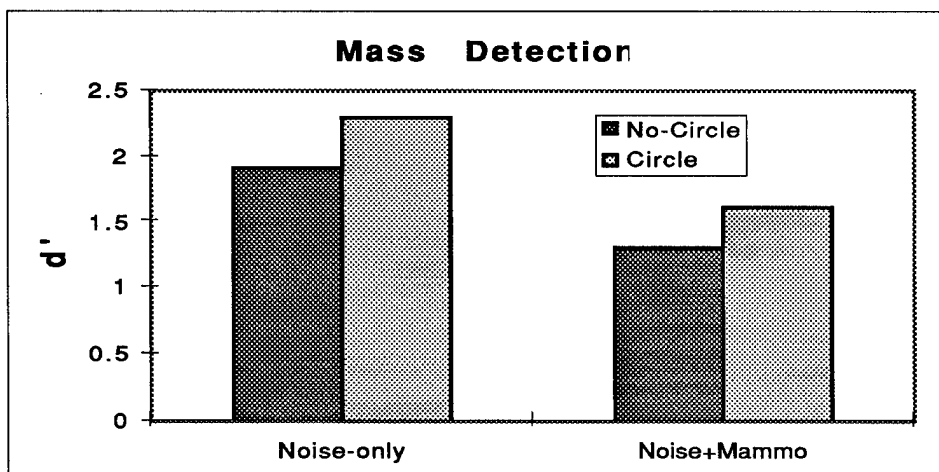
Observations on the Method for Providing Visual Feedback

Visual feedback is provided by putting a five degree circle around the suspicious site. Krupinski et al. [1993] observed that the circle itself increased the detectability of lung tumors. We performed two experiments to study the effect of using a bold circle as a visual prompt.

The first experiment used a background of gaussian noise containing a 1 cm object that simulated a mass on a mammogram. Three observers participated in a two alternative forced choice (2AFC) task to measure the detectability of the mass as a function of contrast. The index of detectability d' was measured using standard signal detection procedures. The mass was always displayed in the center of a defined field with a uniformly noisy gray background. Two conditions were compared: the uniform field and the field containing a bold 5 degree circle. The results in the graph below show that the circle enhanced detectability.



The second experiment used a section of a mammogram as the background in addition to the same level of gaussian noise as was used in the first experiment. The results show that the addition of the mammogram as a background decreases the detectability at the two contrast levels and that the addition of a bold circle to the display enhances the detectability.



We hypothesize that the circle acts as a fiducial marker for the visual scanning system allowing stabilization of visual drift which has the effect of increasing the contrast sensitivity of the retina [Kundel, 1995]. Data to test this hypothesis has been collected but has not been fully analyzed.

Comparison of Detection Performance With and Without Perceptual Feedback

The eye-position recording system is functioning in a satisfactory manner. We and others have shown that areas containing masses on mammograms receive prolonged visual dwell even when they are not reported. We also have shown that a 5 degree bold circle placed on the image enhances the detectability of masses embedded in gaussian noise and in breast parenchyma. It now remains to couple the two phenomena in real-time, in order to demonstrate that computer assisted visual search improves performance. This portion of the experiment will be completed as funding becomes available.

SUMMARY

We have developed a system for providing visual feedback in response to measurement of gaze duration during the viewing of mammograms on a video display. We have shown that the display has satisfactory fidelity and that the precision and accuracy of the eye-position tracker is adequate to provide reliable feedback. The feedback consists of drawing a bold circle of 5 degrees diameter around the suspicious site. The circle has been studied independently as a visual prompt and has been shown to be an effective method for enhancing visual performance. The neurophysiologic reason for the enhancement is under investigation. A practical test of computer assisted visual search is being planned.

PUBLICATIONS AND ABSTRACTS

Kundel HL, Nodine CF, Orel SG, Barudin JL, Toto L. Computer assisted visual search in mammography. *Radiology* 1994;193(P):475.

Kundel HL, Toto, LC and Lauver, S. Further observations on the k effect. Presented at the Sixth "Far West" Perception Conference. Philadelphia, PA. 13 Oct 1995.

REFERENCES

Bird RE, Wallace TW, Yankaskas BC. Analysis of cancers missed at screening mammography. *Radiology* 1992;184:613-617.

Krupinski EA, Nodine CF, Kundel HL. Perceptual enhancement of tumor targets in chest x-ray images. *Percep & Psychophys* 1993;53:519-526.

Krupinski EA, Nodine CF. Gaze duration predicts the locations of missed lesions in mammography. In: Gale AG, Astley SM, Dance DR, Cairns AY, ed. *Digital Mammography*. Amsterdam: Elsevier, 1994: 399-403.

Kundel HL, Nodine CF, Krupinski EA. Searching for lung nodules : Visual dwell indicates locations of false positive and false negative decisions. Invest Radiol 1989;24:472-478.

Kundel HL, Nodine CF, Krupinski EA. Computer displayed eye position as a visual aid to pulmonary nodule interpretation. Invest Radiol 1990;25:890-896.

Metz CE. ROC methodology in radiologic imaging. Invest Radiol 1986; 21:720-723.

Project 1B: Digital Imaging Processing of Mammography Films.

Project Director: Peter Bloch, Ph.D

Introduction

The treatment of small breast lesions (less than 1 cc in volume) with lumpectomy and definitive radiation therapy results in excellent clinical results with 10 year disease free survival better than 95 %. Thus early detection and treatment of breast neoplasms when the lesions are too small to be palpable is most likely to be effective in sterilizing the tumor (Tabar et al.,1992). Mammography examinations are a proven diagnostic procedure for detecting early breast cancer in asymptomatic women (Moskowitz,1984,Kopans,1984 and Feig,1988).

Despite the documented potential for mammography to result in decreased breast cancer mortality, there is some concern that some segments of the population are not fully benefitting from the examination because of variations in quality and interpretation of the mammograms performed. The radiographic appearance of the female breast differs among women in relation to the amounts of fat and fibroglandular (connective and epithelial) tissue present. Areas of fat are radiographically lucent while fibroglandular tissue are radiographic dense. Many studies have looked at the relationship between mammographic density and the risk of developing breast cancer, and the majority of the studies have found an association between parenchymal patterns and risk of developing breast cancer. A recent meta-analysis confirms the association of increasing risk with increasing percentage of density of the breast (Oza and Boyd,1993 and Warner et.al.,1992). The degree of increased risk associated with elevated density may be greater than any other generally recognized risk factor for breast cancer, with the exception of the presence of the BRCA1 gene (Oza and Boyd,1993).

A subjective evaluation of parenchymal density on mammograms, the Wolfe classification scheme (Wolfe,1976), was used for many years, however interobserver variability was a significant problem (Moskowitz et.al.,1980,Myers et.al.,1983, and Carlisle et.al.,1983). It is widely assumed that the sensitivity of mammography is lower in women with increased mammographic density, but the magnitude of the decrease sensitivity has not been studied. This is partially due to the lack of a quantitative measure of mammographic density. A computer assisted method for quantifying mammographic density as a percentage of the image area can overcome this limitation (Boyd et.al.,1995 and Byng et.al.,1994). One of the goals of this research project was to use computer techniques to quantify stromal or parenchymal patterns on mammograms.

Characterization of the breast parenchyma involves analyzing the diffuse mammographic density pattern which depends on the low frequency components in the mammography image. Tumors of diffuse histology are more difficult to detect in the presence of increased mammographic density (Kopans,1992), thus breast density may be the primary cause of missed carcinomas (Kopans,1992 and Hollingsworth et.al.,1993). Estimates of the number of women with mammographically dense breast varies between

10-35 percent (Kopans,1992),decreasing with age. For example,Wolfe et. al.(1987),showed that 66% of women over 53 years old had less than 25% parenchyma density compared to 37% of younger women in that category. Computer identification and processing of mammographic dense mammograms could be an important tool for reading these difficult mammographic cases.

Another goal of this research project was to improve the detectability of breast lesions using computer assisted identification of clusters of microcalcifications on mammograms. Clusters of microcalcification on mammograms is a radiographic feature often identified in early stage breast cancer (Sickles,1986). Approximately 30-50% of the breast carcinomas are detected by microcalcification on mammograms and 60-80% of biopsied confirmed breast carcinomas show microcalcification on histopathology samples. Thus reliable identification of small clusters of microcalcification is a major importance in screening women for early stage disease. Research groups are developing computerized techniques for identifying microcalcifications on mammograms (Chan et al.,1987,1988,1992,Fam et al.,1988,Davies and Dance 1990). Studies from the University of Chicago report 85 percent true microcalcification identification on mammograms using computer-aided detection (CAD) of microcalcification (Wu et al.,1992,Zhang et al.,1992,and Ema et al.,1993). CAD techniques developed by Zheng et.al.,(1995) using topographic feature analysis also report a false-positive detection rate to 0.18/image or 82% true microcalcification detection. In the above studies the mammograms were digitized at 100-175 microns with 10 bits of dynamic range. To further improve on the computer-aided detection of microcalcification a higher quality,high resolution mammographic film digitizer was employed to preserve the spatial resolution and wide latitude of the original mammography film image.

B: Body : Accomplishments of the Project:

B.1 Digitized Mammography Database

Software and hardware tools for archival and retrieval of high resolution digital mammography images are now available for routine use. The software for rapid display of digitized mammographic images with user selected contrast and magnification has been developed using the Interactive Data Language, IDL, package which is readily transportable to different computer platforms. A database of clinical mammograms was established. Dr. Susan Orel, a mammographer, identified 87 clinical mammograms; twenty-five normals, thirty-four with histopathology confirmed microcalcifications and twenty-eight with solid tissue masses. Each mammogram was scanned twice with two different microdensitometers: (1) Lumisys-100 microdensitometer, using a 100 micron pixel size and 12 bit dynamic range and, (2) a DBA microdensitometer with a 42 micron pixel size and 16 bit gray-scale. The digitized images were stored for archival on an optical disk. The size of the database of digitized mammography images is approximately 6 gigabytes.

B.2 Performance Characteristics of Microdensitometers:

The performance characteristics of two microdensitometers; (1) Lumisys-100 employing 100 micron pixels and (2) DBA were evaluated for digitizing mammography films. Their characteristics are summarized below.

B.2.1 LUMISYS-100 MICRODENSITOMETER

The microdensitometer employs a 2 mW helium-neon laser beam. Precision mirrors mounted on a precision galvanometer movement is used to sweep a 100 micron light spot across the image plane. The light transmitted through the film is detected with a photomultiplier tube, the signal from which is logarithmically amplified and digitized. Linear regression analysis of the microdensitometer output with optical density is shown in fig. 1. The maximum signal intensity occurs at approximately 2.5 OD, corresponding to a useful dynamic range of 11 bits. However the noise evaluated from the analysis of the relative standard deviation in the output from a region of interest, ROI, of 10,000 pixels increases from approximately 0.3% at 2 OD to 0.9 % at 2.5 OD which further reduces the useful dynamic range of the scanner.

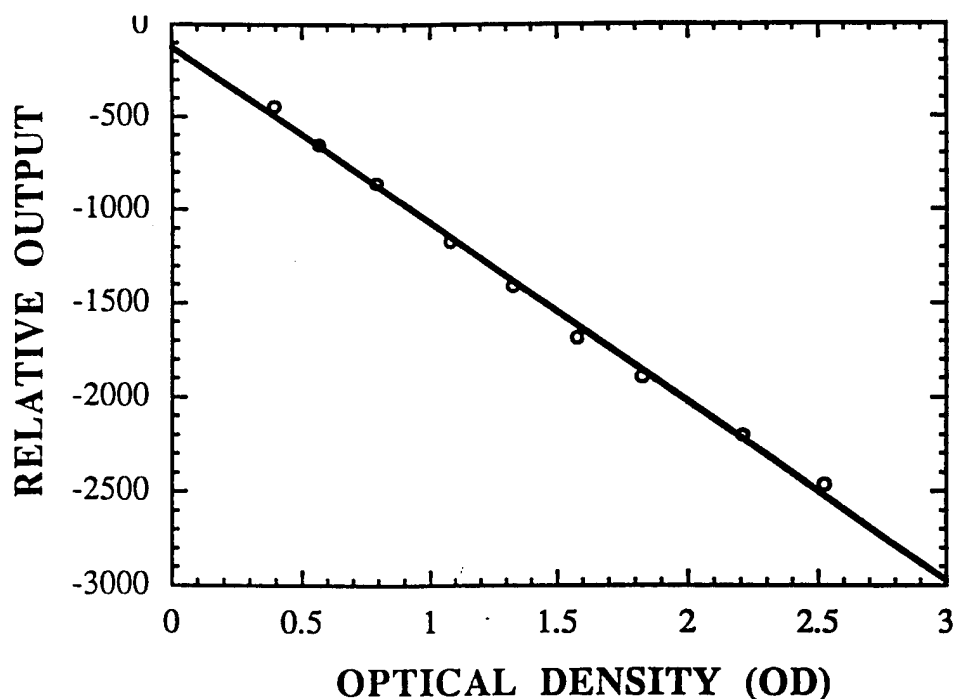


Fig.1: Lumisys microdensitometer output with optical density

The modulation transfer function, MTF, for the microdensitometer was determined by taking the Fourier transform of a line spread function derived from the gradient of a measured edge spread function. The edges of square cut-outs in opaque films, 4 OD, were scanned to measure the edge spread function. The edge spread function was found to be nearly the same for all the edges of the square cutouts. The calculated MTF is shown in fig.2. The highest spatial frequency is the Nyquist cutoff frequency, 5 cycles/mm, associated with the 100 micron pixel size.

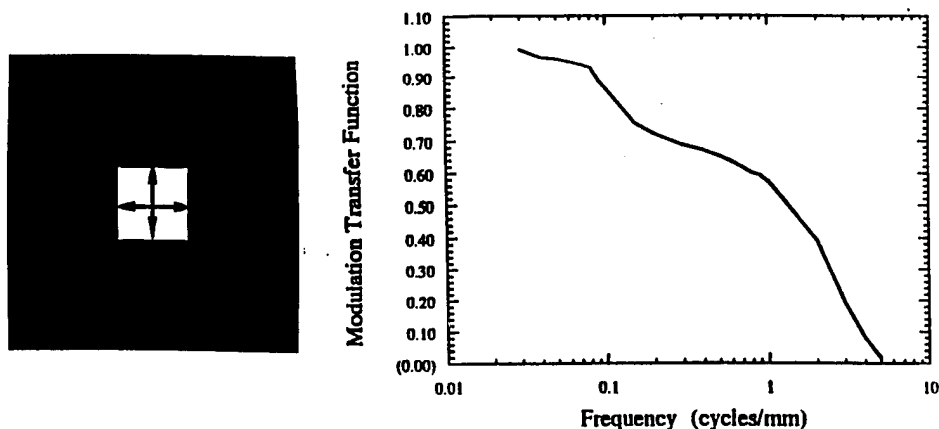


Fig. 2 Modulation Transfer Function for Lumisys Microdensitometer

B.2.2 DBA Microdensitometer

The DBA microdensitometer scans the image plane with a 42 micron wide line light source obtained from a temperature controlled masked straight fluorescent tube. The light is detected with a 6048 linear array charge coupled detector (CCD). An image is digitized by moving the film across the line source. Digitizing a 10x12 inch mammogram requires approximately 22 seconds.

The output of the densitometer is exponential in the optical density range of 0- 4 OD (fig. 3). Routine clinical mammograms contain regions of high density thus the wide range of digitization is important for preserved all the information on the original image.

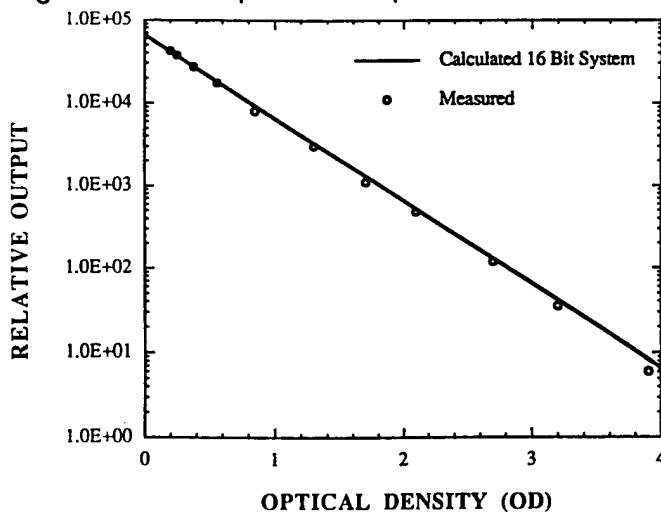


Fig. 3 Output of DBA scanner as a function of optical density

The MTF for the densitometer was derived from the measured edge profile along a single 42 micron wide scan line. The measured edge was found to depend on the edge of the square cutout scanned. Fig. 4 shows that in the direction of the light source the edge is blurred, and sharp in the direction that the film is being scanned. The light in the direction of the line source is scattered, producing glare, whereas in the direction that the film moves the registration of the light source and detectors eliminates the effects of glare.

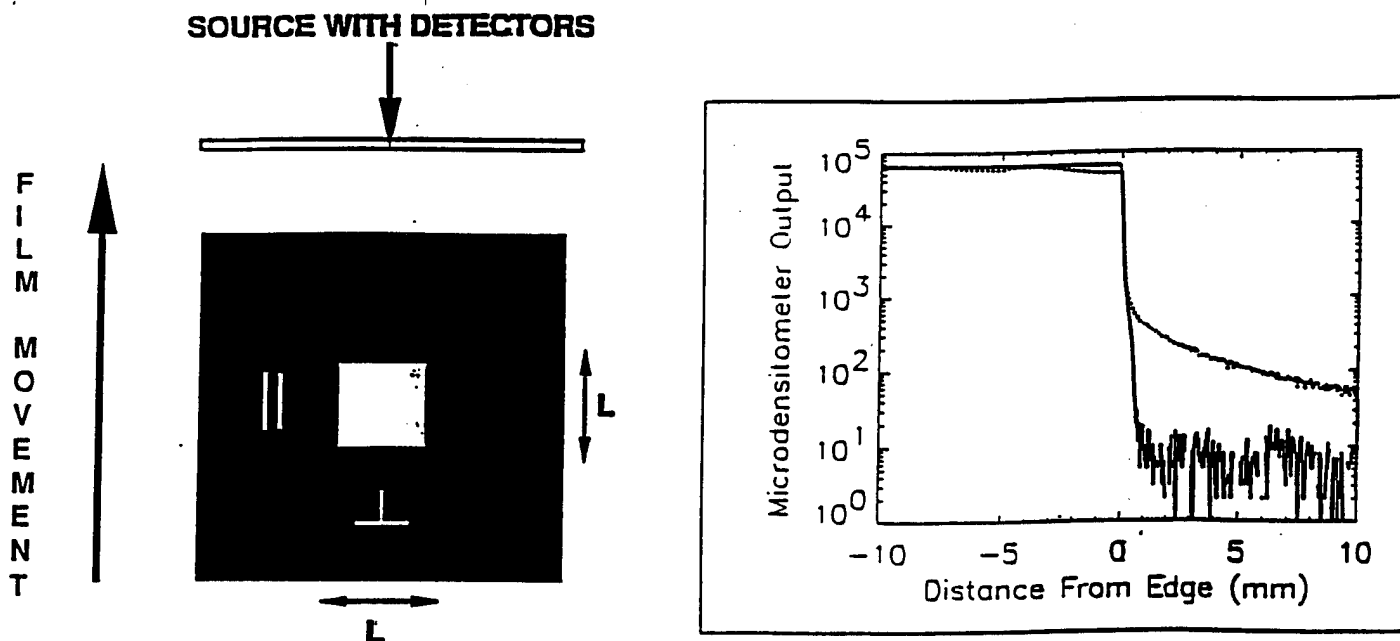


Fig. 4. Edge measured with the DBA microdensitometer. Scanned in the direction of the line light source,(solid line),and perpendicular to the light source (dotted line).

The edge spread function, ESF, in the direction of the line light source was found to be nearly independent of irradiated area, over the range studied 1-25 cm². This area was defined by cutouts in opaque films. In addition, placing neutral density filters between, 0.25-0.98 OD, over the square opening did not significantly alter the measured ESF.

The MTF derived for edge spread functions are shown in fig. 5. The high frequency cutoff is at the Nyquist frequency 11.9 cycles/mm corresponding to the pixel size of 42 microns. The MTF at lower frequencies is significantly reduced in the direction of the line source. Thus the degradation in image quality associated with the presence of glare is predominately in the low frequency components. This would suggest that the effects of glare on the image can be significantly reduced by filtering the low frequency components measured in the direction of the light source.

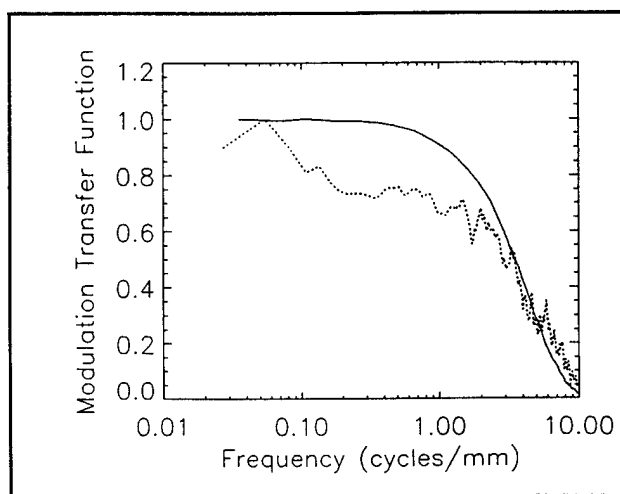


Fig. 5: MTF for the DBA microdensitometer. Scanned in the direction perpendicular to the line light source,(solid line),and in the direction of the light source (dotted line).

Figure 5 indicates that the noise in the direction of the line source is much greater than the noise in the direction perpendicular to the light source. Noise could arise from fluctuations in the; (1) light intensity along the light source, (2) cross talk between elements in the large linear CCD detector array, and (3) analog to digital conversion.

Figure 6 shows the relative noise power spectra measured in three regions: (1) within the square cutout region containing no film, (solid line), (2) in an opaque area lateral to the square cutout in the direction of the line source, (dashed line), and (3) in an opaque area perpendicular to the direction of the line source, (dotted line). In region 2, the noise is associated with glare, which decreases with increasing spatial frequency. In region 3, the noise is a low level white noise. In region 1, superimposed on the noise due to glare is shot noise associated with the linear array CCD detector.

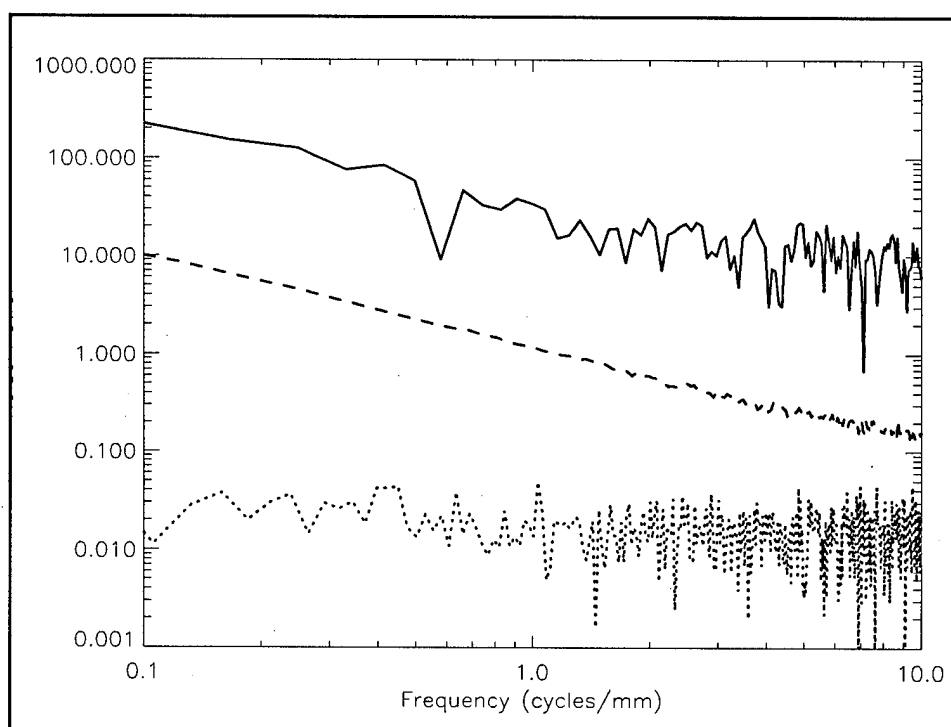


Fig. 6 Relative noise power for the DBA scanner. Solid line, region of high light signal, and opaque regions; (dashed line), lateral to the square cutout in the film in the direction of the light source, and (dotted line) perpendicular to the direction of the linear light source.

The implication of noise on visual perception of microcalcification and masses on digitized images is not clear. However, the directional dependence of the noise may have some implications in computer aided detection, CAD, of clusters of microcalcification. The increase in shot noise associated with the signal intensity may have implication in using CAD for identifying microcalcification in regions of dense breast tissues.

A comparison of the two MTF's in figures 2 and 5 for the Lumisys and DBA scanners respectively demonstrates the improvement in the physical performance of the higher resolution scanner. The results of the observer testing described in project 1B showed however that digitized images produced by both microdensitometers resulted in comparable performance in identifying clustered microcalcifications and masses on mammograms. However, this evaluation did not permit the observer to alter the display contrast. The ability to vary contrast may be an useful tool for the reader in searching for microcalcification in difficult high mammographic density regions of the mammogram (Taylor et al.,1994). The 16 bit digitization depth available with the DBA scanner may be important for preserving the wide latitude of the mammographic film study,however the dynamic range requirements for digital mammography continues to be investigated (Maidment et al.,1993,Neitzel,1994).

Algorithms were developed for identifying clusters of microcalcifications by analyzing the regional distribution in the image of the; (1) power at high spatial frequencies (2) fractal dimension (Lefebvre et al.,1992,1995 and Priebe et al.,1994) and (3) entropy. The analysis used the digitized images obtained with the high resolution microdensitometer.

B.3 Quantitative Determination of Mammographic Density

B.3.1 Background

To quantitate mammographic density, we used the high resolution digitized film set described above. The DBA digitized images were reduced in size to display on a 1k x 1k monitor. We developed software for quantitative analysis of mammographic density based on the method described and validated by Byng et. al. (1994) but with modifications to make the method more operator-independent. To determine the projected area of the breast on the image, the reader selects a background area of approximately 4 x 4 cm² which contains no breast tissue. The edge of the breast (i_{edge}) is then determined automatically by excluding the region containing all signal less than the mean +4 times the standard deviation of the selected background region. This differs from Byng in that this method requires a knowledgeable observer to select the skin edge of the breast. With our modification, total breast area can be determined by an untrained, naive observer, and is highly reproducible. The total area of the breast is designated A_{br} . The reader then superimposes on the digitized image color computer-generated contour lines of constant signal or optical density and selects the contour line (i_{dens}) that encompasses the region of high mammographic density (Figure 7). The area of increased parenchymal density is equal to the sum of pixels above the threshold (i_{dens}) value designated A_{pd} . The percentage of parenchymal density, PD, is:

$$PD = (A_{pd}/A_{br}) \times 100 \quad (1)$$

In addition, software has been developed to produce a histogram of signal intensities from the digitized image. The threshold for i_{dens} can be interactively selected by the observer, as described above by Byng et. al.,(1994) and compared with the histogram.



Fig.7. Example of digitized mammogram with computer generated skin edge (i_{edge} , red) to determine breast area, and computer generated contour line (i_{dens} , yellow) demarcating area of increased parenchymal density.

A typical histogram of signal intensities associated with fatty, low density tissue is shown in Fig. 8 (left panel) . Region 2, above a signal intensity of approximately 250 corresponds to the higher density fibroglandular tissue. The first derivative of the histogram, (dashed line insert in fig.8), often helps to demarcate the start of region 2.

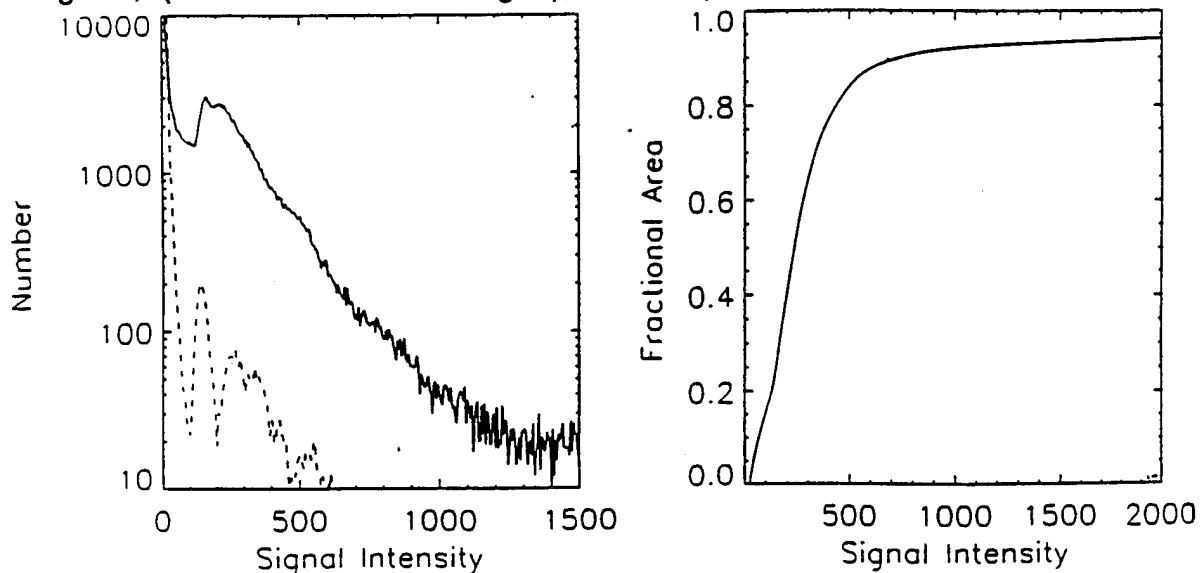


Fig. 8 Analysis of signal intensities in mammogram; Lt. Panel: Histogram showing number of pixels with various intensities (solid line), derivative of histogram(dashed line); Rt. Panel: Fractional breast area-signal cumulative histogram.

The cumulative histogram could also be of use to evaluate the fractional area of the image above a particular signal intensity. A cumulative histogram can be modeled as a sum of normal distributions with different means $x(i)$ and Gaussian spread parameter $\sigma(i)$ by the integral. The breast tissue area $F(\xi)$ having signal intensity less than ξ is

$$F(\xi) = \int_0^{\xi} \{N(1)\exp(-\sigma(1)^2 (\xi-x(1))^2) + N(2)\exp(-\sigma(2)^2 (\xi-x(2))^2) + \dots\} d\xi \quad (2)$$

where $N(1)$ and $N(2)$ are the number of events in peaks $x(1)$ and $x(2)$ respectively. The Gaussian spread parameters can be evaluated from the full-width half-maximum for each peak in the histogram distribution. The fractional area of a mammogram having a signal intensity below a particular level ξ , $F(\xi) / F(\infty)$ is shown in fig. 8 (right panel). As a first approximation the break from the linear portion of the sigmoid curve was used to determine the fraction of elevated density in the image which is $1 - 0.64 = 0.36$ or 36% for this example. In practice, however, a least-square-fit to the cumulative histogram is employed to extract the fraction of elevated tissue in a mammogram.

B.3.2 Results of Mammographic Density Analysis

Twenty mammograms from a test set were randomly selected for this preliminary study to demonstrate methods and data analysis of (a) the inter-radiologist reliability of the radiologists' assessments of density; and (b) the concordance between radiologist assessment of density and computer-measured density. The original films were presented independently to 3 radiologists who assigned 1 of 4 subjective categories of density to each case. The 4 categories were: (1) less than 25% high density, (2) 25 to 49% high density, (3) 50 to 75% high density, and (4) greater than 75% high density.

Computer-assisted measurement of high density parenchyma was performed as described above on the digitized images of the same cases. The quantitative measurements were performed by a physicist unfamiliar with interpreting mammograms, assisted by a student research assistant with no mammography experience. The cumulative histograms were used to evaluate the percentage of mammographic area with high density.

1. Table 3 gives mean radiologist assessment (1-4 scale) for each radiologist:

Table 3

Radiologist	Mean	SD
1	2.5	1.1
2	2.8	1.1
3	2.5	1.2

An analysis of variance (ANOVA) model including radiologist and patient number as factors, showed significant differences among radiologists ($p = 0.017$) on this assessment.

The patient terms are needed to control for the correlation induced by having three assessments done on each patient. Essentially, the patient terms force the comparison among radiologists to be made within patient.

2. We calculated the intraclass correlation coefficient (ICC) as a measure of agreement among radiologists. The ICC is defined as the ratio of the among-patient variance in radiologist assessments to the total variance (among-patient and within-patient) in radiologist assessments of density. Because the within-patient variability results from disagreements among radiologists, the ICC provides a measure of agreement. The values of the ICC range from 0 to 1. When there is perfect agreement among radiologists, there will be no within-patient variability, and the ICC would be 1.

We estimated the ICC using an ANOVA model with radiologist assessment as the outcome variable and patient as the grouping factor. The ICC is then calculated as:

$$ICC = BMS / (BMS + (m-1)WMS) \quad (3)$$

where BMS is the "between" patient mean square from the ANOVA model, WMS is the "within" patient mean square from the ANOVA, and m is the number of measurements on each patient, in this case, 3. The calculated value of the ICC for the data was 0.89, indicating excellent agreement among radiologists. This probably reflects the fact that the three radiologists practice together.

3. Associations between the quantitative measure of density and the radiologists' assessments were evaluated in several ways. For each radiologist individually, and then for all radiologists together, we estimated the Spearman correlation coefficient between the assessment and the quantitative data using the radiologist's assessment as an ordinal predictor variable. Because the regression R^2 values were in nearly perfect agreement with the Spearman coefficients, only the Spearman correlations are presented (Table 4).

Table 4

Radiologist	Spearman Rho
1	0.85
2	0.79
3	0.76
Overall	0.79

These correlations show that there is excellent agreement between the radiologists subjective assessments and the quantitative measurements made by untrained observers. The overall R^2 for the regression described above was 0.64, corresponding to a Pearson correlation of 0.8, again nearly perfectly consistent with the Spearman correlations.

4. Table 5 shows the ranges of quantitative values for each category of the radiologist's subjective assessment, along with the means and standard deviations of the means for each category. The mean was calculated for all assessments at a particular

value, regardless of the radiologist or the patient. In other words, every radiologist's assessment of every patient that was a "1", is included in the summary.

This again shows the strong association between the subjective and objective scores, but there is considerable overlap of the ranges of quantitative values between categories of the subjective assessments. Note the range of quantitative values grouped by radiologists into a single category.

Table 5

Radiologist's Assessment	Range of Quantitative value(%)	Mean Quantitative value (%)	SD
1 (<25%)	12-36	18.7	6.7
2 (25-49%)	17-71	38.3	14.5
3 (50-75%)	29-85	54.3	21.5
4 (>75%)	53-85	67.8	11.6

B.4 Computer Aided Detection of Microcalcification

B.4.1 Background

The use of computer aided detection (CAD) of microcalcifications on a mammogram is being extensively explored. No one single image feature, however, by itself has been identified for segmenting a possible microcalcification from normal tissue and image noise. CAD techniques have been developed where the signal to noise ratio of microcalcifications are first enhanced by reducing the high frequency quantum noise, and removing the low frequency structured background from the image. Extraction of image features from these filtered images using local adaptive thresholding procedures in conjunction with artificial neural networks have been successfully employed to achieve a true positive microcalcification detection rate of 80-85% (Chan et al., 1987, 1988, 1990). CAD techniques developed by Zhang et al., (1995) using topographic feature analysis also report a false-positive detection rate to 0.18/image or 82% true microcalcification detection. To further improve on the computer-aided detection of microcalcification a higher quality, high resolution mammographic film digitizer was employed to preserve the spatial resolution and wide latitude of the original mammography film image.

The spatial frequencies in mammography images is greater than 10 cycles/mm with the film-screen combination typically employed. The Nyquist frequency corresponding to 10 cycles/mm requires that the pixel size be less than 50 microns. In the above studies the mammograms were digitized at 100-175 microns with 10-11 bits of dynamic range. Chan et al., (1994) showed however that detection of subtle microcalcification in mammograms may require much finer resolution e.g. 35 micron pixels. The preservation of the higher spatial frequencies in the digitized mammogram permitted us to explore use of the high frequency components for computer identification of microcalcifications.

B.4.1.1 Feature Extraction from Digitized Mammography Images

The following features within small 5x5 mm² (128x128 pixels) region of interests (ROI) on the mammogram were evaluated; (1) signal intensities (2) power spectrum (3) fractal dimension and (4) entropy.

(1) A histogram of the signal intensities within each ROI is calculated and used to identify pixels within the region with elevated signals that may be associated with microcalcifications. The histogram is used to determine the average signal value within each ROI and the contrast between the individual pixel signal and the average value. The region is flagged as suspicious if a small fraction (0.002) of the pixels in the ROI have a signal intensity that results in a contrast of greater than 5%.

(2) The power spectrum in each ROI was analyzed, using a two dimensional Fourier transform (2DFT). Regions of the mammogram with power at spatial frequencies greater than 2 cycles/mm were flagged as regions that may contain small microcalcifications. In addition, the directionality Θ , of power $P(v)$ at spatial frequency v was evaluated with the following expression:

$$\Theta(v) = \tan^{-1} \{P_y(v) / P_x(v)\} \quad (4)$$

where $P_y(v)$ and $P_x(v)$ are the spatial frequency components of the 2D-Fourier transform in the two orthogonal directions x and y . Information on the directionality of the power spectrum is used to help separate ROIs with significant power at high spatial frequencies due to microcalcification from those ROIs that have sharp boundaries between fat and high density parenchyma tissue. The directionality of power associated with clusters of microcalcifications is often isotropic, whereas interfaces between tissue types have a preferred direction.

(3) The fractal dimension (FD) within a ROI is a measure of the irregularity of the signal intensities in the region. A constant or a smooth variation of signal intensities within an ROI would approach a FD of 2, whereas the presence of an abnormality such as microcalcifications on a relatively smooth background of breast tissue would correspond to a rough surface approaching a FD of 3. Fractal analysis has been employed by Lefebvre et.al.,(1995) and Priebe et al.,1994 to identify microcalcifications within small regions of a mammography image. We developed an algorithm to calculate the FD from the variation of the power spectrum with spatial frequency (Ruttimann et.al.,1992). The calculated power spectrum $P(v)$ at frequency v is expressed as a power function

$$P(v) = av^b \text{ or } \log(P(v)) = \log(a) + b\log(v) \quad (5)$$

where a least square fit of $\log\{P(v)\}$ vs $\log(v)$ was used to determine the value of b and its associated correlation coefficient. The FD in each ROI was calculated from the absolute value of b by the relationship given by Ruttimann, et al, (1992)

$$FD = 3-(b-1)/2 \quad (6)$$

Due to the sharp discontinuities associated with microcalcifications, the fractal dimension in regions containing microcalcifications is expected to be both elevated with a larger standard deviation compared to normal tissue.

(4) Entropy is a measure of the disorder within an ROI. Regions containing microcalcifications may be more disordered than a region containing normal parenchyma breast tissue. The first order entropy b_E (Pratt, 1978) in each ROI was evaluated using Shannon's Information Law

$$b_E = - \sum_{b=0}^{L-1} (N(b) / M) * \log_2 (N(b) / M) \quad (7)$$

where $0 \leq b \leq L-1$ denotes the quantized amplitude levels, M is the number of pixels in the region, and a base-two logarithm is utilized resulting in the entropy measured in bits.

B.4.1.2 Results of Extraction of Microcalcification on Mammograms

An example is shown in using the above feature extraction algorithms to identify suspicious regions on a mammograms. The original matrix size of the mammogram shown in fig.9 was approximately 3000x5000 X 16 bit which was reduced 5 fold to fit on the display monitor. The analysis was performed using the full data set. The power spectrum was analyzed, using 2DFT, within small regions 5x5 mm² (128x128 pixels) of the mammogram. The total number of regions, ROIs, analysed was 738. Regions with power at spatial frequencies greater than 2 cycles/mm are marked on fig. 9. The DBA scanner used to digitize the mammogram has an MTF of 0.75 at 2 cycles/mm and a Nyquist frequency 11.9 cycles/mm. The 100 micron pixel size used with the Lumisys scanner resulted in an MTF less than 0.4 at the 2 cycles/mm threshold frequency used in this analysis (and zero above 5 cycles/mm). Regions 64 and 106 in fig. 9 are biopsy confirmed microcalcification, region 256 is a lead marker placed on the breast, and regions 172,214,218 are near signal intensity gradients associated with the interface of dense and more usual parenchymal tissue.

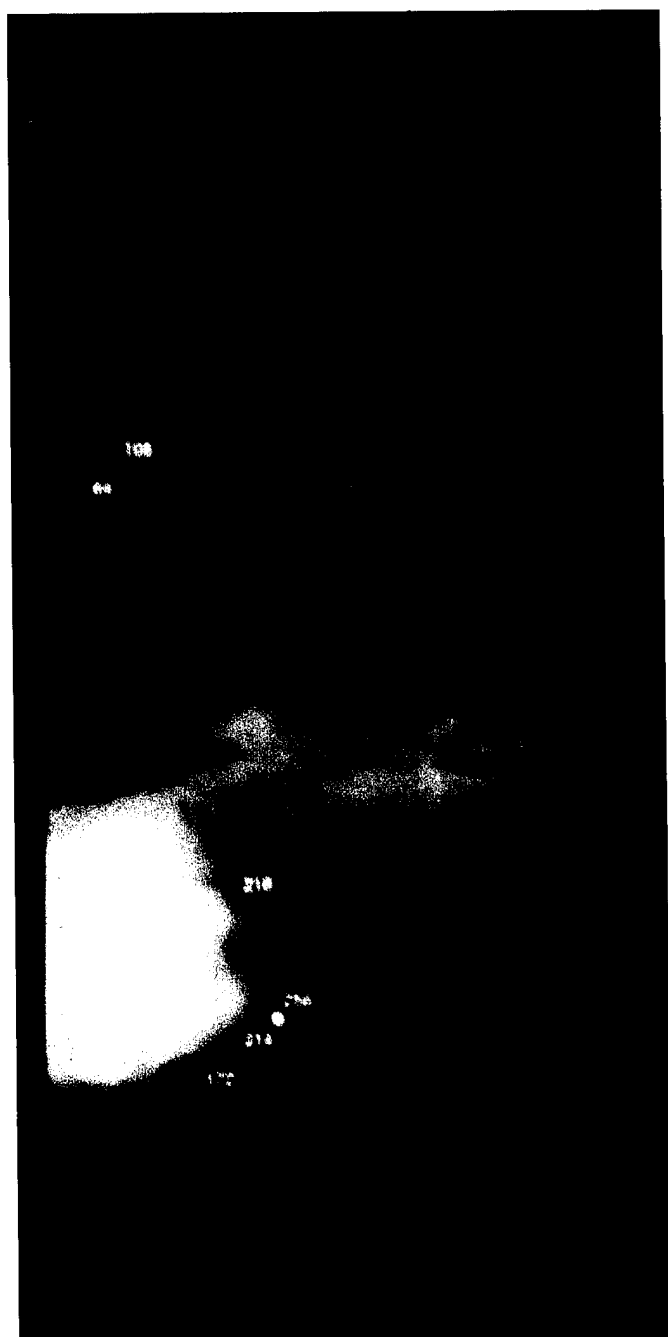


Table 6

Region #	Relative Entropy
64 (μ Ca)	1.0
106 (μ Ca)	1.87
172 (tissue interface)	2.56
214 (tissue interface)	3.47
218 (tissue interface)	2.65
256 (lead marker)	4.46

Fig.9 Computer designated suspicious regions on mammogram

Besides the power spectrum the additional image features evaluated in each ROI includes; signal intensity distribution, fractal dimension and entropy. In this example, the most striking difference between the regions with microcalcifications and tissue gradients was in the entropy. Table 6 shows the relative entropy in the ROIs of the image that were flagged. Entropy is a measure of order, the lower the entropy the greater the structure within that region of the image.

B.5 Summary and Accomplishments:

In summary, the goal of the project was to use computer techniques to assist the radiologist in reading mammograms. To accomplish this task, we developed a data base of high resolution digitized mammograms consisting of nearly 100 studies (two views per study). The storage, retrieval, and the processing of these large data files has been shown to be achievable using existing computer technology.

Algorithms were developed during the course of the project to quantify tissue densities on mammograms. The presence of increased mammographic density has been previously identified by radiologists as a primary cause for not detecting carcinomas on mammograms. The ability to quantify parenchymal density mammograms will thus allow physicians to readily separate the "difficult" mammograms for additional study or analysis.

To detect microcalcification on mammograms we developed algorithms that evaluated image features in 5×5 mm² regions on the high resolution digitized mammograms. The features that were analyzed include: (1) signal intensity distribution (2) spatial frequency power spectrum, (3) fractal dimension and (4) entropy. The high spatial frequencies preserved in the digitized images helped in computer identifications of microcalcifications. In addition, the disorder in the tissue parenchyma associated with the presence of clusters of microcalcifications can be quantified by evaluating the entropy in the region.

As these findings warrant further studies (particularly observer performance confirmation) we are requesting continuation of the project without any additional funding.

B.6 Literature Cited:

- Boyd, N., Byng, J., Jong, R., Fishell, E., Little, L., Miller, A., Lockwood, G., Trichler, D., & Yaffe, M. (1995) Quantitative Classification of Mammographic Densities and Breast Cancer Risk: Results From the Canadian National Breast Screening Study. *Journal of the National Cancer Institute*, 87(9): p. 670-675.
- Byng, J.W., Boyd, N.F., Fishell, E., Jong, R.A., & Yaffe, M.J. (1994) The quantitative analysis of mammographic densities. *Phys Med Biol*, 39: p. 1629-1638.
- Carlisle, T., Thompson, D.J. & Kopecky, K.J. (1983) Reproducibility and consistency in classification of breast parenchymal patterns. *AJR*, 140: p. 1-7.
- Chan, H.P., Niklason, L.T., Ikeda, D.M. et al., (1994) Digitization requirements in mammography: Effects on computer aided detection of microcalcification. *Med Phys*. 21: p. 1203-1213.
- Chan, H.P., Doi, K., Vyborny, C.J., Schmidt, R.A., Metz, C.E., Lam, K.L., Ogura, T., Wu, Y., & MacMahon, H. (1990), Improvement in radiologists' detection of clustered microcalcifications on mammograms. The potential of computer-aided diagnosis. *Invest. Radiol*. 25: p. 1102-1110
- Chan, H.P., Doi, K., Galhorta, S., et al., (1987), Image feature analysis and computer-aided diagnosis in digital radiography. 1. Automated detection of microcalcifications in mammography. *Med Phys* 14: p. 538-548 .
- Chan, H.P., Doi, K., Vyborny, C.J., Lam, L. & Schmidt, R.A. (1988), Computer-aided detection of microcalcifications in mammograms: Methodology and preliminary clinical study. *Invest. Radiol*. 23: p. 664-671
- Chan, H.P., Niklason, L.T., Ikeda, D.M., & Adler, D.D. (1992) Computer-aided diagnosis in mammography: Detection and characterization of microcalcifications. *Med Phys* 19: p. 831
- Ema, T., Doi, K., Nishikawa, R.M. et al., (1993) Computer-aided diagnosis of clustered microcalcification in digital mammograms: Reduction in false-positive findings using edge-gradient analysis. (1993) *Radiology Supp*. 189: p. 186.
- Fam, B.W., Olson, S.L., Winter, P.F. & Scholz, F.J. (1988) Algorithm for the detection of fine clustered calcifications on film mammograms. *Radiology* 169: p. 333-337.
- Feig, S.A., (1988) Decreased breast cancer mortality through mammographic screening: Results of clinical trials. *Radiology*, 167: p. 659-665.
- Hollingsworth, A.B., Taylor, L.D., & Rhodes, D.C. (1993) Establishing a histologic basis for false-negative mammograms. *American Journal of Surgery*, 166(6): p. 643-648.
- Kopans, D., (1992) Detecting Breast Cancer Not Visible by Mammography. *JNCI*, 84(5): p. 745-747.
- Kopans, D.B., (1984) Early breast cancer detection using techniques other than mammography. *Am. J. Roentgenol*. 143: p. 465-468.
- Lefebvre, F., Benali, H., & Kahn, E. (1992) Fractal analysis of clustered microcalcifications in digital mammograms. *Acta. Stereol*. 11: p. 611-616.
- Lefebvre, F., Benali, H., Gilles, R., Kahn, E., & DiPaola, R., (1995) A fractal approach to the segmentation of microcalcifications in digital mammograms. *Med Phys*. p. 381-391.
- Maidment, A.D.A., Fahrig, R., & Yaffe, M.J. (1993) Dynamic range requirements in digital

- mammography. *Med. Phys.* 20: p. 1621-1633.
- Moskowitz, M. (1984) Mammography to screen asymptomatic women for breast cancer. *Am. J. Roentgenol.* 143: p. 457-459.
- Moskowitz, M., Gartside, P. & McLaughlin, C. (1980) Mammographic patterns as markers for high-risk benign breast disease and incident cancers. *Radiology*, . 134(2): p. 293-5.
- Myers, L.E., McLelland, R., Stricker, C.X., Feig, S.A., Martin, J.E., Moskowitz, M., & Nielsen, M.E.J.(1983). Reproducibility of Mammographic Classifications. *AJR*, 141: p 445-450.
- Neitzel, T.J. (1994) Discernible gray levels and digitization requirements in digital mammography. *Med Phys.* 21: p. 1213-1214.
- Nishikawa, R.M. et al., (1993) Computer-aided detection and diagnosis of masses and clustered microcalcifications from digital mammograms. *Proc. SPIE* 1905: p. 422-431 .
- Oza, A.M. and Boyd, N.F.1993.Mammographic parenchymal patterns: a marker of breast cancer risk. [Review]. *Epidemiologic Reviews*, 15(1): p. 2507-2517.
- Priebe, C.E., Solka, et al., (1994) The application of fractal analysis to mammographic tissue classification *Cancer Letters*. 77(2-3): p. 183-189.
- Ruttimann, E., Webber, R.L., & Hazelrig, J.B. (1992) Fractal dimension from radiographs of periodental alveolar bone. *Oral Surg Oral Med Oral Pathology* 74: p. 98-109.
- Sickles, E.A., (1986) Mammographic features of 300 consecutive nonpalpable cancers. *Am. J. Roentgenol.* 146: p. 661-663.
- Tabar, L., Fagerburg, G., Duffy, S.W., Day, N.E., Gad, A., & Grontoft, O. (1992) Update to the Swedish two-country program of mammographic screening for breast cancer. *Radiol.Clin. N. America.* 30: p. 187-210.
- Taylor, P., Haynal, S., Dilhuydy, M.H. & Barreau, B., (1994) Measuring image texture to separate difficult from easy mammograms. *Brit. J. of Radiology* 67: p. 456-463.
- Warner, E., Lockwood, G., Trichler, D., & Boyd, N.F. (1992)The risk of breast cancer associated with mammographic parenchymal patterns: a meta-analysis of the published literature to examine the effect of method of classification. *Cancer Detection & Prevention*, 16(1): p. 67-72.
- Wolfe, J.N., (1976)Breast patterns as an index of risk for developing breast cancer. *American Journal of Roentgenology*, . 126(6): p. 1130-7.
- Wolfe, J.N., Saftlas, A.F., & Salane, M.(1987) Mammographic parenchymal patterns and quantitative evaluation of mammographic densities: a case-control study. *AJR*. 148(6): p. 1087-92.
- Wu, Y., Doi, K., Giger, L., & Nishikawa, M., (1992) Computerized detection of clustered microcalcifications in digital mammograms: Applications of artificial neural networks. *Medical Physics* 19: p. 555-560.
- Zhang, D., Doi, K., Giger, et al., (1992) Computerized detection of cluster microcalcification in digital mammograms: application of artificial neural networks. *Med.Phys.* 19: p. 555-560.
- Zheng, B., Chang, Y.H., Staiger, M., Good, W. & Gur, D (1995) Computer-aided detection in digitized mammograms.*Acad. Radiol* 2: p. 655-662.

EARLY DETECTION OF BREAST CANCER WITH ULTRASOUND MAMMOGRAPHY

Final report under USArmy Med. R&D.Com. grant DAMD17-93-J-3014.

B.D.Steinberg, Q.Zhu, J.Schwartz, D.Carlson
Valley Forge Research Center
Moore School of Electrical Engineering
University of Pennsylvania

1. INTRODUCTION

The long term objective of the project is ultrasonic echo-scanning demonstration of the detection and diagnosis of small breast tumors of a few mm (~ 2 mm) in size. Small tumor detection requires large ($\sim f/1$), 2-D transducer array (5-10cm) to achieve the high lateral resolution. Imaging from so large an aperture suffers wavefront aberration. The wavefront aberration problems inside the female breast are caused by distortion sources of two distinct types, isotropic scattering and nonisotropic multipath caused by refraction and/or reflection. Scattering diminishes contrast resolution (CR), and multipath create false targets or ghost image artifacts. Both reduce CR in image. We seek -60 to -70 dB CR for echo imaging so as to prevent contamination of otherwise black cysts with scattered and/or refracted echo energy and thereby to cause them to look like speckled tumors.

The tools that we proposed to investigate were adaptive signal processing methods for wavefront distortion compensation. In addition, we also proposed to study large aperture design principles for next generation high resolution ultrasound breast scanner. In the last year, we found that applying a time delay type algorithm developed by Flax and O'Donnell (1988) to *in vitro* 2-D breast data and the algorithm has suppressed scattered energy and folded it into the target image, increasing CR by 10-20 dB (Hinkelman et al, 1995, Zhu and Steinberg, 1994). Such adaptive algorithms have been developed in many fields in the last 20 years (optics, Muller, 1974; radar, Steinberg, 1981; radio astronomy, Cornwell, 1989; ultrasound, Flax and O'Donnell, 1988, Nock *et al.*, 1989, Fink, 1992). These are global algorithms that correct time delay errors in wavefronts caused by inhomogeneous tissue and leave the wavefront amplitude distortion intact. This type of algorithm is well understood and can be applied to echoscanners with modest success. Recently, we have had a leap in understanding as to how to properly treat the wavefront amplitude distortion and multipath interference problems. Our newest Toward Inverse Filter (TIF) approach, submitted for publication (Appendix A), has shown 6-10 dB improvement in CR more than phase conjugation, the best phase correction procedure. Our spatial location diversity and coherent CLEAN approach, though preliminary, increases CR by ~ 7 dB (Appendix G).

2. SUMMARY OF THE ACHIEVEMENTS

There were four major tasks in the proposal. These items were either completed or are in progress. Publications resulting from this work are referenced in subpar. 1-4 immediately below.

1. Analyze and evaluate 1-D *in vivo* breast wavefront data from a point source measured with a 10-cm 1-D linear array. Extract statistical information about waveform

distortion from the data. This information is valuable for the design of stronger wavefront compensation algorithms.

The 1-D data had been taken at Hosp. Univ. Pennsylvania (HUP) on an earlier Commonwealth of Pa. grant. 44 asymptomatic women who had x-ray mammography were studied. They were divided into three approximately equal size groups - premenopausal dense breasts, premenopausal fatty and postmenopausal. Propagation path in tissue was 12 cm. Frequencies were 3 and 4 MHz. Waveforms were wideband (to emulate echo) and narrowband (to avoid frequency selective phenomena). Statistics were obtained and published on wavefront amplitude distribution, correlation distance and image sidelobe levels caused by wavefront distortion [1,2,3,4].

2. Extend measurement capability to 2-D. Obtain 2-D breast data. Analyze as in item 1.

2-D breast data obtained and analyzed, from collaboration with URochester group [5, 6]. In addition to data analysis, we also completed a theoretical scattering model [7]. It predicts halo around target, calculates halo width and intensity, calculates loss in target contrast and dynamic range vs array size, frequency, propagation depth in tissue, phase or time delay variance in tissue, scatterer size, correlation distance. Compares favorably with reported experimental data. The model can be used to guide the design of high resolution ultrasound systems.

3. Test existing phase deaberration algorithms. Determine suitability to high resolution imaging in the breast. Develop stronger wavefront compensation algorithms as needed to the extent possible.

Existing phase deaberration algorithms were tested and compared both theoretically and experimentally upon 2-D measurement data (dominant scatterer (Steinberg, 1981)/ time reversal mirror (Fink, 1993), time delay correction (Flax and O'Donnell, 1988, Nock, et al., 1989), backpropagation plus time delay (Liu and Waag, 1994)) [6,8]. Two types of stronger wavefront compensation algorithms have been developed. These are:

a. Toward Inverse Filtering Approach

2-D data analysis and 2-D algorithmic studies indicate that ultrasonic wavefront distortion inside the female breast falls into two categories, incoherent scattering and coherent multipath. Scattering reduces target strength, broadens image lobe and lowers the image contrast while refraction creates coherent multipath interference that produces false targets or ghost artifacts in the image [6,8]. Time-delay type compensation algorithms are useful to minimize scattered energy and to improve image contrast to a large extent (15 dB) [5,6]. Further improvement of contrast resolution requires compensation algorithms that can compensate wavefront amplitude distortion and remove false targets. A new approach, Toward Inverse Filtering, which is designed to solve scattering problem, is developed and experimentally demonstrated using 2-D *in vitro* measurement data [6,8]. Contrast resolution has been improved 6 - 10 dB more than the best phase deaberration procedure (phase conjugation) at the aperture.

b. Multipath Identification and Cancellation Procedure

Multipath interference is a much more difficult problem than scattering. Because it is not a stationary, stochastic process, two distinct steps are required to deaberrate refraction-contaminated image. It is first necessary to recognize which target is the true target and which is the false one caused by interference. In [9] we demonstrate that when a cluster of true and false targets is imaged from several different array locations the true target remains in position and changes very little in size and shape. The images of false targets, on the

other hand, are highly sensitive to the direction from which they are viewed. Therefore, they change sufficiently in location, size and shape to classify them as false. In this way the recognition problem is solved. The second key problem is the cancellation of the multipath arrivals. In [9], we show that coherent CLEAN deconvolution technique can be used as a tool to solve the second problem; a single pole cancellor has offered average of 7 dB improvement in target dynamic range. Sophisticated cancellations, which are now being studied, are expected to offer more. These results, though preliminary, lead to considerable optimism that this approach may lead to the solution of the second problem.

4. Design and test 2-D large acoustic transducers for higher resolution imaging.

a. 2-D Acoustic Array Design

Dramatically reducing the number of transducer elements in a large 2-D array, called element thinning, is essential for designing a practical 2-D transducer array. Analysis revealed that by using the ultrawideband (UWB) property of this array, very thin high resolution arrays can be built. Several groups have studied random, sparse, two-dimensional ultrasonic arrays (Turnbull *et al* , 1992, Cassereau *et al* 1992, Davidsen *et al* , 1994). They chose a random allocation of elements in order to avoid the grating lobes of a periodically thinned array. Consequently, the resulting side energy of the radiation field is much higher than that of a filled array, as predicted by random array theory. These groups did not consider the ultrawideband nature of currently available transducers in their array design. The distribution of sidelobe energy from an UWB array is very different from a conventional narrowband (NB) array. Due to the UWB nature of the pulse, the radiated waveform from UWB arrays varies in time which is not the case in NB arrays. As a result, the waveform has an extra dimension with respect to NB radiation fields across which undesired side energy can be distributed. We have found that UWB arrays can be highly thinned and achieve a much lower side energy level than NB arrays.

Our theory and simulations show that when UWB arrays are highly thinned, there exist regions of the radiation fields where there is no interference. NB array analysis is based on the assumption that the entire radiated field has interference; therefore, conventional NB analysis does not apply in highly thinned UWB arrays. The analysis to date established a method for characterizing the radiation from highly thinned UWB one- and two-dimensional arrays. This method simplified the radiation field by analyzing its interfering and a non-interfering regions separately. The results showed that, contrary to conventional wisdom, a periodic array is preferred over a random array. Furthermore, to achieve the same high resolution and low side radiation level, the highly thinned periodic UWB array is capable of reducing the number of elements required in a conventional filled array to approximately the square root of that number. We call such an array a \sqrt{N} array.

As a consequence of element thinning, there is a loss in signal-to-noise because of the loss in aperture area. A parametric relation was derived which gives the minimum number of elements required to insure an adequate signal-to-noise ratio. Theoretically, it can be shown that the \sqrt{N} array is capable of achieving a sufficient signal-to-noise ratio for pulse-echo ultrasonic imaging.

b. Equipment for Experiment Program

The ultrasound laboratory is fully operational and is used daily in support of the experimental program. The facility includes a water tank test chamber that is designed for 3-D synthetic aperture imaging with arbitrary transducer array configurations within a 15-cm cube. A three-axis micro-positioner table with linear encoders (purchased from New England Affiliated Technology) provides for the control of element position accuracy within 3 microns. In a typical experiment, a fixed hemispherical transducer radiates a short pulse (500 nsec) at 3.75 MHz, and a 0.6 mm hydrophone receives the resulting waveform

at each desired measurement position. Each received waveform is sampled well above the Nyquist rate, displayed and digitized by a HP54120T sampling oscilloscope, and stored in a desktop computer. The entire experiment is under preprogrammed computer control. The output data set includes a received waveform from each receiving element-position. Each data set is then operated upon by relevant software, i.e., imaging, Fourier transform, correlation, etc.

3. CONCLUSION

Adaptive wavefront compensation is an useful tool to increase CR for ultrasonic breast imaging and the total CR improvement in point source image is about 25 dB. The next step will be the careful evaluation of these methods using 2-D large aperture pulse-echo system upon in vitro samples and in vivo volunteers.

Simulations show that highly thinned UWB arrays are able to achieve high resolution and a low side radiation level while maintaining a sufficient signal-to-noise level. A periodic configuration of elements gives a lower side radiation level than a random array and is able to reduce the number of elements conventionally required by a filled array to about the square root of that number. The next step in the array design is to experimentally verify the properties of this \sqrt{N} array in our ultrasonic experimental system.

4. PUBLICATIONS

- [1]. Zhu, Q. and Steinberg, B. D., "Wavefront Amplitude Distribution in the Female Breast," J. Acoust. Soc. Am. (46) 1-9 (1994).
- [2]. Zhu, Q., Steinberg, B. D. and Arenson, R., "Correlation Distance Measurements of the Female Breast," J. Acoust. Soc. Am, (98) 694-705 (1995).
- [3]. Zhu, Q. and Steinberg, B. D., "Wavefront Amplitude Distortion and Image Sidelobe Levels - Part I: Theory and Computer Simulation," IEEE Transactions on Ultrasonic, Ferroelectrics and Frequency Control (40) 747-753 (1993).
- [4]. Zhu, Q., Steinberg, B. D. and Arenson, R., "Wavefront Amplitude Distortion and Image Sidelobe Levels -Part II: In Vivo Experiments," IEEE Transactions on Ultrasonic, Ferroelectrics and Frequency Control (40) 754-761 (1993).
- [5]. Hinkelman, L. M., Liu, D-L., Zhu, Q., Steinberg, B. D. and Waag, R. C., "Measurement and Correction of Ultrasonic Pulse Distortion Produced by the Human Breast," J. Acoust. Soc. Am. (97) 1958-1969 (1995).
- [6]. Zhu, Q., Steinberg, B.D., Hinkelman, L. M., and Waag, R. C., "Deaberration of Incoherent Wavefront Distortion: An Approach Toward Inverse Filtering," submitted to IEEE Transactions on Ultrasonic, Ferroelectrics and Frequency Control (Jan. 1996).
- [7]. B.D.Steinberg, "Scattering from a Multiple Random Phase Screen Model of a Random Inhomogeneous Medium," submitted to JASA (Feb. 1995).
- [8]. Zhu, Q. and Steinberg, B.D., "Modelling and Correction of Incoherent Wavefront Distortion" (Invited paper) Submitted to Inal. J. Sci. Tech. Imaging, Wiley (Sept., 1995).
- [9]. Zhu, Q. and Steinberg, B.D., "Correction of Multipath Interference by Spatial Location Diversity and Coherent CLEAN," Proc. IEEE Ultrasonic Symp. (1995).
- [10]. Schwartz, J. L. and B. D. Steinberg, "The Characteristics of Interference Patterns Produced by Ultra-Wideband Arrays," URSI, Nat'l Radio Sci. Meeting, January 1995.
- [11]. Schwartz, J. L. and B.D. Steinberg, "Highly-Thinned, Two-Dimensional Arrays," Ultrasound Deaberration Workshop, Wash., DC, June 1995.
- [12]. Schwartz, J. L. and B.D. Steinberg, "Highly-Thinned Arrays for Ultrasonic Imaging," accepted to the AIUM conference in March 1996 in New York.
- [13]. Schwartz, J.L. and B.D. Steinberg, "UltraSparse, Ultrawideband, Phased Arrays," submitted to the IEEE AP-S and URSI Radio Science Meeting in July 1996 in Baltimore.

REFERENCES

Cassereau, D., N. Chakroun, F. Wu, M. Fink and F. Datchi, "Synthesis of a specific wavefront using 2D full and sparse arrays," 1992 IEEE Ultrason

Cornwell, T. J., "The Application of Closure Phase to Astronomical Imaging," *Science* **245**, 4915 (1989).

Davidson, R. E., J.A. Jensen, and S. W. Smith, "Two-Dimensional Random Arrays for Real Time Volumetric Imaging," Ultrasonic Imaging **16**, 143-163, 1994.

Fink, M., "Time reversal of ultrasonic fields – part I: basic principles," *IEEE Trans. Ultrason. Ferroelec. Freq. Contr.*, vol. 39, pp. 555-566, 1992.

Flax, S. W. and O'Donnell, M. "Phase Aberration Correction using Signals from Point Reflectors and Diffuse Scatterers: Measurements," *IEEE Trans. Ultrason. Ferroelec. Freq. Contr.*, **35**(6):768-774, Nov. 1988.

Hinkleman, L.M., Liu, D-L., Waag, R.C., Q. Zhu and B.D.Steinberg, "Measurement and correction of ultrasonic pulse distortion produced by the human breast," *JASA* (97) No.3, 1958-1969 (1995).

Liu D-L and Waag, R.C., "Correction of Ultrasonic Wavefront Distortion Using Backpropagation and Reference Waveform Method for Time-shift Compensation," *J. Acoust. Soc. Am.* **96**, 649-660 (1994).

Muller R.A., and Buffington, A., "Real-Time Correction of Atmospherically Degraded Telescope Images through Image Sharpening," *J.Opt. Soc. Am.*, **64**(9) 1200-1210 (September 1974).

Nock, L., Trahey, G. E., and Smith, S.W., "Phase Aberration Correction in Medical Ultrasound Using Speckle Brightness as a Quality Factor," *J. Acoust. Soc. Am.*, **85**(5) 1819-1833 (1989).

Steinberg, B.D., "Radar Imaging from a Distorted Array: The Radio Camera Algorithm and Experiments," *IEEE. Trans. Antennas Propag.*, **AP-29**(5) 740-748 (Sept. 1981).

Turnbull, D. H., P. Lum, A. K. Kerr and F. S. Foster, "Simulation of B-scan images from two-dimensional transducer arrays: Part I:- Methods and quantitative contrast measurements," Ultrasonic Imaging **14**, 323-343. 1992.

Zhu, Q. and Steinberg, B. D., "Modeling, Measurement and Correction of Wavefront Distortion Produced By Breast Specimens," *Proc. IEEE Int'l Symp. Ultrason. Ferroelec. Freq. Contr.*, Cannes, Nov. 1994.

Appendices

Appendix A: Zhu, Q. and Steinberg, B. D., "Modeling and Correction of Incoherent Wavefront Distortion" submitted to the special issue of International Journal of Imaging Systems and Technology (Nov.7., 1995). Invited.

Appendix B: Zhu, Q., Steinberg, B.D., Hinkelman, L. M., and Waag, R. C., "Deaberration of Incoherent Wavefront Distortion: An Approach Toward Inverse Filtering," submitted to IEEE Transactions on Ultrasonic, Ferroelectrics and Frequency Control (Jan. 1996).

Appendix C: Hinkelman, L. M., Liu, D-L, Zhu, Q., Steinberg, B. D., and Waag, R.C., "Measurement and Correction of Ultrasonic Pulse Distortion Produced by the Human Breast", JASA, 1958-1969, 1995.

Appendix D: Zhu, Q. and Steinberg, B. D., "Wavefront Amplitude Distortion and Image Sidelobe Levels - Part I: Theory and Computer Simulation," IEEE Transactions on Ultrasonic, Ferroelectrics and Frequency Control (40) 747-753 (1993).

Appendix E: Zhu, Q., Steinberg, B. D. and Arenson, R., "Wavefront Amplitude Distortion and Image Sidelobe Levels -Part II: In Vivo Experiments," IEEE Transactions on Ultrasonic, Ferroelectrics and Frequency Control (40) 754-761 (1993).

Appendix F: Zhu, Q. and Steinberg, B. D., "Wavefront Amplitude Distribution in the Female Breast," J. Acoust. Soc. Am. (46) 1-9 (1994).

Appendix G: Zhu, Q. and Steinberg, B.D., "Correction of Multipath Interference by Spatial Location Diversity and Coherent CLEAN", Proc. of IEEE Ultrasonic Symposium, Seattle Washington, 1995.

Appendix H: Steinberg, B.D., "Scattering from Multiple Random Phase Screen Model of a Random Inhomogeneous Medium," submitted to J. Acoust. Soc. Am. (Feb. 1995)

Modelling and Correction of Incoherent Wavefront Distortion

Qing Zhu, Department of Radiology and Valley Forge Research Center
Bernard Steinberg, Valley Forge Research Center, The Moore School of Electrical
Engineering, University of Pennsylvania, Philadelphia, PA 19104

ABSTRACT — There are two types of wavefront distortion inside the female breast, incoherent scattering and coherent interference. Adaptive wavefront compensation algorithms developed so far are useful for correction of incoherent distortion caused by scattering. The performances of these algorithms differ according to the extent of wavefront amplitude distortion. It is shown analytically and experimentally in this paper that the matched filtering approach while optimal for detection is not so for imaging when the wavefront amplitude is distorted in addition to phasefront distortion. Matched filtering algorithms increase wavefront amplitude variance and therefore decrease image contrast. The inverse filtering approach while ideal for fidelity is not stable when SNR is low. An approach toward inverse filtering, amplitude compression operation in addition to phase deaberration, is introduced in this paper. Analysis and experiments show that its performance is superior to matched filtering algorithms and to time-delay type correction algorithms without introducing stability problems.

I. INTRODUCTION

In principle, high ultrasound resolution can be achieved with very large ultrasound transducers. However, large transducers are more susceptible to wavefront distortion caused by inhomogeneous tissue because the transducers cover large volumes of tissue and the beams interact with more spatial variations in tissue composition. The distortion inside the female breast falls into two categories: incoherent scattering reduces the target strength, broadens the image lobe [1-2] and raises the background level and therefore lowers the image contrast [3-4]. Refraction creates coherent multipath interference that produces false targets or image artifacts in addition to true targets in the image [10],[4]. The interference problem is more severe when the aperture is large.

Numerous efforts have been made to correct wavefront distortion produced by breast, liver and abdominal wall [9],[13-17]. Basic deaberration algorithms [5-7] are recognized to be suitable only for weak scattering that can be modeled as a thin random phase screen located in the plane of the receiving aperture [8-9],[18]. Extensions of the basic algorithms are made to correct amplitude distortion caused by strong scattering or distributed scattering [8-9]. A model-based approach, that used *a priori* information of the speeds of the rectus muscle layers inside the abdominal wall, has been developed to correct double image artifacts caused by refraction [17]. The proposed technique is not model based and therefore is freed from the necessity of having a prior information about the source of the distortion.

The motivation of this study stems from the following. The algorithms [5-9] that require no *a priori* knowledge about the propagating medium function differently upon

incoherent scattering and coherent interference; therefore it is important to understand the effects of the two distortion processes upon the image and then apply suitable correction mechanisms to the algorithms. The scattered energy increases with the propagation depth in the breast; therefore the performance of descattering algorithms [5-9] is expected to deteriorate with depth. Modeling and quantification of depth dependent distortion and correction are extremely valuable for the design of next generation high quality breast scanners.

In this paper we analyze, through modeling and experiment, image distortion caused by scattering and coherent interference, and the extent to which image quality improvements are affected by deaberration. Wavefront compensation algorithms based on matched filtering are first recognized to be unsuitable for imaging in distributed scattering because the algorithms increase wavefront amplitude distortion and therefore decrease image contrast. A compression operation on wavefront amplitude, akin to inverse filtering, which can significantly reduce wavefront amplitude variance is introduced. We demonstrate through experiments that a combination of the amplitude compression and either phase-deaberration at the aperture or backpropagation plus phase-deaberration at some optimal distance from the aperture can significantly improve image contrast and restore the mainlobe diffraction shape to a -30 dB level. Linear regression analysis of sidelobe energy vs. propagation depth from available data indicates that good focusing with high contrast resolution throughout the 100 mm propagation depth by deaberration is possible.

II. SCATTERING MODELS

The wave propagation problem is formulated similarly to the line-of-sight propagation problem through a tenuous distribution of particles [19]. A narrowband wave is used to simplify the description and derivation. The analytic results can be taken as rules of thumb applicable to the wideband case to characterize contrast resolution due to wavefront amplitude and phase distortions.

An ultrasound wave (either spherical or planar) propagates in an inhomogeneous medium (Fig.1). It consists of coherent and incoherent waves. The incoherent wave is also called a scattered wave. As the wave propagates, the coherent intensity I_c is attenuated due to absorption and scatter, and the incoherent intensity I_i is scattered broadly.

A. Weak Scattering

The field E at a receiving aperture is predominantly coherent and the magnitude of the incoherent field is much smaller than that of the coherent field. E is the sum of the coherent and incoherent fields.

$$E(x) = E_c(x) + E_i(x) \quad (1)$$

$$E_c(x) \gg E_i(x), \quad \langle E_c(x_1)E_i(x_2) \rangle = 0 \text{ and } \langle E_i(x) \rangle = 0 \quad (2)$$

where $\langle \rangle$ is the ensemble average and x is the spatial variable at the receiving aperture.

The spatial correlation or mutual coherence function of the field at the aperture is given by $\Gamma = \langle E(x_1)E(x_2) \rangle$. Since $\langle E_i(x) \rangle = 0$ and $\langle E_c(x_1)E_i(x_2) \rangle = 0$, the spatial correlation function satisfies $\Gamma = \Gamma_c + \Gamma_i$. If the receiver is located in the far field or within the focal region of the source, the angular source intensity distribution or intensity image is the Fourier transform of the spatial correlation function and equals the summation of the coherent and *statistically* smoothed symmetrical incoherent spectra (Fig.2(a)). For each realization, however, the incoherent spectrum can have valleys and hills. The Fourier relationship between the incoherent spatial correlation function Γ_i and incoherent spectrum is commonly known as the Van-Cittert Zernike theory [20].

The wavefront distortion is primarily in the phasefront and can be modeled approximately as due to a thin, random phase screen located in the plane of the receiving aperture and defined by a spatial correlation distance. Such distortion is correctable by phase-deaberration or time-delay compensation algorithms [5-7]. The algorithms operate upon the incoherent field. They fold the scattered energy into the coherent field and thereby restore the full diffraction-limited image (Fig.2(b)).

The most relevant wavefront measurement in a weak scattering field is the spatial correlation function of the phasefront or time-delay profile as reported by several groups [1],[16],[21-22]. From this information, the performance of the phase deaberration process can be predicted.

B. Strong Scattering or Distributed Scattering

The coherent component is attenuated and the incoherent component is scattered broadly. Wavefront amplitude is distorted in addition to phasefront distortion. A more suitable representation of the field is the Rytov model. A distributed random distortion medium can be represented as a cascade of thin, independent distortion layers (Fig.3(a)) or phase screens [19]. At the i th layer, the field can be written as $E_i = A_i \exp(j\phi_i)$. Phasefront distortion is developed due to time shift through each layer. Wavefront amplitude distortion is developed as the phase-aberrated wavefront propagates through the medium to successive layers (Fig.3(b)). Let $E_0 = A_0 \exp(j\phi_0)$ be the reference field. The distorted field is then a product of contributions from each layer

$$E(x) = E_0 E_1 E_2 \dots E_i \dots E_N \quad (3)$$

The amplitude of $\frac{E(x)}{E_0(x)}$ denoted as A_t is $A_t = A_1 A_2 \dots A_i \dots A_N$ and the phase $\phi_t = \phi_1 + \phi_2 + \dots \phi_i \dots + \phi_N$. Assume that the layers are statistically independent and have common statistics; therefore $A_i = \bar{A} + \delta A_i$ and

$$A_t = (\bar{A})^N \prod_{i=1}^N \left(1 + \frac{\delta A_i}{\bar{A}}\right) = (\bar{A})^N \left(1 + \sum_{i=1}^N \frac{\delta A_i}{\bar{A}} + \text{higher order products}\right) \quad (4)$$

Since \bar{A} is close to unity and $\frac{\delta A_i}{\bar{A}}$, $i=1,2,\dots, N$, are independent variables, the amplitude variance of A_t normalized to $(\bar{A})^N$ is $\sigma_{A_t}^2 \approx N \sigma_{\frac{\delta A}{\bar{A}}}^2$, where $\sigma_{\frac{\delta A}{\bar{A}}}^2$ is the normalized amplitude variance of a single screen. $\sigma_{A_t}^2$ grows linearly with the total number of phase screens N and therefore with the propagation distance D . The phase variance $\sigma_{\phi_t}^2 = N \sigma_{\phi}^2$, where σ_{ϕ}^2 is the variance of a single phase screen; therefore $\sigma_{\phi_t}^2$ grows linearly with N and D .

The overall spectrum (sum of coherent and incoherent spectra) is broadened (see outline of Fig.4(a)) and reduced in strength. The background level is increased and therefore image contrast is reduced.

The scattered energy increases with the propagation depth. The energy ratio (ER), which is the energy outside the main image lobe to the energy inside the main image lobe, is a useful tool to quantitatively evaluate the depth-dependence distortion upon image contrast. The relationship between ER and propagation depth D (see Appendix for derivation) is

$$ER = C(\sigma_{\phi_t}^2 + \sigma_{A_t}^2) = CN(\sigma_{\phi}^2 + \sigma_{\frac{\delta A}{\lambda}}^2) = C \frac{D}{d} (\sigma_{\phi}^2 + \sigma_{\frac{\delta A}{\lambda}}^2) \quad (5)$$

where C is a function of the source illumination profile and d is the thickness of the screen and is approximately the correlation distance of the medium. ER linearly grows with the propagation distance. This relationship is analogous to the average sidelobe floor in the radiation pattern of an array with errors [23] and to the average sidelobe floor in an arbitrary source distribution imaged through a distorting medium [18]. Eq. (5) can be applied to wideband as an approximation.

So long as certain correlation properties exist in the wavefront, phase compensation algorithms are still useful in strong scattering to partially remove phase distortion and build up the strength of the coherent field (Fig.4(b)). Wavefront amplitude distortion remains, as does residual phase distortion, and produces a significantly high incoherent background level in the spectrum. Any phase-deaberration procedure that provides a better phase error estimate than that of the basic algorithms [5-7] can reduce this background level. Wavefront-deaberration algorithms that take amplitude distortion into account can further reduce this background level if the algorithms reduce wavefront amplitude variance.

Consider the distortion vector $\mathbf{f} = \frac{E}{E_o} = A_t \exp(j\phi_t)$. Fig.5 shows such a distortion vector \mathbf{f} for some instantaneous sample of the radiation field. The optimum compensation weight vector or transformation $w_{opt} = A_t^{-1} \exp(-j\phi_t)$ is the right-most one which carries the distortion component of the complex sample to the intersection of the x-axis and the unit circle, for then both amplitude and phase are exactly corrected. The left-most transformation $w = A_t \exp(-j\phi_t)$ is matched filtering (MF) which squares the amplitude and conjugates the phase. MF is theoretically optimum for maximizing SNR on a white, Gaussian channel. It is an optimum solution for detection but not when fidelity is an important criterion, as in imaging. But it does satisfy the requirement for phase correction. Examples of MF algorithms are Dominant Scatterer Algorithm (DSA) [24] and Time Reversal Mirror (TRM)[8]. We should expect that MF algorithms are useful when wavefront distortion resides principally in phase, with amplitude relatively unaffected. Otherwise MF algorithms would be less effective than if amplitude were ignored and phase only were corrected. Later we show that by squaring the amplitude, a MF algorithm increases the wavefront amplitude variance and thereby increases the energy in the sidelobe region.

Consider what happens when a phantom consisting of a random phase screen is placed at a receiving transducer. The element signal samples are correct in amplitude and distorted only in phase by a random additive component. Phase aberration correction (PAC), consisting of phase conjugation (PC), is then the optimum compensator. The signal amplitude is unchanged. This operator is represented by the 2nd (from the left) transformation. Time delay compensation (TDC)[5-7] is in the same class.

The right-most transformation which corrects both amplitude and phase is the inverse filter (IF). It is theoretically ideal for fidelity but has drawbacks. Because the IF adjusts the channel gain to be the reciprocal of the signal strength, at points in the receiving aperture where signal strength is weak the enhanced channel gain raises the noise to the point where SNR can be impaired. This is particularly troublesome when there is coherent refractive interference in the receiving array. A second potential problem, which we have avoided by not working too close to the IF point, is that an IF is unstable when the distorting medium has zeroes in the complex plane. Thus the right-most transformation carries the correction too far.

The complex weights of MF, PC and IF are, respectively, A_t , 1 and A_t^{-1} , each multiplied by $\exp(-j\phi_t)$. The signal after weighting is A_t^2 , A_t and 1. The first and last are far from optimum for the reasons given. The 3rd from the left transformation is a compromise. The correction vector is $A_t^{-1/2} \exp(-j\phi_t)$. The signal after weighting is $A_t^{1/2}$ (called later the square rooter). Another transformation to the right of the square rooter is fourth rooter (signal amplitude is $A_t^{1/4}$ after weighting). In general, the correction vector is $A_t^{-(M-1)/M} \exp(-j\phi_t)$ and signal amplitude is $A_t^{1/M}$ after transformation of the Mth rooter. In part C, we demonstrate experimentally that low order rooters (square rooter and fourth rooter), in addition to phase deaberration at the aperture, can significantly improve contrast resolution without encountering the stability problem.

The dominant scatterer algorithm (DSA) developed in narrowband radar [24] is designed for adaptively focusing a large distorted receiving array upon a point target and is a matched filter process in space. DSA creates a compensating weight vector w from the complex conjugate of the received echo, i.e., $w = A_t \exp(-j\phi_t)$. The DSA-corrected receiving beam is the Fourier transform of $w A_t \exp(j\phi_t) = A_t^2$. Consequently, DSA uses wavefront amplitude to provide additional SNR gain than phase conjugation only, for which $w = \exp(-j\phi_t)$. However, when the wavefront amplitude is distorted, the amplitude weight further increases the sidelobe level in the beam. The measure in the increase is the increased wavefront amplitude variance. Since $A_t^2 = A_1^2 A_2^2 \dots A_t^2 \dots A_N^2$, therefore eq. (4) is changed to

$$A_t^2 = (\bar{A})^{2N} \prod_{i=1}^N \left(1 + \frac{\delta A_i}{\bar{A}}\right)^2 = (\bar{A})^{2N} \left(1 + \sum_{i=1}^N 2 \frac{\delta A_i}{\bar{A}} + \text{higher order products}\right) \quad (6)$$

The variance of square amplitude $\sigma_{A_t^2}^2 \approx 4N \sigma_{\frac{\delta A}{\bar{A}}}^2$ which is 4 times larger than without amplitude weight. Assuming phase error $\sigma_{\phi_t}^2$ is compensated, ER will rise from $C \frac{D}{d} \sigma_{\frac{\delta A}{\bar{A}}}^2$ to $C \frac{D}{d} 4 \sigma_{\frac{\delta A}{\bar{A}}}^2$ which is about a 6 dB decrease in image contrast.

The time reversal mirror (TRM) developed by Fink [8] provides optimal focusing of a wideband transducer upon a target through a scattering medium and is a matched filter

process in both space and time (waveform). The operation reverses the received waveforms, retransmits them through the medium and then focuses the array on the target. The transmitting beam pattern is the convolution of the received waveforms and their time-reversed version. In the frequency domain, TRM is a phase conjugation procedure (with amplitude weight) at each frequency within the signal band. It is anticipated that TRM focusing produces poorer illumination in the neighborhood of the target than phase conjugation focusing does for the reason discussed in the previous paragraph.

Square root amplitude weighting changes eq. (4) to

$$A_i^{1/2} = (\bar{A})^{N/2} \prod_{i=1}^N \left(1 + \frac{\delta A_i}{\bar{A}}\right)^{1/2} = (\bar{A})^{N/2} \left(1 + \sum_{i=1}^N \frac{\delta A_i}{2\bar{A}} + \text{higher order products}\right) \quad (7)$$

The amplitude variance $\sigma_{A_i^{1/2}}^2 \approx \frac{N\sigma_{\frac{\delta A}{\bar{A}}}^2}{4}$ which is 4 times less than with unit amplitude weight.

Assuming phase error is compensated. ER will reduce from $C \frac{D}{d} \sigma_{\frac{\delta A}{\bar{A}}}^2$ to $C \frac{D}{4d} \sigma_{\frac{\delta A}{\bar{A}}}^2$ which

implies about a 6 dB increase in image contrast. Mth rooter will reduce the amplitude variance by 2M if the SNR is still adequate. This nonlinear transformation upon wavefront amplitude is a compression operation (see Fig.6). The detailed evaluation of the effects of this compression operation upon image can be performed by studying the amplitude distributions of images before and after the operation. This is a subject of a later study.

Backpropagating the received wavefront to an optimal backpropagation distance and performing phase deaberration at this optimal distance (BPT) [5] provides first order correction of wavefront amplitude distortion due to propagation from the backpropagation distance to the receiving aperture and therefore performs better than phase deaberration at the aperture. In part C, we demonstrate experimentally that the BPT transformation is somewhere to the right of TDC and PC and left of PC and rooter. We also demonstrate that square rooter in addition to BPT can significantly improve the performance of BPT.

The relevant measurement in a strong scattering region is wavefront amplitude variance [15] (narrowband) or wavefront energy fluctuation [16],[21] (wideband) in addition to arrival time variance. Since wideband waveforms can be Fourier decomposed into a set of narrowband complex wavefronts within a signal band, waveform distortion therefore implies complex wavefront amplitude distortion and vice versa. In the following text, waveform distortion and wavefront amplitude distortion are used indistinguishably.

C. Correction upon Scattering Samples

To develop an understanding of deaberration, our studies have concentrated on one-way propagation measurements and corrections of point source fields. The 2-D measurement system and procedure were described in [16],[11]. Briefly, a breast specimen was placed between hemispherical source and receiving array. The 2-D array consisted of a 92-mm 1-D linear array translated 46 mm perpendicular to its axis to form a synthetic 2-D array 92 mm x 46 mm. Element pitch in the receiving transducer was 0.72 mm and a reflecting mask reduced the receiving elevation to 1.44 mm. Frequency was 3.7 MHz. Bandwidth was 2 MHz. Waveforms were measured at each element, from which 2-D wavefronts were reconstructed as functions of time. 3-D image data were calculated by (1) Fourier decomposition of the temporal waveforms at each (x,y) position in the aperture,

(2) calculation of a complex CW 2-D image at each Fourier frequency in the focal plane by using the angular spectrum technique [18], and (3) summation of the 2-D images to form the 3-D transient image. The final 2-D image used in this report was obtained by detecting the peak pressure value at each (x,f,y) position in the image plane within the transient period. Contour maps of 2-D point source images at different thresholds were used to quantitatively evaluate image quality. The implementations of different correction methods and correction results were reported in [11]. The total measurements made were 16 with breast sample thickness varied from 1 to 4 cm. The following is a typical example of correction upon a scattering sample.

Figs.7 (a) and (b) show -6 dB contour plots of images obtained from the water path and the 3.5-cm breast tissue path (brs005). Contour spacing is 1 dB. Abscissa and ordinate are azimuth and elevation in mm in the image plane. Fig.7(a) shows the system diffraction pattern at -6 dB. The azimuthal beamwidth is about 1.5 mm (at a distance of 180 mm) meaning that the point (or lateral) resolution is 1.5/180 or 8.3 mrad. Because the size of the receiving array in elevation is half the size in the array direction, the width of the image in elevation is twice as large as in azimuth. When tissue is present (b), the image lobe is broadened. In (b) the beamwidth has grown from 1.5 mm to 3 mm in azimuth and 3.1 mm to 9.3 mm in elevation and the point resolution has worsened approximately 2:1 in azimuth and 3:1 in elevation. A symmetrical scattering pattern appears when the threshold is reduced. Fig.7 (c) shows a -20 dB contour plot of the sample image brs005. Contour spacing is 2 dB. Energy is spread out over a large area. No distinct structure or multipath lobe can be identified from the image.

Fig.8 (a)-(g) shows the correction result of the sample image brs005 by using different methods. Part (h) is the -30 dB level contour of a water path image. The contour spacings in Fig.8 are the outer contour levels divided by 10. Fig. 8 (a)-(c) shows TDC at -6, -20 and -30 dB levels (see Fig.7(b) and (c) for comparison). Image quality improved significantly and the system diffraction pattern is restored up to -20 dB level. The symmetrical scattering pattern outlined by outer contours at the -30 dB level is caused by residual phase errors after phase deaberration and incoherent amplitude distortion. Fig.8 (d) is the correction result of PC at the -30 dB level. Because of the complete removal of phase errors except for a 2π jump, the scattering pattern is further improved as compared to (c). Fig. 8 (e) is the result of BPT, and the scattering pattern is much better than that of PC at the aperture. The optimum backpropagation distance of this tissue sample is 30 mm. It is interesting to note that the beamwidth is narrower than that obtained through other methods. The reason is that the actual aperture is moved 30 mm closer to the source and the beamwidth is $(R\text{-optimal backpropagation distance}) \frac{\lambda}{L}$ instead of $R \frac{\lambda}{L}$, where R is the distance between source and the receiving aperture, and L is the aperture size. Fig.8 (f) is the correction result of PC and square rooter on wavefront amplitude at -30 dB. The pattern is very close to the system diffraction pattern (see (h) for comparison). Fig.8(g) is the result of wideband DSA at the -30 dB level. The correction result is worse than those of other methods.

Correction statistics of a simple metric, the lowest level at which mainlobe diffraction shape is maintained when different methods are used, are given in [11]. The average levels of using wideband DSA, PC and PC and rooter are 14.8 (std. 2.34), 19.5 (2.61) and 25.4 dB (2.55 dB), respectively. These results closely agree with the analysis in Section II of 6 dB decrease and increase in image contrast from squaring the amplitude (DSA) to amplitude intact (PC) and amplitude intact to square root of the amplitude (PC and rooter). The average levels of using TDC and BPT are 19.3 (2.43) and 24.0 dB(1.99 dB).

III. SCATTERING AND REFRACTION MODEL

A. Strong Scattering and Refraction Model

In a refractive medium coherent rays can be bent and split after they pass through tissue beds with different sound speeds [10]. The interference of refracted coherent ray bundles with incident rays produces image artifacts which appear as false targets. A simple representation of such a field is

$$E(x) = E_0 E_1 E_2 \dots E_i \dots E_N + E_{r1}(x)e^{(jf_1(x))} + E_{r2}(x)e^{(jf_2(x))} \quad (8)$$

where $f_1(x)$ and $f_2(x)$ define directions of secondary fields caused by refraction (see Fig.9).

The angular source intensity distribution is the superposition of the intensity image lobe, coherent interference lobes and incoherent spectrum (Fig.10(a)). The strengths and the numbers of interference lobes depend on orientations, curvatures, sizes and numbers of refractive bodies in the insonified medium, and may not be directly related to propagation depth. Although the chance of incident rays passing through more refractive bodies increases with the propagation depth, the strengths of interference lobes resulting from multiple refraction may not be significant compared with those resulting from single refraction. One quantitative measure of coherent interference phenomenon is the ratio of a large interference lobe or artifact to image lobe. For nine samples that were determined to have significant levels of coherent interference, the ratio varied randomly from sample to sample and showed no increase with thickness. The average strength (peak value) is 10 dB (std. 4 dB) [11]. Another quantitative measure is the total number of large refractive lobes in each image. The average is 2 and standard deviation is 0.53. The lobe number is independent of propagation depth. The refractive lobes are tightly clustered around the main lobe with an average radius of 5.6 mm (std. 1.8 mm) which is about 2 degrees. This is because the speed variations across glandular tissue and fat boundaries are small (5-10%).

The correction mechanism in a strong scattering and refraction medium is interesting. If the primary field is stronger than secondary refraction fields, the scattered energy removed by the deaberration process strengthens the primary field by folding the removed scattered energy into the primary field. As a result the ratio of image lobe to interference lobe is improved (Fig.10(b)). If, however, the primary field is weaker than the refracted field, the scattered energy removed by the deaberration process may strengthen the refracted field. The corrected result could then be worse than without correction. However, we have seen no evidence of this so far in our experiments reported in [11].

TRM or wideband DSA on reception is a matched filter process in both space and time, resulting in maximization of the signal relative to the background white noise. Correlation-based time-delay compensation algorithms, on the other hand, perform a different function; they adjust time-delay to maximize image sharpness or image contrast. In a refractive medium, the problem is more complicated. Neither TRM or wideband DSA nor time-delay algorithms have a way of knowing which signal is real and which is an artifact caused by coherent multipath. Because TRM or wideband DSA is a spatial matched filter its weight vector forms a lobular radiation pattern that matches the sum of both the real and false signals. Hence all targets, whether real or false, are enhanced. In our experiments reported in [11], with nine samples that have well-defined multipath artifacts, we found an

average 5 dB (std.2.5 dB) increase in peak artifact to image lobe ratio by using wideband DSA rather than by using time-delay compensation.

BPT backpropagates waveforms to the optimum distance before applying time-delay compensation. It removes wavefront amplitude distortion caused by propagation and reduces residual phase distortion by improving the performance of time-delay correction, but will not remove large lobes caused by refraction. A simple thought experiment is convincing: Backpropagating two plane waves produces two plane waves at whatever distance the waves are backpropagated.

Thus it is important to understand the deaberration operations and to design appropriate algorithms that offer optimal performance in the corresponding distorting medium. Aperture measurement alone can not distinguish between wavefront distortions caused by refraction or by strong scattering. Distinction can be made in the image domain where refraction appears as large, coherent interference lobes while strong scattering spreads into an incoherent background. While the refracted energy may or may not be significantly larger than the energy in the incident wave, it nevertheless produces image artifacts which will destroy the quality of a high resolution image.

B. Correction upon Samples with Well-defined Multipath

In most breast samples (9 out of 16), scattering and coherent interference are both present. Fig.11 (a) and (b) are -10 dB contour plots of images obtained from the water path and the 4-cm breast tissue path (brs006). Contour spacing is 2 dB. In tissue image (b), three lobes instead of one central image lobe appear. Inner contours of the image lobe are close to the system diffraction pattern (Fig.11(a)) while the outer contours are highly irregular due to scattering. The point resolution is worsened by approximately 2:1 in azimuth and 3:1 in elevation. Two refractive lobes appear at (-4, -2.5) and (3.5, 1.5), and their strengths are -6 and -8 dB. A closer examination is obtained from 45 degree cuts (Fig.12) of the Fig.11 (a) and (b) images. In Fig.12 (a), the peak sidelobe is -36 dB, which is the best we can obtain from the measurement system. In the tissue image, two large sidelobes (-6 dB and -8 dB) appear on either side of the mainlobe. The two nulls between the lobes are deep (left: -13 dB below peak, right: -15 dB), which is a typical coherent interference phenomenon [15].

A symmetrical scattering pattern generally appears when the threshold is reduced, as shown Fig.11(c) with a -16 dB threshold contour and contour spacings of approximately 1.5 dB. The outer contours show a roughly symmetrical pattern typical of scattering while the inner contours show an asymmetric lobular interference pattern.

Fig.13 shows correction results of the sample image brs006 after applying different methods. The contour spacings are the outer contour levels divided by 10. Fig.13(a) is the -16 dB contour map of applying TDC (see Fig.11(c) for comparison). Image quality improved significantly because of the minimization of the phasefront distortion caused by scattering. The area within the -16 dB inner contour is reduced by a factor of 11. The mainlobe pattern is close to the system diffraction pattern although the area is still 1.6 times larger than the area in water at the same level. Two large lobes remain as expected and appear as two additional sources. Fig.13(h) is the correction result at a -16 dB level of applying wideband DSA. It is evident that the procedure enhances interference in this example; the artifacts are 5 dB higher than in Fig.13(a). Figs.13(b) and (c) show -25 and -30 dB contour plots of TDC. In Fig.13(b) the outer contours show an asymmetric interference pattern with scattered energy distributed around the two interference lobes. In Fig.13(c) the outer contours show the more symmetrical scattering pattern caused by incoherent wavefront amplitude distortion and residual phase distortion. Fig.13(d) is the result of PC at -30 dB. The approximately symmetrical scattering pattern outlined by outer

contours in (c) is improved due to better phase deaberration. The energy is more concentrated around the image lobe and interference lobes. Part (e) is the result of BPT, and the scattering pattern is further improved as compared with the result of PC at the aperture. The backpropagation distance of this sample is 50 mm. Part (f) is the result of PC and square rooter at -30 dB. The pattern is very close to the system diffraction pattern. PC and fourth rooter shown in Fig.13(g) restores the diffraction-limited image to a -30 dB level.

It is interesting to note that the strengths of the two interference lobes are also reduced by 8 dB after TDC and PC. They are further reduced by 5, 7 and 15 dB after BPT, PC and square rooter, and PC and fourth rooter, respectively. The improvement comes from the scattered energy which is originally distributed around the mainlobe and each of the refracted multipath lobes. This energy is coherently added back, by the deaberration process, to the dominant lobe, which in this case is the mainlobe. The overall result is an improvement of the image lobe to the interference lobe ratio.

Determination of whether interference was coherent or scattered was based upon whether or not large lobes could be removed by applying phase-deaberration algorithms. Another indicator is whether or not a lobe location moves (scattering) or remains relatively the same (refraction) after the phase deaberration process. Both means were used to identify whether these lobes were produced by refraction or scattering. Large lobes in nine samples are believed to be caused by the interference process. In these samples, we have found an average of a 10 dB (std. 4dB) improvement in the range of 5-16 dB after TDC, due to the coherent strengthening of the mainlobe.

IV. EXPERIMENTS

The significance of appropriate amplitude weighting discussed in Section II is experimentally evaluated using ER introduced in eq. (5). When phase error is removed, ER is proportional to $\sigma_{A_t}^2$. The detailed measurement procedures of ER and $\sigma_{A_t}^2$ are reported in [11]. Fig.14 shows regression plots of ER, measured after reducing the phase error using PC, wideband DSA, and PC and square rooter, vs. $\sigma_{A_t}^2$. The three methods compensate phase errors. ER and $\sigma_{A_t}^2$ measured in water using the three correction procedures are also incorporated into the three data sets to represent the system performance. The linear relationships are statistically significant. The average ERs are 103% (std. 33.9%), 25% (6.9%) and 6.8% (1.6%) when wideband DSA, PC and PC and rooter are used, respectively. An approximate factor of 4 reduction in ER from amplitude squaring (wideband DSA) to amplitude intact (PC) and amplitude intact to square root of amplitude (PC and rooter) is obtained. The results agree with the analysis in Section II and indicate that intelligent use of amplitude weighting is crucial for improving image contrast.

Scattered energy increases with the propagation depth as predicted by eq. (5) and performances of descattering algorithms deteriorate with propagation depth. In Ref.11, regression plots of ER vs. approximate thickness of 16 breast samples were given by using 7 descattering procedures. The regression plot without correction was also given. The linear relationships were statistically significant. Fig.15 shows partial results taken from Ref.11. The five curves in the figure are obtained by using wideband DSA (circle), TDC (solid square), PC (triangle), PC and rooter (solid triangle) and no correction (solid circle). ER reduction from amplitude weighting (wideband DSA) to square root of amplitude weighting (PC and rooter) is clearly shown by the regression plots. The regression lines are extrapolated to 100 mm propagation depth, which is considered the average maximum penetration depth required for breast.

Before we discuss the predicted performance of the descattering algorithms at 100 mm depth, we need to find the relationship between ER and image contrast, which is defined as the lowest level of the mainlobe diffraction shape. Image contrast increases monotonically with ER. Table I lists the measured average ER (first row) and the measured average image contrast (second row) when different correction methods as well as no correction are used [11]. The relationship between ER and image contrast can be predicted by using ER and image contrast obtained from PC (or any correction method) as base line (bold numbers in Table I). For example, the measured image contrast with PC is 19.5 dB. The ER ratio of PC alone to PC and rooter is $2.5 / 6.8 = 3.7$, corresponding to increase of 5.7 dB. Thus the predicted image contrast is $19.5 \text{ dB} + 5.7 \text{ dB} = 25.2 \text{ dB}$ which closely agrees with the measured value 25.4 dB. The third row of Table I lists the predicted image contrast based on the measured ER. The predicted values are in reasonably good agreement with the measured values except for the pair without correction. The reason is due to ER measurement error in images without correction. For some severely distorted images, it is often difficult to identify the mainlobe region.

At 100 mm depth ER after PC reaches 85% which corresponds to 14.0 dB image contrast. Therefore, PC, the best linear phase correction procedure at the aperture, is likely to result in only ~14 dB image contrast at this depth. ER after wideband DSA reaches 324.3% which corresponds to only ~8.4 dB image contrast. ER after PC and rooter reaches 22%, which provides ~20.1 dB image contrast. ER after TDC reaches 148%, which offers only ~11.8 dB image contrast.

The data used to test the analysis developed in Section II are sparse; nevertheless they do provide information for designers of next generation high quality breast scanners.

V. DISCUSSION

A. Application to Diffuse Scattering Medium

The compression operation upon wavefront amplitude, in addition to phase deaberration or BPT, introduced in the paper is applicable to a diffuse scattering medium. Experiments with TDC and rooter and TDC alone show that ER can be reduced from 44.2% to 28.6%, the ratio of which indicates 1.3 dB improvement in image contrast. However, experiments with PC and rooter and PC alone show that ER can be reduced from 25.1% to 6.8%, which is about 6 dB improvement in image contrast. The large difference is due to the fact that PC corrects phase in every signal spectrum while TDC makes single correction which applies to all frequencies. The consequence is that TDC leaves significant phase residual. Therefore, to successfully improve image contrast, good phase deaberration is the first crucial step to reduce ER, and followed by amplitude compression such as rooter.

B. Application to Coherent Interference upon Pulse-echo Imaging

High resolution, high dynamic range breast imaging implies seeing a black cyst 60 dB weaker than a bright speckled target. In this paper, we show that 30 dB image contrast on reception is obtainable by taking low order rooters provided that phase error is completely compensated. In pulse echo, refracted energy from the targets insonified by the subbeam will arrive at angles of $1 - 30^\circ$ from the target direction [11] and therefore in the sidelobe region of array. The sidelobe level of the receiving beam will be ~ -30 dB. The average level of refracted multipath is found to be -10 dB relative to the target image [11] and therefore the average multipath signal level entering the system is $\sim (10+30) \text{ dB} = -40 \text{ dB}$ below the echo strength of the illuminated target. Cancellation algorithms [16-17] must

suppress these multipath signals to achieve 60 dB contrast resolution. Hence about 20 dB further cancellation is required.

VI. CONCLUSIONS

We conclude, through analysis and experiment, that 1) matched filtering compensation algorithms while optimal for detection are not suitable for imaging in distributed scattering, because the algorithms increase wavefront amplitude variance and therefore decrease image contrast; and 2) low order rooters upon wavefront amplitude, akin to inverse filtering, in addition to phase deaberration can significantly improve image contrast without encounter stability problem. Further study is needed to optimize the required degree of compression as a function of SNR and image contrast.

Incoherent scattering and coherent multipath affect an image differently. Scattering reduces target strength, broadens the image lobe and increases background level while refraction creates coherent multipath interference which produces false targets or image artifacts. Adaptive compensation algorithms developed so far are useful to partially remove the scattered energy and coherently add it back to the coherent image. The result is the improvement of both lateral and contrast resolution to a large extent. The ratio of image lobe to artifacts is also improved because of the strengthening of the coherent field by descattering processes.

ACKNOWLEDGMENTS

The *in vitro* measurements were done with the collaboration of Ms. Laura M. Hinkelman and Prof. Robert C. Waag, Departments of Electrical Engineering and Radiology, University of Rochester, Rochester, who also give valuable comments on the paper. Invaluable consultation was provided by Dr. Kai Thomenius, Director of Research, Interspec, Inc., Ambler, PA., a division of ATL, in the course of this study. Funding was provided by the Army (DAMD 17-93-J-3014 and DAMD 17-94-J-4133) and NSF (BCS92-09680).

APPENDIX

Let $s(u)$ represent the complex angular source distribution, where $u = \sin(\theta)$ and θ is the angle from the array normal. Its complex radiation field in the axis of the receiving array in a homogeneous medium is the inverse Fresnel transform of $s(u)$ or inverse Fourier transform of $s(u)$ after correcting for near-field curvature and is denoted as $E_o(x)$. In an inhomogeneous medium, the radiation field is $i(x) = \alpha W(x) E_o(x) M(x)$ where $w(x)$ is the aperture weighting function, $M(x) = A_t \exp(j\phi_t)$ is the medium induced distortion and α is a constant to reflect any signal loss. The complex image is

$$\hat{s}_i(u) = \alpha F[W(x) E_o(x) M(x)] = \alpha f(u) * s(u) * F(M(x)) \quad (1)$$

where $F(M(x)) = \mu(u)$ is the angular impulse response of the medium. F denotes Fourier transform. The subscript i denotes inhomogeneous medium. For $\alpha = 1$ and $M(x) = 1$, the complex image corresponds to the image in homogeneous medium and is denoted as $\hat{s}_h(u)$.

The derivation is made with discrete rather than continuous variables. Thus x is replaced by $n=1, 2, \dots, N$, where N = number of elements in the array. The following assumptions are made:

1. Medium induced amplitude and phase errors are uncorrelated.
2. The phase errors of $\phi_t(n)$, $n=1, 2, \dots, N$, are statistically uncorrelated random variables with a common probability density function (pdf).
3. The amplitude errors of $A_t(n)$, $n=1, 2, \dots, N$, are statistically uncorrelated random variables with a common pdf.

The complex image $\hat{s}_i(u)$ can be written as

$$\hat{s}_i = \alpha F[E_o(n)A_t(n)] = \alpha \sum_{n=1}^N E_o(n)A_t(n) \exp(jkndu) \quad (2)$$

where the aperture taper $W(n)$ has been chosen as unity.

The image intensity is the product of (2) and its complex conjugate:

$$\begin{aligned} \hat{s}_i(u) \hat{s}_i^*(u) &= \alpha^2 \sum_{n=1}^N \sum_{m=1}^N E_o(n)E_o^*(m)A_t(n)A_t(m) \exp(j(\phi_t(n) - \phi_t(m))) \exp(jk(n-m)du) \\ &= \alpha^2 \left\{ \sum_{n=m}^N E_o(n)E_o^*(n)A_t^2(n) + \right. \\ &\quad \left. \sum_{n \neq m}^N E_o(n)E_o^*(m)A_t(n)A_t(m) \exp(j(\phi_t(n) - \phi_t(m))) \exp(jk(n-m)du) \right\} \end{aligned} \quad (3)$$

The average intensity is

$$\begin{aligned} \overline{\hat{s}_i(u) \hat{s}_i^*(u)} &= \alpha^2 \left\{ \sum_{n=m}^N E_o(n)E_o^*(n)A_t^2(n) + \right. \\ &\quad \left. \sum_{n \neq m}^N E_o(n)E_o^*(m)A_t(n)A_t(m) \exp(j(\phi_t(n) - \phi_t(m))) \exp(jk(n-m)du) \right\} \\ &= \alpha^2 \left\{ \sum_{n=m}^N E_o(n)E_o^*(n)(\sigma_{A_t}^2 + (\overline{A_t})^2) + \sum_{n \neq m}^N E_o(n)E_o^*(m)(\overline{A_t})^2 \exp(j(\phi_t(n) - \phi_t(m))) \exp(jk(n-m)du) \right\} \end{aligned} \quad (4)$$

where $\overline{A_t(n)A_t(m)} = \overline{A_t(n)}\overline{A_t(m)} = \overline{A_t}^2$ and

$\overline{\exp(j\phi_t(n))\exp(-j\phi_t(m))} = \overline{\exp(j\phi_t(n))}\overline{\exp(-j\phi_t(m))} = \overline{\exp(j\phi_t)}^2$ because of the assumptions 2 and 3, respectively.

$$\begin{aligned} \overline{\hat{s}_i(u) \hat{s}_i^*(u)} &= \alpha^2 \left\{ \sum_{n=m}^N E_o(n)E_o^*(n)(\sigma_{A_t}^2) + \sum_{n=m}^N E_o(n)E_o^*(n)(1 - \overline{\exp(j\phi_t)}^2)(\overline{A_t})^2 \right. \\ &\quad \left. + \overline{A_t}^2 \overline{\exp(j\phi_t)}^2 \sum_{n=1}^N \sum_{m=1}^N E_o(n)E_o^*(m) \exp(jk(n-m)du) \right\} \end{aligned} \quad (5)$$

The term $\overline{A_t}^2 \overline{\exp(j\phi_t)}^2 \sum_{n=m}^N E_o(n)E_o^*(n)$ is added to the second term of (4) resulting in the third term of (5). The same term is subtracted from (4) resulting in the second term of (5).

$$\overline{\hat{s}_i(u) \hat{s}_i^*(u)} = \alpha^2 \left\{ \sum_{n=m}^N E_o(n) E_o^*(n) (\sigma_{A_t}^2) + \sum_{n=m}^N E_o(n) E_o^*(n) (1 - \overline{\exp(j(\phi_t)^2)}) (\overline{A_t})^2 \right. \\ \left. + (\overline{A_t})^2 \overline{\exp(j(\phi_t)^2)}^2 \hat{s}_h(u) \hat{s}_h^*(u) \right\} \quad (6)$$

Integration with respect to u on both side of eq. (6) yields

$$\int_{\text{mainlobe}} \hat{s}_i(u) \hat{s}_i^*(u) du + \int_{\text{sidelobe}} \hat{s}_i(u) \hat{s}_i^*(u) du \\ = \alpha^2 \left\{ \int_{\text{mainlobe}} \left[\sum_{n=m}^N E_o(n) E_o^*(n) (\sigma_{A_t}^2) + \sum_{n=m}^N E_o(n) E_o^*(n) (1 - \overline{\exp(j(\phi_t)^2)}) (\overline{A_t})^2 \right] du \right. \\ \left. + \int_{\text{mainlobe}} (\overline{A_t})^2 \overline{\exp(j(\phi_t)^2)}^2 \hat{s}_h(u) \hat{s}_h^*(u) du \right. \\ \left. + \alpha^2 \left\{ \int_{\text{sidelobe}} \left[\sum_{n=m}^N E_o(n) E_o^*(n) (\sigma_{A_t}^2) + \sum_{n=m}^N E_o(n) E_o^*(n) (1 - \overline{\exp(j(\phi_t)^2)}) (\overline{A_t})^2 \right] du \right. \right. \\ \left. \left. + \int_{\text{sidelobe}} (\overline{A_t})^2 \overline{\exp(j(\phi_t)^2)}^2 \hat{s}_h(u) \hat{s}_h^*(u) du \right\} \right\} \quad (7)$$

$$\text{ER} = \frac{\Delta \text{energy} - \text{outside} - \text{mainlobe}}{\text{energy} - \text{inside} - \text{mainlobe}} \\ = \frac{\int_{\text{sidelobe}} \sum_{n=m}^N E_o(n) E_o^*(n) du \{ \sigma_{A_t}^2 + (1 - \overline{\exp(j(\phi_t)^2)}) \overline{A_t}^2 \}}{\int_{\text{mainlobe}} (\overline{A_t})^2 \overline{\exp(j(\phi_t)^2)}^2 \hat{s}_h(u) \hat{s}_h^*(u) du} \quad (8)$$

where $\int_{\text{sidelobe}} (\overline{A_t})^2 \overline{\exp(j(\phi_t)^2)}^2 \hat{s}_h(u) \hat{s}_h^*(u) du$ is small compared with the rest of the sidelobe terms and is dropped from the numerator and

$\int_{\text{mainlobe}} \left[\sum_{n=m}^N E_o(n) E_o^*(n) (\sigma_{A_t}^2) + \sum_{n=m}^N E_o(n) E_o^*(n) (1 - \overline{\exp(j(\phi_t)^2)}) (\overline{A_t})^2 \right] du$ is small compared with another mainlobe term and is dropped from the denominator. Since $\overline{A_t}$ is close to unity and $\overline{\exp(j(\phi_t)^2)}$ is also close to unity when the phase error is moderate, therefore the right side of (8) is $C \{ \sigma_{A_t}^2 + (1 - \overline{\exp(j(\phi_t)^2)}) \}$, where

$$C = \frac{\int \sum_{n=m}^N E_o(n) E_o^*(n) du}{\int_{mainlobe} \hat{s}_h(u) \hat{s}_h^*(u) du}$$

which is related to the source properties only. When the phase error is moderate, $1 - \overline{\exp(j(\phi_t))^2} \approx \sigma_{\phi_t}^2$ and $ER \approx C\{\sigma_{A_t}^2 + \sigma_{\phi_t}^2\}$.

REFERENCES

- [1] G. E. Trahey, P. D. Freiburger, L. F. Nock, and D. C. Sullivan "In Vivo Measurements of Ultrasonic Beam Distortion in the Breast," *Ultrason. Imag.* 13, 71-90 (1991).
- [2] M. Moshfeghi, and R.C. Waag, In Vivo and in Vitro Ultrasound Beam Distortion Measurements of a Large Aperture and a Conventional Aperture Focused Transducer, *Ultrasound Med. Biol.* 5, 415-428 (1988).
- [3] B.D.Steinberg, "Scattering from a Multiple Random Phase Screen Model of a Random Inhomogeneous Medium," submitted to J. Acoust. Soc. Am. (1995)
- [4] Q. Zhu and B. Steinberg, "Modelling, Measurements and Correction of Wavefront Distortion Produced by Breast Specimens", *Proc. IEEE Ultrasonic Symp.* 1613-1617(1994).
- [5] S. W. Flax and M. O'Donnell, "Phase Aberration Correction using Signals from Point Reflectors and Diffuse Scatterers: Basic Principles," *IEEE Trans. Ultrason., Ferroelec. and Freq. Contr.*, 35(6),758-767 (1988).
- [6] E. H. Attia and B. D. Steinberg, "Self-Cohering Large Antenna Arrays Using the Spatial Correlation Properties of Radar Clutter," *IEEE Trans. Antennas Prop.*, AP-37(1), 30-38 (1989).
- [7] L. Nock, G. E. Trahey, and S. W. Smith, "Phase Aberration Correction in Medical Ultrasound using Speckle Brightness as a Quality Factor," *J. Acoust. Soc. Am.* 85(5), (1989)
- [8] M. Fink, "Time reversal of ultrasonic fields – part I: basic principles," *IEEE Trans. Ultrason. Ferroelec. Freq. Contr.*, vol. 39, pp. 555-566, 1992.
- [9] D.-L. Liu and R. C. Waag, "Correction of Ultrasonic Wavefront Distortion Using Backpropagation and Reference Waveform Method for Time-shift Compensation," *J. Acoust. Soc. Am.* 96, 649-660 (1994).
- [10] Q. Zhu and B. D. Steinberg, "Large-Transducer Measurements of Wavefront Distortion in the Female Breast," *Ultrason. Imag.*, 14, 276-299 (1992).
- [11] Q. Zhu, B. D. Steinberg, L. M. Hinkelman and R. C. Waag, "Deaberration of Incoherent Wavefront Distortion: An approach toward inverse filtering" submitted to *IEEE Trans. Ultrason. Ferroelec. Freq. Contr.* (Nov. 1995).
- [12] Q. Zhu and B. Steinberg, "Coherent Cancellation of Refraction Artifacts," 20 Int. Symp. on Ultrasonic Imaging and Tissue Characterization (June 1995).
- [13] M. O'Donnell and S. W. Flax, "Phase Aberration Measurements in Medical Ultrasound: Human Studies," *Ultrasonic Imaging.* 10(1), 1-11 (1988).
- [14] D.-L. Liu and R. C. Waag, "Time-shift Compensation of Ultrasonic Pulse Focus Degradation Using Least-mean-square Error Estimates of Arrival Time, *J. Acoust. Soc. Am.* 95(1), 542-555 (1994).
- [15] Q. Zhu, Q., B. D. Steinberg and R. Arenson, "Wavefront amplitude distortion and image sidelobe levels – parts II, In vivo Experiments," *IEEE Trans. Ultrason. Ferroelec. Freq. Contr.* 40(6) 754-762 (1993).
- [16] L. M. Hinkelman, D-L. Liu, and R. C. Waag, Q. Zhu, and B.D. Steinberg, "Measurement and Correction of Ultrasonic Pulse Distortion Produced by the Human Breast", *J. Acoust. Soc. Am.* 97(3), 1958-1969 (1995).

- [17] D. Carpenter and G. Kossoff, "Correction of Distortion in US Images Caused by Subcutaneous Tissues: Results in Tissue Phantoms and Human Subjects," *Radiology* (195): 563-567, (1995).
- [18] Q. Zhu, Q. and B. D. Steinberg, "Wavefront amplitude distortion and image sidelobe levels – parts I, theory, " *IEEE Trans. Ultrason. Ferroelec. Freq. Contr.* 40(6) 747-753 (1993).
- [19] A. Ishimaru, *Wave Propagation and Scattering in Random Media*, Academic Press, New York (1978).
- [20] M. Born and E. Wolf, *Principles of Optics*, Pergamon Press (1980).
- [21] L. M. Hinkelman, D-L. Liu, L.A. Metlay, and R. C. Waag, "Measurements of Ultrasonic Pulse Arrival Time and Energy Level Variations Produced by Propagation through Abdominal Wall," *J. Acoust. Soc. Am.* 95, 530-541 (1994).
- [22] Y. Sumino and R.C. Waag, "Measurements of Ultrasonic Pulse Arrival Time Differences Produced by Abdominal Wall Specimens," *J. Acoust. Soc. Am.*, 90(6), 2924-2930 (1991).
- [23] B. D. Steinberg, *Principles of Aperture and Array System Design* (Hohn Wiley & Sons, New York, 1976).
- [24] B. D. Steinberg, "Radar Imaging from a Distorted Array: The Radio Camera Algorithm and Experiments," *IEEE Trans. Antennas Prop.* AP-29(5), 740-748 (1981).

Table I.

Table I Relation of ER and image contrast (predicted and measured)								
	w/o Corr.	TDC	PC	Wideband DSA	BPT	PC	BPT	PC
ER	214.7%	44.2%	25.1%	103.5%	12.8%	6.8%	3.7%	2.1%
Image Contrast								
measured	4.2 (dB)	19	19.5	14.8	24.0	25.4	29.4	31.1
predicted	10.2 (dB)	17	19.5	13.3	22.4	25.2	27.8	30.3

FIGURES

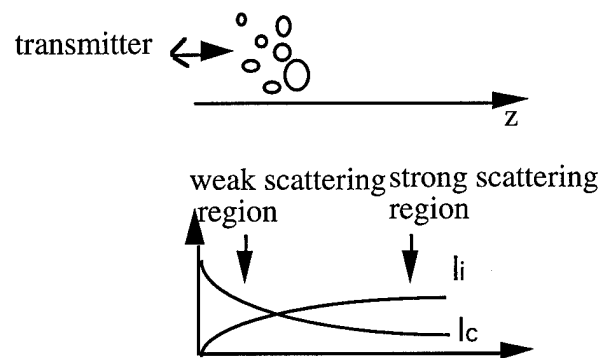
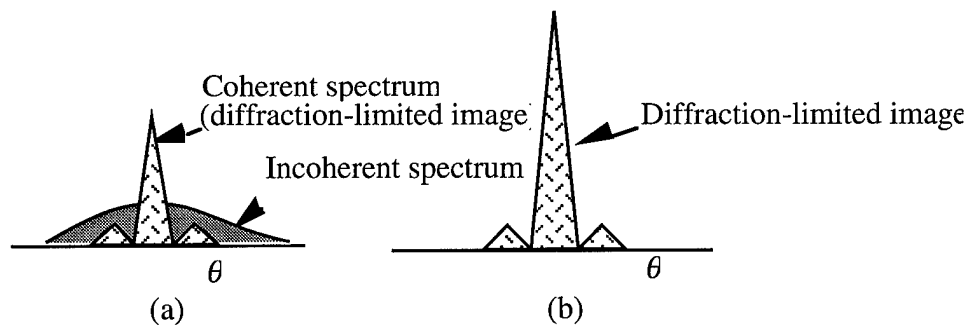
Figure 1. Approximate behavior of the coherent intensity I_c and the incoherent intensity I_i .

Fig.2. Angular source intensity distribution. Statistical model. (a) Before phase deaberration showing reduced coherent spectrum and of incoherent spectrum. (b) After phase deaberration.

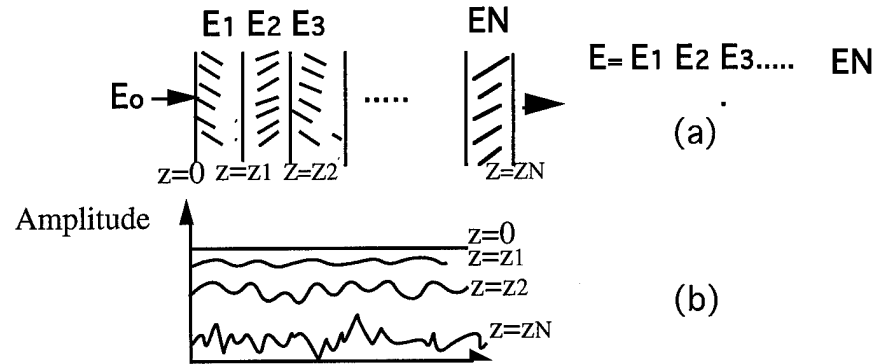


Fig.3 The field is the product of contributions from each layer. Wavefront amplitude fluctuation increases as wave propagates.

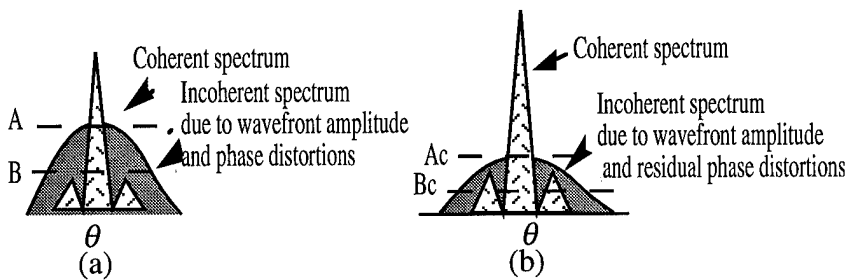


Fig.4. Statistical models of angular source intensity distribution. (a) Before phase correction. (b) After phase correction.

DEABERRATION TRANSFORMATIONS

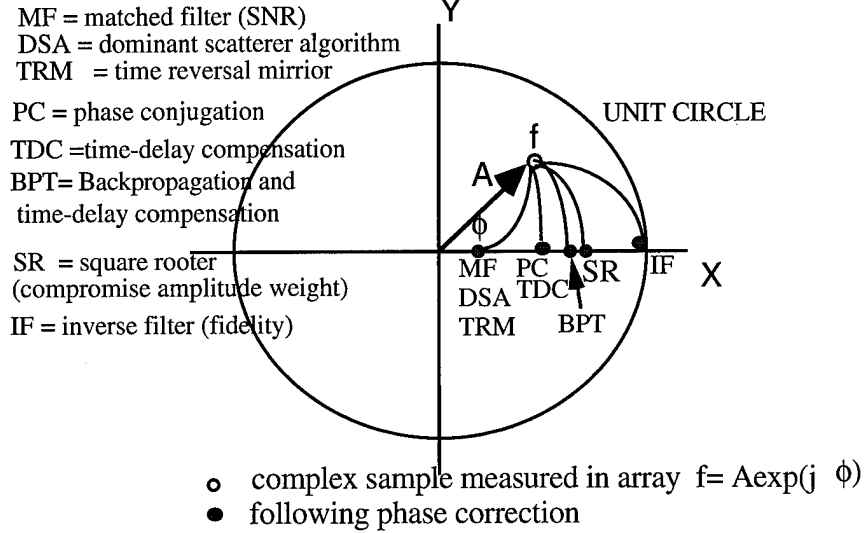


Fig.5. Deaberration transformations. f is distortion vector for instantaneous sample of the radiation field. Transformations to the real axis all correct phase. Left (MF) maximizes SNR but increases amplitude distortion. Right (IF) maximizes imaging fidelity but increases noise. SR is good compromise.

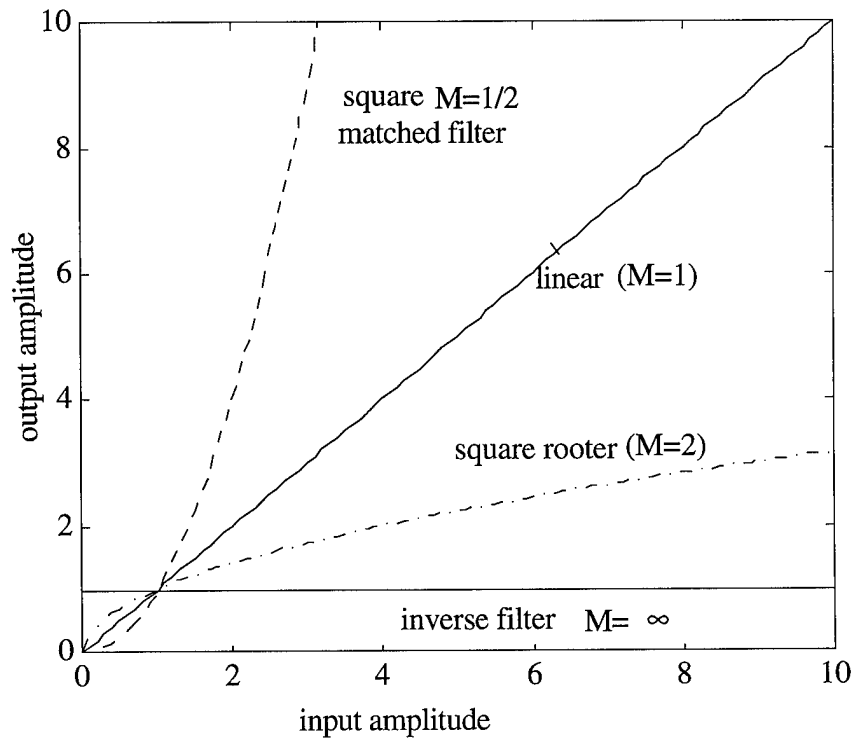
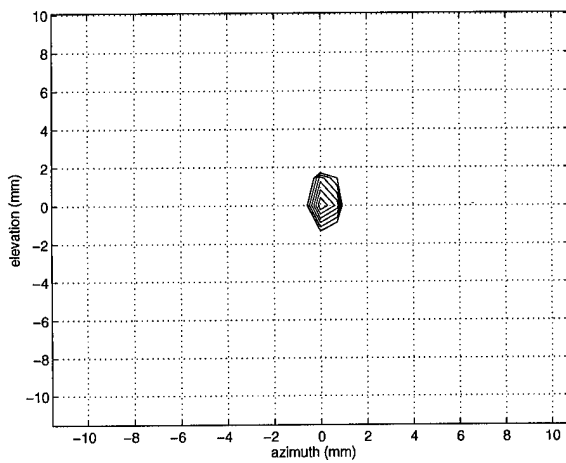
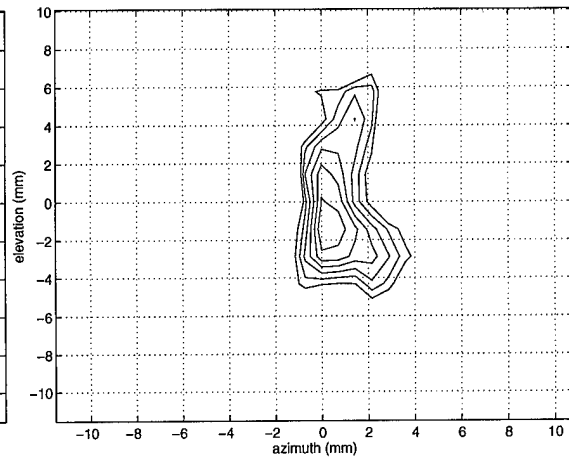


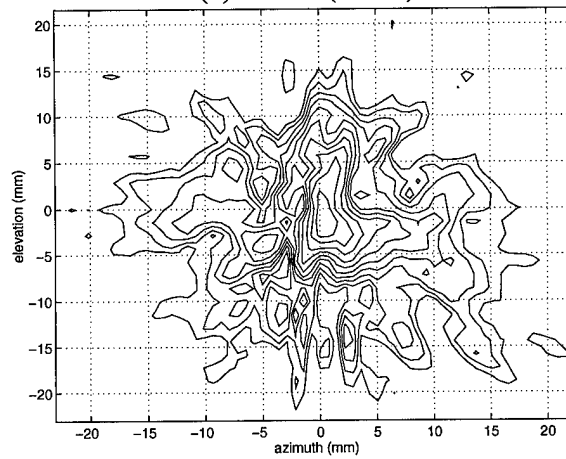
Fig.6. Plots of the input and output amplitude transforms.



(a) -6dB (water)

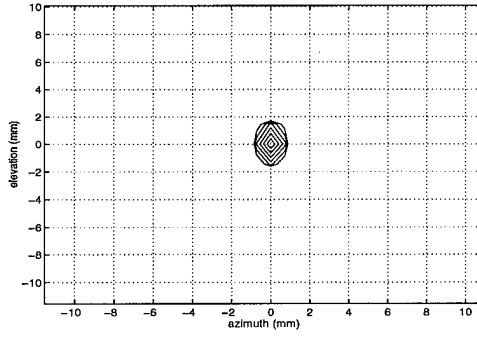


(b) -6 dB (brs005)

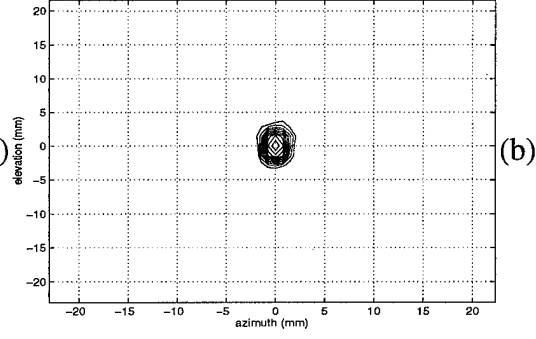


(c) -20 dB (brs005)

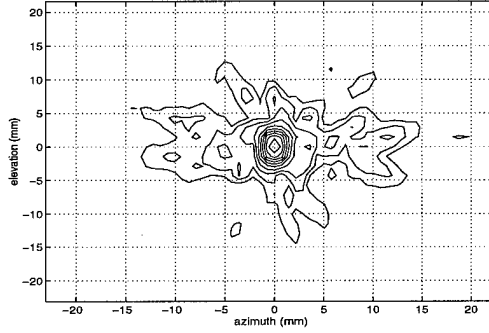
Fig.7. 2-D contour maps of point source images. (a) water data showing diffraction pattern of system. Outer contour is -6 dB level. (b) measured through the 3.5-cm tissue (brs005), showing asymmetric scattering effect. Outer contour is -6 dB level. (c) Image brs005 at -20 dB contour level. The outer contour shows symmetrical scattering pattern. No distinct structure or multipath is observed. Note the change of scale from (a) and (b).



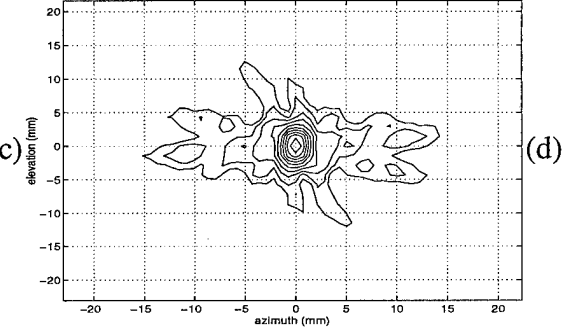
TDC at -6 dB



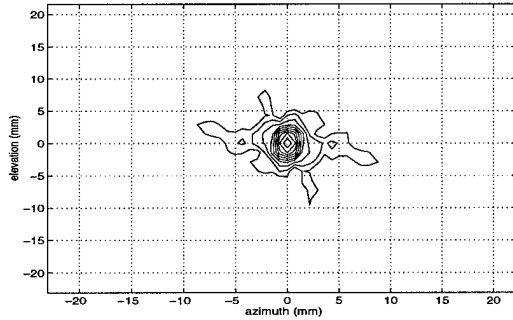
TDC at -20 dB



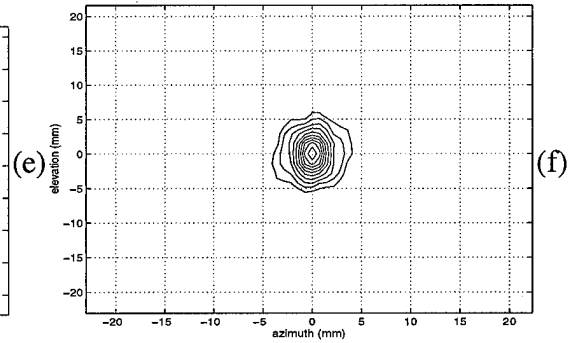
TDC at -30 dB



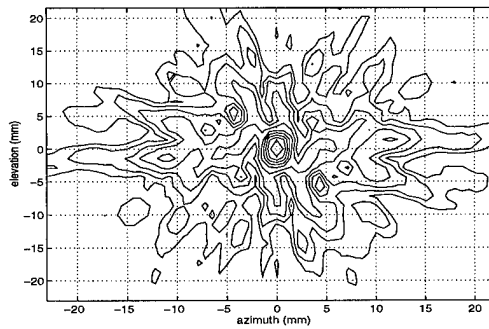
PC at -30 dB



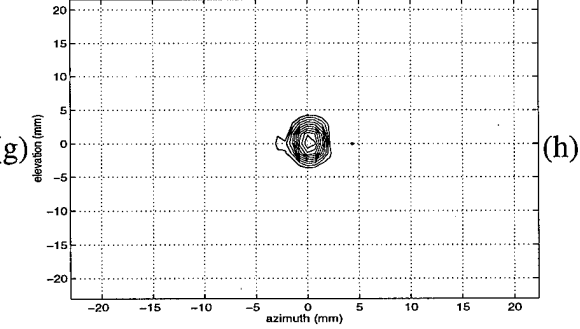
BPT at -30 dB



PC and square rooter
at -30 dB



Wideband DSA at -30 dB



Water at -30 dB

Fig.8. Distortion corrected contour maps of the sample image brs005 (see Fig.4(b) and (c) for comparison) (a) TDC at -6 dB. (b) TDC at -20 dB. (c) TDC at -30 dB. (d) PC at -30 dB. (e) BPT at -30 dB. (f) PC and square rooter at -30 dB. (g) Wideband DSA at -30 dB. (h) Water at -30 dB. Note the scale change of (b)-(h) from (a).

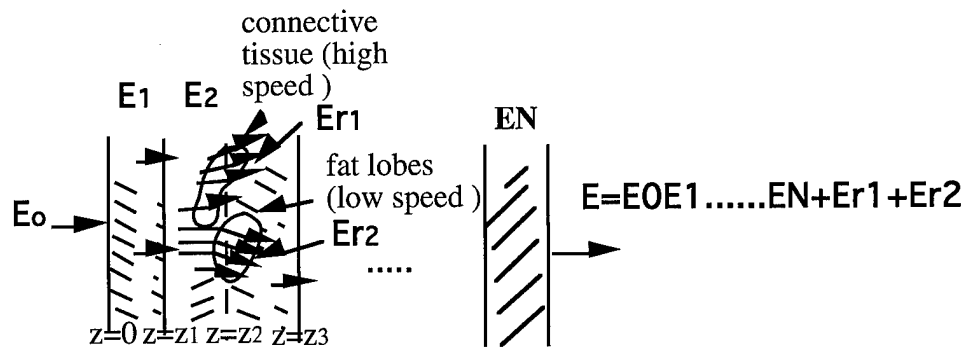


Fig.9 The field is the original field plus refracted fields.

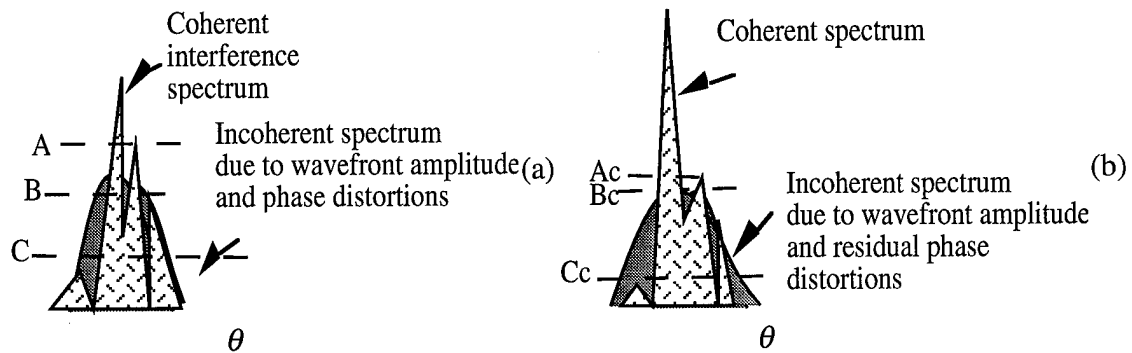


Fig.10. (a) Before phase compensation. (b) After.

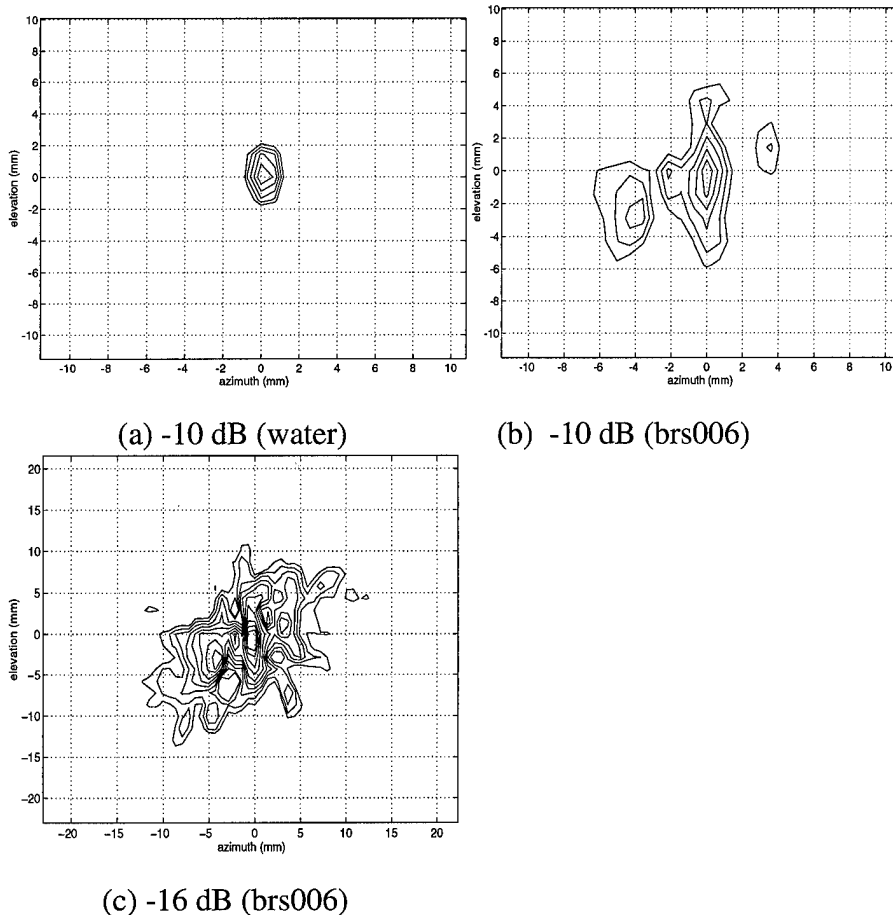


Fig.11. 2-D contour maps of point source images. (a) water data showing diffraction pattern of system. Outer contour is -10 dB level. (b) measured through the 4-cm tissue (brs006), showing highly asymmetric interference pattern. Outer contour is -10 dB level. (c) Image brs006 at -16 dB contour level. The outer contour shows more symmetrical scattering pattern. Note the change of scale from (a) and (b).

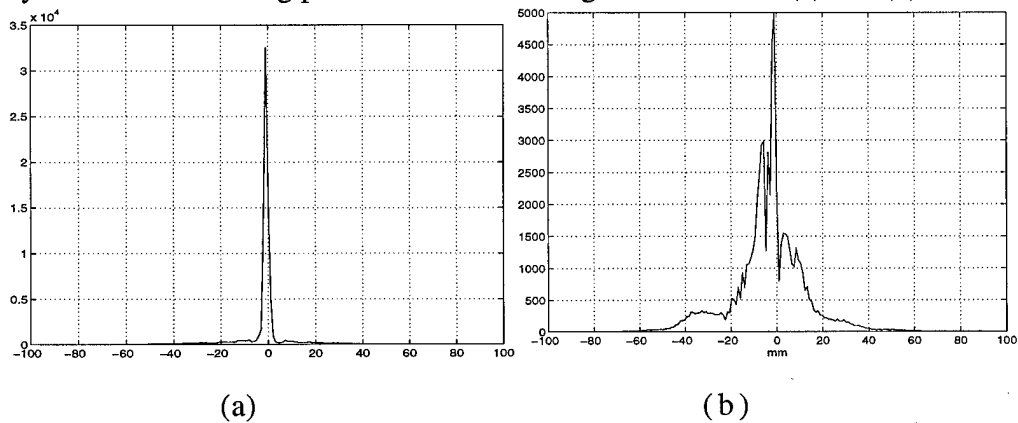


Fig. 12. (a) 45 degree cuts of 2-D images (a) water. (b) brs006.

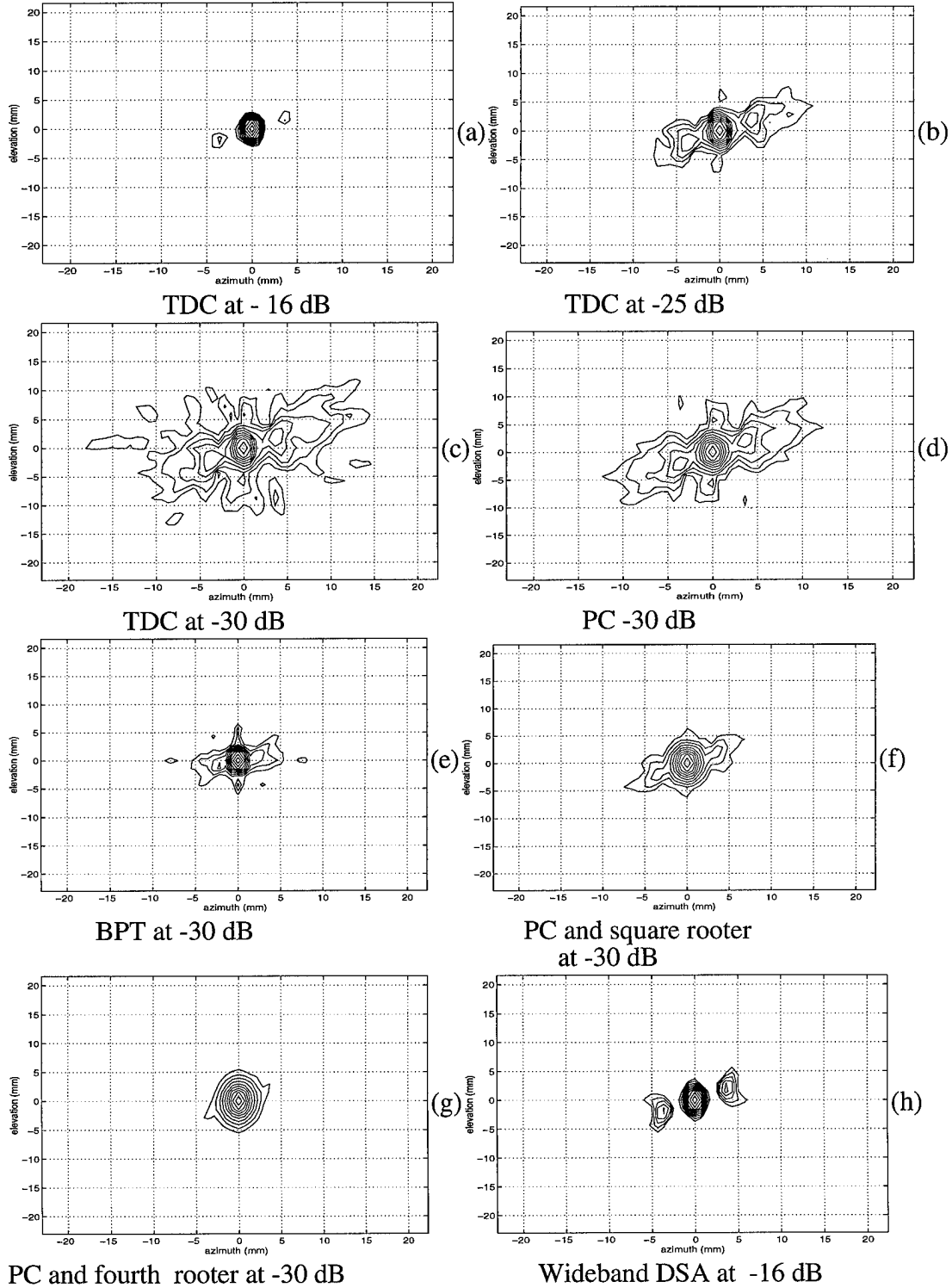


Fig.13. Distortion corrected contour maps of the sample image brs006 (see Fig.11 (b) and (c) for comparison) (a) TDC at -16 dB level. (b) TDC at -25 dB level and (c) TDC at -30 dB level. (d) PC at -30 dB level. (e) BPT at -30 dB. (f) PC and square rooter at -30 dB. (g) PC and fourth rooter at -30 dB. Wideband DSA at -16 dB. Artifacts are 5 dB higher than time-delayed correction shown in Fig.8(a).

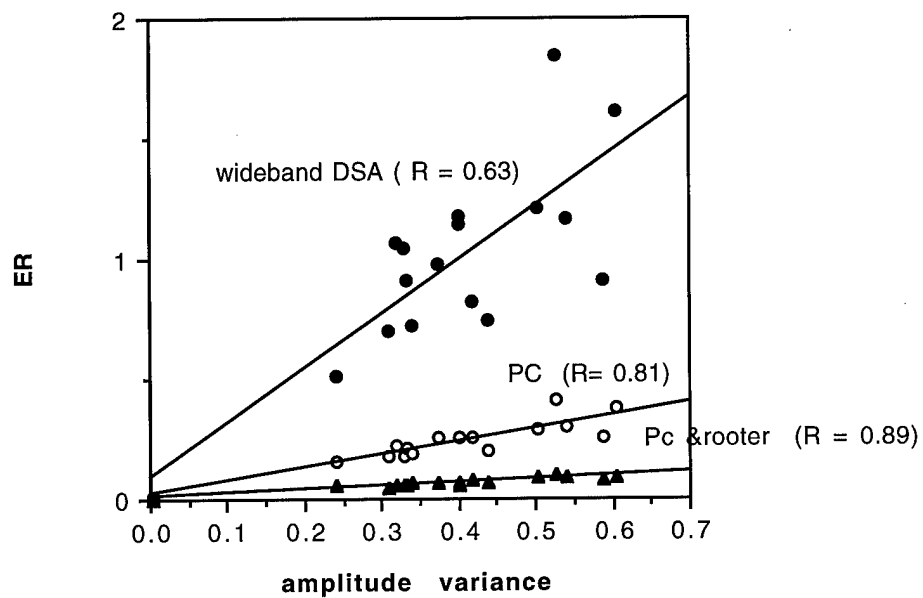


Fig.14. Linear regression plots of ER, after wideband DSA (upper), phase conjugation (middle) and phase conjugation & square rooter (bottom), vs. wavefront amplitude variance.

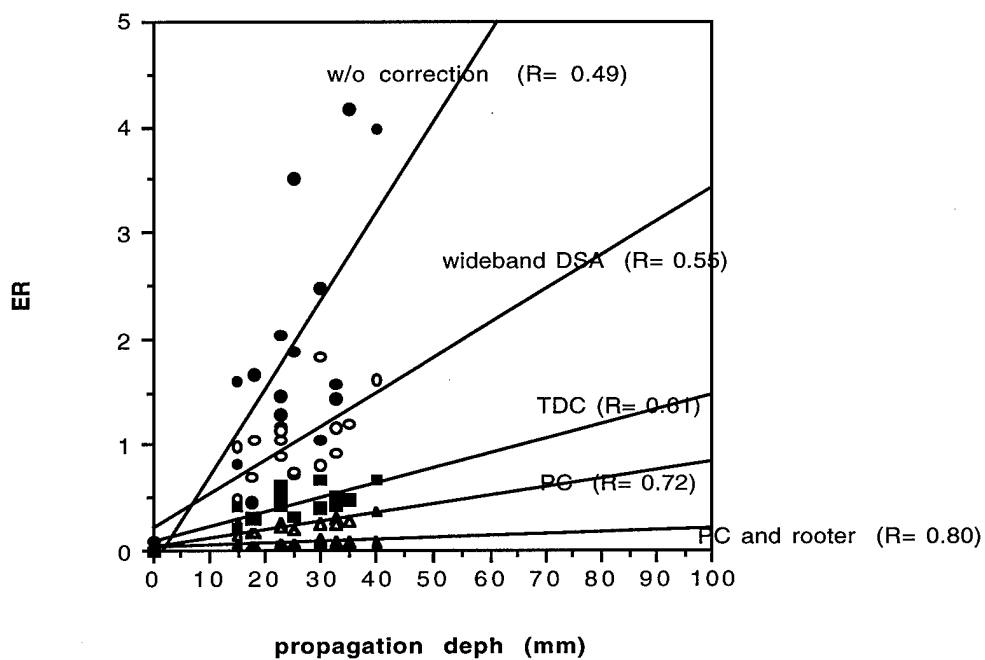


Fig.15. Linear regression plots of ER vs. propagation depth obtained from without correction (solid circle), wideband DSA (circle), TDC (solid square), PC (triangle) and PC and rooter (solid triangle). The correlation coefficients are give by R. One outlier was removed from (a).

January 1996

Deaberration of Incoherent Wavefront Distortion: An Approach Toward Inverse Filtering

Qing Zhu, Member IEEE, Department of Radiology and Valley Forge Research Center
Bernard Steinberg, Life Fellow IEEE, Valley Forge Research Center, The Moore School of
Electrical Engineering, University of Pennsylvania, Philadelphia, PA 19104
Laura M. Hinkelman, Department of Electrical Engineering, University of Rochester
Robert C. Waag, Fellow IEEE, Departments of Electrical Engineering and Radiology,
University of Rochester, New York 14627

ABSTRACT — There are two wavefront distortion problems inside the female breast that are caused by aberration sources of two distinct types, incoherent scattering and coherent interference. Scattering reduces the target strength, broadens the image lobe and raises the background level and therefore lowers the image contrast, while refraction creates coherent multipath interference that produces false targets or image artifacts in addition to true targets in the image. Scattered energy increases with the propagation depth while refracted energy does not seem to change with the depth. Phase deaberration algorithms partially remove scattered energy and coherently add it back to the primary field. As a result, the mainlobe diffraction shape is restored to -19.4 dB (std. 2.5 dB) level on average with a net 15 dB (std. 3 dB) improvement compared with that without correction. Because of the strengthening of the primary field and consequently the target strength by the phase-deaberration process, the ratio of peak image artifact to target strength is also improved by an average of 10 dB (std. 4dB) from breast samples that have well-defined multipath artifacts. Backpropagation in addition to phase deaberration can further strengthen the primary field and improve the above numbers by another 5 dB. A compression operation upon wavefront amplitude, akin to inverse filtering, in addition to phase deaberration or to backpropagation and phase deaberration, can further restore the mainlobe diffraction shape

to the -30 dB region. Linear regression analysis of sidelobe energy vs. propagation depth indicates that high quality focusing with ~ 25 dB contrast resolution throughout 10 cm thick breast tissue is possible.

I. INTRODUCTION

Adaptive compensation of wavefront distortion induced by tissue inhomogeneity is an active area of current research. Basic phase deaberration algorithms are recognized to be suitable only for weak scattering that can be modeled as a thin random phase screen located in the plane of the receiving aperture [1-3]. Extensions of the basic algorithms have been made to correct amplitude distortion in addition to phase distortion caused by strong scattering or distributed scattering [4-5]. However, it is shown analytically in [6] and experimentally in this paper that algorithms that take amplitude distortion into account can further improve contrast resolution than phase deaberration algorithms only if the algorithms reduce wavefront amplitude variance.

Consider complex signal vectors S_0 and S received at an array in the absence and presence of distortion, respectively. (S_0 and S are functions of position in the array which is identified by element number.) The multiplicative distortion $A \exp(j\phi)$ is the ratio of S to S_0 . Fig.1 shows such a distortion vector \mathbf{f} for some instantaneous sample of the radiation field. The optimum compensation transformation is the right-most one which carries the distortion component of the complex sample to the intersection of the x-axis and the unit circle, for then both amplitude and phase are corrected. The left-most transformation is matched filtering (MF) which squares the amplitude and conjugates the phase. MF is theoretically optimum for maximizing SNR on a white, Gaussian channel. It is an optimum solution for detection (radar) but not so when fidelity is an important criterion, as in imaging. But it does satisfy the requirement for phase correction. Examples of MF

to the -30 dB region. Linear regression analysis of sidelobe energy vs. propagation depth indicates that high quality focusing with ~ 25 dB contrast resolution throughout 10 cm thick breast tissue is possible.

I. INTRODUCTION

Adaptive compensation of wavefront distortion induced by tissue inhomogeneity is an active area of current research. Basic phase deaberration algorithms are recognized to be suitable only for weak scattering that can be modeled as a thin random phase screen located in the plane of the receiving aperture [1-3]. Extensions of the basic algorithms have been made to correct amplitude distortion in addition to phase distortion caused by strong scattering or distributed scattering [4-5]. However, it is shown analytically in [6] and experimentally in this paper that algorithms that take amplitude distortion into account can further improve contrast resolution than phase deaberration algorithms only if the algorithms reduce wavefront amplitude variance.

Consider complex signal vectors S_0 and S received at an array in the absence and presence of distortion, respectively. (S_0 and S are functions of position in the array which is identified by element number.) The multiplicative distortion $A \exp(j\phi)$ is the ratio of S to S_0 . Fig.1 shows such a distortion vector \mathbf{f} for some instantaneous sample of the radiation field. The optimum compensation transformation is the right-most one which carries the distortion component of the complex sample to the intersection of the x-axis and the unit circle, for then both amplitude and phase are corrected. The left-most transformation is matched filtering (MF) which squares the amplitude and conjugates the phase. MF is theoretically optimum for maximizing SNR on a white, Gaussian channel. It is an optimum solution for detection (radar) but not so when fidelity is an important criterion, as in imaging. But it does satisfy the requirement for phase correction. Examples of MF

algorithms are Dominant Scatterer Algorithm (DSA) [7] and Time Reversal Mirror (TRM) [4]. We should expect that MF algorithms are useful when wavefront distortion resides principally in phase, with amplitude relatively unaffected. Otherwise MF algorithms would be less effective than if amplitude were ignored and phase only were corrected. By squaring the wavefront amplitude, the MF algorithms increase amplitude variance which contributes to the increase of energy in the sidelobe region [6].

This is what happens when a phantom consisting of a random phase screen is placed at a receiving transducer. The element signal samples are correct in amplitude and distorted only in phase by a random additive component. Phase aberration correction (PAC), consisting of phase conjugation (PC), is then the optimum compensator. The signal amplitude is unchanged and phase error is completely compensated by conjugation. This operator is represented by the 2nd (from the left) transformation. Time delay compensation (TDC) [1-3] is in the same class.

The right-most transformation which corrects both amplitude and phase is the inverse filter (IF). It is theoretically ideal for fidelity but has drawbacks. Because the IF adjusts the channel gain to be the reciprocal of the signal strength, at points in the receiving aperture where signal strength is weak the enhanced channel gain raises the noise to the point where SNR can be impaired. This is particularly troublesome when there is coherent refractive interference in the receiving array. A second potential problem, which we have avoided by not working too close to the IF point, is that an IF is unstable when the distorting medium has zeroes in the complex plane. Thus the right-most transformation carries the correction too far.

The complex weights of MF, PC and IF are, respectively, A , 1 and A^{-1} , each multiplied by $\exp(-j\phi)$. The signal after weighting is A^2 , A and 1 . The first and last are

far from optimum for the reasons given. The 3rd from the left transformation is a compromise. The correction vector is $A^{-1/2}\exp(-j\phi)$. The signal after weighting is $A^{1/2}$ (called later the square rooter or rooter). Another transformation to the right of the square rooter is fourth rooter (signal amplitude is $A^{1/4}$ after weighting). In general, the correction vector is $A^{-(M-1)/M}\exp(-j\phi)$ and signal amplitude is $A^{1/M}$ after transformation of the Mth rooter. In Section III, we demonstrate that low order rooters (square rooter and fourth rooter), in addition to phase deaberration at the aperture, can significantly improve contrast resolution without encountering stability problem.

Backpropagating the received wavefront to an optimal backpropagation distance and performing phase deaberration at this optimal distance (BPT) [5] provides first order correction of wavefront amplitude distortion due to propagation from the backpropagation distance to the receiving aperture and therefore performs better than phase deaberration at the aperture. In Section III, we demonstrate experimentally that BPT transformation is somewhere to the right of TDC and PC and left of PC and rooter. We also demonstrate that square rooter in addition to BPT can significantly improve the performance of BPT.

The rooter transformation upon wavefront amplitude is a nonlinear compression operation (Fig.2). The detailed evaluation of the effects of this operation upon image can be performed by studying the amplitude distributions of images before and after the operation. This is a subject of a later study.

II. METHODS

A. *In Vitro Measurement*

The 2-D wavefront measurement system and procedure were described in detail in [8] and are summarized here for convenience. A breast tissue specimen was placed in the specimen holder with the skin facing the direction of the receiving transducer. The source

was a hemispherical transducer emulating a virtual point source. The 2-D array consisted of a 92-mm 1-D linear array translated 46 mm perpendicular to its axis to form a synthetic 2-D array 92 mm x 46 mm. The element pitch in the receiving transducer was 0.72 mm and a reflecting mask reduced the receiving elevation to 1.44 mm. Transmission was one-way. Frequency was 3.7 MHz. Bandwidth was 2 MHz. Waveforms were measured at each element, from which 2-D wavefronts were reconstructed as functions of time.

Breast tissue specimens were obtained fresh from reduction mammoplasty surgery and were stored frozen; they were later defrosted and degassed for the experiments. Each specimen was essentially planar and had a surface area of at least $7 \times 11 \text{ cm}^2$. The average thickness was 26.9 mm. The tissue donors were women ranging in age from 18 to 65 with a mean age of 34 years.

Three groups of measurements were made. The primary set consisted of independent measurements using nine different specimens. In addition, two specimens were employed for sequential measurements in which an approximately 1-cm layer was removed from the bottom of the specimen before each subsequent measurement. For three other specimens, a pair of measurements was made with the source in each of two positions located 12 mm apart in the array direction. A total of 16 measurements were made. Water measurement was also made for comparison. In the following analysis, the sequential measurements were treated as measurements from different samples because the samples resulting from approximately 1-cm removal from the original samples were replaced into the sample holder after cutting, and their relative positions to the 2-D transducer aperture changed unpredictably. The pair measurements resulting from 12 mm lateral source translation were also treated as measurements from different samples because the measured parameters and the point-source image properties were changed due to the highly inhomogeneous nature of the breast tissue.

B. Data Processing

Pulse arrival time at each element was calculated by using a differential edge detector to locate the first negative peak of the pulse. Geometric effects were removed by fitting a two-dimensional, fourth-order polynomial to the calculated arrival time surface and subtracting the result. The reasons for using fourth-order polynomial fitting were given in [5]. 3-D image data were calculated by (1) Fourier decomposition of the temporal waveforms at each (x,y) position in the aperture, (2) calculation of a complex CW 2-D image at each Fourier frequency in the focal plane by using the angular spectrum technique [18], and (3) summation of the 2-D images to form the 3-D transient image. The final 2-D image used in this report was obtained by detecting the peak pressure value at each (xf,yf) position in the image plane within the transient period. Contour maps of 2-D point source images at different thresholds are used to quantitatively evaluate image quality.

Before Fourier decomposition, the received pulse at each element was temporally weighted by a 10-point cosine taper over the trailing 10 points of a 40-point time window that contained the main arrival pulse. The original 40-point interval was padded with zeros to a 128-point interval.

In step (1), a frequency range (0.31 - 6.25 MHz) that contained most of the signal energy was chosen. This range corresponds to the 3rd through 41st harmonic of the FFT of a signal sampled at 20 MHz over a 6.4 μ s interval containing 128 points.

In step (2), the complex signals in the 128×32 spatial aperture were zero padded symmetrically to 256×64 before each harmonic component in the 2-D aperture was focused in the image plane via the angular spectrum technique. Spatial raised cosine taper was employed. The system bandwidth is about 50%; therefore $Q = \frac{f_0}{\Delta f} \approx 2$, where f_0 is the

central frequency. For such Q , the first sidelobes (due to finite aperture size) in both principal axes remain [9], and are reduced to about -30 dB level by employing the raised cosine taper [10].

C. Correction Methods

Two basic phase deaberration algorithms, time-delay compensation (TDC) and phase conjugation (PC), and two wavefront compensation algorithms, wideband DSA and BPT, were applied to each measured 2-D wavefront set and their effects upon focusing were compared. Square rooter and fourth rooter on wavefront amplitude in addition to PC and square rooter in addition to BPT were also implemented and their effects upon focusing were compared with the other four deaberration algorithms.

TDC: An arrival time fluctuation profile at the aperture is calculated in three steps. Step 1: A reference waveform with good signal-to-noise ratio is first selected from geometrically corrected waveforms. The selected waveform is continuously modified to reduce the effect of the arbitrariness in the initial selection as waveforms in the aperture are cross-correlated with it. The modification is accomplished by time-shifting and adding a new waveform to the reference pulse if the peak value of the correlation function between the new waveform and the current reference waveform is greater than 0.8. The average total number of waveforms that are incorporated into the final reference waveform selection is 2690 (std. 391), which accounts for 66% (9.5%) of the total pulses. The average is calculated upon a total of 16 *in vitro* samples. This selection procedure is similar to the one developed in [5].

Step 2: The arrival time fluctuation profile is first calculated from cross-correlation peaks of geometrically corrected waveforms and the reference waveform when the peak values of the correlation function between the waveforms and the reference waveform are greater than

0.7. At this step, the average total number of waveforms that are incorporated into the calculation of the arrival time profile is 3518 (std. 173), which accounts for 86% (std. 4.2%) of the total pulses.

Step 3: For the bad waveforms with cross-correlation peaks less than 0.7, the arrival time fluctuations at these positions are calculated as follows: (1) calculate cross-correlation peaks between each bad waveform and neighbor waveforms (within a 5 by 5 spatial window) that are incorporated in Step 2; (2) select those neighbor waveforms having cross-correlation peaks, calculated in (1), greater than 0.5; (3) calculate the average of arrival time fluctuation from arrival time differences between the bad waveform and the selected neighbor waveforms, and the arrival time fluctuations of the corresponding neighbor positions. This average is assigned to the bad waveform position. A justification of this step is that for badly distorted waveforms, they are dissimilar to the reference waveform to a large extent, but they are somehow similar to the waveforms in the closest neighborhood which are reasonably correlated with the reference waveform. After this step, the average total number of pulses that are incorporated into the calculation of the arrival time profile is 3966 (std. 41) which accounts for 97% (std. 1%) of the total pulses.

For the waveforms that have not been incorporated into the calculation of the arrival time profile after Step 3, arrival time fluctuations at these positions are assigned to zero. The calculated average arrival time fluctuation of the entire 16 profiles is 37.6 ns with a 10.5 ns standard deviation.

Except for TDC, the following correction procedures were implemented upon complex wavefront at each frequency after Fourier decomposition. The image formation procedures after using each correction method were the same as the procedures described in part B steps (2) and (3).

PC: Let $A_f(x,y)\exp(j\phi_f(x,y))$ represent the complex signal at each frequency after Fourier decomposition, where A_f and ϕ_f are functions of positions (x,y) in the 2-D array and frequency f . The complex weight vector of phase conjugation is $w_f=\exp(-j\phi_f)$ and the signal after weighting is A_f . The image formation after phase conjugation is the same as the procedures described in part B steps (2) and (3). Phase conjugation at each frequency within the signal band (without amplitude weight) provides perfect phase compensation except for a 2π phase jump. The result is better than TDC because of the removal of residual phase error. The wavefront amplitude distortion remains, however. The objective here is to evaluate the limit of phase compensation and the extent of the wavefront amplitude distortion effect.

Wideband DSA: The complex weight vector of DSA at each frequency is $w_f=A_f\exp(-j\phi_f)$ and the signal after weighting is A_f^2 .

Wideband DSA is an approximation of the TRM receive mode developed in [11]. The difference between wideband DSA and TRM receive mode is the scanning procedure. At target position A (Fig.3), wideband DSA and TRM receive mode produce exactly the same responses, because of the reciprocity principle. At non-target position B, wideband DSA uses linear geometry between A and B to scan the beam while the TRM receive mode could backpropagate the wave to the aberrator position, and then use linear geometry to scan the beam [11]. However, for points that are within the correlation distance of A, wideband DSA and the TRM receive mode should produce similar responses. The correlation distance of the breast is about 4-5 mm [8],[12],[13-14]. Therefore within a 4 - 5 mm radius, we should expect similar performances of wideband DSA and TRM receive mode. The objective of using wideband DSA here is to evaluate the possible improvement of deaberration due to the additional SNR gain provided by amplitude weighting.

BPT: BPT developed in [5] is implemented by backpropagating the complex wavefront at each frequency after Fourier decomposition to the optimal distance and then using *phase conjugation* at the optimal distance. The use of phase conjugation instead of TDC at the backpropagation distance reduces the complexity in the calculation. The backpropagation distances are taken from [8].

Rooters:

PC and square rooter: The weight vector of PC and square rooter at each frequency is $w_f = A_f^{-1/2} \exp(-j \phi_f)$ and the signal after weighting is $A_f^{1/2}$

PC and fourth rooter: The weight vector at each frequency is $w_f = A_f^{-3/4} \exp(-j \phi_f)$ and the signal after weighting is $A_f^{1/4}$.

BPT and square rooter: BPT and square rooter was implemented the same as PC and square rooter but the procedure was done at the optimal back propagation distance after backpropagating each complex wavefront to the optimal distance.

III. EXPERIMENTAL RESULTS

A. Correction of Scattered Energy

1) Correction upon scattering samples

Figs.4 (a) and (b) show -6 dB contour plots of images obtained from the water path and the 3.5-cm breast tissue path (brs005). Contour spacing is 1 dB. Abscissa and ordinate are azimuth and elevation in mm in the image plane. Fig.4(a) shows the system diffraction pattern at -6 dB. The azimuthal beamwidth is about 1.5 mm (at a distance of 180 mm) meaning that the point (or lateral) resolution is 1.5/180 or 8.3 mrad. Because the size of the receiving array in elevation is half the size in the array direction, the width of the image in

elevation is twice as large as in azimuth. When tissue is present (b), the image lobe is broadened. In (b) the beamwidth has grown from 1.5 mm to 3 mm in azimuth and 3.1 mm to 9.3 mm in elevation and the point resolution has worsened approximately 2:1 in azimuth and 3:1 in elevation. A symmetrical scattering pattern appears when the threshold is reduced. Fig.4 (c) shows a -20 dB contour plot of the sample image brs005. Contour spacing is 2 dB. Energy is spread out over a large area. No distinct structure or multipath lobe can be identified from the image.

Fig.5 (a)-(g) shows the correction result of the sample image brs005 by using different methods. Part (h) is the -30 dB level contour of a water path image. The contour spacings in Fig.5 are the outer contour levels divided by 10. Fig. 5 (a)-(c) shows TDC at -6, -20 and -30 dB levels (see Fig.4(b) and (c) for comparison). Image quality improved significantly and the system diffraction pattern is restored up to -20 dB level. The symmetric scattering pattern outlined by outer contours at the -30 dB level is caused by residual phase errors after phase deaberration and incoherent amplitude distortion. Fig.5 (d) is the correction result of PC at the -30 dB level. Because of the complete removal of phase errors except for a 2π jump, the scattering pattern is further improved as compared to (c). Fig. 5 (e) is the result of BPT, and the scattering pattern is much better than that of PC at the aperture. The optimum backpropagation distance of this tissue sample is 30 mm. It is interesting to note that the beamwidth is narrower than that obtained through other methods. The reason is that the actual aperture is moved 30 mm closer to the source and the beamwidth is $(R\text{-optimal backpropagation distance})\frac{\lambda}{L}$ instead of $R\frac{\lambda}{L}$, where R is the distance between source and the receiving aperture, and L is the aperture size. Fig.5 (f) is the correction result of PC and square rooter on wavefront amplitude at -30 dB. The pattern is very close to the system diffraction pattern (see (h) for comparison). Fig.5(g) is the result of wideband DSA at the -30 dB level. The correction result is worse than those of other methods (see Section IV).

2) Correction upon samples with well-defined multipath

In most breast samples, scattering and coherent interference are both present. Fig.6 (a) and (b) are -10 dB contour plots of images obtained from the water path and the 4-cm breast tissue path (brs006). Contour spacing is 2 dB. In tissue image (b), three lobes instead of one central image lobe appear. Inner contours of the image lobe are close to the system diffraction pattern (Fig.6(a)) while the outer contours are highly irregular due to scattering. The point resolution is worsened by approximately 2:1 in azimuth and 3:1 in elevation. Two refractive lobes appear at $(-4, -2.5)$ and $(3.5, 1.5)$, and their strengths are -6 and -8 dB. A closer examination is obtained from 45 degree cuts (Fig.7) of the Fig.6 (a) and (b) images. In Fig.7 (a), the peak sidelobe is -36dB, which is the best we can obtain from the measurement system. In the tissue image, two large sidelobes (-6 dB and -8 dB) appear on either side of the mainlobe. The two nulls between the lobes are deep (left : -13 dB below peak, right: -15 dB), which is a typical coherent interference phenomenon [15].

A symmetric scattering pattern generally appears when the threshold is reduced, as shown Fig.6(c) with a -16 dB threshold contour and contour spacings of approximately 1.5 dB. The outer contours show a roughly symmetric pattern typical of scattering while the inner contours show an asymmetric lobular interference pattern.

Fig.8 shows correction results of the sample image brs006 after applying different methods. The contour spacings are the outer contour levels divided by 10. Fig.8(a) is the -16 dB contour map of applying TDC (see Fig.6(c) for comparison)). Image quality improved significantly because of the minimization of the phasefront distortion caused by scattering. The area within the -16 dB inner contour is reduced by a factor of 11. The mainlobe pattern is close to the system diffraction pattern although the area is still 1.6 times larger than the area in water at the same level. Two large lobes remain as expected and

appear as two additional sources. Fig.8(h) is the correction result at a -16 dB level of applying wideband DSA. It is evident that the procedure enhances interference in this example; the artifacts are 5 dB higher than in Fig.8(a). The reason is given in [6]. Figs.8(b) and (c) show -25 and -30 dB contour plots of TDC. In Fig.8(b) the outer contours show an asymmetric interference pattern with scattered energy distributed around the two interference lobes. In Fig.8(c) the outer contours show the more symmetric scattering pattern caused by incoherent wavefront amplitude distortion and residual phase distortion. Fig.8(d) is the result of PC at -30 dB. The approximately symmetric scattering pattern outlined by outer contours in (c) is improved due to better phase deaberration. The energy is more concentrated around the image lobe and interference lobes. Part (e) is the result of BPT, and the scattering pattern is further improved as compared with the result of PC at the aperture. The backpropagation distance of this sample is 50 mm. Part (f) is the result of PC and square rooter at -30 dB. The pattern is very close to the system diffraction pattern. PC and fourth rooter shown in Fig.8(g) restores the diffraction-limited image to a -30 dB level.

It is interesting to note that the strengths of the two interference lobes are also reduced by 8 dB after TDC and PC. They are further reduced by 5, 7 and 15 dB after BPT, PC and square rooter, and PC and fourth rooter, respectively. The improvement comes from the scattered energy which is originally distributed around the mainlobe and each of the refracted multipath lobes. This energy is coherently added back, by the deaberration process, to the dominant lobe, which in this case is the mainlobe. The overall result is an improvement of the image lobe to the interference lobe ratio.

Determination of whether interference was coherent or scattered was based upon whether or not large lobes could be removed by applying phase-deaberration algorithms. Another indicator is whether or not a lobe location moves (scattering) or remains relatively

the same (refraction) after the phase deaberration process. Both means were used to identify whether these lobes were produced by refraction or scattering. Large lobes in nine samples are believed to be caused by the interference process. In these samples, we have found an average of a 10 dB (std. 4dB) improvement in the range of 5-16 dB after TDC, due to the coherent strengthening of the mainlobe.

B. Correction statistics

We analyzed images at different contour levels and classified the total of 16 samples into three categories: 1) Primarily scatter (4 samples); 2) More scatter than refraction (3 samples); and 3) Scatter plus well-defined refraction (9 samples). Statistics of -6 dB point resolution of three groups is given in Table I. The average beam-broadening as compared with water is 70% in azimuth and 57% in elevation. These numbers are larger than the result reported in [14] where an 18% increase in beamwidth at the same threshold is observed. This is likely due to the different aperture sizes used. For the samples with refractive artifacts, the point resolution is evaluated upon the central image lobe. The percentage increase in beamwidth of the scatter group is significantly larger than that of the other two groups. It is obvious that point resolution is not enough to evaluate image distortion when multiple lobes are present. Statistics of refractive lobes of the third group is given in Table II. In this group, we found 1-3 refractive lobes at levels between -4 and -17 dB (peak value), all within a radius of $1-3^\circ$.

A simple metric, the lowest level at which mainlobe diffraction shape is maintained, is used here to quantitatively evaluate improvement upon image quality by using different correction algorithms. The mainlobe diffraction shape is identified when the elevation-image width to the horizontal width is approximately a 2 to 1 ratio and the outermost image contour has an elliptical shape. This metric is closely related to contrast resolution. For a

simple scattering case, the measurement of this metric is straightforward. For a complicated scattering and multipath case, the meaningful measurement is the level at which the mainlobe diffraction shape is maintained and is also above any multipath artifacts.

The average levels (std. dev) of the restored mainlobe diffraction shape before and after corrections of the three groups classified earlier are given in Table III. The mainlobe shape is restored up to -19.3 (2.4) and -19.5 dB(2.6 dB) by using two phase-deaberration algorithms, TDC and PC, respectively. The fact that the correction result of TDC is very close to that of PC suggests that the limit of phase correction with respect to the selected metric has been achieved by TDC. Further improvement requires correction algorithms that can take wavefront amplitude distortion into account. Wideband DSA is able to restore the mainlobe shape to -14.8 dB(2.3 dB). This result is about 5 dB worse than that of using two phase-deaberration algorithms. The reason is the increase of wavefront amplitude variance by squaring the amplitude. Wavefront amplitude variance contributes to the energy in the sidelobe region [6]. BPT at an optimal backpropagation distance improves the performance of PC at aperture by 5 dB. PC and square rooter on wavefront amplitude restores the mainlobe diffraction shape to -25.4 dB (2.6 dB). The correction result of BPT is similar to PC and square rooter. PC and fourth rooter achieves a -31.1 dB (1.7 dB) level, which is about a 12 dB improvement more than that of using two phase deaberration algorithms. This level is very desirable for a high quality ultrasound echo scanner. BPT and square rooter at an optimal backpropagation distance further improves the BPT by another 5 dB.

The restored mainlobe diffraction levels among different groups are similar when different correction methods are used. But the improvements are, in general, 6 dB larger in the scatter group than that of the other two groups because the mainlobe shape is distorted at zero dB in the scatter only group.

C. Depth-dependent Distortion and Correction

Scattered energy increases with the propagation depth D . Using first order approximation, it is shown analytically in [6] that wavefront amplitude variance $\sigma_{A_t}^2$, and phase variance or arrival time variance σ_t^2 linearly increase with propagation depth. $\sigma_{A_t}^2$ is calculated as follows: 1) calculate energy at each (x,y) position at the aperture by summing up the energy over the time window; 2) calculate amplitude at each (x,y) position by taking the square root of the energy; 3) calculate the reference amplitude profile which is the fourth order polynomial fit of the measured amplitude profile; and 4) calculate normalized amplitude variance of the measured amplitude profile divided by the reference amplitude profile. The calculation of σ_t^2 is described in Section II.C. Fig.9 shows the linear regression plots of $\log(\sigma_t^2)$ and $\log(\sigma_{A_t}^2)$ vs. $\log(D)$. The correlation coefficients are 0.55 and 0.74, respectively. Two outliers are removed from (a). The slopes are in the order of unity. In both plots, the linear relationships are statistically significant*.

A quantitative measure of scattered energy at the image plane is the energy ratio ER, which is defined as the energy outside the main image lobe to the energy inside the main image lobe. It is shown analytically in [6] that ER linearly grows with the propagation distance D . ER is directly related to image contrast and is calculated by taking the ratio of energies measured outside the mainlobe region and inside the mainlobe region. The mainlobe region is identified by linear extrapolation between the peak image value and the outer contour of the mainlobe diffraction pattern at the lowest recognizable level. Fig.10 illustrates the measurement procedure. Fig.11(a) upper curve is the linear regression plot of ER vs. D without correction. One outlier was removed from the data. ER in water

* The linear relationship is statistically significant ($\alpha=0.05$) if the correlation coefficient is greater than 0.53 for sample size 14 and 0.497 for sample size 16.

image is 0.088, which is included in the data points to represent system performance at zero depth. The correlation coefficient is 0.49 and the linear relationship is significant. The low correlation coefficient is due to the difficulty of identifying the diffraction pattern for some severely distorted images.

The performances of descattering algorithms deteriorate with propagation depth. The rest of the regression curves in Fig.11 (a) show ER vs. propagation depth obtained by using five different correction methods. ERs in water image after using different correction methods are included into the corresponding data to represent the calibrated ERs at zero depth. The correlation coefficients of regression curves are indicated in the figure by R. The average values of ER (std. dev.) are given in Table IV. The linear relationships are statistically significant for all curves.

The performance of wideband DSA is the worst among all correction procedures. Data sets of wideband DSA, PC and PC and rooter are clearly separated with averages 103% (std. 33.9%), 25% (6.9%) and 6.8% (1.6%), respectively. The ER ratios of wideband DSA and PC, and PC and PC and rooter are 4.1 and 3.7, respectively. These results agree very well with the factor of 4 prediction given by analysis in [11]. At 100 mm depth, ER after PC reaches 0.85, which is in the neighborhood of the average ER with DSA correction at the average 2.7 cm propagation depth. Therefore, the best linear phase correction procedure at the aperture is likely to result in only 15 dB image contrast at this depth. The average ER after TDC is 19% more than that of PC while the averages of the lowest level at which mainlobe diffraction shape is maintained are the same when TDC and PC are used. This implies that the residual phase error due to imperfect phase correction contributes primarily to energy in the sidelobe lobe region. BPT reduces the average ER by 12.2% below that of PC and is the best among the linear operations. The performance of PC and square rooter at the aperture is slightly better than that of BPT. At 100 mm, the PC

and rooter curve reaches 0.22 which is about the average ER level of PC. The BPT curve reaches 0.38, which is about the average ER of TDC. These energy ratios are useful to provide image contrast of ~20 dB.

Fig. 11 (b) shows the results of ER by using BPT and square rooter and PC and fourth rooter at the aperture. Regression curves obtained from PC and square rooter and BPT are also included in (b) for comparison. At 100 mm depth, the regression curves of BPT and square rooter and PC and fourth rooter reach 10.6% and 5%, respectively. These ERs are about the average levels of BPT and PC and square rooter obtained from the average 2.7 cm propagation depth (see Table IV). The result indicates that focusing with image contrast of ~25 dB throughout the 100 mm propagation depth is achievable by taking the low order root on wavefront amplitude in addition to phase deaberration at the aperture or in addition to BPT.

Image contrast, the lowest level of the mainlobe diffraction shape, increases monotonically with ER. The relation of the two can be predicted by using ER and image contrast obtained with PC (or any correction method) as base line (bold numbers in Table V). For example, the measured image contrast with PC is 19.5 dB. The ER ratio of PC alone to PC and rooter is $2.51/6.8 = 3.7$, corresponding to increase of 5.7 dB. Thus the predicted image contrast is $19.5 \text{ dB} + 5.7 \text{ dB} = 25.2 \text{ dB}$ which closely agrees with the measured value -25.4 dB. Table V lists the measured ER (first row), predicted image contrast from the measured ER (second row) and the measured image contrast (third row). The predicted and measured image contrasts are in reasonably good agreement except for the pair without correction. The reason is due to ER measurement error in images without correction. For some severely distorted images, it is often difficult to identify the mainlobe region.

Refracted energy exhibits a different depth distortion effect than scattered energy. The strengths and the numbers of interference lobes depend on orientations, curvatures, sizes and numbers of refractive bodies in the insonified medium, and may not be directly related to propagation depth. Although the chance of incident rays passing through more refractive bodies increases with the propagation depth, the strengths of interference lobes resulting from multiple refraction may not be significant compared with those resulting from single refraction. One quantitative measure of coherent interference phenomenon is the ratio of a large interference lobe or artifact to image lobe. For nine samples that were determined to have significant levels of coherent interference, the ratio varied randomly from sample to sample and showed no increase with thickness. The average strength (peak value) is 10 dB (std. 4 dB). Another quantitative measure is the total number of large refractive lobes in each image (Table II). The average is 2 and standard deviation is 0.53. The lobe number is independent of propagation depth. The refractive lobes are tightly clustered around the main lobe with an average radius of 5.6 mm (std. 1.8 mm) which is about 2 degrees. This is because the speed variations across glandular tissue and fat boundaries are small (5-10%).

IV. DISCUSSION

A. Importance of Better Phase Correction

We have shown in Table IV that PC, the best phase deaberration procedure at the aperture and ideal for a point target, improves ER 19% more than TDC, while the averages of the lowest level at which mainlobe diffraction shape is maintained are the same by using both procedures. This implies that residual phase error due to imperfect phase correction of TDC primarily contributes to the energy in the sidelobe region. Therefore better phase deaberration procedures that improve the performance of TDC are valuable to improve the contrast resolution. Furthermore, the amplitude compression operation in addition to PC is more effective in reducing ER than the same compression operation in addition to TDC.

The average ER of PC and square rooter is 18.2% less than using PC alone while the average ER of TDC and square rooter is 15.6% less than using TDC alone.

The procedure to calculate TDC profile used in this paper is ad hoc. Steps 2 and 3 in TDC calculation (Section II) smooth the arrival time fluctuation estimate to a certain extent. To test the effect of the ad hoc smoothing, another TDC estimate procedure was used. We call this procedure nonsmoothing TDC. In this procedure, the reference waveform selection in previous TDC estimate was unchanged but steps 2 and 3 in previous TDC estimate were replaced by simply calculating the cross-correlation peaks of correlation functions between geometrically corrected waveforms and the reference waveform. The image formation was the same as before. The simple metric, lowest level at which the mainlobe diffraction shape was maintained, and ER after using nonsmoothing TDC were measured. The average level of the simple metric is -18.9 dB (std 2.4 dB) and the average ER is 41.4% (11.2%). The corresponding results of using smoothing TDC are -19.3 dB (std. 2.4 dB) and 44.2% (13%). Thus, smoothing does not significantly improve image quality. The reasons are 1) on average 86% of pulses are highly correlated with the reference waveform (correlation coefficient 0.7) and arrival time fluctuations calculated at these positions are reasonably good; and 2) for 14% of pulses that are not correlated well with the reference waveform, estimation errors of arrival time fluctuation occur at these positions. But signals at these positions are, in general, weak and therefore arrival time estimation errors at these positions contribute little to image quality.

B. Effects of Amplitude Weight of Compensation Vector

The complex weights of MF, PC and PC and rooter are, respectively, A , 1 and $A^{-1/2}$, each multiplied by $\exp(-j\phi)$. The signal after weighting is A^2 , A and $A^{1/2}$. By using first order approximation, it is shown in [6] that the variance of A^2 is about 4 times larger

than $\sigma_{A_t}^2$ while the variance of $A^{1/2}$ is about 4 times less than $\sigma_{A_t}^2$ when narrowband waveform is used, where $\sigma_{A_t}^2$ denotes the variance of A . These increases and decreases in amplitude variance account for the linear increase and decrease in sidelobe energy ER [6]. Experimentally, we measured 4.1 and 3.7 increase and decrease in ER compared with the ER of using PC when wideband DSA and PC and rooter are used, respectively (Table IV). The results agree with the analysis and indicate that intelligent use of amplitude weighting is crucial for improving image contrast.

C. Application to Diffuse Scattering Medium

The compression operation upon wavefront amplitude, in addition to phase deaberration or BPT, introduced in the paper is applicable to a diffuse scattering medium. Experiments with square root amplitude weighting and TDC show that ER can be reduced by 15.6% on average relative to TDC alone. Further comparison studies of image amplitude distributions before and after compression will be performed to quantify the nonlinear effects upon image quality. The required degree of compression will be optimized as a function of contrast resolution and SNR.

D. Significance of Coherent Interference upon Pulse-echo Imaging

A coherent interference phenomenon was demonstrated in the 1-way transmission model and experiments. Its impact upon 2-way echo scanning is illustrated in Fig.12. A transmitting beam illuminates a tumor or target T (part a). Because of refraction, a subbeam is split from the original beam and insonifies targets along θ_1 . On reception, if no echo signal is coming back from the targets illuminated by the subbeam (simplest case), the receiving beam upon T (part b) may split in the same fashion as the transmitting beam (reciprocity) and a dual image may result. This simplest case corresponds exactly to the

situation in the 1-way transmission experiments reported in this paper, and in [13-15], where an active point source instead of a passive point target is used. In reality, refracted energy from the targets insonified by the subbeam will arrive at angles of $1 - 3^\circ$ from the target direction and therefore in the sidelobe region of array. The sidelobe level of the receiving beam will be ~ -30 dB as achieved by the procedure described in this paper. The average level of refracted multipath is found to be -10 dB relative to the target image and therefore the average multipath signal level entering the system is $\sim (10+30)$ dB below the echo strength of the illuminated target. The cancellation algorithms [16-17] must suppress these multipath signals to achieve a -60 dB contrast resolution, which is essential for preventing contamination of otherwise black cysts with scattered and/or refracted echo energy and thereby causing them to look like speckled tumors.

V. CONCLUSIONS

The evidence of both scattering and refraction is observed from point source images obtained from *in vitro* breast samples with thickness varied from 1-4 cm. Scattering reduces target strength, broadens the mainlobe and increases background level and therefore lowers the image contrast. Refraction creates coherent multipath interference that produces false targets in addition to the true target in the image. Scattered energy increases with the propagation depth while refracted energy does not appear to increase with the depth.

Phase deaberration algorithms are useful to partially remove scattered energy and build up the strength of the coherent image. As a result, the diffraction-limited image is restored up to -20 dB level for average thickness of 2.7 cm. Better phase deaberration procedures are valuable to improve energy ratio and therefore image contrast. Improvement of a diffraction-limited image to the -30 dB region requires wavefront-deaberration algorithms that can further remove scattered energy caused by wavefront amplitude

distortion and consequently strengthen the coherent image. BPT reduces wavefront amplitude variance and provides 5 dB improvement in addition to that of using phase deaberration procedures at the aperture. Wideband DSA increases wavefront amplitude variance and the result is 5 dB worse than that of using phase-deaberration procedures for the tissue thickness studied. A low order root on wavefront amplitude in addition to phase-deaberration at the aperture or BPT can further reduce the amplitude variance and restore the diffraction-limited image to the -30 dB region. Linear regression analysis of ER vs propagation depth indicates that high quality focusing throughout 100 mm propagation depth is possible.

The ratio of multipath artifact to image lobe is improved by an average of 10 dB when phase deaberration is used and further improved by another 10 dB when the low order root upon wavefront amplitude in addition to phase deaberration or in addition to backpropagation and phase deaberration is used. The improvement comes from the coherent build up of the target strength by descattering processes.

ACKNOWLEDGMENTS

Invaluable consultation was provided by Dr. Kai Thomenius, Director of Research, Interspec, Inc., Ambler, PA., a division of ATL, in the course of this study. Funding was provided by the Army (DAMD 17-93-J-3014 and DAMD 17-94-J-4133) and NSF (BCS92-09680).

REFERENCES

- [1] S. W. Flax and M. O'Donnell, "Phase Aberration Correction using Signals from Point Reflectors and Diffuse Scatterers: Basic Principles," IEEE Trans. Ultrason., Ferroelec. and Freq. Contr., 35(6), 758-767 (1988).
- [2] E. H. Attia and B. D. Steinberg, "Self-Cohering Large Antenna Arrays Using the Spatial Correlation Properties of Radar Clutter," IEEE Trans. Antennas Prop., AP-37(1), 30-38 (1989).

- [3] L. Nock, G. E. Trahey, and S. W. Smith, "Phase Aberration Correction in Medical Ultrasound using Speckle Brightness as a Quality Factor," J. Acoust. Soc. Am. 85(5), (1989)
- [4] M. Fink, "Time reversal of ultrasonic fields – part I: basic principles," IEEE Trans. Ultrason. Ferroelec. Freq. Contr., vol. 39, pp. 555-566, 1992.
- [5] D.-L. Liu and R. C. Waag, "Correction of Ultrasonic Wavefront Distortion Using Backpropagation and Reference Waveform Method for Time-shift Compensation," J. Acoust. Soc. Am. 96, 649-660 (1994).
- [6] Q. Zhu and B. Steinberg, "Modelling and Correction of Incoherent Wavefront Distortion," will submit to international Journal of Imaging Systems and Technology, Sept., 1995.
- [7] B. D. Steinberg, "Radar Imaging from a Distorted Array: The Radio Camera Algorithm and Experiments," IEEE Trans. Antennas Prop. AP-29(5), 740-748 (1981).
- [8] L. M. Hinkelman, D-L. Liu, and R. C. Waag, Q. Zhu, and B.D. Steinberg, "Measurement and Correction of Ultrasonic Pulse Distortion Produced by the Human Breast", J. Acoust. Soc. Am. 97(3), 1958-1969 (1995).
- [9] B. D. Steinberg and H. Subbaram, *Microwave Imaging Techniques*, Chapter 3, John Wiley and Sons, New York (1991).
- [10] B. D. Steinberg, *Principles of Aperture and Array System Design* (Hohn Wiley & Sons, New York, 1976).
- [11] C. Dorne and M. Fink, "Focusig in transmit-receive mode through inhomogeneous media: The time reversal matched filter approach," J. Acoust. Soc. Am. 98, 1155-1162 (1995).
- [12] Q. Zhu, B. D. Steinberg and R. Arenson, "Correlation Distance of the Female Breast," J. Acoust. Soc. Am. August (1995).
- [13] G. E. Trahey, P. D. Freiburger, L. F. Nock, and D. C. Sullivan "In Vivo Measurements of Ultrasonic Beam Distortion in the Breast," Ultrason. Imag. 13, 71-90 (1991).
- [14] P. D. Freiburger, D. C. Sullivan, B. H. LeBlanc, S. W. Smith, and G. E. Trahey, "Two Dimensional Ultrasonic Beam Distortion in the Breast: In vivo measurements and effects," Ultrason. Imag. 14(4), 398-414 (1992).
- [15] Q. Zhu and B. D. Steinberg, "Large-Transducer Measurements of Wavefront Distortion in the Female Breast," Ultrason. Imag., 14, 276-299 (1992).
- [16] Q. Zhu, and B. D. Steinberg, "First Experiments of Coherent Cancellation of Refractive Artifacts," 39 AIUM Proceeding (1995)
- [17] Q. Zhu and B. Steinberg, "Coherent Cancellation of Refraction Artifacts," 20 Int. Symp. on Ultrasonic Imaging and Tissue Characterization (June 1995).
- [18] J. W. Goodman, *Introduction to Fourier Optics* (McGraw-Hill, New York, 1968).

Table I. Statistics of increase in -6 dB beamwidth (percent)

Sample size	Classification	Azimuth	Elevation
4	A	130 (std. 131.3)	100(std. 96.5)
3	B	50 (std. 53.3)	30 (std. 30.0)
9	C	30 (std. 33.3)	40 (std. 42.2)

A. Primarily scatter

B. More scatter than refraction

C. Scatter plus well-defined refraction

Table II. Statistics of refracted lobes from 9 *in vitro* breast samples

	Average	Std.Dev.
Number of refractive lobes	2	0.53
Relative peak strength (dB)	10	4.7
Distance from primary lobe (deg)	1.8	0.57

Table III Statistics of mainlobe diffraction shape (dB)

Diffraction pattern (dB)		Diffraction pattern after correction (dB)						
w/o correction	TDC	PC	Wideband DSA	BPT	PC &square rooter	BPT &square rooter	PC &fourth rooter	
A	-0(0)	-18.8 (1.9)	-19.0 (2.2)	-14.8 (2.6)	-24.3(2.1)	-25.3(3.0)	-29.5(2.7)	-32.3 (2.8)
B	-5.8(1.3)	-19.7 (2.3)	-19.7 (3.5)	-14.7 (1.5)	-23.7(0.6)	-25.3(2.1)	-29.3(2.3)	-30.7(1.2)
C	-6.1(3.5)	-19.3 (2.7)	-19.6 (2.5)	-14.8 (2.5)	-23.9(2.4)	-25.4(2.5)	-29.3(3.0)	-30.7(1.4)

Table IV Statistics of ER before and after corrections

w/o Corr.	TDC	PC	Wideband DSA	BPT	PC & square rooter	BPT &square rooter	PC &fourth rooter
214.7% (std.130.1%)	44.2% (13.4%)	25.1% (6.9%)	103.5% (33.9%)	12.8% (2.9%)	6.8% (1.6%)	3.7% (0.7%)	2.1% (0.4%)

Table V Relation of ER and image contrast (predicted and measured)

	w/o Corr.	TDC	PC	Wideband DSA	BPT	PC &square rooter	BPT &square rooter	PC &fourth rooter
ER	214.7%	44.2%	25.1 %	103.5%	12.8%	6.8%	3.7%	2.1%
(predicted)	-10.2 (dB)	-17.1	-19.5	-13.3	-22.4	-25.2	-27.8	-30.3
(measured)	-4.2 (dB)	-19.3	-19.5	-14.8	-24.0	-25.4	-29.4	-31.1

FIGURES

DEABERRATION TRANSFORMATIONS

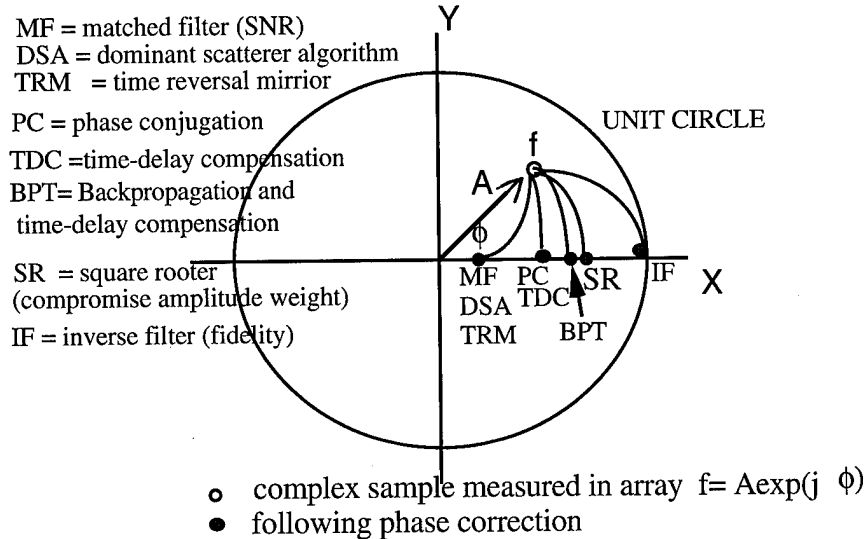


Fig.1. Deaberration transformations. f is distortion vector for instantaneous sample of the radiation field. Transformations to the real axis all correct phase. Left (MF) maximizes SNR but increases amplitude distortion. Right (IF) maximizes imaging fidelity but increases noise. SR is good compromise.

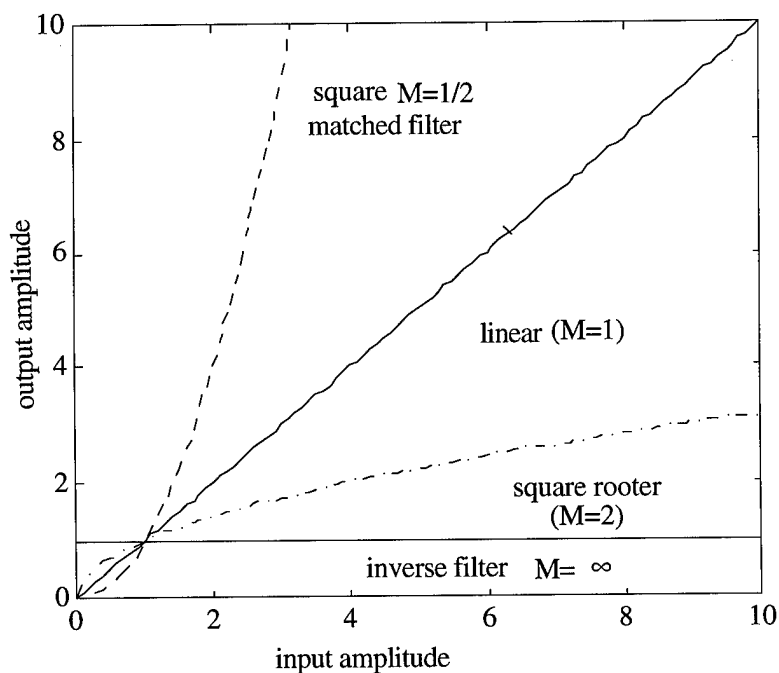


Fig.2. Plots of the input and output amplitude transforms.

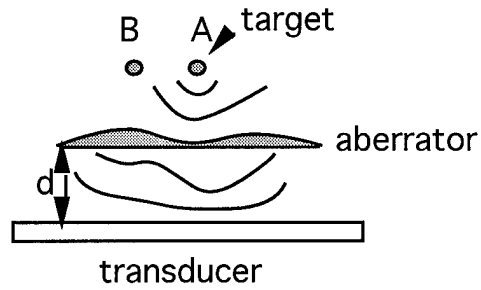


Fig.3. Illustration of scanning configuration.

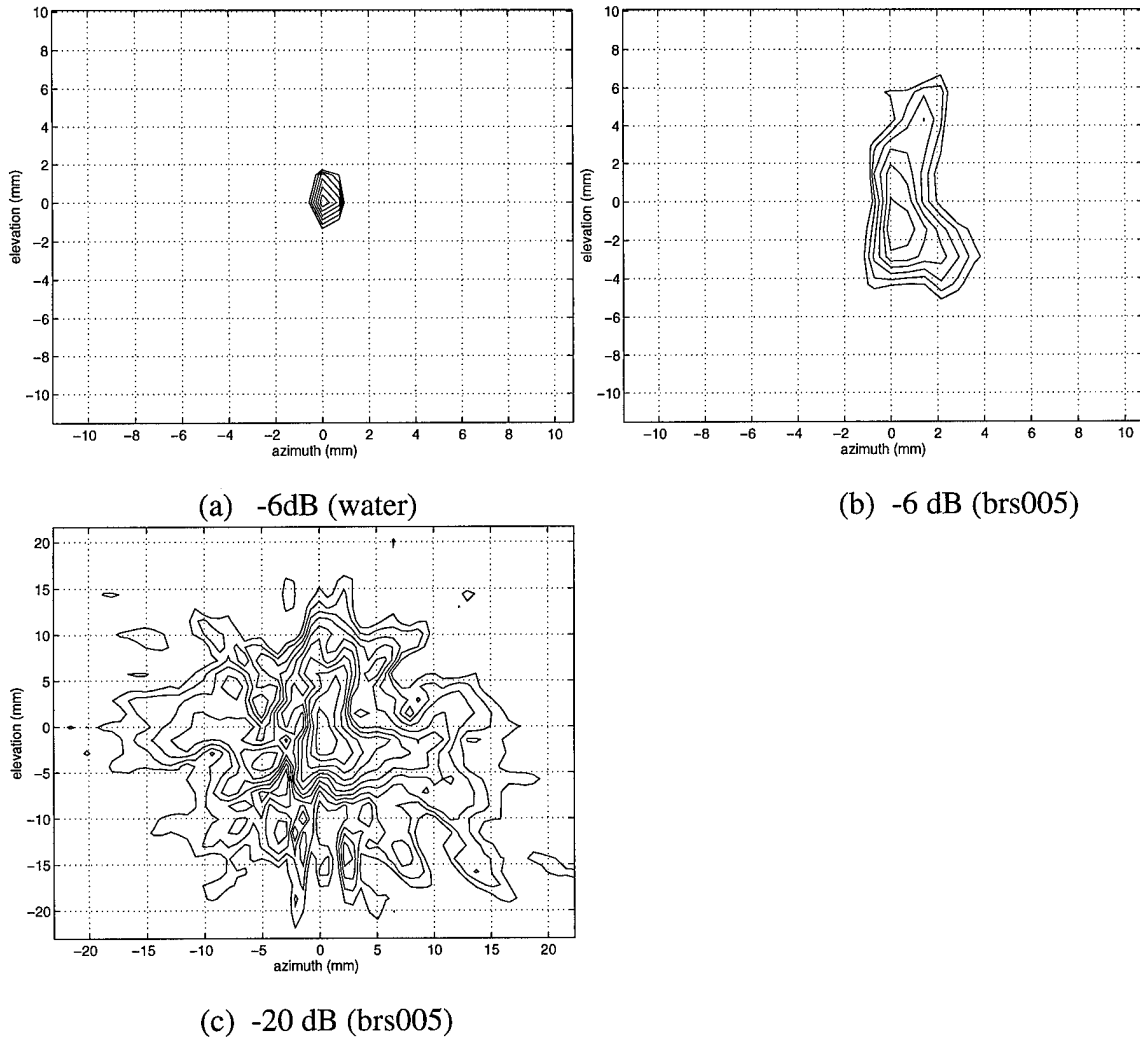


Fig.4. 2-D contour maps of point source images. (a) water data showing diffraction pattern of system. Outer contour is -6 dB level. (b) measured through the 3.5-cm tissue (brs005), showing asymmetric scattering effect. Outer contour is -6 dB level. (c) Image brs005 at -20 dB contour level. The outer contour shows symmetrical scattering pattern. No distinct structure or multipath is observed. Note the change of scale from (a) and (b).

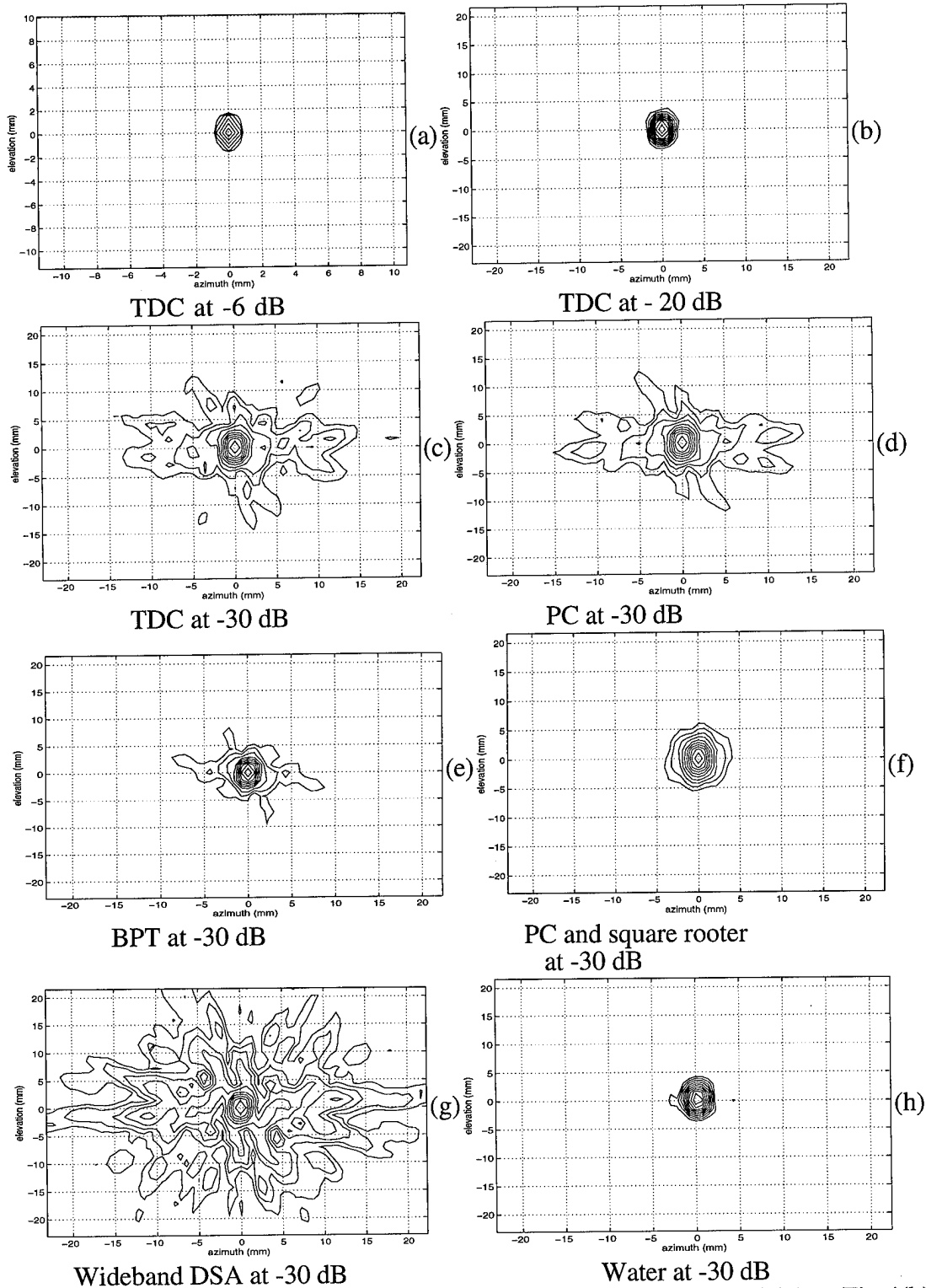


Fig.5. Distortion corrected contour maps of the sample image brs005 (see Fig.4(b) and (c) for comparison) (a) TDC at -6 dB. (b) TDC at -20 dB. (c) TDC at -30 dB. (d) PC at -30 dB. (e) BPT at -30 dB. (f) PC and square rooter at -30 dB. (g) Wideband DSA at -30 dB. (h) Water at -30 dB. Note the scale change of (b)-(h) from (a).

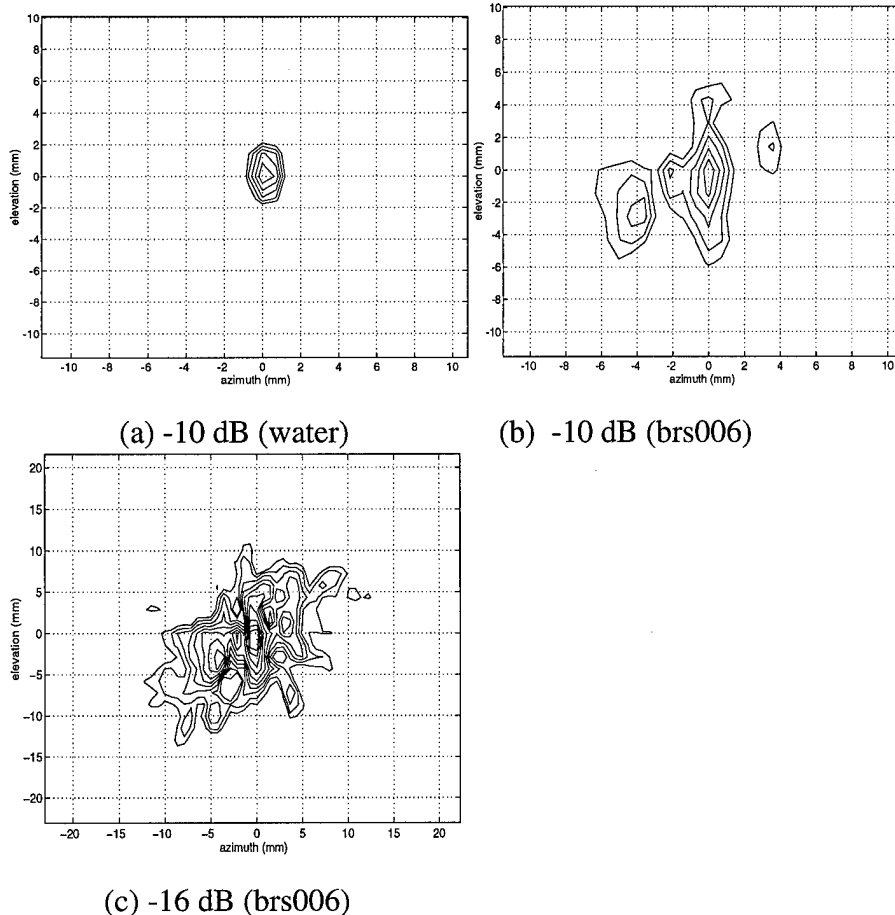


Fig.6. 2-D contour maps of point source images. (a) water data showing diffraction pattern of system. Outer contour is -10 dB level. (b) measured through the 4-cm tissue (brs006), showing highly asymmetric interference pattern. Outer contour is -10 dB level. (c) Image brs006 at -16 dB contour level. The outer contour shows more symmetrical scattering pattern. Note the change of scale from (a) and (b).

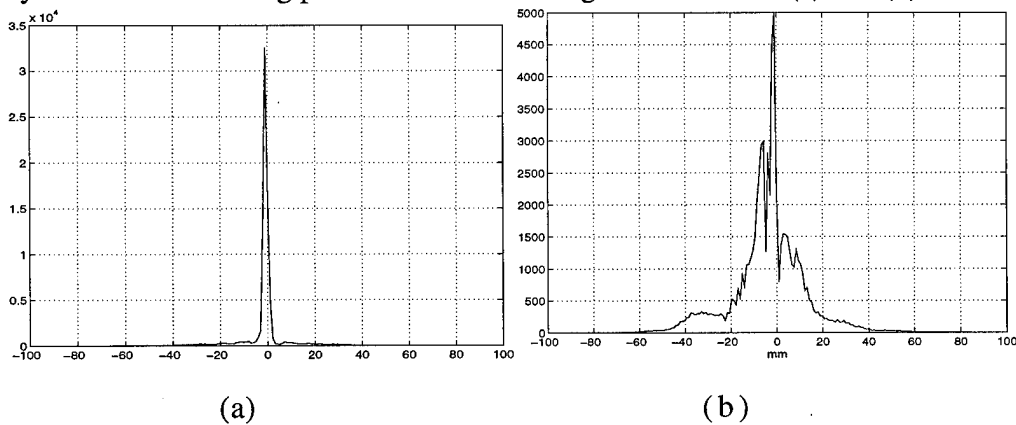


Fig. 7. (a) 45 degree cuts of 2-D images (a) water. (b) brs006.

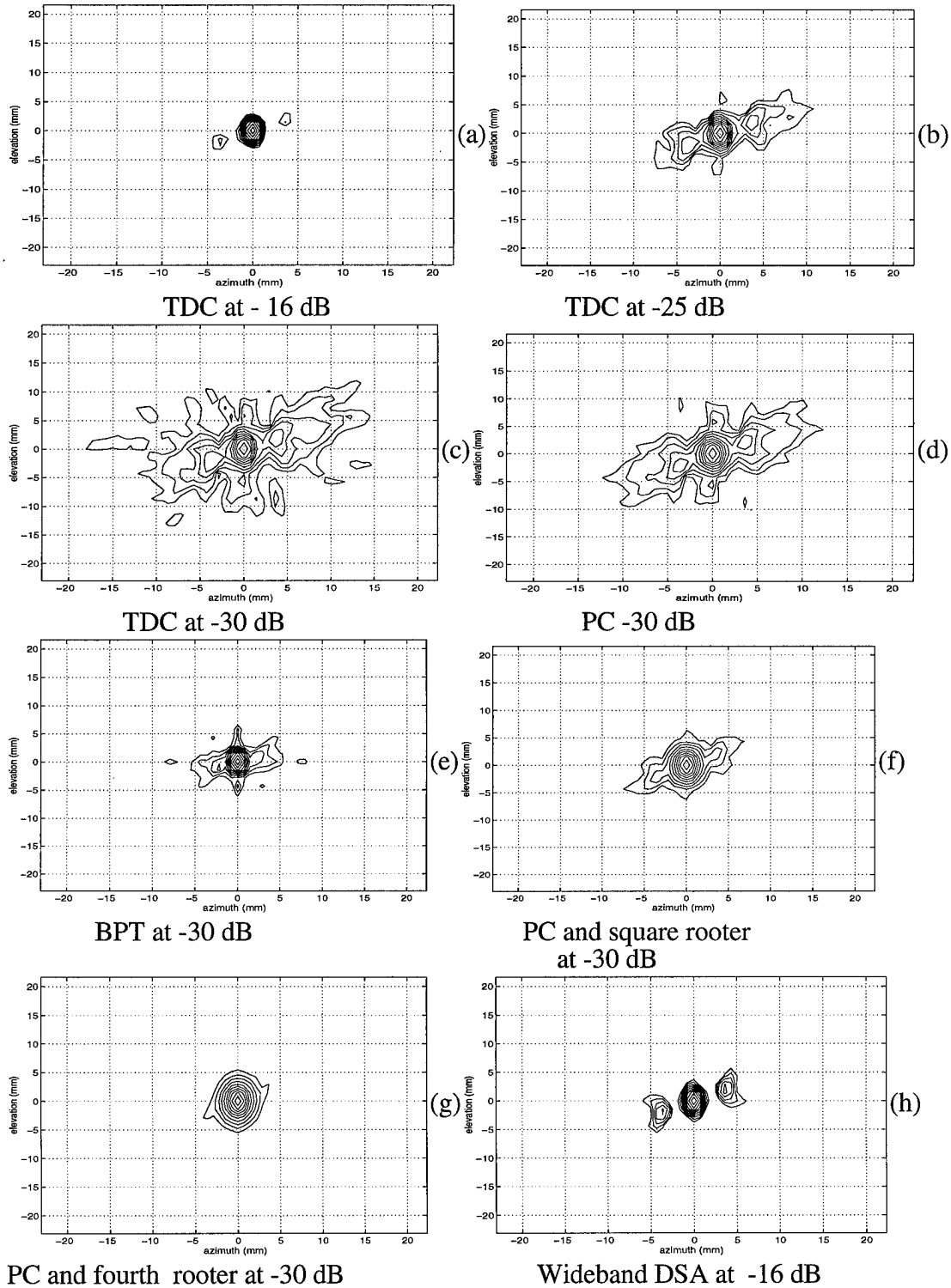
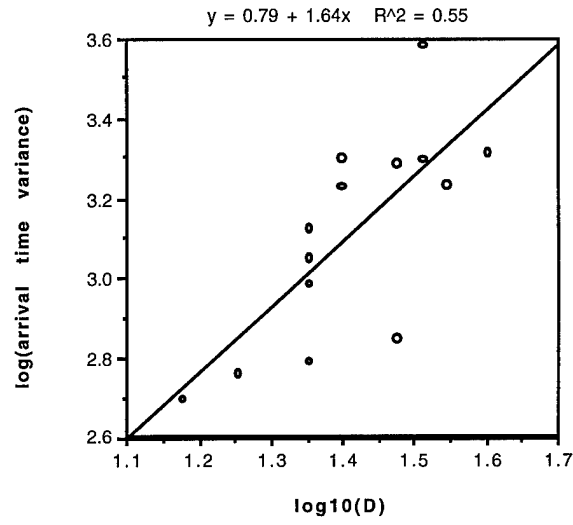
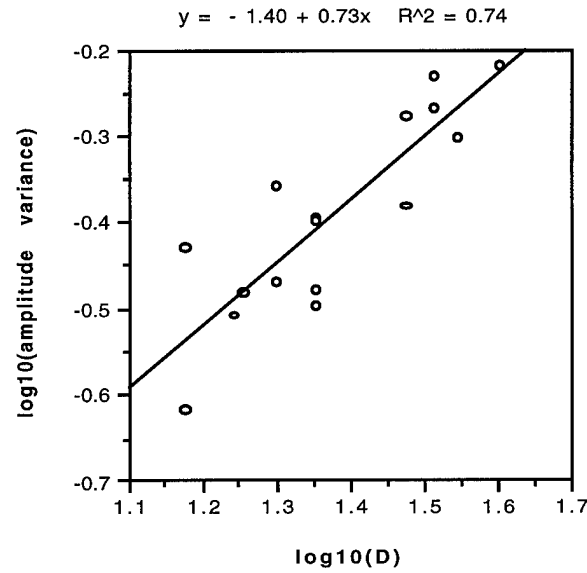


Fig.8. Distortion corrected contour maps of the sample image brs006 (see Fig.6 (b) and (c) for comparison) (a) TDC at -16 dB level. (b) TDC at -25 dB level and (c) TDC at -30 dB level. (d) PC at -30 dB level. (e) BPT at -30 dB. (f) PC and square rooter at -30 dB. (g) PC and fourth rooter at -30 dB. Wideband DSA at -16 dB. Artifacts are 5 dB higher than time-delayed correction shown in Fig.8(a).

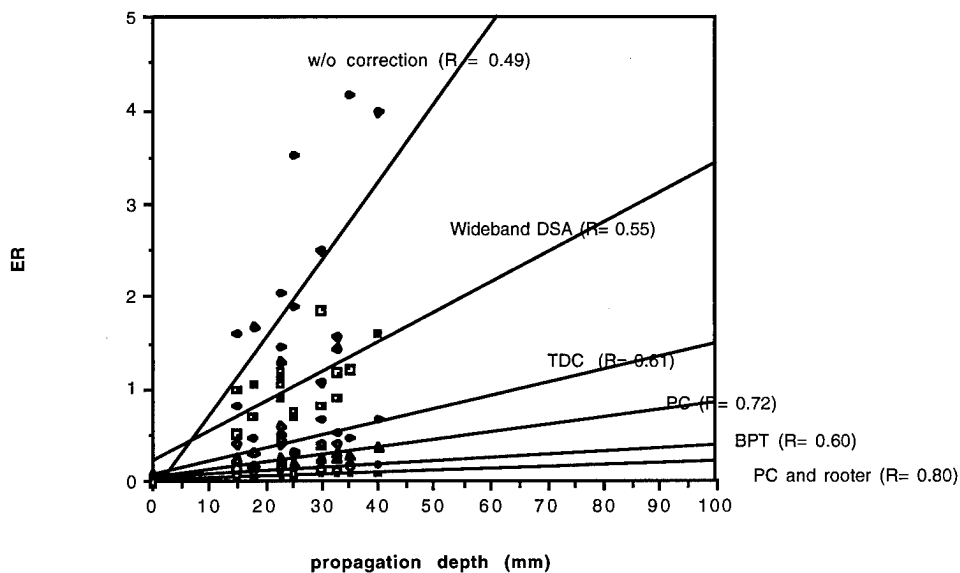


(a)

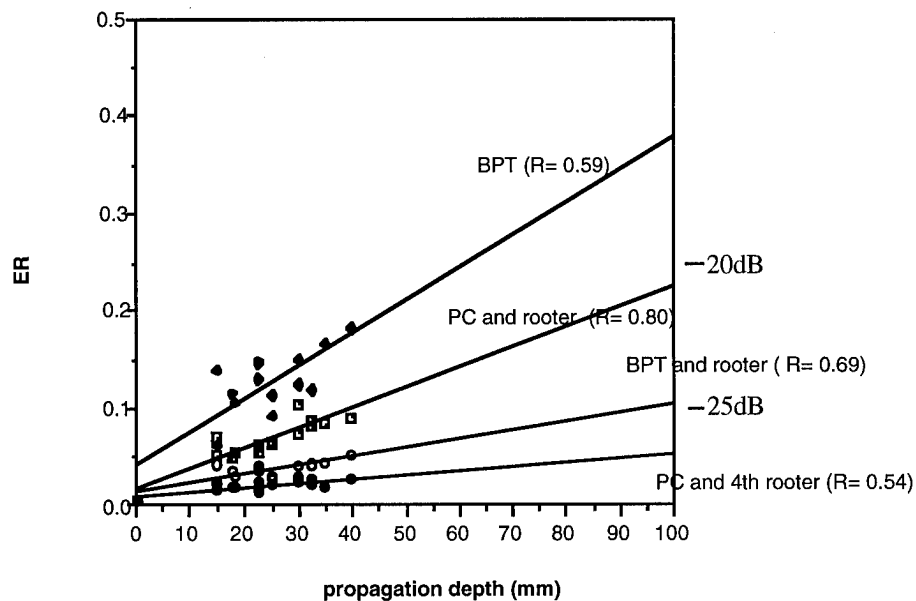


(b)

Fig.9. Linear regression of (a) $\log(\sigma_{\tau}^2)$ vs. $\log(D)$ and (b) $\log(\sigma_{A_t}^2)$ vs. $\log(D)$. D is in mm, arrival time variance σ_{τ}^2 is in ns^2 and $\sigma_{A_t}^2$ is the normalized amplitude variance (no dimension).



(a)



(b)

Fig.11. (a) Linear regression curves of ER vs. propagation depth obtained from five correction procedures. (b) Results of ER vs. propagation depth obtained from four correction procedures. The vertical scales of part b is the predicted image contrast (see text).

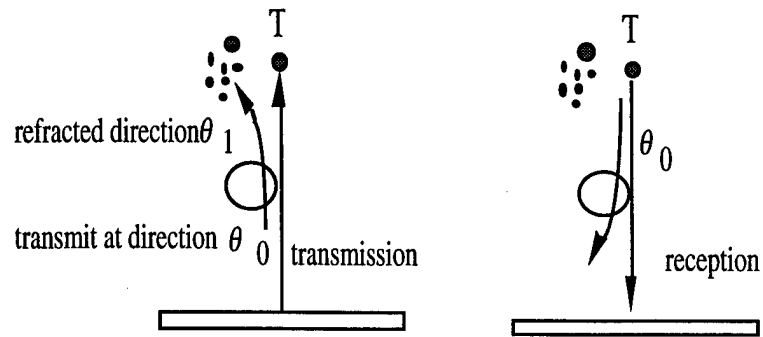


Fig.12. Illustration of effect of refraction upon pulse echo imaging (simplest case with no interference echo signal coming back from targets insonified by subbeam).

Measurements of ultrasonic pulse arrival time and energy level variations produced by propagation through abdominal wall

Laura M. Hinkelman and Dong-Lai Liu

Department of Electrical Engineering, University of Rochester, Rochester, New York 14627

Leon A. Metlay

Department of Pathology and Laboratory Medicine, University of Rochester, Rochester, New York 14642

Robert C. Waag

Departments of Electrical Engineering and Radiology, University of Rochester, Rochester, New York 14627

(Received 22 February 1993; accepted for publication 3 September 1993)

Ultrasonic pulse arrival time and energy level variations introduced by propagation through human abdominal wall specimens have been measured. A hemispheric transducer transmitted an ultrasonic pulse that was detected by a linear array transducer after propagation through an abdominal wall section. The array was translated in the elevation direction to collect data over a two-dimensional aperture. Differences in arrival time and energy level between the measured waveforms and calculated references that account for geometric delay and spreading were found. Plots of waveforms compensated for geometric path, maps of time delay differences and energy level fluctuations, and statistics derived from these for water paths and tissue paths characterize the measurement system and describe the time delay differences and energy level fluctuations caused by 14 different human abdominal wall specimens. Repeated measurements using the same specimens show that individual tissue path measurements are reproducible, the results depend on specimen position, and frozen storage of a specimen for three months does not appear to alter the time delay differences and energy level fluctuations produced by the specimen. Comparison of measurements at room and body temperature indicates that appreciably higher time delay differences occur at body temperature while energy level fluctuations and time delay difference patterns are less affected. For the 14 different abdominal wall specimens, the rms time delay differences and energy level fluctuations have average values of 43.0 ns and 3.30 dB, respectively, and the associated correlation lengths of the time delay differences and energy level fluctuations are 7.90 and 2.28 mm, respectively. The spatial patterns of time delay difference and energy level fluctuation in the reception plane appear largely uncorrelated, although some background variations in energy level fluctuation are similar to features in time delay difference maps. The results provide important new information about the variety and range of ultrasonic wave front arrival and energy variations caused by transmission through abdominal wall.

PACS numbers: 43.80.Ev, 43.80.Jz

INTRODUCTION

Ultrasonic imaging has become an important tool for medical diagnosis. Because of its nonionizing nature and its ability to distinguish between various soft tissues by their mechanical properties, ultrasound is the modality of choice for such applications as examination of heart valve motion, studies of the fetus, and surveys for disease in abdominal organs. The usefulness of ultrasound is limited, however, by its relatively low resolution as compared to radiologic or magnetic resonance imaging.

Over the years, efforts have been made to improve the resolution of ultrasonic scanners. Higher frequency signals have been used, but are accompanied by increased attenuation levels. Larger transducer arrays have been used effectively. However, this approach is also limited because the ultrasonic beam is distorted by the tissues through which it passes and this distortion is not removed by any clinical instruments now commercially available. Informa-

tion about the degradation of ultrasonic beams is needed and appropriate compensation methods must be developed if this fundamental source of resolution loss is to be eliminated.

Ultrasonic wave front distortion produced by propagation through tissue has been the topic of several recent investigations. Moshfegi and Waag¹ found that the resolution improvement obtained by increasing aperture size from $f/2.6$ to $f/1.0$ is one third lower in the presence of tissue than in water alone, illustrating the loss of resolution caused by wave front distortion. From scattering measurements, Waag *et al.*² have also estimated that propagation through 100 mm of calf liver produces an rms path difference of about 20 μm and that the correlation length of calf liver is about 100 μm . O'Donnell and Flax³ have examined *in vivo* b-scan images of the human liver for the effect of wave front distortion, finding that ultrasonic images from patients for whom phase distortion is mild are good while

those from patients for whom phase distortion is severe are poor.

A number of direct measurements of wave front distortion produced by human tissues have also been made. A pilot study by Aindow and Chivers⁴ was aimed at the determination of the instrumental and procedural requirements for making these measurements accurately. They also found that liver specimens may disrupt ultrasonic wave fronts mildly. In another early study, Krämmer and Hassler⁵ made a one-dimensional measurement of the time delay fluctuations caused by the human abdominal wall, and determined that the level of wave front distortion produced by abdominal wall samples varies significantly between individual specimens. Using a somewhat different experimental design that included a two-dimensional aperture, Sumino and Waag⁶ found that the human abdominal wall can cause time delay fluctuations sufficient to degrade focusing in large aperture ultrasonic imaging systems operating in the low megahertz range. Other investigators^{7,8} have made one-dimensional measurements of wavefront distortion produced by the human breast. At the same time, active research to develop algorithms for the correction of phase distortion in clinical machines is being reported at meetings.^{9,10} However, while all the aforementioned work indicates recognition of the important role played by wavefront distortion in limiting resolution, a paucity of data exists and additional measurements are needed to describe the variety and range of wavefront distortion encountered clinically. Information concerning amplitude distortion is particularly limited at this time.

This paper reports on a new study of wave front distortion caused by the human abdominal wall. This study employed fourteen different abdominal wall specimens and measurements were made at body temperature using improved instrumentation and data processing techniques. Variations in both arrival time and energy level are described. The new information is expected to be useful for the theoretical design and engineering development of wave front distortion correction algorithms.

I. METHOD

A. Experimental protocol

The experimental method used here was essentially that of Sumino and Waag.⁶ In their study, a hemispheric transducer transmitted ultrasonic pulses that were received by a linear array immediately after passing through an abdominal wall specimen. The array was translated in the elevation direction by a computer-controlled stage, thus scanning a two-dimensional aperture. A multiplexer accessed each of the 128 array elements sequentially. At each element, the received signal was digitized into 12-bit samples at a rate of 20 MHz over an 11.8- μ s interval. This was repeated 21 times at each element to permit signal averaging for noise reduction. Both transducers operated at a 3.75-MHz center frequency and the -6-dB bandwidth of the received pulse was about 2.2 MHz. The spacing of elements in the array direction of the receiving transducer

was 0.72 mm and the dimension of the receiving area in the elevation direction was restricted to 2.50 mm by a reflecting mask. Signals were collected from all 128 elements at each of 16 elevations for a total of 2048 collection positions, spanning a 92.16 \times 40.0-mm² aperture, during a period of about 45 min. Data collection was performed at room temperature with a source-receiver separation of approximately 165 mm.

For the present study, the measurement system was modified in several ways in order to improve spatial resolution, signal-to-noise ratio, acquisition speed, and the simulation of *in vivo* tissue conditions.

In order to improve spatial resolution, the elevation dimension of the linear array was decreased to 1.44 from 2.50 mm, thus reducing the measurement spot size to 58% of the 0.72 \times 2.50-mm² size used previously. To offset the associated signal loss, the amplitude of the transmitted pulse was increased by increasing the voltage supplied to the ultrasonic pulse generator and using a special double pulse input to the transducer. Attenuation of the signal on its path to the receiving transducer was reduced by removing the acoustic lens from the otherwise standard ultrasonic probe, without altering the original source-receiver separation. Finally, the receiver amplification was raised significantly. The total increase in gain was sufficient to offset the loss due to decreased spot size and to compensate for array element directivity at the edge of the aperture while maintaining the received pulse -6-dB bandwidth at about 2.2 MHz and extending the output signal amplitude to cover the entire 12-bit range of the analog-to-digital converter.

When the elevation dimension of the linear array was reduced, the elevation step size was simultaneously decreased to 1.44 mm and the number of elevation positions at which data was collected was increased from 16 to 32. This expanded the total aperture to 92.16 \times 46.08 mm² and the number of sampling positions to 4096, or twice the number scanned previously. However, modifications to the data acquisition software increased the speed of data collection, so that the total scan time over the two-dimensional aperture decreased to about 35 min.

A major improvement in this study was the addition of a heater and circulator to the experimental water chamber. This was motivated by experimental results¹¹ showing that the speed of sound in mammalian tissue changes with temperature and that the sign of the change depends on tissue type, with the speed of sound in fat and muscle changing in opposite directions as temperature increases. Since temperature dependencies such as these in known components of abdominal wall could, as noted by Sumino and Waag,⁶ increase arrival time variations in particular and could also increase wave front distortion in general, measurements were made at both room and body temperature to investigate the importance of temperature. Once an appreciable temperature effect had been demonstrated, data collection took place at or about body temperature for the remainder of the study. The result is that the wave front distortion

measured here should be similar to that encountered clinically.

The cross talk evident in the results of Ref. 6 was eliminated through a reconfiguration of the multiplexer wiring and crosstalk was not observed in the present study.

Fourteen abdominal wall specimens, each from a different autopsy, were employed in this study. The specimens were taken from regions over the liver, gall bladder, pancreas, aorta, and kidneys. Similar to those used previously for the measurements reported in Ref. 6, the specimens consisted of a surface covering of skin, layers of fat, a lower layer of muscle, and the peritoneal membrane. They ranged in thickness from 10 to 35 mm, averaging about 21.6-mm thick. Muscle constituted 2 to 5 mm of this thickness but did not extend across the entire area of every specimen. Each sample had a surface area of at least 7×13 cm². Specimens were stored frozen from their receipt until shortly before their use in measurements. Most specimens were employed for more than one measurement. All specimens were examined grossly and showed no macroscopic changes due to this storage and handling.

Specimen donors were mainly older adults ranging from 54 to 96 years in age with a mean lifespan of 72.8 years. The leading causes of death were heart failure (36%), cancer (21%), and stroke (14%). The donor population was 71% female and 29% male. None of the donors were particularly obese. Selection of donors was made on the basis of availability, specimen quality, and the absence of contagious pathogens.

In addition to measurements using the specimens, measurements were made through water alone in order to ascertain the inherent nonidealities of the measurement system.

B. Data processing

The data processing method employed in this experiment paralleled that of Sumino and Waag⁶ but relied on different mathematical techniques and faster algorithms. In Ref. 6, the 21 signals from each array position were first averaged to reduce random noise. The delay differences between signals received at neighboring elements along the array were determined by locating the peaks of the corresponding cross-correlation functions. Time delays across the two-dimensional receiving aperture were then calculated by summing the delay differences along the array direction at each elevation and then using the cross correlation between the central elements at neighboring elevations to couple the sums across the elevations. The central 96×10 waveforms were temporally windowed to a 1.8- μ s range determined by the location of a fitted fourth-order polynomial surface. Then, the cross-correlation procedure was repeated to obtain the time delays more accurately. The expected geometric delay, obtained by fitting a new fourth-order polynomial to the second time delay surface, was removed from the calculated time delay. Statistics such as the rms value and correlation length were then computed for the remaining delay differences.

The data processing method employed in this study used different algorithms to accomplish essentially the

same results over the full set of 128×32 waveforms. After averaging for noise reduction, a reference pulse was selected for the ideality of its shape from the waveforms in the central part of the aperture. The pulse was next windowed to 48 points, including a cosine taper over the trailing 24 points. Spectral fitting¹² was then used to locate the rough position of each pulse in the 11.8- μ s collection interval relative to the reference pulse. In order to eliminate spurious values in the rough position, a fourth-order polynomial surface was fitted to the calculated positions and any of the initially calculated values that deviated from this curve by more than 50 ns were replaced by the corresponding value from the fit. A second fourth-order polynomial surface was then fit to the remaining data, which no longer included extreme values that could inappropriately bias the fit. Finally, a 2.0- μ s temporal window beginning and ending with a 0.5- μ s cosine taper was placed 0.5 μ s ahead of the resulting curve, in order to isolate the main received pulse. This process is equivalent to and significantly faster than the first cross correlation and curve-fitting step that it replaced.

The most important change made was the method used to calculate the relative arrival time at each position in the aperture from the arrival time differences normally obtained by cross correlation. While Ref. 6 employed an accumulation of arrival time differences calculated in the array direction added to those calculated down the center of the array in the elevation direction, the new method utilized the results produced by cross correlating every signal with each of its neighbors, a process that yields about four times as many arrival time differences. In the new method, the relative arrival times were then computed by solving a set of overconstrained linear equations, which related the unknown arrival times and the arrival time differences obtained from cross correlation, in the least-mean-square error sense. This approach gave more reliable results and eliminated the streaks occasionally produced by the accumulation method in the time delay difference plots. More detail about the least-mean-square error technique for calculation of arrival time in a two-dimensional aperture can be found in Ref. 13.

Because transmission through the human abdominal wall may alter the shape of ultrasonic pulses as well as their arrival time and energy content, the cross-correlation method is sometimes inadequate for calculation of the arrival time difference between two signals. In this study, pulse pairs were considered too dissimilar for meaningful cross correlation if their maximum cross-correlation coefficient was not greater than 0.8. In such cases, the second pulse was assumed to be more severely deformed because the previous one had already been cross correlated successfully. The second pulse was consequently discarded and a forward search was made until a usable pulse was found. The total arrival time difference between this new pulse and the last acceptable pulse was then evenly divided over the interval between them. If ten steps were taken or the edge of the aperture was reached without obtaining a usable arrival time difference, the search was ended, and the difference between the roughly calculated arrival times was

inserted at the position of the original failure. After the calculation was completed for the entire aperture, such substitutions were replaced by the average of those immediately preceding and following arrival time differences that originated from a successful cross correlation. These methods are also described in more detail in Ref. 13.

Energy fluctuations across the receiving aperture were calculated using the isolated and tapered pulses obtained from the windowing process described above. The total energy arriving at each aperture position was computed as the sum of the squared amplitudes of the signal detected at that position. In the rare occurrence (five times in all the reported studies) when a waveform at a position in the measurement aperture was lost due to a failure during data acquisition, the energy for that position was obtained by an average of the energies at two neighboring array positions. Also, the values at positions corresponding to transducer element number 125 were replaced by the average of the energy values for element number 124 and number 126 in the same row because element number 125 was sometimes plagued by an intermittent connection. The computed energy values were converted into decibel units in order to eliminate the negative fitted values that very low energy occasionally produced with data on a linear scale. No significant error from uncertainty in the energy data was introduced in this process because the ratio of signal power to noise power in the energy data averaged more than 40 dB and the dynamic range of the logarithmic data was restricted to 20 dB below the maximum value to minimize the effect of extremely low values on the ensuing least-mean-squares fit. The contributions of geometry, bulk attenuation by specimens, and measurement system gain to the overall energy distribution were eliminated by fitting a fourth-order polynomial to these values and then subtracting this curve from them. This subtraction of logarithms corresponds to normalization of energy by a smoothly varying reference throughout the aperture. The use of energy level fluctuations to describe pulse amplitude variations in this study is comparable to the use of the scintillation index¹⁴ in radio science to describe intensity variations resulting from electromagnetic wave propagation in a random medium.

The time delay differences and energy level fluctuations that resulted from the processing described above were then displayed as two-dimensional gray scale maps and various statistics describing their features were calculated. The statistics employed here include the rms value as well as the 99.5% value that defines the absolute limit beyond which only 0.5% of the values are found. This 99.5% value measures the range of the data in a way that is relatively unaffected by anomalous outlying points. The spatial variability of the maps is described by the array and elevation direction correlation lengths that are defined as the interval between the half maximum amplitude points of the autocorrelation function in the corresponding direction.

II. RESULTS

Representative rf waveforms compensated for geometric path and windowed in time appear in Fig. 1. The waveforms in Fig. 1(a) are for a water path (H_2O) while those in Fig. 1(b)–(d) are for three human abdominal wall (HAW) specimens that respectively illustrate low, moderate, and high levels of the arrival time variation, as well as low, high, and moderate amounts of the energy level fluctuation measured for specimens in this study. The uniformity of the water path waveforms contrasts with the variability of the specimen waveforms in both arrival time and energy level. In this figure and throughout the remainder of this paper, individual measurements are identified by codes consisting of a prefix that identifies the object of study and a suffix that is the serial number of the specific measurement.

Water path time delay differences and energy level fluctuations for two representative measurements are presented in Fig. 2 and a statistical summary of all the water path measurements is given in Table I. Two water path studies are shown in Fig. 2 because the hemispheric source transducer failed during the period over which the studies were conducted and was replaced by a physically equivalent unit that provided a higher acoustic output with essentially the same center frequency and bandwidth. The variations in both the time delay differences and energy level fluctuations are small, although improvement resulting from replacement of the first transducer is evident. The statistical summary provides a quantitative description of the spread, correlation lengths, and extrema of the data. Together, these water path data characterize the measurement system error and variability for distortionless transmission in the study reported here.

The results obtained from repeated study of four different abdominal wall specimens are shown in the time delay difference and energy level fluctuation maps that comprise Fig. 3 and in the statistical summary presented in Table II. Two of the specimens were studied twice in a single day without removal from the specimen holder while the other two were studied before and after being frozen for 3 months. The spatial patterns of time delay difference and energy level fluctuation are very similar for both measurements on each specimen. The associated statistics are similar as well.

Body temperature and room temperature time delay differences and energy level fluctuations are compared in Fig. 4 and Table III using measurements made on four different specimens without removal from the sample holder. The data show that the amplitude of time delay differences increases considerably from room to body temperature, but that the spatial pattern of time delay differences remains similar. Both the amplitude and spatial pattern of the energy level fluctuations are less affected by temperature than those for the time delay differences.

The results obtained from 14 different specimens of abdominal wall at body temperature are the time delay difference and energy level fluctuation maps of Fig. 5 and the statistical summary in Table IV. The maps of time delay difference generally have larger spatial features than

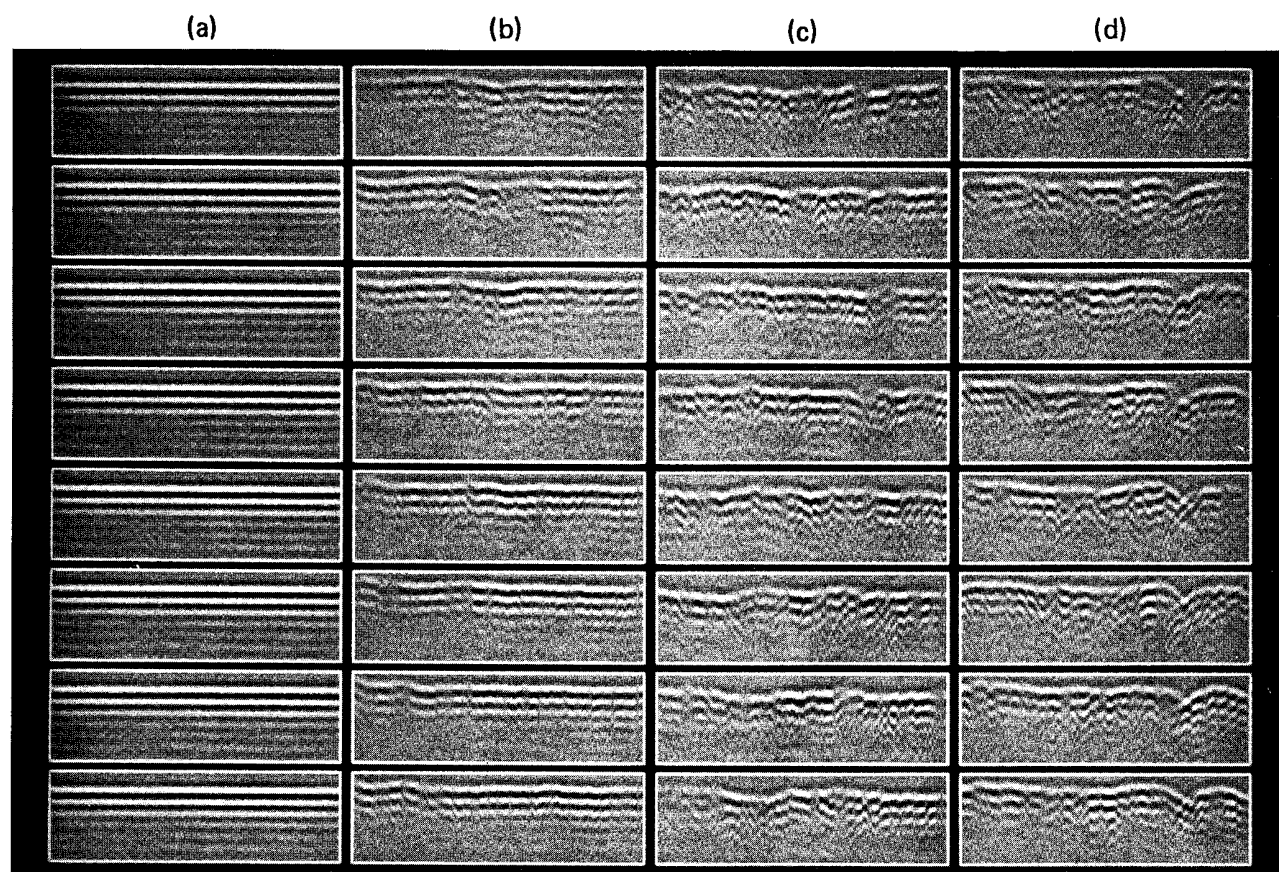


FIG. 1. Representative waveforms compensated for geometric path. (a) H₂O-58. (b) HAW37A-81. (c) HAW42-69. (d) HAW65-74. Each column of panels shows waveforms at sequential increments of 2.88 mm in elevation across the first half of the 46.08-mm aperture. At each elevation, the horizontal coordinate is the array direction and spans a distance of 92.16 mm in 0.72-mm increments while the vertical coordinate is time and spans an interval of 2.0 μ s in 0.05- μ s increments. Signal amplitude is shown linearly on a gray scale with the maximum signal in the two-dimensional aperture for each measurement represented by white and the corresponding negative value by black.

the maps of energy level fluctuation, and the relatively high spatial-frequency speckle of the energy level fluctuations appears largely uncorrelated with the time delay differences, although some background variation in the energy level fluctuations is apparently related to features in the time delay difference maps. The variability of the time delay difference patterns produced by different specimens in comparison to the relative uniformity of the speckle pat-

terns in the energy level fluctuations is evident as well.

Time delay difference and energy level fluctuation statistics for water path measurements, for room temperature and corresponding body temperature specimen path measurements, and for measurements of 14 different (independent) specimens are summarized graphically in Fig. 6, which employs a bar chart format to allow rapid visual assessment of the relationships between the results for dif-

TABLE I. Water path statistics.

Data set	Time delay differences				Energy level fluctuations			
	rms value (ns)	99.5% value (ns)	Corr. len. array dir. (mm)	Corr. len. elev. dir. (mm)	rms value (dB)	99.5% value (dB)	Corr. len. array dir. (mm)	Corr. len. elev. dir. (mm)
H ₂ O-58	6.3	19.0	0.85	1.90	0.76	3.21	1.05	23.00
H ₂ O-59	6.4	21.8	0.87	1.90	0.57	1.75	1.21	23.10
H ₂ O-60	6.1	21.2	0.81	1.67	0.55	1.80	1.85	22.40
H ₂ O-64	3.2	10.0	4.21	14.19	0.47	1.48	3.74	19.10
H ₂ O-65	3.3	9.7	4.13	10.25	0.48	1.94	1.42	21.93
H ₂ O-67	3.1	8.8	4.40	20.28	0.46	1.29	3.80	17.58
Mean	4.7	15.1	2.55	8.37	0.55	1.91	2.18	21.19
s.d.	1.7	6.2	1.87	7.85	0.11	0.68	1.26	2.30

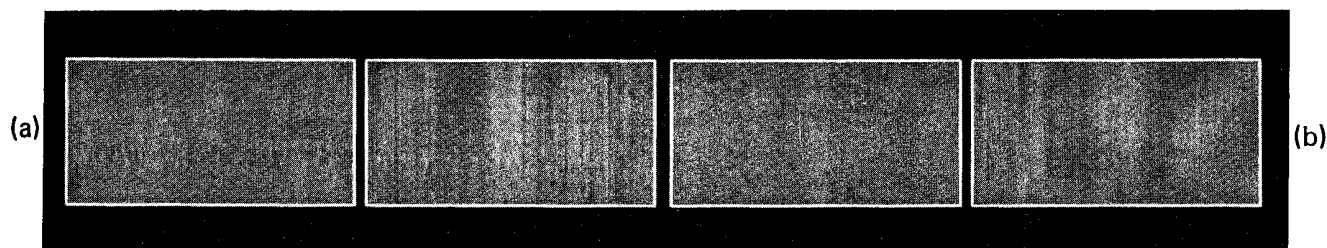


FIG. 2. Representative water path time delay differences and energy level fluctuations. (a) H₂O-59. (b) H₂O-67. In the left panel of each pair, arrival time difference is shown on a linear scale with a maximum time delay difference of 150 ns represented by white and a minimum time delay difference of -150 ns represented by black. In the right panel of each pair, energy level fluctuation is shown on a log scale with a maximum positive excursion of +10 dB represented by white and a maximum negative excursion of -10 dB represented by black. In all panels, the horizontal coordinate is the array direction and spans a distance of 92.16 mm in 0.72-mm increments while the vertical coordinate corresponds to position of the array in elevation and spans a distance of 46.08 mm with points interpolated from measurements at 1.44-mm intervals to produce data at 0.72-mm increments.

ferent sets of measurements and the variability within them.

III. DISCUSSION

Development of the data processing procedure used in this investigation required various choices. Important among the choices were the selection of the least-mean-square error approach to determine relative arrival time throughout the aperture, and the use of fourth-order polynomial fits as references for the calculation of time delay differences and energy level fluctuations. These decisions were guided by theoretical considerations and experience. Since other choices could yield appreciably different nu-

merical results, the same basic processing techniques were employed throughout this study to yield consistent data for comparisons.

The least-mean-square error method of calculating relative wave front arrival times used 15 906 arrival time differences to determine relative arrival times at the 4096 points in the 128×32 aperture. The redundancy built into this method minimized the effect of errors in arrival time differences calculated by cross correlation of neighboring waves. When signal correlation was low, the algorithm for arrival time difference estimation provided reasonable arrival time difference approximations that could be employed to maintain the matrix structure that simplified the solution of the overconstrained equations. On average, 29.5% of the cross-correlation coefficients calculated in the

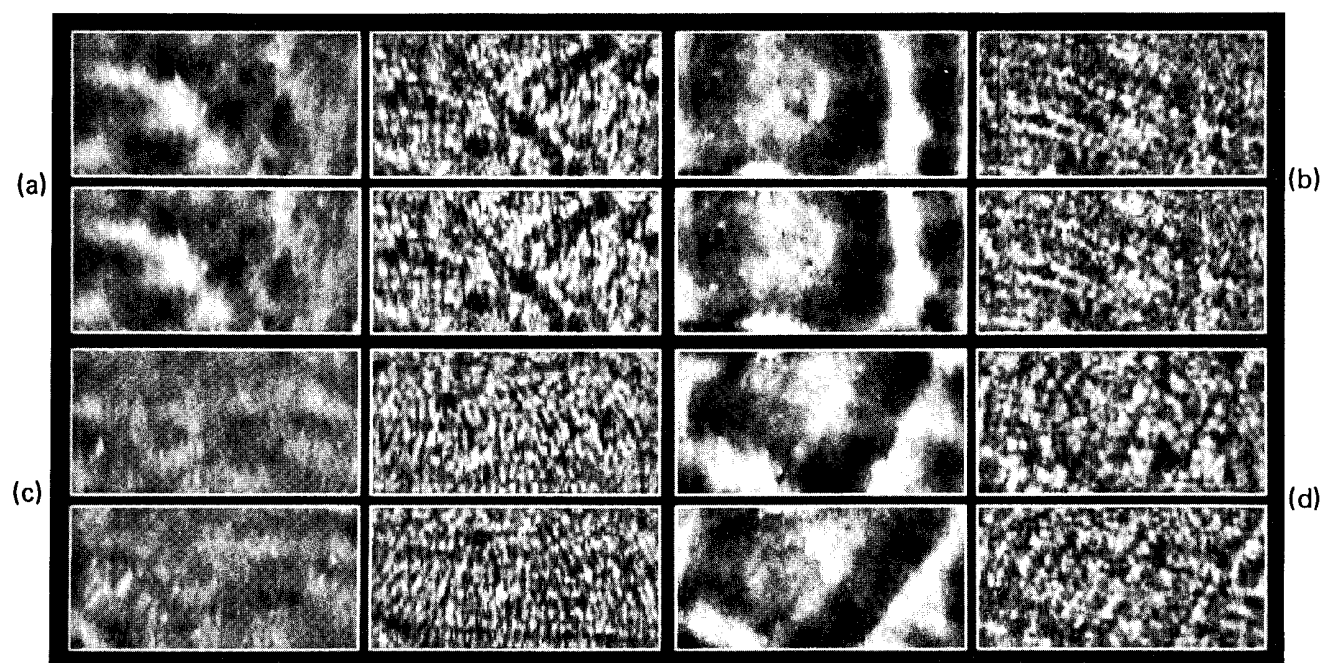


FIG. 3. Abdominal wall path time delay differences and energy level fluctuations for repeated body temperature measurements. (a) HAW42-69 and HAW42-70. (b) HAW65-74 and HAW65-75. (c) HAW55-54 and HAW55-59. (d) HAW60-55 and HAW60-71. Specimens 42 and 65 were studied twice in a single day, while the two studies of specimens 55 and 60 were separated by 3 months. For each specimen, the results of the first study are presented above those of the second study. The format and scales in each pair of panels are the same as in Fig. 2.

TABLE II. Abdominal wall path statistics for repeated body temperature measurements.

Specimen (HAW number)	Specimen thickness (mm)	Run No.	Date	Time delay differences				Energy level fluctuations			
				rms value (ns)	99.5% value (ns)	Corr. len. array dir. (mm)	Corr. len. elev. dir. (mm)	rms value (dB)	99.5% value (dB)	Corr. len. array dir. (mm)	Corr. len. elev. dir. (mm)
42	20	69	09/01/92	42.2	118.1	8.65	7.86	3.50	9.40	1.97	2.68
		70	09/01/92	41.9	123.8	8.11	7.73	3.49	9.00	1.98	2.71
65	15	74	12/16/92	63.9	187.1	7.79	16.59	3.27	8.11	2.03	1.92
		75	12/16/92	62.8	187.8	8.83	14.46	3.21	8.28	2.08	1.92
55	25	54	05/14/92	23.9	72.5	3.27	4.43	2.92	7.68	1.49	2.15
		59	08/14/92	29.3	98.7	3.65	4.65	3.14	8.27	1.31	2.08
60	10-30	55	05/22/92	60.2	156.0	10.74	10.54	3.28	8.56	2.39	2.35
		71	09/02/92	57.0	160.8	9.25	9.37	3.36	8.61	2.29	2.05

14 independent tissue path studies were less than the 0.8 level considered acceptable here, while less than 0.1% of all the water path cross-correlation coefficients were unacceptable. This indicates that, on average, 2.7 times the minimum number of equations necessary to calculate relative arrival time throughout a tissue path measurement aperture were available from cross correlation of neighboring waveforms and that the reliance on arrival time difference calculation techniques other than the cross correlation of neighboring waveforms was not high.

The utilization of two-dimensional, fourth-order curve fits as references to eliminate geometric effects and the average characteristics of each specimen for the calculation of time delay differences and energy level fluctuations is an empirical approach. Although use of a theoretical model

based on spherical wave propagation may be desirable, a straightforward solution to the problem can only be found for the simple water path case. When abdominal wall specimens are used, gradual variations in specimen thickness as well as refraction at the various surfaces make such calculations dependent on accurate knowledge of the thickness, average sound speed, and bulk attenuation of the sample throughout the entire scan region, but such detailed information is not readily obtainable. Two-dimensional, fourth-order curve fits were chosen as an appropriate method to obtain reference values because these fits yielded consistently lower time delay difference and energy level fluctuation rms values for water path data than spherical fits did. In addition, the fourth-order fits were better able to accommodate small equipment misalignments. Finally, this

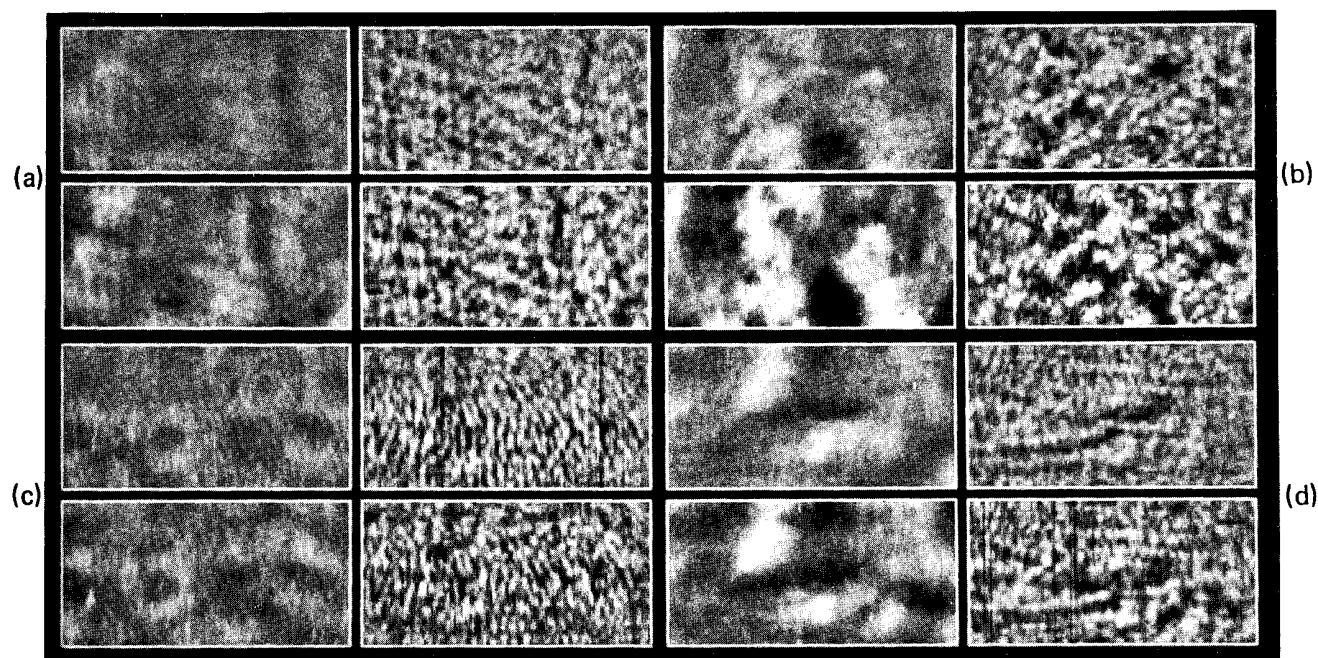


FIG. 4. Abdominal wall path time delay differences and energy level fluctuations for measurements at room and body temperature. (a) HAW36-66 and HAW36-67. (b) HAW54-64 and HAW54-65. (c) HAW55-53 and HAW55-54. (d) HAW57-51 and HAW57-52. For each specimen, the room temperature results are shown above the results at body temperature. The format and scales in each pair of panels are the same as in Fig. 2.

TABLE III. Abdominal wall path statistics for room and body temperature measurements (C=room temperature, H=body temperature).

Specimen (HAW number)	Specimen thickness (mm)	Run No.	Temp.	Time delay differences				Energy level fluctuations			
				rms value (ns)	99.5% value (ns)	Corr. len. array dir. (mm)	Corr. len. elev. dir. (mm)	rms value (dB)	99.5% value (dB)	Corr. len. array dir. (mm)	Corr. len. elev. dir. (mm)
36	15	66	C	16.0	47.0	4.34	5.25	2.02	5.84	2.26	2.01
		67	H	25.6	76.6	5.88	6.92	2.74	8.08	2.32	2.20
54	20	64	C	26.5	88.9	7.06	7.24	2.93	9.05	2.88	2.18
		65	H	60.4	195.3	9.19	11.94	3.70	9.42	2.90	2.48
55	25	53	C	18.3	52.6	2.69	3.99	2.59	7.14	1.35	2.52
		54	H	23.9	72.5	3.27	4.43	2.92	7.68	1.49	2.15
57	15	51	C	25.6	71.8	10.94	7.51	2.32	6.68	2.43	1.81
		52	H	39.3	119.4	11.11	7.58	3.23	11.31	2.53	2.19
Room temp.		Avg. thickness									
Mean		18.8		21.6	65.1	6.26	6.00	2.47	7.18	2.23	2.13
s.d.		4.8		5.2	19.1	3.60	1.68	0.39	1.36	0.64	0.30
Body temp.											
Mean		18.8		37.3	116.0	7.36	7.72	3.15	9.12	2.31	2.26
s.d.		4.8		16.9	57.0	3.48	3.12	0.42	1.64	0.60	0.15

method takes into account slow variations across the plane of the receiving aperture but is relatively uninfluenced by more rapid fluctuations, thus leaving the important higher spatial-frequency information, which is of interest here, intact.

The success of the polynomial fit as a reference for the calculation of time delay due to geometry is evident in Fig. 1. The water path waveforms corrected for geometric delay exhibit only minute differences in ultrasonic pulse arrival time in both the array and elevation directions, while the tissue path waveforms corrected for geometric delay exhibit local arrival time variations around an average arrival time. Thus, the polynomial fit has both corrected for geometric path and retained local arrival time variations.

The water path results in Fig. 1(a), Fig. 2, and Table I show the absolute level and variability of the systematic and random errors in measurements utilizing an ideal transmission path. The water path data indicate that the measurement system nonidealities generally contribute less than 5 ns of rms error to the time delay measurements and less than 0.6 dB of rms error to the energy level fluctuations. The data also indicate that the spatial variation of these errors is dependent on differences in sensitivity among elements in the receiving array as well as on the source that was employed. The uniformity of the distortion maps and the minimal rms values again demonstrate the success of the polynomial fit as a reference for the calculation of energy level fluctuations and time delay differences.

The systematic and random errors associated with an ideal transmission path are small relative to the fluctuations observed in tissue path measurements. A review of the data in Table I–Table IV as well as the water path and specimen data in the bar charts comprising Fig. 6 shows that the water path time delay difference rms and 99.5% values both average about one ninth of those measured for

the 14 abdominal wall specimens at body temperature, and that the corresponding energy level fluctuation statistics, on a logarithmic scale, both average about one fifth of those measured for the 14 specimens. Consequently, system error, as measured for the water paths, does not greatly influence the time delay difference and energy fluctuation maps for tissue path studies.

The results in Fig. 3 and Table II for the two specimens studied on a single day without removal from the sample holder describe the repeatability of tissue path measurements. Although the time delay difference and energy level fluctuation maps indicate that one specimen (HAW65) shifted slightly during preparations for the second measurement, the rms time delay difference values for the two measurements on this specimen differ by less than 2% and the correlation lengths of the time delay differences agree within 14%, while the corresponding energy level fluctuation amplitude and correlation length statistics differ by less than 3%. The data from the other specimen (HAW42) indicate reproducibility of rms time delay difference and energy level fluctuation values to 1% and 0.3%, respectively, and of all correlation length measurements to within 6%. On balance, the reproducibility of measurements without removal of the specimen from the holder is considered very good.

The other repeated study data in Fig. 3 and Table II show that time delay difference and energy level fluctuation measurements are relatively unaffected when specimens are frozen for a period of about three months. While the statistics of the two measurements on each of these specimens vary more than the statistics of same day measurements without removal of the specimen from the holder, the time delay difference and energy level fluctuation maps indicate a greater difference in specimen placement for each study repeated after three months than in the case where the specimen (HAW65) was inadvertently

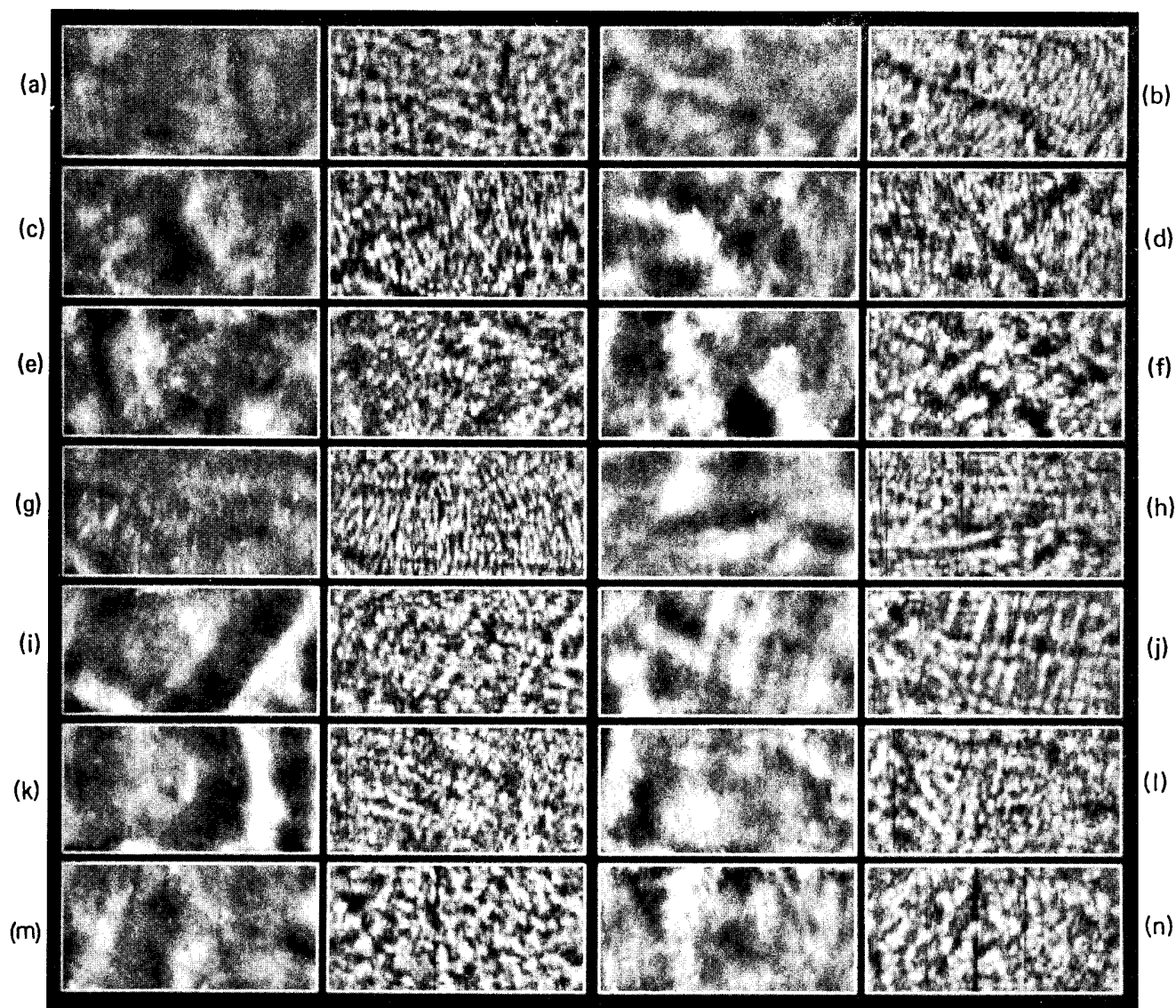


FIG. 5. Abdominal wall path time delay differences and energy level fluctuations for 14 different specimens studied at body temperature. (a) HAW36-67. (b) HAW37A-81. (c) HAW38-72. (d) HAW42-69. (e) HAW46-68. (f) HAW54-65. (g) HAW55-59. (h) HAW57-52. (i) HAW60-71. (j) HAW62-56. (k) HAW65-74. (l) HAW66-80. (m) HAW68-78. (n) HAW69-79. The format and scales in each pair of panels are the same as in Fig. 2.

shifted without removal from the holder. Given the effect of the small inadvertent shift of HAW65 on its measurement statistics, most of the statistical variation in these studies is attributed to changes in specimen position relative to the source and receiving aperture rather than to the frozen storage of specimens.

Specimen surface irregularities could also contribute to measured distortion in the tissue path measurement configuration of this study. However, the surfaces of all the specimens studied were smooth. The outer layers of the abdominal wall are skin on one side and the peritoneal membrane on the other, both of which are naturally smooth. The gentle pressure of the taut membranes of the specimen holder against the pliant and almost neutrally buoyant specimen maintained this smoothness during measurements. Thus, wavefront distortion due to surface irreg-

ularities is believed to be negligible in the measurements reported here.

Wave front distortion may similarly be induced by refraction due to an average difference in sound speed between the sample and the surrounding medium. Two tests were carried out to assess the magnitude of any such disturbance in the tissue path measurements reported here. In the first, received pulse amplitude was measured across the aperture for propagation through comparably thick samples of abdominal wall, clear gel, and gel containing graphite scatters. For both gel samples, the amplitude of the transmitted signal fluctuated insignificantly across the aperture, while for the specimen, the amplitude fluctuated with position as in the tissue path data shown in Fig. 5. In the second, two regular distortion measurements were made for a layer of oil with a sound speed and thickness

TABLE IV. Abdominal wall path statistics for fourteen different specimens studied at body temperature.

Specimen (HAW number)	Run No.	Specimen. thickness (mm)	Time delay differences				Energy level fluctuations			
			rms value (ns)	99.5% value (ns)	Corr. len. array dir. (mm)	Corr. len. elev. dir. (mm)	rms value (dB)	99.5% value (dB)	Corr. len. array dir. (mm)	Corr. len. elev. dir. (mm)
36	67	15	25.6	76.6	5.88	6.92	2.74	8.08	2.32	2.20
37A	81	15	28.2	90.7	5.88	5.41	3.14	8.95	2.03	2.39
38	72	10-25	36.1	100.4	6.70	8.47	3.34	8.92	1.88	2.73
42	69	20	42.2	118.1	8.65	7.86	3.50	9.40	1.97	2.68
46	68	35	46.8	138.7	6.87	8.41	3.01	8.32	2.33	2.05
54	65	20	60.4	195.3	9.19	11.94	3.70	9.42	2.90	2.48
55	59	25	29.3	98.7	3.65	4.65	3.14	8.27	1.31	2.08
57	52	15	39.3	119.4	11.11	7.58	3.23	11.31	2.53	2.19
60	71	10-30	57.0	160.8	9.25	9.37	3.36	8.61	2.29	2.05
62	56	25	42.7	116.6	7.40	9.35	3.19	8.68	2.58	2.67
65	74	15	63.9	187.1	7.79	16.59	3.27	8.11	2.03	1.92
66	80	25	45.3	161.6	5.94	9.24	3.38	8.99	2.26	2.33
68	78	20	40.4	125.0	6.11	9.61	3.64	9.18	2.46	2.30
69	79	35	44.3	151.3	5.93	6.59	3.53	9.25	2.26	2.55
Mean		21.6	43.0	131.5	7.17	8.71	3.30	8.96	2.23	2.33
s.d.		6.8	11.6	35.8	1.90	2.93	0.26	0.82	0.38	0.26

similar to those of the specimens. The resulting time delay difference and energy level variation plots did not differ visibly from those for the water paths shown in Fig. 2. In each case, the time delay difference rms value was within 1 ns of the 4.7-ns average for six water path measurements (Table I), while the energy level fluctuation rms value was within 0.05 dB of the 0.55-dB average for the water paths (Table I). Based on these tests, the conclusion is drawn that wave front distortion caused by refraction at the boundaries between water and specimens studied was not significant.

The combination of water path, repeated study, and other test data provide good evidence that the measurement system and tissue handling in this study do not contribute significant error or artifact to the values of time delay differences and energy level fluctuations presented here.

A comparison of the room and body temperature time delay difference and energy level fluctuation data in Fig. 4, Table III, and Fig. 6 shows that time delay differences are appreciably affected by temperature while energy level fluctuations are less affected. However, the magnitudes of both the time delay differences and energy level fluctuations are more affected by temperature than are the spatial distributions. For example, the average time delay difference rms and 99.5% values each rise more than 70% with the approximately 15 °C increase in temperature, while energy level fluctuation rms and 99.5% values increase about 28%. At the same time, the average time delay difference correlation lengths rise about 23%, while those for the energy level fluctuations change less than 5%. The observed dependence of arrival time and energy level variations on temperature indicates that *in vitro* measurements should be made at body temperature to improve simulation of propagation encountered in clinical imaging.

The specimen waveforms that are presented in Fig.

1(b)-(d) were selected to illustrate the range and combinations of distortion encountered in the group of 14 independent human abdominal wall specimens studied at body temperature. The HAW37A waveforms, which have rms time delay difference and energy level fluctuation values of 28.2 ns and 3.14 dB, respectively, exhibit small arrival time and energy level variations compared to the average rms values of 43.0 ns and 3.30 dB for the 14 independent specimen studies. The HAW42 waveforms, which have rms values of 42.2 ns and 3.50 dB, respectively, exhibit moderate arrival time and high energy level variations. The HAW65 waveforms, which have time delay difference and energy level fluctuation rms values of 63.9 ns and 3.27 dB, respectively, illustrate high arrival time and moderate energy level fluctuations. The time delay difference and energy level fluctuation correlation lengths in the array and elevation directions for these three specimens also span a range of values and can be found in Table IV.

The time delay difference and energy level fluctuation maps for the 14 independent body temperature studies presented in Fig. 5 provide an indication of the variability that may be encountered clinically. The size and shape of features and the absolute magnitude of the time delay differences vary considerably. Although the energy level fluctuation maps share a common speckled appearance, the size and orientation of the speckle varies, as do the larger features that are sometimes visible.

The time delay difference statistics in Table IV and Fig. 6 describe the magnitude, variability, and spatial characteristics of the arrival time distortion measured for the 14 specimens at body temperature quantitatively. The rms time delay difference values range from 25.6 to 63.9 ns, with an average of 43.0 ns, while the 99.5% values range from 76.6 to 195.3 ns, with an average of 131.5 ns. The rms and 99.5% values of time delay differences are well correlated, each 99.5% value being about three times its corre-

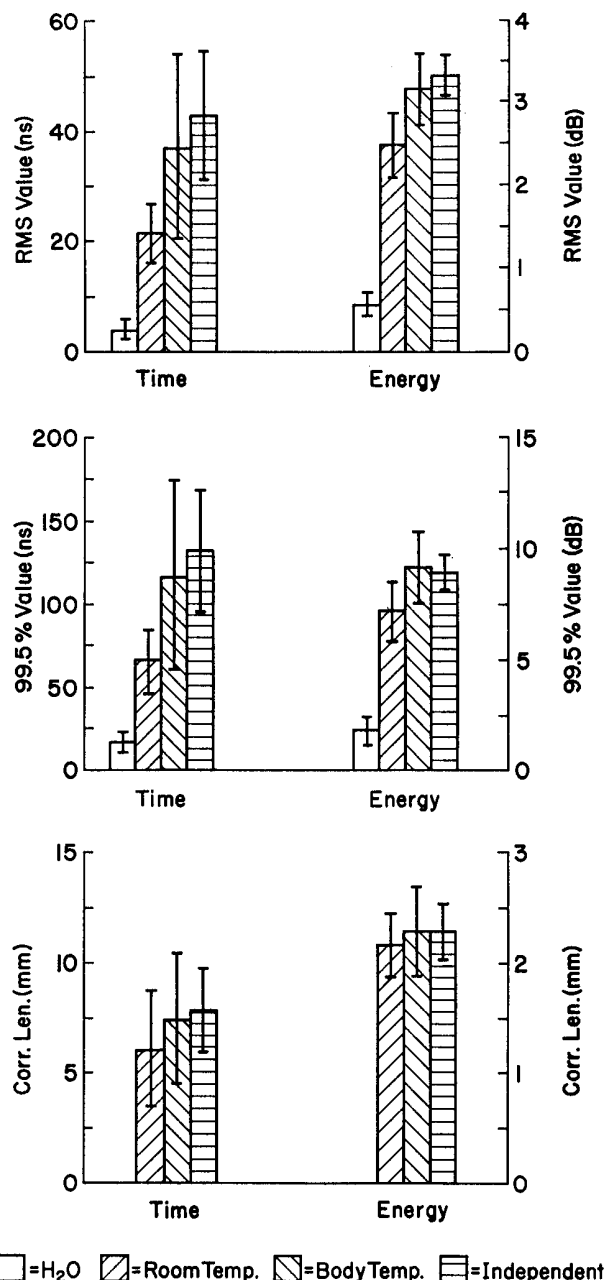


FIG. 6. Summary of time delay difference and energy level fluctuation statistics. In each chart, the average and standard deviation of the measurements within each group are shown. The geometric mean of the array and elevation direction correlation lengths has been used to compute the correlation length statistics.

sponding rms value. The array and elevation direction correlation lengths, which describe the size and orientation of the features in the time delay difference maps of Fig. 5, vary widely. Since arrival time variations are caused by the specific morphology of the tissue used for measurements and since the specimens were taken from different abdominal wall locations, both the orientation and size of detected features are unique for each specimen and random among the group of specimens. As a result, the average array and elevation correlation lengths, at 7.17 and 8.71 mm, respectively, are roughly equal, given the size of their

standard deviations. The geometric mean of the array and elevation direction average time delay difference correlation lengths is 7.90 mm.

The energy level fluctuations produced by the 14 abdominal wall specimens at body temperature are similarly characterized by the data in Table IV and Fig. 6. The magnitude of energy level fluctuations is much more uniform from specimen to specimen than that of the time delay differences. The average rms and 99.5% values are 3.30 and 8.96 dB, respectively, with standard deviations of only 0.26 and 0.82 dB, respectively. The correlation lengths are less variable from specimen to specimen as well, with average values of 2.23 and 2.33 mm, and standard deviations of 0.38 and 0.26 mm in the array and elevation directions, respectively. The geometric mean of the array and elevation direction average energy level fluctuation correlation lengths is 2.28 mm.

Additional information about wave front distortion is provided by the average and standard deviation of the cross-correlation peak values in the measurement aperture. The average (\pm s.d.) values of the cross-correlation peaks found for the 14 independent tissue paths in this study were 0.88 (\pm 0.03), 0.84 (\pm 0.05), and 0.83 (\pm 0.05) in the array, elevation, and diagonal directions, respectively. Corresponding average values for the six water path measurements were all greater than 0.99. These statistics show that the shape of the waveforms is altered significantly by ultrasonic propagation through abdominal wall.

Time delay differences and energy level fluctuations like those reported here can have an important effect on beam formation in ultrasonic systems used today for diagnostic imaging. For example, consider an imaging system that has a 3.75-MHz center frequency, an aperture of $30 \times 10 \text{ mm}^2$, and a beamformer with time delay and amplitude tolerances of $\lambda/10$ and 1 dB, respectively. The 43.0-ns average rms time delay difference is about 1.6 times the 27 ns value of $\lambda/10$ while the 3.3-dB average rms energy level fluctuation is more than three times the 1-dB amplitude specification. The aperture dimensions range from about 1 to 4 correlation lengths of the time delay differences and from about 4 to 13 correlation lengths of the energy level fluctuations. These relationships indicate that the magnitude of time delay differences and energy level fluctuations can be greater than design specifications and that the spatial extent of the aperture can result in the unintentional random (destructive or constructive) summation of signals.

Overall, the results for the 14 different specimens show that both energy level fluctuations and arrival time variations can arise when ultrasonic pulses traverse the human abdominal wall and indicate that more than arrival time compensation is required if ultrasonic imaging techniques are to achieve *in vivo* resolution limited only by aperture and pulse characteristics.

IV. CONCLUSION

Ultrasonic pulse wavefront distortion has been investigated by recording and processing transmitted waveforms to obtain maps and statistics of both time delay differences

and energy level fluctuations in six water path studies and 22 human abdominal wall studies that employed a total of 14 different specimens. Comparison of water path and tissue path results indicates that the measurement system does not contribute significant error to time delay difference and energy level fluctuation values in the tissue path data. Repeated study of specimens shows that the results of individual tissue path measurements are reproducible, and that, while measurements depend on specimen position, frozen storage of a specimen for a period of 3 months appears to have no appreciable effect on the time delay differences and energy level fluctuations produced by the specimen. Appreciable differences between time delay differences and energy level fluctuations obtained at room and body temperature indicate that *in vitro* measurements should be made at body temperature to simulate better the propagation conditions encountered in clinical imaging. In fourteen independent tissue path measurements, the time delay differences had an average rms value of 43.0 ns and an associated correlation length of 7.94 mm, while the energy level fluctuations had an average rms value of 3.3 dB and a correlation length of 2.28 mm. The time delay differences and energy level fluctuations appear largely uncorrelated in the reception plane, even though some background variation in the energy level fluctuation is apparently related to features in the time delay difference maps. In addition, the time delay difference patterns are more variable among specimens than are the energy level fluctuations. The results show that time delay differences and energy level fluctuations produced by human abdominal wall can be appreciable and provide important new information about the variety and range of wave front arrival and energy variations for the development of methods to compensate for wave front distortion in abdominal imaging applications.

ACKNOWLEDGMENTS

The authors thank Dr. Per-Lennart Westesson, Gordon Ballard, and Michael Norton for their assistance in obtaining human abdominal wall specimens from autopsy. Technical assistance with data acquisition hardware and software from Timothy J. Case and Ryoichi Kanda is acknowledged with appreciation. Ryoichi Kanda also contributed to this work through his discussions with the authors. Funding for this investigation was provided by the

University of Rochester Diagnostic Ultrasound Research Laboratory Industrial Associates, NIH Grants DK 45533 and HL150855, and the Alexander von Humboldt Foundation. Computations were performed at the University of Rochester Computing Center and the Cornell National Supercomputing Facility, which is supported in part by the National Science Foundation, New York State, and the IBM Corporation.

- ¹M. Moshfeghi and R. C. Waag, "In-Vivo and In-Vitro Ultrasound Beam Distortion Measurements of a Large Aperture and a Conventional Aperture Focused Transducer," *Ultrasound Med. Biol.* **14**(5), 417-430 (1988).
- ²R. C. Waag, D. Dalecki, and W. Smith, "Estimates of wave front distortion from measurements of scattering by model random media and calf liver," *J. Acoust. Soc. Am.* **85**(1), 406-415 (1988).
- ³M. O'Donnell and S. W. Flax, "Phase Aberration Measurements in Medical Ultrasound: Human Studies," *Ultrason. Imag.* **10**(1), 1-11 (1988).
- ⁴J. D. Aindow and R. C. Chivers, "Ultrasonic Wave Fluctuations through Tissue: An Experimental Pilot Study," *Ultrasonics* **26**, 90-101 (1988).
- ⁵P. Krämmer and D. Hassler, "Measurement of Spatial Time-of-Flight Fluctuations of Ultrasound Pulses Passing through Inhomogeneous Layers," in *IEEE 1987 Ultrasonics Symposium Proceedings* (IEEE, New York, 1987), Vol. 2, pp. 939-942.
- ⁶Y. Sumino and R. C. Waag, "Measurements of ultrasonic pulse arrival time differences produced by abdominal wall specimens," *J. Acoust. Soc. Am.* **90**(6), 2924-2930 (1991).
- ⁷G. E. Trahey, P. D. Freiburger, L. F. Nock, and D. C. Sullivan, "In Vivo Measurements of Ultrasonic Beam Distortion in the Breast," *Ultrason. Imag.* **13**(1), 71-90 (1991).
- ⁸Q. Zhu and B. D. Steinberg, "Large-Transducer Measurements of Wavefront Distortion in the Female Breast," *Ultrason. Imag.* **14**(3), 276-299 (1992).
- ⁹Session on "Focusing and Aberration Correction," IEEE 1991 Ultrasonics Symposium, 8-11 December 1991, Lake Buena Vista, FL, in *IEEE 1991 Ultrasonics Symposium Proceedings* (IEEE, New York, 1991), Vol. 2, pp. 1181-1210.
- ¹⁰Session on "Imaging in Inhomogeneous Media," Program and Abstracts of the 17th International Symposium on Ultrasonic Imaging and Tissue Characterization, 1-3 June 1992, Arlington, VA, in *Ultrason. Imag.* **14**(2), 195-197 (1992).
- ¹¹J. C. Bamber and C. R. Hill, "Ultrasonic Attenuation and Propagation Speed in Mammalian Tissues as a Function of Temperature," *Ultrasound Med. Biol.* **5**(2), 149-157 (1979).
- ¹²D.-L. Liu and M. Saito, "Restoring a δ -Pulse Train by Spectral Fitting," *IEEE Trans. Signal Process.* **40**(10), 2616-2619 (1992).
- ¹³D.-L. Liu and R. C. Waag, "Time-shift compensation of ultrasonic focus degradation using least-mean-square error estimates of time delay," *J. Acoust. Soc. Am.* **95**, 542-555 (1994).
- ¹⁴A. Ishimaru, *Wave Propagation and Scattering in Random Media* (Academic, New York, 1978), Vol. 2, Chap. 20.

Wavefront Amplitude Distortion and Image Sidelobe Levels: Part I—Theory and Computer Simulations

Qing Zhu, *Member, IEEE*, and Bernard D. Steinberg, *Life Fellow, IEEE*

Abstract—The quality of an imaging system is degraded by propagation anomalies that distort wavefronts propagating through the medium. Adaptive phase-deaberration algorithms compensate for phase errors in the wavefront. The algorithms suffer, however, when the wavefront *amplitude* is also significantly distorted. This paper derives a theory which shows that the rise of image background level, which is the average sidelobe floor (*ASF*), in a single point-like source image is proportional to the amplitude distortion of the wavefront and inversely proportional to the effective number of array elements. From the theory, the tolerance to the amplitude distortion (after the phasefront has been corrected by a deaberration algorithm) can be calculated based on the design requirement of the sidelobe floor for a given array. Computer simulations show good agreement with the theory. Experimental verification of the theory is given in the companion paper [1].

I. INTRODUCTION

ULTRASONIC WAVES propagating through soft tissue experience wavefront distortion. Phasefront distortion has long been recognized to degrade the performance of an imaging system [2]–[9] and adaptive phase-deaberration algorithms are designed to correct such distortion [10]–[15], [26]. However, severe amplitude errors can not be compensated by these algorithms. Since phase plays a vastly more important role in imaging than amplitude [16]–[17], phase-aberration correction is the first line of defense. But when the wavefront amplitude error is severe it must also be taken into account.

There is little published literature on attempts to measure the amplitude distortion of wavefronts in tissue phantoms or *in vivo*. Notable is the work of O'Donnell and Flax [7] who made *in vivo* measurements in human liver of several subjects with a 64-element array and reported 0.11 and 0.16 rms wavefront amplitude distortion in high and low quality images, respectively. From these measured values of amplitude distortion, they concluded that "amplitude variations may not be a significant factor in clinical image quality". This conclusion is consistent with the theory developed in this paper that shows that these small values lead to sidelobe floors of -37 and -34 dB, respectively, for a 64-element array. Our work with *in vivo* wavefront measurements of the female breast shows that wavefront amplitude distortion is significantly higher. The rms amplitude distortion varies

from 0.30 to 0.82 in 1708 samples obtained from 44 breasts [1]. The sidelobe floor after perfect phase correction of the wavefront measurements varies from -27 to -15 dB and the peak sidelobe level (*PSL*) varies from -22 to -5 dB for an array of the same size. We believe that the primary reason for the greater amplitude distortion and the higher sidelobe level lies in the nature of the test tissue. Liver is a large body of relatively homogeneous tissue characterized by local density variations. Such a body will scatter energy from a propagating wave. If the scattering is weak, the primary effect upon the wavefront is distortion of the phase, while the amplitude is relatively unchanged. To the extent that such a model characterizes liver, this would account for the observations of O'Donnell and Flax. Female breast, on the other hand, is a highly refracting medium. It is not homogeneous, not even in a statistical sense. It contains many interfaces between tissues of different acoustic speeds, involving subcutaneous fat, glandular tissue, intramammary fat, fibrous tissue, sometimes cysts and tumors. The sharp changes in propagation speed, which can be as much as 10%, cause refraction or strong scattering which in turn result in beam bending, beam splitting or overlapping of the beams, leading to multiple arrivals at the receiving transducer from different directions. The interference that follows can result in severe amplitude distortion of the wavefront, as well as phase distortion [18], [19].

The most damaging effect of severe amplitude distortion is the rise of the sidelobe level in the image, even after phase aberration correction is applied. High sidelobes can destroy the desired contrast in the image and make it impossible to distinguish between normal tissue and abnormal tissue, e.g., small tumors and cysts. The theory of the effect of random amplitude errors upon the sidelobe level of the radiation pattern of a phased array has been developed by Steinberg [20], [25]. The effects of deterministic amplitude quantization errors upon the sidelobe level of the radiation pattern have been discussed by Bates [21].

This paper shows that the rise in the *ASF* in a single-source image, after phasefront compensation, is proportional to the wavefront amplitude variance normalized to the square of its mean value (normalized variance) at the receiving aperture and inversely proportional to the effective number of array elements. From this relationship the tolerable level of amplitude distortion can be calculated in terms of *ASF* design requirements for a given array. The companion paper [1] reports the results of an experiment that has been conducted to measure the rise of sidelobe level in the image as a function

Manuscript received October 19, 1992; revised March 31, 1993; accepted April 1, 1993. This work was supported by the Commonwealth of Pennsylvania; Interspec, Inc., Ambler, PA; and the National Science Foundation under Grant BCS92-09680.

The authors are with Valley Forge Research Center, The Moore School of Electrical Engineering, University of Pennsylvania, Philadelphia, PA 19104.
IEEE Log Number 9209833.

of the distortion of the wavefront amplitude. The result is consistent with the prediction of the theory.

The *in vivo* measurements were conducted with a large acoustic aperture (9.6 cm) at the Hospital of the University of Pennsylvania (HUP). The female breast was the propagation medium. The measurements show severe wavefront amplitude distortion in addition to phasefront distortion. The measured high sidelobe levels indicate that either the wavefront amplitude distortion must be compensated by an adaptive algorithm or a large two-dimensional array with more than 1000 elements must be used.

Section II derives the theory relating the average sidelobe floor (*ASF*) in the image to the normalized variance of the wavefront amplitude distortion at the receiving aperture. Section III validates the theory with computer simulation. Section IV discusses the effect of residual phase errors upon the *ASF*. Discussion and summary are in Sections V and VI.

II. THEORY

A. Image Formation

Let $s(u)$ represent the complex angular source distribution, where $u = \sin(\theta)$ and θ is the angle from the array normal. Its complex radiation field in the axis of the receiving array in a homogeneous medium is the inverse Fresnel transform of $s(u)$. The measured field, *after* correcting for near-field curvature, is the inverse Fourier transform of $s(u)$

$$v(x) = F^{-1}(s(u)) = \int s(u) \exp(-jkxu) du \quad (1)$$

where $k = 2\pi/\lambda$, λ is the wavelength and x represents position in the array. The measured field at the finite receiving aperture is $i(x) = w(x)v(x)$, where $w(x)$ is the aperture weighting function. The weighting function describes the array in terms of its length, the amplitude taper introduced for sidelobe control, and the number of array elements and their spacings. The complex image is the Fourier transform of $i(x)$, that is

$$\begin{aligned} \hat{s}_h(u) &= F[i(x)] = F[w(x)v(x)] \\ &= F[w(x)] * F[v(x)] = f(u) * s(u) \end{aligned} \quad (2)$$

where $f(u) = F[i(x)]$ is the radiation pattern of the array and $*$ denotes convolution. The absolute value of $\hat{s}_h(u)$ is the modulus of the source image. The subscript h denotes the image in the homogeneous medium in which the propagation speed is the same everywhere. If the source approximates a point source, the complex image can be equated to the radiation pattern of the array.

In an inhomogeneous medium, the radiation field at the receiving array, after correcting for near-field curvature, is

$$i(x) = \alpha w(x)v(x)m(x) \quad (3)$$

where $m(x)$ is the medium induced distortion and α is a constant to reflect any signal loss. The complex image is

$$\hat{s}_i(u) = \alpha F[w(x)v(x)m(x)] = \alpha f(u) * s(u) * F[m(x)] \quad (4)$$

where $F[m(x)] \triangleq \mu(u)$ is the angular impulse response of the medium, which can (and does) vary with position in the array.

The subscript i denotes inhomogeneous medium. For a point-like source, the complex image approximates the convolution of the radiation pattern of the array and the angular impulse response of the medium.

B. Weak Scattering

In the weak scattering problem most of the energy passes the scattering body unaffected while a small portion is scattered. The result is the superposition of the original field plus a scattered field, and the wavefront distortion is primarily in the phasefront. The medium induced distortion $m(x)$ can then be modeled as a quasirandom phase screen at the receiving aperture, i.e., $m(x) = \exp(j\beta(x))$. Phase deaberration algorithms deduce phase distortion information from the wavefront and create a compensating weight vector $w_c(x)$, which approximates the conjugate of $m(x)$ to correct the phase distortion, i.e., $w_c(x) = \exp(-j\hat{\beta}(x))$ where $\hat{\beta}$ is an estimate of β . The induced signal at the receiving aperture then becomes

$$\begin{aligned} i(x) &= \alpha w_c(x)w(x)v(x)m(x) \\ &= \alpha \exp(-j\hat{\beta}(x))w(x)v(x)\exp(j\beta(x)) \\ &\approx \alpha w(x)v(x). \end{aligned} \quad (5)$$

The phase-compensated complex image $\hat{s}_c(u) \approx \alpha f(u) * s(u)$, which approximates the diffraction-limited image. The subscript c denotes phase compensation.

C. General Case

In the general case (which includes strong scattering and refraction), the wavefront amplitude is also distorted. Therefore, it is appropriate to model $m(x)$ as $a(x)\exp(j\beta(x))$, where $a(x)$ is an amplitude screen at the receiving aperture. The weight compensating vector $w_c(x)$ obtained from the phase deaberration algorithms corrects the phase aberration but leaves the amplitude distortion intact. In this paper we assume that phase distortion in the wavefront has been corrected and only amplitude errors remain. With phase deaberration complete, the signal at the receiving array is

$$\begin{aligned} i(x) &= \alpha w_c(x)w(x)v(x)m(x) \\ &= \alpha \exp(-j\hat{\beta}(x))w(x)v(x)a(x)\exp(j\beta(x)) \\ &\approx \alpha w(x)v(x)a(x). \end{aligned} \quad (6)$$

The phase-compensated complex image is

$$\begin{aligned} \hat{s}_c(u) &= F[i(x)] \\ &= \alpha F[w(x)v(x)a(x)] \\ &= \alpha f(u) * s(u) * F[a(x)] \end{aligned} \quad (7)$$

instead of $f(u) * s(u)$, as it would be in a distortion free medium.

Thus, significant medium-induced amplitude distortion $a(x)$ can induce artifacts in the image $|\hat{s}_c(u)|$. The characteristics of the image artifacts that are of primary concern are *ASF* and *PSL*. A quantitative relation between *ASF* and the normalized variance of $a(x)$ is derived in part D of this section. In the companion paper [1] the relation between *ASF* and *PSL* is determined from experiment. Together they enable

us to assess at what level of amplitude distortion the phase-deaberration algorithms alone are useful.

D. Theory

The derivation is made with discrete rather than continuous variables. Thus $w(x)$ is replaced by $w(n)$, $n = 1, 2, \dots, N$, where N = number of elements in the array. Three assumptions are made (the second and third are validated experimentally for the single source in the companion paper) :

1. The source is a single source.
2. Phase errors in the received wavefront are successfully removed by a phase-deaberration algorithm and only amplitude errors remain.
3. The $a(n)$, $n = 1, 2, \dots, N$, are statistically uncorrelated random variables with a common probability density function (pdf).

The phase-deaberrated complex image can be written as

$$\hat{s}_c(u) = \alpha F[v(n)a(n)] = \alpha \sum_{n=1}^N v(n)a(n) \exp(jkndu) \quad (8)$$

where the aperture taper $w(n)$ has been chosen as unity.

The image intensity is the product of (8) and its complex conjugate:

$$\begin{aligned} \hat{s}_c(u)\hat{s}_c^*(u) &= \alpha^2 \sum_{n=1}^N \sum_{m=1}^N v(n)v^*(m)a(n)a(m) \\ &\quad \times \exp(jk(n-m)du) \\ &= \alpha^2 \left\{ \sum_{n=m} v(n)v^*(n)a^2(n) \right. \\ &\quad \left. + \sum_{n \neq m} v(n)v^*(m)a(n)a(m) \exp(jk(n-m)du) \right\} \end{aligned} \quad (9)$$

The ensemble average intensity is

$$\begin{aligned} \overline{\hat{s}_c(u)\hat{s}_c^*(u)} &= \alpha^2 \left\{ \sum_{n=m} v(n)v^*(n)a^2(n) \right. \\ &\quad \left. + \sum_{n \neq m} v(n)v^*(m)a(n)a(m) \exp(jk(n-m)du) \right\} \\ &= \alpha^2 \left\{ \sum_{n=m} v(n)v^*(n)a^2(n) \right. \\ &\quad \left. + \sum_{n \neq m} v(n)v^*(m)a(n)a(m) \exp(jk(n-m)du) \right\} \\ &= \alpha^2 \left\{ \sum_{n=m} v(n)v^*(n)(\sigma_a^2 + (\bar{a})^2) \right. \\ &\quad \left. + \sum_{n \neq m} v(n)v^*(m)a(n)a(m) \exp(jk(n-m)du) \right\} \\ &= \alpha^2 \left\{ \sum_{n=m} v(n)v^*(n)(\sigma_a^2) + \sum_{n=m} v(n)v^*(n)(\bar{a})^2 \right. \\ &\quad \left. + \sum_{n \neq m} v(n)v^*(m)(\bar{a})^2 \exp(jk(n-m)du) \right\} \\ &= \alpha^2 \left\{ \sum_{n=m} v(n)v^*(n)(\sigma_a^2) \right. \\ &\quad \left. + (\bar{a})^2 \hat{s}_h(u)\hat{s}_h^*(u) \right\} \end{aligned} \quad (10)$$

where σ_a^2 is the variance of a , $\overline{a(n)a(m)} = \overline{a(n)a(m)}$, for $n \neq m$, because of the assumption that $a(n)$ and $a(m)$ are statistically uncorrelated, and $\hat{s}_h(u)\hat{s}_h^*(u)$ is the image intensity obtained through a homogeneous medium.

Equation (10) contains an angle-independent term and a term proportional to the uncorrupted image intensity. The first term is the theoretical asymptotic average background level. The contrast in the image can be defined as the ratio of this quantity to the maximum intensity in the image, denoted $\hat{s}_h(0)\hat{s}_h^*(0)$. This ratio is called the average sidelobe floor or ASF, which is given by

$$ASF = \frac{\sum_{n=1}^N v(n)v^*(n) \sigma_a^2}{\hat{s}_h(0)\hat{s}_h^*(0) (\bar{a})^2} \quad (11)$$

$\hat{s}_h(0)$ is the sum of the measured signal samples $v(n)$. Therefore $\hat{s}_h(0)\hat{s}_h^*(0) = \left| \sum_{n=1}^N v(n) \right|^2 = |N\bar{v}|^2$, where \bar{v} is the average of v . Also, $\sum_{n=1}^N v(n)v^*(n) = N|\bar{v}|^2$. The ratio $\frac{\sum_{n=1}^N v(n)v^*(n)}{\hat{s}_h(0)\hat{s}_h^*(0)} = \frac{|\bar{v}|^2}{|\bar{v}|^2 N} \triangleq \gamma$, which is a function of the radiation pattern of the source. Thus

$$ASF = \frac{\gamma}{N} \frac{\sigma_a^2}{(\bar{a})^2} \quad (12)$$

It is proportional to γ and the normalized variance of wavefront amplitude distortion and inversely proportional to the number of the array elements. N/γ can be interpreted as the effective number of elements N' .

The sidelobe pattern resulting from random process $a(n)$ is itself a random process, of which ASF is its average power level. In any particular pattern the peak sidelobe (PSL) will be larger. *In vivo* experiments in breast (see companion paper [1]) find that the PSL is typically 7 dB larger than ASF.

E. Analysis

Equation (12) can be written as

$$ASF|_{dB} = 10 \log ASF = 10 \log \left(\frac{\gamma}{N} \right) + 10 \log \left(\frac{\sigma_a^2}{(\bar{a})^2} \right) \quad (13)$$

From this relation, a tolerable threshold to wavefront amplitude distortion based on ASF design requirement, after phasefront correction, can be established. For example, if the required ASF is A in dB, then the allowed $\frac{\sigma_a^2}{(\bar{a})^2} \leq 10^{\frac{A - 10 \log \frac{\gamma}{N}}{10}}$.

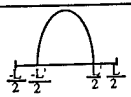
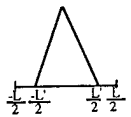
γ involves the geometry of the source. $\gamma = 1$ when $s(u) = \delta(u - u_0)$, for the wavefront in a homogenous medium is spherical and its amplitude is the same everywhere. For any other source geometry, $\gamma > 1$ and consequently the ASF rises. The point source, therefore, is

$$ASF|_{dB} = 10 \log \left(\frac{1}{N} \right) + 10 \log \left(\frac{\sigma_a^2}{(\bar{a})^2} \right) \quad (14)$$

which is the same result obtained by Steinberg for the ASF of a phased array subject to amplitude errors in its weights [20]. Under this condition, ASF is affected only by the number of array elements and the normalized amplitude variance of the wavefront.

In general γ is also a function of transducer size L and, therefore, the number of elements N and the element spacing

TABLE I
RERADIATION PROFILES, γ AND N'

$v(x)$	profiles	γ	N'
$[1 - (\frac{2x}{L})^2] \text{rect}(L)$		$\frac{6}{5} \frac{L}{L'} = 0.6 \frac{NdT}{\lambda D}$	$\frac{5}{6} (\frac{L'}{d}) = 1.66 (\frac{\lambda D}{Td})$
$\text{tri}(L')$		$\frac{4}{3} \frac{L}{L'} = 0.65 \frac{NdT}{\lambda D}$	$\frac{3}{4} (\frac{L'}{d}) = 1.5 (\frac{\lambda D}{Td})$

d. Let the size of a source or target be T and its reradiation beamwidth be approximated by λ/T . At the focal distance D , the cross-section of the reradiation pattern is $D\lambda/T$, which can be larger or smaller than L . When $D\lambda/T \gg L$, the entire transducer is approximately illuminated, $\gamma \approx 1$ and the effective number of elements $N' = N$. In this case (14) is appropriate. When $D\lambda/T < L$ the problem is more complicated. To calculate γ it is necessary to know or assume the shape of the reradiation pattern v of the target, which is a function of its reflection profile. Fortunately the exact shape is not very significant because γ involves integrations of functions of v , and integration diminishes the differences in γ attributable to different v . Consequently simple calculations are sufficient to estimate typical values. To demonstrate the relation between the beamwidth of the reradiation profile $v(n)$ and γ and N' , we use two simple functions to approximate $v(x)$, a parabola and a triangle, each of base $L' = 2D\lambda/T < L$. γ is calculated analytically. Column 1 in Table I gives the two reradiation functions. Column 2 shows the profiles. γ , third column, is shown to be proportional to the ratio $L/L' = NdT/2D\lambda$. Thus the larger the target size T , the higher the frequency, the shorter the focal distance D and the larger the element spacing d , the larger is γ , the smaller is the effective number of array elements N' (column 4) and the larger is the ASF . The -3 dB width of the triangle profile is narrower than that of parabola. This difference is reflected in γ which is larger in the triangular case than in the parabolic case. In general, a skinny profile will produce a larger γ than a fat profile for the same target size, focal distance and aperture. It is evident, however, that the shape of $v(x)$ has a weak influence on γ .

Table II is an example for $D = 120$ mm, $N = 100$ and $d = 1$ mm. A rectangular target is assumed, for which the radiation pattern is a sinc function, and γ is evaluated numerically as a function of λ/T . Increasing the target size narrows its reradiation beamwidth, which increases γ and the ASF . When the target size is fixed, increasing the frequency also narrows the reradiation beamwidth and increases ASF . For a target width of 1 mm, the rise in the ASF at 3 MHz ($\lambda \approx 0.5$ mm in soft tissue) is in the neighborhood of 0.5 dB and can be neglected, but it increases to the order of 5–6 dB at 6 MHz ($\lambda \approx 0.25$ mm), which is normally significant. Thus this factor must be accounted for in system design.

TABLE II
EFFECT OF λ/T ON ASF : $D = 120$ mm, $N = 100$ mm, and $d = 1$ mm

λ/T	γ	Increase in ASF (dB)
0.25	3.413	5.33
0.5	1.136	0.55
1.0	1.008	0.03
2.0	1.005	0.02

TABLE III
EFFECT OF D ON ASF : $\lambda/T = 1/3$, $N = 100$ mm, and $d = 1$ mm

D (mm)	γ	Increase in ASF (dB)
120	1.787	2.52
100	2.664	4.26
80	4.291	6.33
60	4.889	6.89

TABLE IV
EFFECT OF $N' = N/\gamma$ ON ASF

N'	10^2	10^3	10^4
Increase in ASF	-20 dB	-30 dB	-40 dB

Table III lists the effect of D on ASF for the same aperture ($N = 100$, $d = 1$ mm) and $\lambda/T = 1/3$. The decibel increase in ASF almost triples when the focal distance D is reduced by a factor of two.

Table IV lists decrease in ASF as a function of the effective number of elements N' .

The second term in (13) is determined by the propagation medium. Weak scattering induces a small but acceptable perturbation in the amplitude of the wavefront and contributes little to the ASF . For example, a radar phase deaberration experiment published in 1981 [22] exhibited a 0.05 rms amplitude perturbation, corresponding to $\sigma_a^2/(\bar{a})^2 = 2.5 \times 10^{-3}$ or -26 dB. The amplitude rms values 0.11 and 0.16 found in human liver [7] correspond to $\sigma_a^2/(\bar{a})^2 = 1.2 \times 10^{-2}$ and 2.6×10^{-2} or -19 and -16 dB, respectively. In the general case (which includes strong scattering and refraction), $\sigma_a^2/(\bar{a})^2$ can be much larger. The *in vivo* wavefront experiments in breast found that the pdf of $a(n)$ is approximately Rayleigh [29]. For this case, therefore, $10 \log(\sigma_a^2/(\bar{a})^2) = 10 \log((4 - \pi)/\pi) = 10 \log(0.27) = -5.7$ dB, which is at least 10 dB higher than the weak scattering experiments reported above. Hence an algorithm which produces satisfactory sidelobes in weak scattering is likely to fail when operating in a more general distorting medium, unless transducers with huge numbers of elements are employed. All known phase deaberration algorithms have this failing.

The following is a realistic example for the Rayleigh case ($\sigma_a^2/(\bar{a})^2 = 0.27$). Let $N = 100$ elements and consider the favorable situation in which the entire array is illuminated by the reradiation from a target, for then $\gamma = 1$. Assuming further that phase deaberration has been successfully accomplished, ASF from (13) is -26 dB and PSL would be about 7 dB higher (from experiment).

In this theory ASF has been calculated on a one-way propagation basis. It may be casually assumed that in two-way echo scanning the sidelobe levels established above

will double (in dB), in which case the *ASF* and *PSL* values reported above may suffice. However, this will not be the case unless the transmitting elements weights can be adjusted to form the same radiation pattern that the deaberration procedure gives to the received radiation pattern. In that case the two-way pattern is the square of the receiving pattern and the sidelobe levels are doubled. Because the distribution is unknown a priori, an iterative procedure must be employed to achieve sidelobe doubling. This is difficult to achieve. This topic is discussed further in Section V.

Irrespective of how the target is illuminated, if the modulus of the reradiation field develops characteristics that approximate the Rayleigh distribution, we can expect an *ASF* and *PSL* of approximately -26 dB and -19 dB, respectively, for an array of 100 elements. Only by increasing N will a successful scanner result. A 2-D design is a way to preserve the scale of the transducer while increasing the number of the elements to $N = M^2 = 10^4$. With the scale preserved, γ would remain at unity and *ASF* & *PSL* would reduce to -46 dB and -39 dB, respectively. These values are more useful for high contrast and high dynamic imaging.

There are two factors that affect the construction of phased arrays with huge numbers of elements. First is the increased cost associated with a large number of channels. State-of-the-art phased array scanner currently have 128 channels. Increasing this number by nearly a factor of 80 may not be practical or affordable with current techniques. One possible alternative is to apply the synthetic aperture technique to the available parallel channels and thereby form large synthetic subarrays from the transducer elements [23], [24]. The trade off is between the increase of sidelobe levels due to target motion, degraded performance of phase-only correction, and the reduction of sidelobe levels due to the effective increase in the number of elements.

III. SIMULATION RESULTS

Computer simulations were made to verify the relation derived in (13). In the simulations, we chose $v(n) = 1$, which corresponds to an ideal point-source insonification. $a(n)$ is generated by computer for 2 pdfs, Rayleigh and uniform $U[0, 2]$. $a(n)$ and $a(m)$ are independent for $n \neq m$. All phase errors are assumed to be removed by a phase deaberration algorithm, which also focuses the array to the target distance. Therefore the image is the Fourier transform of the amplitude profile $a(n)$. The *ASF* is measured outside the mainlobe region in the image. Fig. 1 shows the results of computer simulations of a 40-element array. The Rayleigh pdf (Fig. 1(a)) implies that strong scattering dominates the distortion process while the uniform pdf $U[0, 2]$ Fig. 1(b) implies that coherent interference dominates. Each experiment yielded a pair of points $(\sigma_a^2/(\bar{a})^2, ASF)$, which was plotted in the figures. The abscissa is $\sigma_a^2/(\bar{a})^2$ and the ordinate is *ASF*. The two variables prove to be linearly related as predicted by the theory. The expected slope is $1/N = 0.025$. The measured slopes are 0.025 9 and 0.023 9, which agree very well with the theoretical value. The standard deviations from the

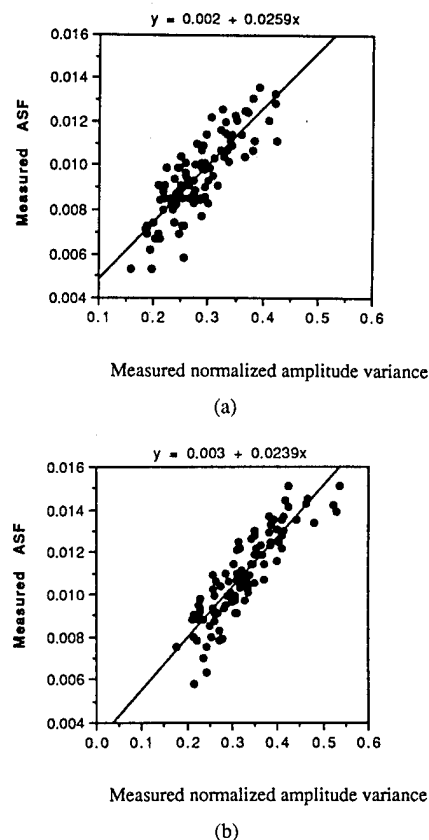


Fig. 1 Computer simulations showing *ASF* versus $\sigma_a^2/(\bar{a})^2$. The abscissa is $\sigma_a^2/(\bar{a})^2$ and the ordinate is *ASF*. The variables are linearly related. (a) Wavefront amplitude profile obeys the Rayleigh distribution. (b) Wavefront amplitude obeys a uniform distribution.

regression lines are 0.001 and 0.000 97, which are exceedingly small.

The correlation coefficients between the measured pairs of data are 0.75 and 0.78, which are far beyond the critical value for a 0.1% level of significance. Therefore, the experimental linear relations in Fig. 1 are statistically significant.

The measured *ASF*'s also compare favorably with the theory. Equation (14) predicts that the average *ASF* for an ideal point source and a 40-element array is -21.7 dB for the Rayleigh distribution and -20.8 dB for the uniform $U[0, 2]$ distribution. The measured average *ASF*'s are -20.32 dB and -19.73 dB. The standard deviations are 0.89 dB and 0.85 dB.

IV. RESIDUAL PHASE ERRORS

The second assumption in the theory was that the phasefront errors are completely compensated by a phase deaberration algorithm and only amplitude errors remain. However, the phase error correction may not be complete and residual phase errors may be left. Thus, it is instructive to examine the combined effect of residual phase error after phase correction, and amplitude distortion. Let $\delta\phi(n) = \beta(n) - \hat{\beta}(n)$ represents the residual phase errors, where $\beta(n)$ is the phasefront error and $\hat{\beta}(n)$ is an estimate of $\beta(n)$ created by a phase deaberration algorithm. Similar to the procedures in deriving (12), the

expression for ASF is

$$ASF = \frac{\frac{\gamma}{N} \left[\frac{\sigma_a^2}{(\bar{a})^2} + (1 - |\exp(j\delta\phi)|^2) \right]}{|\exp(j\delta\phi)|^2} \quad (15)$$

$|\exp(j\delta\phi)|$ is less than unity if $\delta\phi \neq 0$. Therefore ASF is greater than $\frac{\gamma}{N} \frac{\sigma_a^2}{(\bar{a})^2}$ when phase correction is not complete. For modest residual phase errors with variance σ_ϕ^2 (15) reduces to

$$ASF = \frac{\gamma}{N} \left[\frac{\sigma_a^2}{(\bar{a})^2} + \sigma_\phi^2 \right] \quad (16)$$

For point source insonification, $\gamma = 1$ and (15) & (16) are same results obtained by Steinberg for the ASF of a phased array subject to amplitude and phase errors in its weights [20].

V. DISCUSSION

One of the potentially attractive features of ultrasound imaging of the breast is the ability of ultrasound to readily distinguish between tumors and cysts. A cyst consists of clear fluid encapsulated in a nearly spherical membrane. Having no tissue within the membrane, no echos result from insonification. Tumors, however, scatter ultrasound and usually appear speckled. Therefore, in principle, the distinction can be readily made in the image.

To achieve this desired condition, however, the average sidelobe level of the system should be the order of -50 dB or lower to ensure that sidelobe energy does not appear within the image of the cyst. In Section II it was shown that for an array of 100 elements the expected sidelobe level is approximately -26 dB. There are three approaches to reduce this level to the -50 dB neighborhood. The first, discussed in the next paragraph, is through transducer design; the second and the third are algorithmic.

The theory was developed for one-way propagation. When applied to echo scanner design, this model implies broad-beam insonification. This design permits the simplest form of adaptive weight control because only the receiving weights need to be controlled. To reduce the sidelobe floor to a useful level, the conventional transducer must be replaced by a 2-D transducer of, say, 100×100 elements. This would drop the floor another 20 dB while preserving the scale of the transducer. The development of 2-D array technology is already underway and such a design can be anticipated in the future.

The second approach is to use an adaptive iterative procedure for the transducer weights so that the transmitting beam pattern and the receiving beam pattern are identical. The result is a squaring of the side radiation pattern or a doubling of the level in decibels. The iterative phase-deaberration procedure developed in [10] belongs to this category and was reported to be successful in liver. This is a highly desirable condition. To work properly, the initial transmitting beam must have a reasonably good pattern; it must have a well defined mainlobe, although its sidelobe radiation pattern can be high. This condition is achieved in a weak scattering medium such as liver, but not in a refractive medium such as breast. Therefore, in the general case of a complicated wavefront resulting from medium distortion, a satisfactory initial transmitting beam may

not be formed and, as a result, the iterative procedure may or may not converge. Recently, Fink *et al.* [26], [27] demonstrated that an iterative time reversal procedure can improve focusing through an inhomogeneous medium when the insonified volume contains a strong reflector. This technique was demonstrated in lithotripsy experiments but it has limited use in breast imaging, as well as in other soft tissue, because strong reflectors are not generally found there. In the cases where a strong reflector can be found, the time reversal procedure also requires a proper initial transmitting beam to ensure that optimal focusing on the reflector can be achieved through iteration. It was shown in [28] and [15] that an initial transmitting beam with a proper mainlobe can be obtained through the use of a phase conjugation algorithm [11] when the normalized wavefront amplitude variance is less than 0.12 or the rms less than 0.35. The time reversal procedure is the generalized version of a phase conjugation algorithm. However, *in vivo* wavefront measurements of the breast [1] show that only 2.8% of the wavefronts satisfy this wavefront amplitude requirement. Therefore optimal focusing on a strong reflector embedded in a breast may or may not be achieved through iteration.

The third approach is to invent stronger algorithms that correct both wavefront amplitude and phase distortions. This is a topic for future research.

The ASF theory is developed for single source insonification. It is also applicable to multiple sources or scatterers, in which one is very large compared to all the rest. The situation is very different in the other extreme in which there is a large number of scatterers, say K , from the same population. In this case each produces a sidelobe background governed by the ASF theory and, as a result, the total background level can grow by as much as a factor of K . The maximum value of K is the order of the number of azimuthal resolution cells in the scanning sector, which differs markedly according to whether the transmitter and receiver beam patterns are different or the same. In the former case, $\Delta\theta_t =$ transmitting beamwidth and $\Delta\theta_r = \lambda/L =$ receiving beamwidth, and let $\Delta\theta_t \ll \Delta\theta_r$. Then $K_{\max} = L\Delta\theta_t/\lambda$. In broadbeam transmission, $\Delta\theta_t$ is nominally the order of one radian, making $K_{\max} \approx L/\lambda$, which in our experiment is approximately 100. By replacing a single source with 100 sources from a common population the background level can increase by 20 dB. A further increase in ASF can be anticipated because complete phase correction can not be assumed in this case and some residual phase errors may be left. One factor works in favor of this case, however, for γ will be approximately unity if no source or scatterer is significantly stronger than any other.

With an adaptive iterative procedure that forces the transmitting and receiving patterns to be the same, $\Delta\theta_t$ is the available angular resolution of the transducer, which is λ/L . In this case $K_{\max} \approx 1$ and the ASF theory developed in this paper again pertains.

VI. SUMMARY

The theory of the rise in the image background level (ASF) as a function of wavefront amplitude distortion is derived for a single source image. From it one can estimate the effect of wavefront amplitude distortion upon the image contrast and

assess the usefulness of known phase deaberration algorithms. It is found that, after phasefront errors are removed, the *ASF* is proportional to the normalized variance of the wavefront amplitude distortion and inversely proportional to the effective number of array elements. In the general distortion case, where strong scattering and refraction may be present, the *ASF* rises to the mid of -20 dB's for a 100-element array. *PSL* is higher still by about 7 dB. These levels are undesirably high. One possible means to reduce the sidelobe level is to develop stronger algorithms that compensate for amplitude as well as phasefront distortion. An alternative means is through the use of a 2-D 100×100 element array, which provides a 100-fold increase in the number of elements and reduces the sidelobe levels to those of the weak scattering case.

When residual phase errors remain following phase deaberration, *ASF* is proportional to the sum of the normalized amplitude variance and the residual phase variance.

REFERENCES

- [1] Q. Zhu, B. D. Steinberg, and R. Arenson, "Wavefront amplitude distortion and image sidelobe levels: Part II—*In vivo* experiments," *IEEE Trans. Ultrason. Ferroelec. Freq. Contr.*, this issue.
- [2] F. S. Foster and J. W. Hunt, "Transmission of ultrasound beams through human tissue—Focusing and attenuation studies," *Ultrasound Med. Biol.*, vol. 3, pp. 257–268, 1979.
- [3] W. J. Davros, E. L. Madsen, and J. A. Zagzebski, "Breast mass detection by US: A phantom study," *Radiology*, vol. 156, pp. 773–775, 1985.
- [4] P. Krammer and D. Hassler, "Measurement of spatial time-of-flight fluctuations of ultrasound pulses passing through inhomogeneous layers," in *Proc. of IEEE Ultrason. Symp.*, 1987, New York, pp. 939–942.
- [5] G. E. Trahey and S. W. Smith, "Properties of acoustical speckle in the presence of phase aberration—Part I: First order statistics," *Ultrasonic Imaging*, vol. 10, pp. 12–28, 1988.
- [6] S. W. Smith, G. E. Trahey, S. M. Hubbard, and R. F. Wagner, "Properties of acoustical speckle in the presence of phase aberration—Part II: Correlation lengths," *Ultrasonic Imaging*, vol. 10, pp. 29–51, 1988.
- [7] M. O'Donnell and S. W. Flax, "Phase aberration measurements in medical ultrasound: human studies," *Ultrasonic Imaging*, vol. 10, pp. 1–11, 1988.
- [8] R. C. Waag and D. Dalecki, "Estimates of wavefront distortion from measurements of scattering by model random media and calf liver," *J. Acoust. Soc. Am.*, vol. 85, no. 1, pp. 406–415, 1989.
- [9] Y. Sumino, and R. C. Waag, "Measurements of ultrasonic pulse arrival time differences produced by abdominal wall specimens," *J. Acoust. Soc. Am.*, vol. 90, no. 6, pp. 2924–2930, 1991.
- [10] S. W. Flax and M. O'Donnell, "Phase aberration correction using signals from point reflectors and diffuse scatterers: Basic principles," *IEEE Trans. Ultrason. Ferroelec. Freq. Contr.*, vol. UFFC-35, pp. 758–767, 1988.
- [11] B. D. Steinberg, "Radar imaging from a distorted array: The radio camera algorithm and experiments," *IEEE Trans. Antennas Prop.*, vol. AP-29, pp. 740–748, 1981.
- [12] E. H. Attia and B. D. Steinberg, "Self-cohering large antenna arrays using the spatial correlation properties of radar clutter," *IEEE Trans. Antennas Prop.*, vol. 37, pp. 30–38, 1989.
- [13] L. Nock, G. E. Trahey, and S. W. Smith, "Phase aberration correction in medical ultrasound using speckle brightness as a quality factor," *J. Acoust. Soc. Am.*, vol. 85, no. 5, pp. 1819–1833, 1989.
- [14] G. E. Trahey, D. Zhao, J. A. Miglin, and S. W. Smith, "Experimental results with a real-time adaptive ultrasonic imaging system for viewing through distorting media," *IEEE Trans. Ultrason. Ferroelec. Freq. Contr.*, vol. 37, pp. 418–427, 1990.
- [15] B. D. Steinberg and H. Subbaram, *Microwave Imaging Techniques*, ch. 8 and 9. New York: Wiley, 1991.
- [16] A. V. Oppenheim and J. S. Lim, "The importance of phase in signals," in *Proc. IEEE*, pp. 529–541, 1981.
- [17] B. D. Steinberg, "A theory of the effect of hard limiting and other distortions upon the quality of microwave images," *IEEE Trans. Acoustics Speech and Sig. Proc.*, vol. ASSP-35, pp. 1462–1472, 1987.
- [18] Q. Zhu and B. D. Steinberg, "Large-transducer measurements of wavefront distortion in the female breast," *Ultrasonic Imaging*, vol. 14, pp. 276–299, 1992.
- [19] Q. Zhu, "Large-Transducer Measurements of Ultrasonic Wavefront Distortion in the Female Breast," Ph.D. Dissertation, Univ. of Pennsylvania, Philadelphia, PA, 1992.
- [20] B. D. Steinberg, *Principles of Aperture and Array System Design*. New York: Wiley, 1976.
- [21] K. H. Bates, "Tolerance analysis for phased arrays," in *Acoustical Imaging* vol. 9, K. Y. Wang, ed. New York: Plenum, 1979, pp. 239–262.
- [22] B. D. Steinberg, *Microwave Imaging with Large Antenna Arrays*, ch. 5. New York: Wiley, 1983.
- [23] L. F. Nock and G. E. Trahey, "Synthetic receive aperture imaging with phase correction for motion and for tissue inhomogeneities: Part I—Basic principles," *IEEE Trans. Ultrason. Ferroelec. Freq. Contr.*, vol. 39, pp. 489–495, 1992.
- [24] G. E. Trahey and L. F. Nock, "Synthetic receive aperture imaging with phase correction for motion and for tissue inhomogeneities: Part II—Effects of and correction for motion," *IEEE Trans. Ultrason. Ferroelec. Freq. Contr.*, vol. 39, pp. 496–501, 1992.
- [25] S. H. Taheri and B. D. Steinberg, "Tolerances in self-cohering antenna arrays of arbitrary geometry," *IEEE Trans. Antennas Prop.*, vol. AP-24, pp. 733–739, 1976.
- [26] M. Fink, "Time reversal of ultrasonic fields: Part I—Basic principles," *IEEE Trans. Ultrason. Ferroelec. Freq. Contr.*, vol. 39, pp. 555–566, 1992.
- [27] F. Wu, J. L. Thomas and M. Fink, "Time reversal of ultrasonic fields: Part II—Experimental results," *IEEE Trans. Ultrason. Ferroelec. Freq. Contr.*, vol. 39, pp. 567–578, 1992.
- [28] J. Halat, "A Survey of Image-Embedded Passive Beamforming Sources for a Radio Camera," Masters Thesis, The Moore School of Electrical Engineering, Univ. of Pennsylvania, Philadelphia, PA, 1985.
- [29] Q. Zhu and B. D. Steinberg, "Wavefront amplitude distribution of the female breast," *J. Acoust. Soc. Am.*, to be published.



Qing Zhu (S'91–M'92) received the B.S. degree in applied mathematics in 1983 from Northern Jiao-Tong University, Beijing, China, the M.S. degree in biomedical engineering in 1987 from the Chinese Academy of Medical Sciences, and the Ph.D. degree in bioengineering in August 1992 from the University of Pennsylvania.

She is currently a postdoctoral fellow in the electrical engineering department of the University of Pennsylvania. Her research interests are wave propagation in inhomogeneous medium, high-resolution ultrasonic imaging, design of shaped transducers, phase aberration correction, digital beamforming, and adaptive signal processing.



Bernard D. Steinberg (S'48–A'50–SM'64–F'66–LF'90) received the B.E. and M.S. degrees from Massachusetts Institute of Technology, Cambridge, MA, and the Ph.D. degree from the University of Pennsylvania, Philadelphia, PA, all in electrical engineering.

He was co-founder and vice president of research and engineering of General Atronics Corporation, now a division of Magnavox. He is co-founder and chairman emeritus of the board of Interspec, Inc., Philadelphia, PA, a company specializing in sophisticated signal processing for radar and sonar, and making ultrasonic imaging equipment for cardiologists. He is a professor of electrical engineering and director of the Valley Forge Research Center, University of Pennsylvania, Philadelphia, PA. The primary research of the laboratory is in high resolution microwave and ultrasound imaging based on adaptive self-calibration of distorted measurements of radiation fields. The measurement arrays may be real, synthetic, or combinations of both. He is the authors of two books in this field: *Principles of Aperture and Array System Design: Including Random and Adaptive Arrays* (Wiley, 1976), and *Microwave Imaging with Large Antenna Arrays: Radio Camera Principles and Techniques* (Wiley, 1983), and co-author of *Microwave Imaging Techniques* (Wiley, 1991).

Dr. Steinberg is a member of URSI, Commission B (Fields and Waves), Sigma Xi, and AAAS, and is a Distinguished Lecturer of the IEEE Antennas and Propagation Society.

Wavefront Amplitude Distortion and Image Sidelobe Levels: Part II—*In Vivo* Experiments

Qing Zhu, *Member, IEEE*, Bernard D. Steinberg, *Life Fellow, IEEE*, and Ronald L. Arenson

Abstract—The theoretical relationship between the average sidelobe floor (*ASF*) in the image and the medium-induced amplitude variance of the wavefront was developed in the companion paper [1]. This paper describes *in vivo* measurements of the rise of the sidelobe level in a single-source image obtained through the female breast as a function of the distortion of the wavefront amplitude. The measured sidelobe levels are the *ASF* and the peak sidelobe level (*PSL*). The *ASF* is shown to be proportional to the variance of the modulus of the wavefront normalized to the square of its mean value, with a proportionality constant close to the value predicted by theory. The *PSL* similarly increases linearly. The average ratio of *PSL* to *ASF* is 5 (7 dB).

I. INTRODUCTION

PHASEFRONT deaberration algorithms [2]–[9] correct phase errors in the wavefront but not wavefront amplitude distortion. Amplitude distortion increases the sidelobe level in the image. Given the sidelobe specifications for a scanner, the *ASF* theory of the companion paper [1] and measurements of *ASF* and *PSL* reported in this paper disclose the tolerable level of wavefront amplitude distortion such that the sidelobes will not exceed design limits. In the experiments reported, the phasefront errors are removed by using the spatial correlation algorithm (SCA) [3], [5], [8] or the dominant scatterer algorithm (DSA) [2], both developed at the Valley Forge Research Center (VFRC). The correlation-based algorithm described in [4] is easily shown to have the same basis as the SCA.

The following section describes the experimental methods. Section III shows the experimental results. Discussion and conclusion are in Sections IV and V.

II. EXPERIMENTAL METHODS

The experiment was designed to measure the wavefront radiating from a single source through a distorting medium and to image the source after applying either the SCA or the DSA phase deaberration algorithm to correct the phasefront distortion. The quantities measured were the normalized amplitude variance of the wavefront and the *ASF* and *PSL* in the image. The female breast was chosen for the propagation

medium, one reason being that it was possible to introduce a source on one side of the breast and to measure the distorted wavefront from the opposing side.

Part A describes *in vivo* wavefront measurement and near-field focusing of the wavefront. Part B discusses phasefront deaberration and the sidelobe measurement in the image following phase-deaberration of the wavefront measurements. Part C describes measurement of the wavefront amplitude distortion.

A. Wavefront Measurement and Near-Field Focusing of Wavefront

1. Wavefront Measurement: Fig. 1 illustrates the *in vivo* experiment. A single source (a transducer element in the transmitting array) radiates ultrasonic waves to a linear array at a distance of 120 mm. The transmitting frequency was 3 MHz. The width of the source T was 1.49 mm. The ratio $\lambda/T = 1/3$, implying that the beamwidth was approximately $1/3$ radian. The active receiving aperture was 96 mm with 64 elements. The element spacing was 1.5 mm. The height of the element was 10 mm. Transmission was a sequence of 64, 16- μ s pulses spaced by 200 μ s. Reception across the entire aperture was by synthetic aperture: Each of 64 adjacent receiving elements received and stored one of the transmissions. At each receiving element, the received RF pulses, after propagating through the medium, were coherently demodulated by multiplication with an internal oscillator. The analog in phase and quadrature values were measured relative to the transmitted pulse and integrated for 18 μ s. The analog data were digitized by using two high speed 8-bit A/D converters (MAX-150 IC's). In this way the complex wavefront across the receiving aperture was measured. A total of 64 complex values is called a single source profile (SSP). The total data acquisition time for one SSP was 0.0128 s. The long receiving window (18 μ s) was used to match the long transmitted pulse. Thus the overall frequency response of the transmitter and the receiver was about 60 kHz. The narrowband waveform was employed to avoid a possible frequency selective effect upon wavefront distortion¹

A distorting medium, a female breast, was inserted into the reservoir between the source and the array. A liquid path assembly was chosen because of the huge transducer assembly employed and the difficulty to keep good contact between the

Manuscript received October 19, 1992; revised March 31, 1993; accepted April 1, 1993. This work was supported by the Commonwealth of Pennsylvania, Interspec, Inc., Ambler, PA, and by the National Science Foundation under Grant BCS92-09680.

Q. Zhu and B. D. Steinberg are with the Valley Forge Research Center, The Moore School of Electrical Engineering, University of Pennsylvania, Philadelphia, PA 19104-6390.

R. L. Arenson was with the Department of Radiology, University of Pennsylvania, Philadelphia, PA. He is now with the Department of Radiology of the University of California, San Francisco, CA 94143-0628.

IEEE Log Number 9209832.

¹Wideband measurements were also made to test the effect of bandwidth upon the complexity of the wavefront. Discussion of the comparison between the results is deferred to Section IV A, so as not to break the continuity of the discussion of the *in vivo* measurement procedure.

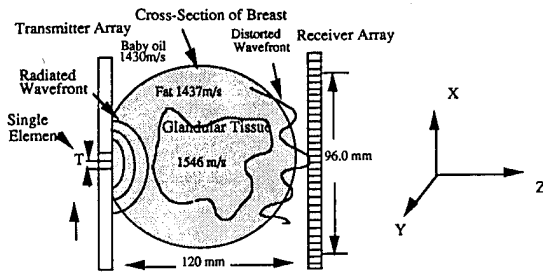


Fig. 1. Wavefront distortion measurement with single source insonification. Z is the wave propagation direction, X is the transducer direction and Y is perpendicular to X and Z .

linear transducers and the cylindrically shaped breast. Johnson and Johnson baby oil filled the reservoir. This oil, which reportedly has a sound speed of 1430 m/s [10], was used to match the speed of sound of subcutaneous fat (1440 m/s) and consequently to reduce refraction at the skin surface. The SSP through oil alone was also taken for each experiment for system calibration and focusing purposes.

Because the beamwidth of the source is about $1/3$ radian, the measured wavefront is primarily confined within this angular sector. To study the wavefront distortion properties through various angular sectors, several transmitter elements located in the middle of the transmitting array were used in sequence. A stepping motor moved the transducer assembly up and down in the elevation direction (Y in Fig. 1, which is toward and away from the chest wall of the volunteer). The intervals were either $1/2$ cm or 1 cm. By sequencing the transmitting sources at each elevation level, a large volume of breast was insonified.

Twenty-two subjects (44 breasts) were selected from 43 volunteers measured at the Hospital of the University of Pennsylvania (HUP). Fourteen were premenopausal women and eight were postmenopausal. These 44 breasts were large both in length and in cross section to ensure good contact between transducers and tissue. This choice reduced refraction due to breast curvature. For each breast, 27–45 SSP's were selected from several elevation levels close to the chest wall. A total of 1708 SSP's were obtained.

2. Near-Field Focusing of the Wavefront: In our experiment, the source was located in the near field of the receiving array and a focusing vector w_f was applied to each of the measured SSP's both through oil and tissue. For each SSP w_f is chosen as the conjugate of the phase profile measured through oil. As a result, w_f contains the near-field geometry of the source relative to the receiving array, as well as system errors which arise from geometrical and electrical errors in array elements and circuitry. w_f is then applied to the SSP's obtained both through oil and tissue. The corrected SSP is denoted FSSP; it is focused and also free of all system errors. The images of the source obtained through oil and tissue are the Fourier transforms of the corresponding FSSP's [1].

Fig. 2(a) and (b) show examples of measured wavefronts obtained through oil and tissue. Fig. 2(a) shows measured amplitude profiles, i.e., moduli of wavefronts, through oil (dashed) and through tissue (solid). The amplitude profile through oil is smooth and shows the expected diffraction pattern of the transducer element, while the amplitude profile

through tissue is jagged and has nulls in the high energy region that are likely due to phase cancellations. Fig. 2(b) shows phase profiles, unwrapped in the middle, measured through oil (dashed) and through tissue (solid). The phase profile obtained through oil reflects the near-field curvature of the transmitter relative to the receiving array, while the phase profile through tissue contains two linear components, one to each side of center, superimposed on the near-field curvature and perturbations. These linear-phase steering factors cause two lobes to appear in the image (Fig. 2(e) solid). The steering factors are caused by refraction at interfaces of different types of tissue with different speeds of sound. Focusing the array through oil or tissue involves subtracting the oil phase (dashed) from the corresponding SSP. The tissue FSSP that results has the amplitude profile of Fig. 2(a) (solid) and a phase profile equal to the difference between the curves of Fig. 2(b). This difference is denoted as $\beta(n)$. It is due to the intervening tissue and is largely corrected by the SCA or the DSA. $\beta(n)$ is shown in Fig. 2(c).

B. Phasefront Correction and Sidelobe Measurement in the Image of Phase-Deaberrated Data

To separately measure the effect of amplitude distortion upon the image sidelobe level, the phasefront errors are first removed. Phasefront deaberration of each FSSP through tissue is accomplished by the SCA [3], [5], [8] and/or the DSA [2]. Both give substantially the same result.

SCA: Following the notation introduced in [1], the complex radiation field sampled at the n th element, after propagation of the wavefront through tissue and corrected for near-field curvature, is

$$i(n) = \alpha v(n)m(n) = \alpha v(n)a(n) \exp(j\beta(n)). \quad (1)$$

$v(n)$ is the sampled radiation field at the n th element, after propagation of wavefront through oil and corrected for near-field curvature, i.e., it is the FSSP through oil. $m(n)$ is the medium-induced wavefront distortion with amplitude $a(n)$ and phase $\beta(n)$, and α is a constant to reflect any signal loss. $i(n)$ is in error because of the wavefront distortion $m(n)$. The components of the proper phase compensation are $w_c(n) = \exp(-j\beta(n))$. The SCA captures the phase distortion information from the spatial correlation information and discloses the $\beta(n)$ to solve the phase aberration problem (the procedure is described in more detail in Appendix A). Note that phase aberration correction alone does not compensate for the amplitude distortion $a(n)$.

DSA: The phase compensation vector $w_c(n)$ derived from the DSA is the phase conjugate of $\alpha v(n)m(n)$, which is exactly $\exp(-j\beta(n))$. The compensation is perfect for a wavefront derived from a point source.

Fig. 2(d) shows the phase profiles after the SCA (solid) and the DSA (zero) are applied to the $\beta(n)$ in Fig. 2(c), which is the phase error caused by tissue. The profiles in Fig. 2(d) are constant. Fig. 2(e) shows the images obtained through oil (dashed) and through tissue (solid) prior to phase aberration correction. The images obtained through tissue after both SCA and DSA correction are shown in Fig. 2(f). Both

TABLE I
SIDELobe LEVELS OF IMAGE OF SINGLE TRANSDUCER.

Propagation Medium	Phase Aberration Correction	ASF	PSL
Oil	None	-37.4 dB	-31.3 dB
Tissue	None	-9.6 dB	-2.4 dB
Tissue	SCA or DSA	-19.8 dB	-15.2 dB

images are the same. In Fig. 2(e) and (f), the abscissa is the lateral distance in the transmitting array centered at the source position. The image through oil shows the expected diffraction pattern of the transducer element convolved with the radiation pattern of the receiving array [1]. Sidelobes are very small. The PSL is -31.3 dB and the ASF is -37.4 dB. The ASF is measured outside of the mainlobe region. These sidelobe levels are typical of images obtained through oil. The image through tissue, which is the Fourier transform of the amplitude profile (solid) in Fig. 2(a) and the phase difference of Fig. 2(c), shows multiple lobe artifacts which we believe were primarily caused by refraction [11]. PSL and ASF are -2.4 and -9.6 dB, respectively. The SCA and the DSA corrected images are Fourier transforms of the amplitude profile (solid) in Fig. 2(a) and the phase deaberrated profiles in Fig. 2(d). The images after the SCA or the DSA correction are improved significantly but the sidelobes are very high. In this case the PSL is -15.2 dB and the ASF is -19.8 dB. Because all phase errors have been corrected, these high sidelobe levels are due to the amplitude distortion of the wavefront². Table I lists these sidelobe levels.

Occasionally, the SCA-corrected phase profile differs from a constant because a random phase discontinuity sometimes occurs within either one or both low energy portions indicated by the outer arrows in Fig. 2(a). However, such a phase discontinuity does not significantly affect image quality because the low amplitude values in the two regions contribute little to the image.

Among 1708 SCA-deaberrated phase profiles, 92% of them were constant and 8% of them had a discontinuity in either one or both of the two low energy portions, the fact that the overwhelming majority of the SCA-corrected phase profiles were constant indicates that the SCA provided complete compensation down to the level of measurement of the system. Thus the SCA deaberration is highly successful and, except for the 8% that had phase discontinuities, gives almost the same results as the DSA. Since the SCA is the more general algorithm, the SCA was applied to the FSSP's in the experiment. Sidelobe levels in the image after SCA correction are presented in this paper.

C. Wavefront Amplitude Distortion Measurement

The normalized variance of the amplitude distortion of wavefronts through tissue was calculated as follows. The

²Fig. 2(d) shows that all phase errors have been corrected down to the quantization level of the 8-bit measurement system. The residual phase error σ_ϕ^2 , therefore, was lower than -43 dB. The ASF induced by a residual phase error is $\gamma\sigma_\phi^2/N$ [1]. In this experiment $N/\gamma \approx 30$. Thus the ASF was not larger than -58 dB.

measured amplitude profiles through oil and tissue are $v(n)$ (shown dashed in Fig. 2(a)) and $\sqrt{c}v_a(n)$ (solid), where $v_a(n) = \alpha v(n)a(n)$ is the measured profile through tissue and c is an energy normalizing constant to account for energy loss in the tissue. c is given by

$$c = \frac{\sum_{n=1}^N v^2(n)}{\sum_{n=1}^N v_a^2(n)},$$

which normalizes the profile for all energy loss including that caused by out-of-plane refraction. N is the total number of receiving array elements. $\sqrt{c}v_a(n)$ is the scaled amplitude profile obtained through tissue. In (1), the wavefront distortion is modeled as a multiplicative processes $m(n)$ with modulus $a(n)$. The theory derived in [1] relates the ASF in the phase corrected image and the normalized variance of $a(n)$, denoted $\sigma_a^2/(\bar{a})^2$. The relation is

$$ASF = \frac{\gamma}{N} \frac{\sigma_a^2}{(\bar{a})^2} \quad (2)$$

where γ is the ratio of the average power to the square of absolute average value of the radiation pattern of the transmitting element and N , as before, is the total number of array elements. In our experiment, the average value of γ was 2.21 with a small standard deviation of 0.043.

It is shown in Appendix B that $\sigma_a^2/(\bar{a})^2$ can be related to $v(n)$, $\sqrt{c}v_a(n)$, and \sqrt{c} by

$$\frac{\sigma_a^2}{(\bar{a})^2} = E \left(\frac{\sum_{n=1}^N \{\sqrt{c}v_a(n) - v(n)\}^2}{\sum_{n=1}^N v^2(n)} \right) \quad (3)$$

where $E(\cdot)$ means expected value. By combining these expressions we can calculate the predicted ASF from wavefront measurements and compare the prediction with direct ASF measurements from the images.

The derivation of (2) involves three conditions/assumptions: (1) single source; (2) phasefront errors are corrected by a phase deaberration algorithm; (3) wavefront amplitude samples $a(n)$, $n = 1, 2, \dots, N$, are statistically uncorrelated random variables with the same pdf. The first-condition is satisfied in our experiment. The second condition was also satisfied in the experiment, as reported in part B of this section, and the third one was validated experimentally as shown in Appendix C.

III. EXPERIMENTAL RESULTS

A. Measured ASF in the Image versus $\hat{\sigma}^2$ of the Wavefront

Twenty-seven to forty-five FSSP's with SCA-deaberrated phasefronts were measured in each breast and their images were formed. The ASF in each image was measured outside the main lobe region. Sample values of (3) were calculated and multiplied by γ/N , where $\gamma = 2.21$ was used. The product is denoted $\hat{\sigma}^2$, which according to (2), should equal ASF.

TABLE II
SINGLE-SOURCE IMAGE, SIDELobe LEVEL COMPARISONS
FOR PROPAGATION THROUGH OIL AND THROUGH BREAST

Propagation Medium	ASF	PSL
Oil	-37.4 dB	-31.3 dB
Breast ID#40L	-20.46 dB	-13.59 dB

Fig. 3 shows an example of measured ASF versus $\hat{\sigma}^2$ obtained from breast ID#40L. The abscissa is $\hat{\sigma}^2$ and the ordinate is the measured ASF . Both variables are linearly related with a very small intercept 0.0005, a close to unity slope 1.15, a correlation coefficient 0.66, which is far beyond the critical value for a 1% level of significance of the corresponding sample size, which indicates that the linear relationship between the two variables is statistically significant, and a small standard deviation from the regression line 0.0019. The range of ASF is from -26.20 to -17.67 dB with mean -20.46 dB, which is 16.9 dB higher than the ASF obtained through oil (see Table II). The corresponding range of amplitude distortion (3) is from 0.10 to 0.39.

Data on the entire population of 44 breasts are given in [12]. The slopes are all in the neighborhood of unity with mean 0.97 and standard deviation 0.30, intercepts are close to zero with mean 0.068×10^{-3} and standard deviation 2.5×10^{-3} , and the correlation coefficients are beyond the critical values for a 1% level of significance in 73% of the breasts and greater than critical values for a 5% level in 89% of the breasts. The standard deviations from the regression lines are exceedingly small with average 0.002 and standard deviation 7.2×10^{-4} .

The data were separated into two subpopulations, one for the premenopausal group and another for the postmenopausal group. The average ages of pre- and postmenopausal groups are 44 and 57 years, respectively. Fig. 4 shows these two data sets of ASF versus $\hat{\sigma}^2$. The equations for the linear best fits are

$$\text{Premenopausal } ASF = 5.29 \times 10^{-4} + 0.93\hat{\sigma}^2 \quad (4)$$

$$\text{Postmenopausal } ASF = 1.006 \times 10^{-3} + 0.86\hat{\sigma}^2. \quad (5)$$

The slopes are close to unity as the theory predicted. The correlation coefficients are 0.52 and 0.45 for the premenopausal group and the postmenopausal group, respectively. The critical values are in the neighborhood of 0.1 for the sample sizes used. Thus the linear relationship between the two variables is statistically significant in each group. Both intercepts approximate zero as they should. The mean differences between the measured ASF 's and the regression lines are 5.03×10^{-7} and 5.72×10^{-8} , with 0.0026 and 0.0033 standard deviations for the premenopausal and postmenopausal groups, respectively. (It is interesting to note that the spread of points is considerably narrower in the premenopausal group than in the postmenopausal group. Partial correlation of the amplitude of the wavefront $a(n)$ is shown in [12] to be a possible cause of this phenomenon.)

For the two experimental curves, the intercepts are negligible and the slopes are not significantly different. Therefore $ASF = 0.9\hat{\sigma}^2$ can be used to represent the experimental relationship between these two variables.

B. Measured PSL in the Image versus $\hat{\sigma}^2$ of the Wavefront

PSL 's were also measured in the SCA-deaberrated images obtained from each breast. Fig. 5 shows an example of PSL versus $\hat{\sigma}^2$ obtained from breast ID#40L. The abscissa is $\hat{\sigma}^2$ and the ordinate is PSL . The two variables are linearly related with a slope of 6.37, a correlation coefficient of 0.41 (critical value is 0.372 for a 1% level of significance) and a small standard deviation of 0.0173 from the regression line. The range of PSL is from -19.07 to -9.41 dB with the average -13.59 dB, which is 17.7 dB higher than the PSL obtained through oil (see Table II).

For the 44 breasts measured, the standard deviation from the corresponding regression line is small with average 0.0196 and standard deviation 0.0076 and the correlation coefficient is larger than the corresponding critical values for a 5% level of significance in 66% of the breasts.

Two composite data sets are shown in Fig. 6. Fig. 6(a) is obtained from the premenopausal group and Fig. 6(b) from the postmenopausal group. The correlation coefficients of two variables are 0.37 and 0.23, respectively, which are well above critical values for a 1% level of significance of for the corresponding sample sizes. The mean differences between the measured PSL 's and the regression lines are 1.323×10^{-7} and 2.32×10^{-8} with 0.0213 and 0.0263 standard deviations, respectively, which are very small. The experimental equations for the linear best fits are

$$\text{Premenopausal } PSL = -7.03 \times 10^{-3} + 5.54\hat{\sigma}^2 \quad (6)$$

$$\text{Postmenopausal } PSL = 4.22 \times 10^{-3} + 4.22\hat{\sigma}^2. \quad (7)$$

The ratios of the slopes of PSL over ASF are 5.93 and 4.89 for the pre- and postmenopausal groups, respectively. Thus, on the average, the PSL is larger than the ASF by a factor of 5, or 7 dB.

C. Tolerance to Wavefront Amplitude Distortion

Given a design requirement on the sidelobe level the tolerance to wavefront amplitude distortion can be obtained from the experimentally verified ASF theory of [1] and the experimentally determined average ratio of PSL to ASF . For example, assume that the specification is -30 dB with 90% confidence (meaning that PSL must be no larger than -30 dB in 90% of the population). The ASF must be 7 dB smaller, or -37 dB, which is a factor of 2×10^{-4} . The allowed normalized amplitude variance is $\sigma_a^2/(\bar{a})^2 \times 10^{-4}$ divided by γ/N , which is 0.0058 for a 64-element phased array and $\gamma = 2.21$. Fig. 7 is the histogram of $\sigma_a^2/(\bar{a})^2$ obtained from the 44 breasts (both pre- and postmenopausal). The lowest measured variance is about 0.1 and, therefore no sample point is below 0.0058. If γ could be reduced to unity this value would rise only to 0.0128. Thus, for no member of this population can the sidelobe requirement be satisfied. Either the number of elements N

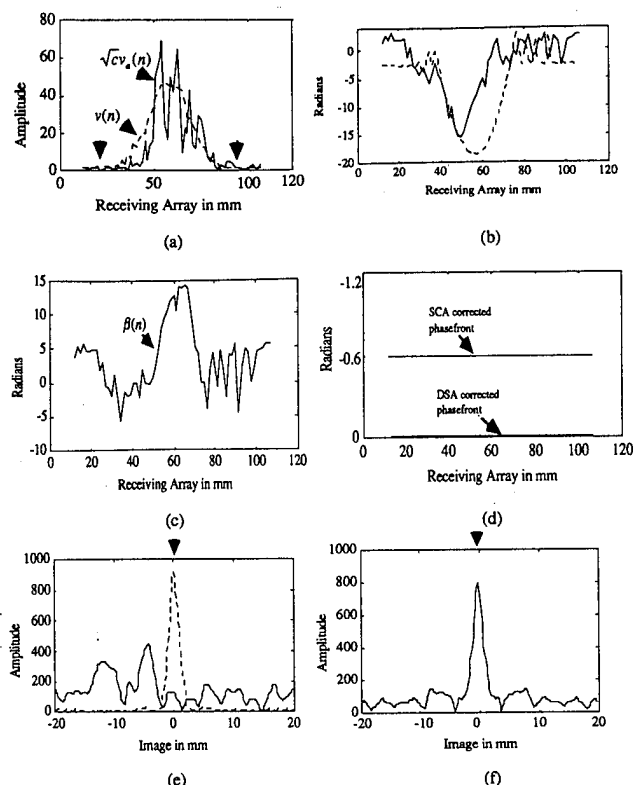


Fig. 2. An example of SCA and DSA phase correction. 9.6-cm receiving array, 3-MHz transmitting frequency. (a) Received amplitude profiles through oil (dashed) and the breast ID#46R. (b) Unwrapped phase profiles received through oil (dashed) and tissue (solid). (c) Phase difference between the curves of (b). (d) SCA (solid) and DSA (zero profile) corrected phase profiles. (e) Source image through oil (dashed) and through tissue (solid) without phasefront correction. (f) Images through tissue with SCA and DSA corrections (solid). SCA and DSA corrected images are the same.

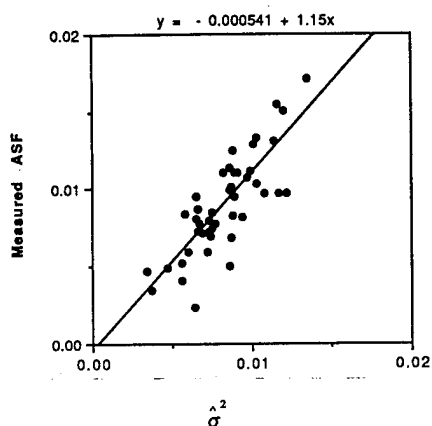


Fig. 3. Measured ASF in image versus σ^2 of wavefront. The ASF is the angular power level in the single-source image outside the mainlobe. The propagation medium is the left breast of a 38-year-old woman. Sample size is 45. Slope of regression line is 1.15. Theoretical slope is unity. Mean slope for 44 breasts is 0.97.

must be increased by more than an order of magnitude, or the wavefront amplitude distortion must be corrected.

Solving the problem by increasing the number of elements is very costly. From Fig. 7 it is seen that about 90% of the population falls below an abscissa value of 0.4. Based on (2) the required number of elements is about 4000. To deal with such a large number of elements, a large number of parallel

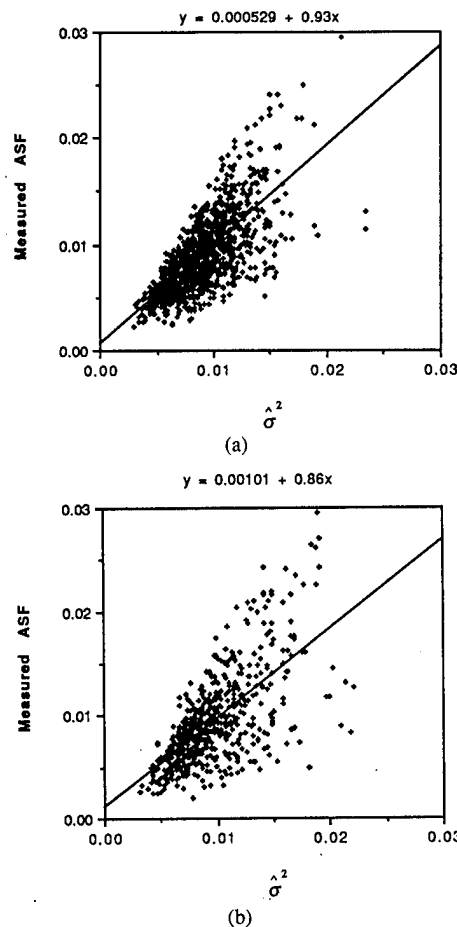


Fig. 4. Measured ASF in image versus σ^2 of wavefront. (a) Data set and the linear best fit obtained from premenopausal group. Sample size is 1134. (b) Data set and the linear best fit obtained from postmenopausal group. Sample size is 574.

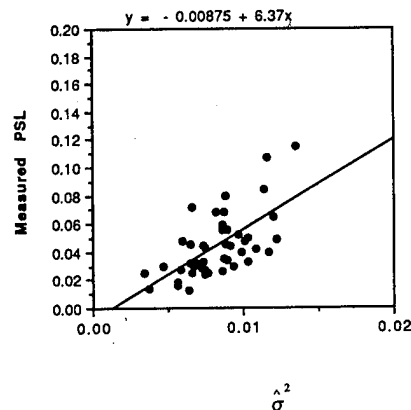


Fig. 5. Measured PSL in image versus σ^2 of wavefront. The propagation medium is the left breast of a 38-year-old woman. Sample size is 45.

channels is required for a real time imaging system. State-of-the-art phased arrays currently have 128 channels. Increasing this number by a factor of 30 may not be practical or affordable with current techniques. The synthetic aperture technique may provide a possible means, but subject motion and degraded performance of phase aberration correction have to be taken into account. 2-D array design is a way to preserve the scale of the transducer while increasing the number of elements to

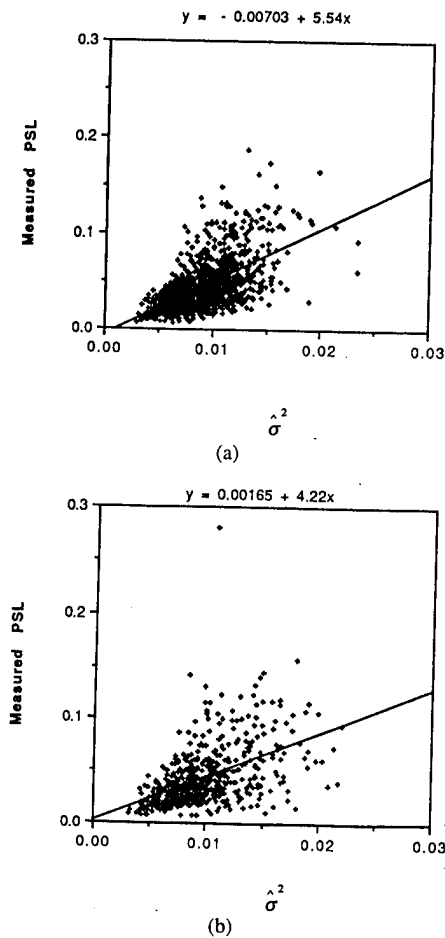


Fig. 6. Measured PSL in image versus σ_a^2 of wavefront. (a) Data set and the linear best fit obtained from premenopausal group. Sample size is 1134. (b) Data set and the linear best fit obtained from postmenopausal group. Sample size is 574.

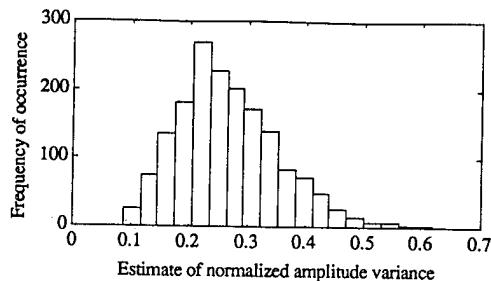


Fig. 7. Histogram of normalized amplitude variances $\sigma_a^2 / (\bar{a})^2$ obtained from 44 breasts. The sample size is 1708.

several thousand. With the scale preserved, γ would be close to unity and the ASF and PSL could be reduced to the desired levels.

Fig. 8 shows ASF and PSL histograms of the measured data obtained from the 44 breasts. The range of ASF measurement is between -27 and -15 dB with an average of -20.8 dB. The range of PSL is between -22 and -5 dB with an average of -14.41 dB. If γ would be reduced to unity these values would improve by only 3.44 dB. Thus neither sidelobe specification in the example above would be satisfied.

Fig. 9 plots the tolerable level of amplitude distortion (solid) against the sidelobe specifications, and the fraction

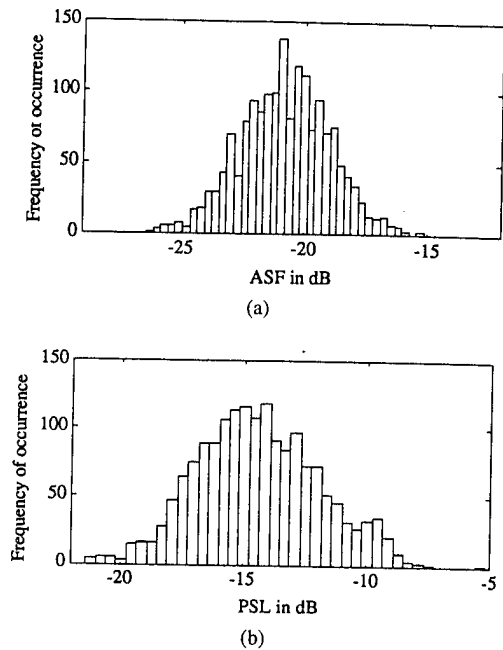


Fig. 8. Histograms of sidelobe levels. The sample size is 1708 obtained from 44 breasts. (a) Histogram of ASF . (b) Histogram of PSL .

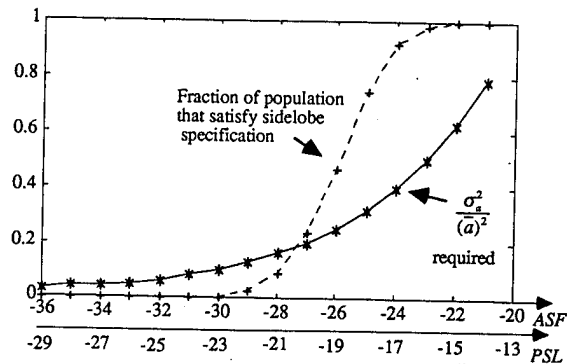


Fig. 9. Abscissa is sidelobe specifications. Ordinates are tolerable level of amplitude distortion (solid) and fraction of population (dashed) that satisfy the specifications. $N = 100$. $\gamma = 1$. Ideal case.

of the population (dashed) that satisfy the specifications. $\gamma = 1$ is assumed. $N = 100$. This is an idealized case based on complete phasefront aberration correction of an ideal point source. In pulse-echo imaging where diffuse scatterers dominate the scene, no complete phase correction can be expected. Residual phase errors will contribute to the sidelobe levels [1] and therefore lower the tolerable levels of amplitude distortion below those shown in the figure.

IV. DISCUSSION

A. Narrowband versus Wideband Waveforms

The bandwidth of the transmitted signal was very narrow (about 60 kHz; the pulse duration was $16 \mu s$) so as to avoid possible frequency selective effects (e.g., absorption of energy by tissue) upon wavefront distortion. During the course of the work it was found that severe amplitude errors exist in the wavefronts, in addition to phasefront errors, as are reported in this paper. Refraction has been shown to be a likely cause of such amplitude distortion [11]. Refraction can induce multiple

arrivals at the receiving aperture via beam bending and beam splitting and overlapping of the beams. It is possible that these multipath arrivals would be separated in time by short pulse, echo scanning, if it were employed. If this were the case we would expect to experience less amplitude distortion with a short pulse than with the 16- μ s pulse. This hypothesis was tested with a 1- μ s short pulse and 1- μ s receiving window (about 1 MHz bandwidth).

Similar to the narrowband case, severe amplitude distortion of the wavefront was observed in each 1- μ s receiving windows in which significant energy was received [12], [13]. No significant late arrivals were found in most subjects. This suggests that multipaths or multiple arrivals developed due to refraction are already established within a 1- μ s period (approximately 3 wavelengths at 3 MHz) and are not significantly separated in time. Therefore the long pulse and the long receiving window used for the main experiment did not significantly increase the amplitude distortion reported in this paper.

B. 1-D versus 2-D

Our measurements are one dimensional (X , in Fig. 1) while the wavefront distortions are in two dimensions (X and Y , both normal to Z). A narrow beam formed by a 2-D aperture would reject some of the energy arriving from outside the (X , Z) plane. The result would be less wavefront interference and, very likely, the wavefront amplitude variation would be smaller than that reported in this paper. This matter needs to be explored experimentally.

C. Element Spacing

In our experimental system, each transducer element consists of six equally spaced subelements which are electrically connected. The width of each subelement is 0.183 mm and the center to center spacing is 0.249 mm, which is about $\lambda/2$ at the 3 MHz operating frequency. As a result, each measured wavefront sample at the receiving array is the complex sum of six wavefronts samples. If the subelements could have been sampled directly, we would have been able to observe the complicated wavefront more closely.

Two questions arise regarding element spacing. The first is the effect of closer spacing upon SCA performance; the second is the effect upon the measurements of the amplitude distortion of the waveform.

1. SCA Performance: Two factors dominate SCA performance, stability of the crossproduct measurement and the number of transducer elements. It is evident from Section II B that the residual phase errors with the large transducer element were below the level of observation of the measuring system; finer sampling could improve it only to a minor extent. The major factor is the increased number of elements required to maintain the same size array, which in this case is a factor of 6. The maximum reduction in *ASF* would be 8 dB. However, it is likely that the $a(n)$ will be correlated to some extent in several portions of the receiving array if $\lambda/2$ spacing is employed; the result will be an improvement in *ASF* of somewhat less than 8 dB.

2. Amplitude Distortion: Some unknown amount distortion can be attributed to the coherent sum of six subelement

samples. With finer sampling, we could anticipate slightly smoother wavefronts and less distortion. A severe test on the increase in mean square amplitude distortion measurement error is found by considering a wavefront $1 + \exp(jkxu_1)$ which is formed from the sum of two equal amplitude plane waves whose arrival directions are spaced by u_1 . The modulus is $2|\cos(kxu_1/2)|$. The mean square measurement error is defined as

$$\text{MSE} = \frac{1}{64 \times 6} \sum_{n=1}^{N=64} \left\{ \sum_{p=0}^{p=5} \left| 2 \cos(k(6n+p)du_1) \right| - \frac{1}{6} \left| \sum_{m=0}^{m=5} (1 + \exp(j(6n+m)du_1)) \right| \right\}^2$$

where where n is the number of the element and d is the interelement spacing = $\lambda/2 \approx 0.25$ mm at 3 MHz and $N = 96 \text{ mm}/6d = 64$. The inner right hand sum is the element measurement. The difference between it (after scaling by the number of its subelements per element) and a field sample at $\lambda/2$ spacing is the error. The squared error is summed over the six subelement positions ($p = 0, \dots, 5$) and this partial sum is summed over the 64 positions in the array. After averaging, the result is the mean square measurement error.

The measurement error grows with u_1 . The largest separation of apparent arrival angle observed in our experiment is approximately the order of 0.1 radian. Using $u_1 = 0.1$, it is found that the error is 0.12. The error normalized to the square of the mean amplitude is 0.08. Therefore, the measured normalized amplitude variance shown in Fig. 7 would be reduced by 0.08 at most if the transducer were sampled at $\lambda/2$ spacing. The *ASF* would improve 1.5 dB at most.

V. CONCLUSION

Experimental results show that the *PSL* and *ASF* in the image are linearly related to the normalized amplitude variance of the wavefront. The *ASF* measurements are consistent with the theory developed in the companion paper. The average ratio of *PSL* to *ASF* is about 5, which implies that on the average the *PSL* is 7 dB higher than the *ASF*. Given design requirements on the sidelobe levels, a tolerable threshold to wavefront amplitude distortion can now be determined.

Experimental SCA results also show complete correction of phasefront errors from a strong point-like source down to the measurement level of the system, which was -43 dB. Amplitude errors remain, however, and are responsible for the high sidelobe level. The average *PSL* in 1708 images obtained from 44 breasts, after SCA correction, is -14.41 dB with 2.51 dB standard deviation. This value is 16.9 dB higher than the *PSL* obtained through oil. The average *ASF* is -20.8 dB with 1.84 dB standard deviation which is 16.6 dB higher than the level obtained through oil. These sidelobe levels are too high to be useful. Furthermore, in pulse-echo imaging where diffuse scatterers dominate the scene, no complete phase correction can be expected. Therefore the *PSL* and the *ASF*, even after SCA correction, will be worse than the situation described here. Therefore, amplitude distortion as well as phasefront distortion must be compensated in future algorithmic design.

Increasing the number of the array elements reduces the sidelobe level proportionally. However, the measured sidelobe levels reported in this paper show that the number of the array elements has to be several thousands to ensure a high dynamic range and high image contrast. While this is beyond the scope of current technology, 2-D array designs will be available in the future that could increase the number of elements sufficiently to satisfy sidelobe design requirements.

APPENDIX A

The following procedure describes the application of the SCA to the single source experimental data measured through breast, for the purpose of correcting phasefront errors.

From (1), the estimate of the lag 1 differential phase error at the n th element is the argument of the adjacent cross product

$$\begin{aligned}\hat{r}_n[1] &= i(n)i^*(n+1) \\ &= \alpha^2 v(n)m(n)v^*(n+1)m^*(n+1) \\ &= \alpha^2 v(n)v^*(n+1)a(n)a(n+1) \\ &\quad \cdot \exp(j(\beta(n) - \beta(n+1))).\end{aligned}\quad (8)$$

$v(n)$ is the radiation profile of the source, after correcting for near-field curvature, measured at the receiving array through homogeneous oil. $m(n)$ is the medium-induced wavefront distortion with amplitude $a(n)$ and phase $\beta(n)$, and α is a constant that reflects any signal loss. In general, $v(n)$ has a constant phase profile because the wavefront of a single point-like source located at the focal zone, propagating through a homogeneous medium, and normal to the receiving array is approximately a plane wave. Therefore, $v(n)v^*(n+1)$ is real. α and a also are real. Thus the argument of the measured value $\hat{r}_n[1]$ is the estimate of the phase error difference between adjacent receiving elements.

To estimate the phase error, we choose some element (say, k) as a reference element, meaning that we set $\beta(k) = 0$. The estimated values of the phase errors are $\hat{\beta}(n+1) = \hat{\beta}(n) - \arg \hat{r}_n[1]$ for $n \geq k$ and $\hat{\beta}(n) = \hat{\beta}(n+1) + \arg \hat{r}_n[1]$ for $n < k$. The n th component of the correction vector is $w_c(n) = \exp(-j\hat{\beta}(n))$. The SCA corrected wavefront is

$$\begin{aligned}w_c(n)i(n) &= \alpha w_c(n)v(n)m(n) \\ &= \alpha \exp(-j\hat{\beta}(n))v(n)a(n)\exp(j\beta(n)) \\ &\approx \alpha v(n)a(n).\end{aligned}\quad (9)$$

The robustness of the phase error estimate depends on the signal to noise ratio (SNR). The argument of the measured value $\hat{r}_n[1]$ is accurate when the SNR is relatively high, as it was in the experiment (see Section II B). The errors in the phase error estimate at low energy portions of the aperture can be cumulative and can be largely avoided by selecting k from a high energy region and starting the bi-directional estimating procedure described above. In the paper, phase deaberration was done by using this procedure.

APPENDIX B

This appendix evaluates (3). The scaled amplitude profile obtained through issue is $\sqrt{cv_a(n)} = \sqrt{c\alpha v(n)a(n)} \approx$

$v(n)a(n)$, where $\sqrt{c\alpha} \approx 1$. Therefore the sample value

$$\frac{\sum_{n=1}^N \{\sqrt{cv_a(n)} - v(n)\}^2}{\sum_{n=1}^N v^2(n)} \approx \frac{\sum_{n=1}^N v^2(n)\{a(n) - 1\}^2}{\sum_{n=1}^N v^2(n)}.\quad (10)$$

$v(n)$ is a deterministic quantity. $a(n)$ is assumed to have the same probability density function (pdf) for all n . The expected value of the left side of (10) is

$$\begin{aligned}\frac{\sum_{n=1}^N v^2(n)\{a(n) - 1\}^2}{\sum_{n=1}^N v^2(n)} &= \frac{\sum_{n=1}^N v^2(n)\overline{\{a(n) - 1\}^2}}{\sum_{n=1}^N v^2(n)} \\ &= \overline{\{a(n) - 1\}^2}\end{aligned}\quad (11)$$

The quantity to be evaluated is

$$\frac{\sigma_a^2}{(\bar{a})^2} \triangleq \frac{\overline{\{a(n) - \bar{a}\}^2}}{(\bar{a})^2}.\quad (12)$$

$a(n)$ approximates unity in the weak scattering case [1] which implies that only the phasefront is distorted (1). In our experiment (which includes strong scattering and refraction), $a(n)$ is also distorted but \bar{a} is close to unity, as shown in Appendix C. Thus

$$\begin{aligned}\frac{\sigma_a^2}{(\bar{a})^2} &= \overline{\{a(n) - 1\}^2} \\ &= \frac{\sum_{n=1}^N v^2(n)\{a(n) - 1\}^2}{\sum_{n=1}^N v^2(n)} \approx \frac{\sum_{n=1}^N \{\sqrt{cv_a(n)} - v(n)\}^2}{\sum_{n=1}^N v^2(n)}.\end{aligned}\quad (13)$$

APPENDIX C

As mentioned in the text, 27–45 SSP's were selected from each breast. The single sources used to sequentially insonify the breast were the nine middle transmitters in the transmitting array. SSP's were obtained from multiple elevations. The spacing in elevation is either 0.5 or 1 cm starting from approximately 2 cm below the chest wall to 5 cm. We denote the region insonified by these sources as the region of interest (ROI). The ROI is approximately 5 cm thick and the angular sector is 30° wide, which is the joint angular sector insonified by the nine middle transmitters.

Each SSP can be treated as a spatial sample of the random process developed in the ROI. The corresponding scaled amplitude profile is $\sqrt{cv_a(n)} = \sqrt{c\alpha v(n)a(n)}$. The wavefront amplitude distortion $a(n)$ is treated as a statistical quantity related to the random medium. If measured covariance of $a(n)$ and $a(m)$ over the ROI for arbitrarily selected $n \neq m$ is small, we can assume that $a(n)$ and $a(m)$ are statistically uncorrelated. Fig. 10 shows the experimental results obtained from 15 randomly selected breasts. In each breast, the estimated covariance of $a(n)$ and $a(n+l)$ over the ROI is calculated for $l = 1, 3, 5, 7$ from amplitude profiles of SSP's obtained from the ROI. The index n is randomly selected from the middle elements of the receiving array where good estimates of

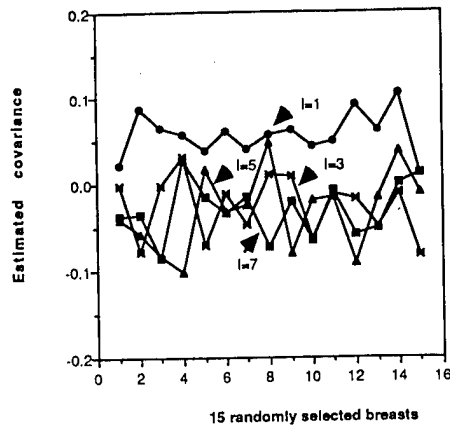


Fig. 10. Estimated covariance versus breast. Estimated covariances over the ROI for $l = 1, 3, 5, 7$ of 15 randomly selected breasts. The estimated covariances are very small.

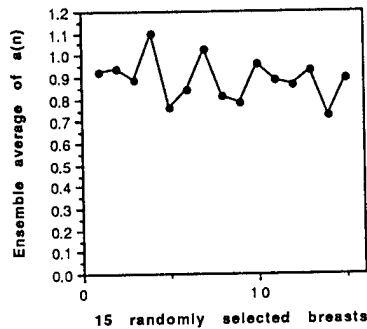


Fig. 11. $\overline{a(n)}$ versus breast. The ensemble average $\overline{a(n)}$ over the ROI is close to unity. n is the randomly selected index from the middle elements in each tested breast.

$a(n) = \sqrt{c}v_a(n)/v(n)$ and $a(n+l) = \sqrt{c}v_a(n+l)/v(n+l)$ can be made, which is in the middle of the receiving array where the signal strength is the greatest (Fig. 2(a)). The measured covariance is very small as shown in Fig. 10. The mean values for 15 breasts are 0.057, -0.026, -0.031, and -0.030 for $l = 1, 3, 5, 7$, respectively. The standard deviations are 0.025, 0.036, 0.046, and 0.032. Thus the assumption that $a(n)$ and $a(m)$ are statistically uncorrelated for any $n \neq m$ is experimentally verified.

To estimate the normalized amplitude variance in (2) we assume that $\overline{a} = 1$. Fig. 11 shows $\overline{a(n)}$ versus breast, where $\overline{a(n)}$ was estimated from the ROI and n was also randomly selected from the middle elements of the receiving array. $\overline{a(n)}$'s are very close to unity. The mean is 0.89 and standard deviation is 0.099.

ACKNOWLEDGMENT

The authors wish to express sincere thanks to all the anonymous volunteers who have participated in this study. Invaluable consultation was freely offered by Dr. Kai Thomeinius, Director of Research of Interspec. The heart of the electronic system, a Vingmed SM-20, was donated by Interspec, Inc., Ambler, PA, and the two linear arrays were donated by Echo Ultrasound, a division of Interspec, Inc., Lewistown, PA. Special thanks to Dr. Richard J. Pauls for his design and construction of the experimental system used in this paper and

to Bruce Carey, research coordinator of the Dept. of Radiology of HUP.

REFERENCES

- [1] Q. Zhu, and B. D. Steinberg, "Wavefront amplitude distortion and image sidelobe levels: Part I—Theory and computer simulations," *IEEE Trans. Ultrason. Ferroelec. Freq. Contr.*, this issue.
- [2] B. D. Steinberg, "Radar imaging from a distorted array: The radio camera algorithm and experiments," *IEEE Trans. Antennas Prop.*, vol. AP-29, pp. 740–748, 1981.
- [3] E. H. Attia, "Phase Synchronizing Large Antenna Arrays Using the Spatial Correlation Properties of Radar Clutter," Ph.D. Dissertation, Univ. of Pennsylvania, Philadelphia, PA, 1984.
- [4] S. W. Flax and M. O'Donnell, "Phase aberration correction using signals from point reflectors and diffuse scatterers: Basic principles," *IEEE Trans. Ultrason. Ferroelec. Freq. Contr.*, vol. UFFC-35, pp. 758–767, 1988.
- [5] E. H. Attia and B. D. Steinberg, "Self-cohering large antenna arrays using the spatial correlation properties of radar clutter," *IEEE Trans. Antennas Prop.*, vol. 37, pp. 30–38, 1989.
- [6] L. Nock, G. E. Trahey, and S. W. Smith, "Phase aberration correction in medical ultrasound using speckle brightness as a quality factor," *J. Acoust. Soc. Am.*, vol. 85, no. 5, pp. 1819–1833, 1989.
- [7] G. E. Trahey, D. Zhao, J. A. Miglin, and S. W. Smith, "Experimental results with a real-time adaptive ultrasonic imaging system for viewing through distorting media," *IEEE Trans. Ultrason. Ferroelec. Freq. Contr.*, vol. 37, pp. 418–427, 1990.
- [8] B. D. Steinberg and H. Subbaram, *Microwave Imaging Techniques*, ch. 8 and 9. New York: Wiley, 1991.
- [9] M. Fink, "Time reversal of ultrasonic fields: Part I—Basic principles," *IEEE Trans. Ultrason. Ferroelec. Freq. Contr.*, vol. 39, pp. 555–566, 1992.
- [10] A. R. Selfridge, "Approximate material properties in isotropic materials," *IEEE Trans. Son. and Ultrason.*, vol. SU-32, pp. 381–394, 1985.
- [11] Q. Zhu and B. D. Steinberg, "Large-transducer measurements of wavefront distortion in the female breast," *Ultrasonic Imaging*, vol. 14, pp. 276–299, 1992.
- [12] Q. Zhu, "Large-Transducer Measurements of Ultrasonic Wavefront Distortion in the Female Breast," Ph.D. Dissertation, Univ. of Pennsylvania, Philadelphia, PA, 1992.
- [13] Q. Zhu and B. D. Steinberg, "Wavefront amplitude distribution of the female breast," *J. Acoust. Soc. Am.*, to be published.

Qing Zhu (S'91–M'92) for a photograph and a biography, please see page 753 of this issue of this TRANSACTIONS.

Bernard D. Steinberg (S'48–A'50–SM'64–F'66–LF'90) for a photograph and a biography, please see page 753 of this issue of this TRANSACTIONS.



Ronald L. Arenson received the B.S. degree in mathematics in 1965 from Duke University and the M.D. degree in 1970 from New York Medical College, NY.

He joined the Department of Radiology of the Hospital of the University of Pennsylvania in 1976 as an assistant professor. From 1984 to 1991 he was associate chairman of the Department of Radiology, and Vice Provost for Computing of the University of Pennsylvania. His research interests include medical imaging; digital imaging network; imaging archive and computer methods; and programs in biomedicine. He is now a professor and chairman of the Radiology Department of the University of California at San Francisco.

Wavefront amplitude distribution in the female breast

Qing Zhu and Bernard D. Steinberg

Valley Forge Research Center, The Moore School of Electrical Engineering, University of Pennsylvania, Philadelphia, Pennsylvania 19104

(Received 5 May 1993; accepted for publication 14 March 1994)

Ultrasound measurements of a large population of wavefronts transmitted through female breasts at 3 and 4 MHz show that the wavefront amplitude distribution is close to Rayleigh. This finding is consistent with a fully developed scatter field, implying that the scatter energy removed from the coherent incident beam dominates the wavefront. The wavefront received from an inhomogeneous medium is the superposition of an incident wave plus a scattered wave. If the scattered field is weak, the received field is dominated by the incident field and the wavefront amplitude distribution is Rician. If the scattered field is strong, the received field is primarily the scattered field and the wavefront amplitude distribution is Rayleigh. If, in addition to scattering, refraction between bodies of different refractive indexes occurs, the total net effect on the wavefront amplitude distribution is the same as for strong scattering. This is what we have observed in the highly refractive female breast. This result has implications for the design of high lateral-resolution echo scanners that will incorporate adaptive phase deaberration algorithms. The published algorithms were developed for weak scattering and therefore may not be powerful enough. Alternatives have to be found to deaberrate the severe wavefront distortion in the breast.

PACS numbers: 43.80.Cs, 43.80.Ev, 43.80.Vj

INTRODUCTION

Several investigators have studied focusing properties at the focal zones of transducers after ultrasonic waves propagate 1-way or 2-way through *in vivo* breast or breast samples.^{1,2} Others have directly measured ultrasonic phasefronts^{3,4} or wavefronts⁵⁻⁸ of spherical waves propagating through *in vivo* breast. Most studies have focused on the effect of breast inhomogeneity upon lateral resolution.¹⁻⁵ Some have concentrated on the sources of wavefront distortion inside the breast⁶ and sidelobe properties of pointlike source images after phase front deaberration.^{7,8}

The principle wavefront distortion sources inside the female breast appear to be scattering and refraction. Scattering is caused by local speed variations. Refraction is caused by speed mismatch across a tissue interface. Refraction can cause ray bending and splitting. Refracted rays can be further refracted at subsequent interfaces and arrive at the receiving transducer from different directions. Such subbeams interfere and can cause cancellation in high energy portions of the aperture.⁶

In scattering, the field E at the receiver after a plane or spherical wave propagates through the breast is the superposition of the incident field E_i plus the scattered field E_s . If the scattered field is weak, i.e., $E_i \gg E_s$, E is dominated by E_i and the wavefront amplitude distribution is Rician. The phasefront of E is primarily the phasefront of E_i plus perturbations caused by the scattered field. If the scattered field is strong, $E_i \ll E_s$, the energy in the incident field is scattered and E is approximately E_s . For a medium containing multiple scattering bodies or diffuse scatterers, the scattered field is a coherent sum of the scattered fields radiated from these scatterers. In the absence of a strong, coherent E_i component to the field, the probability density function (pdf) of the com-

plex wavefront should approach the bivariate Gaussian distribution, implying that the modulus distribution is approximately Rayleigh.⁹

The exact distributions for the two cases are not important. What is important is to determine from experiment which case corresponds to ultrasound transmission through the breast. The reason is that current adaptive phasefront compensation algorithms¹⁰⁻¹⁸ deal with the weak scattering case and their utility in the strong scattering and refraction case is limited.¹⁸

Our measurements indicate that the latter is what occurs in the female breast. It becomes evident in the measured wavefronts when both the breast and the 1-D receiving aperture are large, as in the experiments reported (12 and 10 cm, respectively). Wavefront measurements at this large penetration depth of three populations (premenopausal dense, pre-m fatty, and post-m) show that the wavefront amplitude pdf is close to Rayleigh. In addition, study of the wavefront amplitude profiles discloses deep nulls typical of coherent interference,⁶ which indicates that refraction is the likely cause. At some lesser penetration sufficiently less energy would be scattered from the coherent beam and the wavefront amplitude distribution should be Rician. Up to such a depth adaptive phase aberration (or time shift) correction will be useful, but not for large apertures and significant penetration depth. Either modifications of the existing algorithms have to be made or stronger algorithms have to be invented for penetration from the skin to the chest wall. Furthermore, the success that phase aberration correction has had with phantoms^{12,14} and in small-sample experiments in *in vivo* liver^{15,19} has led to unrealistic expectations for the breast. This makes it essential that the next generation of solutions be tested with breast tissue.

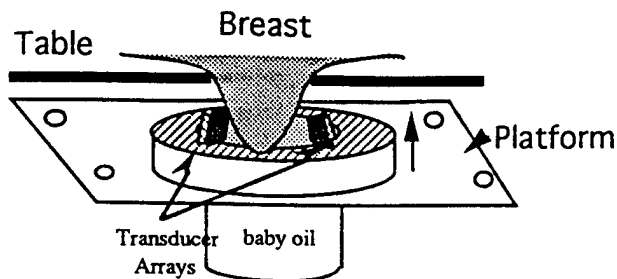


FIG. 1. Experimental configuration of the measurement system (Ref. 3).

The following section describes *in vivo* wavefront measurements of the breast. The wavefront distortion model is introduced in Sec. II. Measured distributions of wavefront amplitude are presented in Sec. III. Discussion and summary are in Secs. IV and V.

I. THE EXPERIMENT

The experiment was designed to measure the wavefront after propagating through *in vivo* breast. The experimental procedure was described in previous papers.^{5,6,8} Figure 1 shows how the experiment was conducted. The volunteer lies on the table with one breast inserted in the baby-oil filled reservoir. Baby oil (speed 1430 m/s²⁰) was chosen to match the speed of subcutaneous fat (1440 m/s) and consequently to reduce refraction at the skin surface. A platform carrying two linear arrays is raised and lowered by a stepping motor under computer control. The elevation increment is either 1/2 or 1 cm.

At each elevation level, a single transducer element radiates ultrasonic waves through the breast to the receiving array (Fig. 2). Both narrow-band and wideband measurements were made. The transmitting frequencies were 3 and 4 MHz for both the narrow-band and wideband experiments. The width of the source T was 1.49 mm and the source beam width λ/T was 20° and 16° at the two frequencies. The portion of the receiving array used in the experiment was 96 mm with 64 elements. Because of the size of the source, the bulk of the transmitted energy was received by the middle half of the receiving array. The receiving element spacing was 1.5 mm; its width was 1.49 mm. The height of the element was 10 mm. Thus the elements were not point detectors but inte-

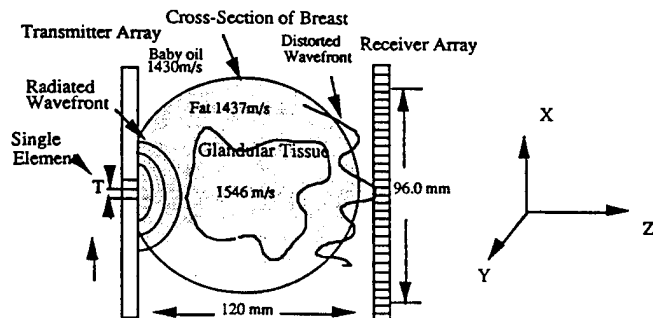


FIG. 2. Wavefront distortion measurement with single source insonification. Z is the wave propagation direction, X is the transducer direction, and Y is perpendicular to X and Z (from Ref. 8).

grated over 3 or 4 λ in azimuth and 20 or 26 λ in elevation. Transmission was a sequence of 64, 16- μ s pulses spaced by 200 μ s and followed by a sequence of 64, 1- μ s pulse spaced by the same time interval. The long pulse had a bandwidth of 60 kHz; this narrow bandwidth was chosen to avoid effects caused by the variation of tissue attenuation with frequency upon the wavefront measurement. The short pulse had a bandwidth of 1 MHz; it was used to test the effect of multipath upon the wavefront. Data for both frequencies are presented for the narrow-band transmissions whereas only the less attenuating 3-MHz data are used for the wideband experiments. An experimental comparison is given in Sec. III and the implications are discussed in Sec. IV.

Reception across the entire aperture was by synthetic aperture: Each of 64 receiving elements received and stored one of the transmissions in sequence. At each receiving element, the received rf pulses, after propagating through the medium, were coherently demodulated. When the transmission was the 16- μ s pulse, analog inphase, and quadrature values were measured and integrated within an 18- μ s window. A sequence of 18 1- μ s receiving windows was used when the transmission was the 1- μ s pulse. The analog data were digitized by using two high speed eight bit A/D converters. In this way the complex wavefront across the receiving aperture was measured. A set of 64 complex values is called a single source profile (SSP). For long pulse transmission and long receiving window, one SSP was obtained. Otherwise 18 SSPs were obtained. The total data acquisition time for one SSP is 0.0128 s, which is 2 orders of magnitude faster than patient cardiac cycle. To measure the wavefront distortion properties through various angular sectors of the breast, several transmitter elements located in the middle region of the transmitting array were used. A set of 64 narrow-band pulses from each transmitter produced one narrow-band SSP and a corresponding set of wideband pulses produced 18 wideband SSPs.

After each *in vivo* experiment, the same sequence of SSPs through oil alone was taken for system calibration purpose.

II. WAVEFRONT MODEL

The measured wavefront through oil at the finite 1-D receiving aperture is $E_o(x) = A_o(x)e^{j\phi_o(x)}$, where x is position at the receiving array and the subscript o represents oil. Because of the absence of scattering and refraction in oil, the measured field E_o equals the incident field E_i . The amplitude profile $A_o(x)$ is the radiation pattern of a transducer element, while the phase profile $\phi_o(x)$ reflects the near-field curvature of the wavefront. Figure 3 shows a measured wavefront through oil with the narrow-band waveform; the solid line is the amplitude profile A_o and the dashed line is the phase ϕ_o unwrapped in the middle to show its quadratic curvature.

The measured wavefront through breast $E(x) = A(x)e^{j\phi(x)}$ can be decomposed into the product of $A_o(x)e^{j\phi_o(x)}$ and a medium induced distortion function $m(x) = a(x)e^{j\beta(x)}$. That is,

$$E(x) = A(x)e^{j\phi(x)} = \alpha m(x) A_o(x) e^{j\phi_o(x)}$$

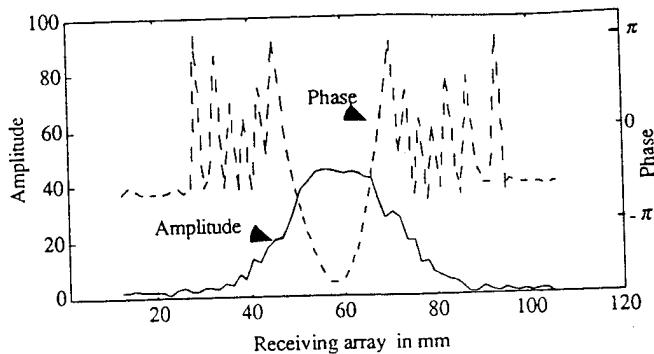


FIG. 3. Example of measured radiation field through oil. The abscissa is position in the receiving array and the ordinates are amplitude and phase. The 96 mm portion of the array used for receiving is from 12 to 108 mm. Transmitting frequency is 3 MHz (from Ref. 3).

$$= \alpha a(x) A_o(x) e^{j\beta(x)} e^{j\phi_o(x)}, \quad (1)$$

where α is a constant that reflects any signal loss inside the breast.

Figure 4 is an example of a wavefront measured through the breast with the narrow-band waveform; the solid line is A and the dashed line is ϕ unwrapped in the middle. The jagged amplitude implies that $a(x)$ is severely distorted. The phase is also highly distorted relative to the expected quadratic curvature.

$A_o(x)$ is a deterministic function and is slightly different for different transmitters while $a(x)$ represents wavefront amplitude distortion caused by the medium. From Eq. (1), $a(x) = A(x)/A_o(x)$ provided that the signal loss α is properly compensated and the denominator $A_o(x)$, sampled at the n th receiver element and denoted $A_o(n)$, is large enough that the ratio $A(n)/A_o(n)$ does not blow up. The first is accomplished by equalizing energies received through breast and oil (the detailed procedure is described in the Appendices of Ref. 8) and the second is guaranteed by calculating $a(n)$ in the middle region of the receiving array where $A_o(n)$ is large (see Fig. 3).

In a weak scattering medium, $a(x) \approx 1$ and wavefront distortion is primarily in the phase $\beta(x)$. With stronger scattering and refraction, wavefront amplitude $a(x)$ also becomes distorted. The statistical distribution of $a(x)$ obtained

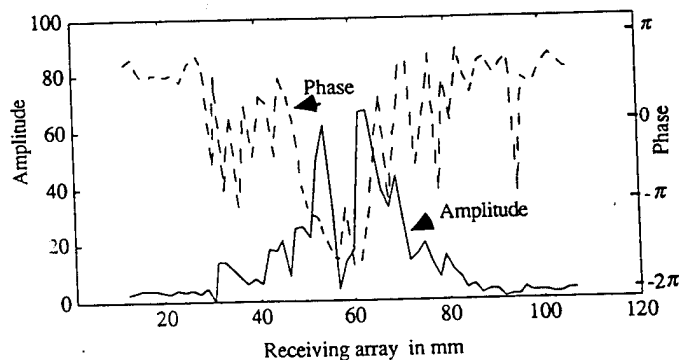


FIG. 4. Example of measured radiation field through breast ID#46L (from Ref. 3).

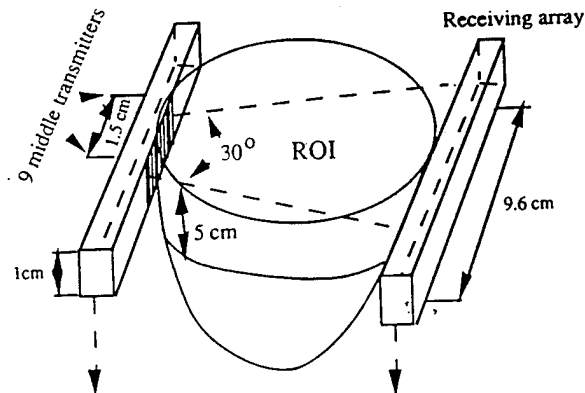


FIG. 5. Illustration of ROI. Nine middle transmitters were used as single sources to insonify the breast. The dashed arrows represent translation of transducers in elevation direction.

from a large insonified region of breast reported in the following section indicates that refraction and strong scattering are the dominant distortion mechanisms.

III. DISTRIBUTION OF A WAVEFRONT AMPLITUDE

A. General

(i) Data selection: Data were taken from the wedge-shaped portion that excludes both lateral and elevation curvature (Fig. 5). This is defined as the region of interest (ROI). It is approximately 5 cm in elevation, 30° wide in azimuth and located close to the chest wall. Because no pathologies exist in the selected breasts used, it is reasonable to assume that the tissue composition within the ROI is statistically homogeneous.

(ii) Noise effects: It is shown in Sec. IV C that the accuracy of amplitude measurement is marginally affected by the SNR.

B. Narrow-band results

To obtain wavefront amplitude distributions of different categories of breasts with similar tissue composition, we divided the selected subjects into premenopausal and postmenopausal groups: [Two selected volunteers were x-ray mammography patients who had regular mammography check ups and the rest were hospital staff of the Hospital of the University of Pennsylvania (HUP) who had x-ray mammograms done within the experimental period. They all signed a consent form approved by the Office of Research Administration of the University of Pennsylvania.] The premenopausal subjects were further divided into premenopausal-dense and premenopausal-fatty subjects based upon whether glandular tissue or fat predominate, as identified from x-ray mammogram readings. The histograms of $a(n)$ (Fig. 6) were obtained from these three groups at 3 MHz. Each group consists of five women (ten breasts). The average ages of the three groups are 38.8, 46.4, and 59.2 years, respectively. The standard deviations are 2.59, 5.77, and 8.11 years. The sample sizes of the histograms of the three groups are 6542, 6405, and 6066, respectively. The

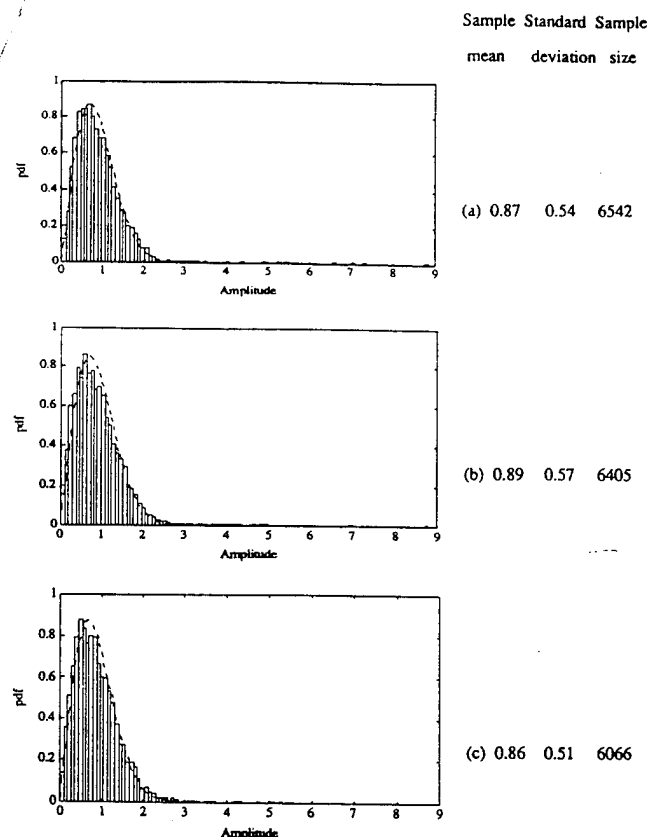


FIG. 6. Histograms of wavefront amplitude at 3 MHz using narrowband waveform obtained from (a) premenopausal-dense breast group. (b) Premenopausal-fatty breast group. (c) Postmenopausal breast. The dashed curves are Rayleigh distributions with means chosen as the sample means.

mean amplitude values are 0.87, 0.89, and 0.86. The standard deviations are 0.54, 0.57, and 0.51. When the effect of noise and measurement error is removed the standard deviation estimates remain almost the same (Sec. IV C). The dashed curves are Rayleigh distributions with mean values chosen as the corresponding sample means. The similarity of these histograms to the Rayleigh distribution suggests a fully developed scatter field.

C. Wavefront amplitude distribution versus bandwidth

In this section, we first discuss the effect of multipath upon wavefront measurement under weak scattering and under strong scattering and refraction. Second, we show a typical example of wideband measurement. Lastly, a comparison of amplitude distributions between narrow-band and wide-band measurements is given.

1. Weak scattering versus bandwidth

Define the scattering coefficient $s = E_s/E_i$. In weak scattering s is typically the order of a few percent. If weak scattering were the dominant distortion mechanism, long pulses (narrow-band waveforms) and short pulses (wideband waveforms) would give similar results on wavefront amplitude measurement, as the following simple calculation shows.

We calculate the differential lengths between a direct path and (1) a close scattering path and (2) a more distant

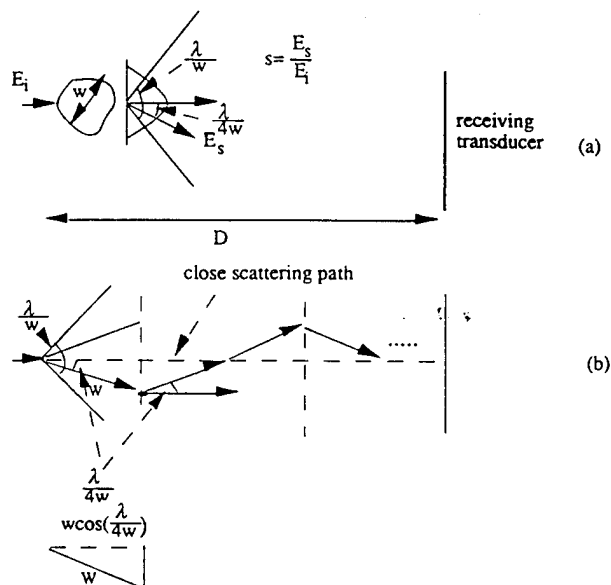


FIG. 7. Sketch of scattering path. (a) Illustration of scattering angle. (b) Illustration of a close scattering path.

scattering path. If the differential length is less than about $\lambda/2$, which is approximately 0.25 mm at 3 MHz, the coherent sum of the scattered field and the direct field at the receiver will be free of destructive interference caused by multipath.

Assume that a plane wave insonifies the scattering medium [Fig. 7(a)]. The distance from the source to the receiver is D . Assume that the widths of the scattering bodies or the correlation length of the medium are w and the total number of scatterers along the propagation path is n . Scattering, therefore, is over a nominal angle of λ/w . Consequently, a typical scattered ray between the direct path and the edge of the scattering pattern would emanate at an angle, say, of $\lambda/4w$. From Fig. 7(b) the closest scattering path length is $nw \cos(\lambda/4w) = D \cos(\lambda/4w)$. The differential path length is

$$\Delta l = D[1 - \cos(\lambda/4w)] \approx (1/2)D(\lambda/4w)^2 = (\frac{1}{32})D(\lambda/w)^2. \quad (2)$$

The differential length as a fraction of wavelength is $\Delta l/\lambda = D\lambda/32w^2$. It is listed in Table 1 at 3 MHz over a range of values of w . It is seen that the scattered rays from all but the smallest scatterers can not cause destructive interference with the direct rays.

Longer paths increase $\Delta l/\lambda$ but the field strength decreases exponentially. The total number of scatterers along the propagation path is $n = D/w$ and the scattering gain is therefore s^n . Doubling the scatter path length implies that n doubles and the scattering gain becomes s^{2n} . Since s is only

TABLE I. Fractional differential path length $\Delta l/\lambda$ vs scattering width or correlation length w . $D=120$ mm and $\lambda=0.5$ mm ($f=3$ MHz).

w (mm)	2	3	4	5	6	7	8	9	10
$\Delta l/\lambda$	0.47	0.21	0.12	0.08	0.05	0.04	0.03	0.02	0.02

a few percent, s^{2n} is vanishingly small. Thus the scattered rays from more distant scattering paths are too weak to cause significant interference with the direct rays.

2. Strong scattering and refraction versus bandwidth

If strong scattering and refraction are the dominant wavefront distortion mechanisms, scattered waveforms and refracted subbeams can overlap. In this case temporal interference can result from the long pulse. These overlapped waveforms and subbeams all contribute to the wavefront distortion observed at the receiving aperture. However, it is possible that the multiple arrivals are sufficiently separated in time so that they can be resolved by the short pulse typically used in echo scanning. For example, assume that one propagation path contains l cm glandular tissue and $D-l$ cm fat while the second is fat alone. The differential travel time is $\Delta\tau = [D/c_f - (D-l)/c_f - l/c_g]$, where c_f and c_g are sound speeds of fat and glandular tissue. Taking $c_f = 1.44$ mm/ μ s and $c_g = 1.55$ mm/ μ s, $\Delta\tau = 0.049l$. When $l > 20$ mm, the differential time $\Delta\tau$ exceeds 1 μ s and the wavefront received within the first 1- μ s window would be free of interference. Wavefront in subsequent windows, however, could be distorted. To test this hypothesis of potential temporal interference, we incorporated wideband measurements into our *in vivo* experiment.

3. A typical example of wideband measurements

Figure 8 shows the amplitude profiles of wideband measurements obtained through oil and through breast ID#66R. The transmitted pulse is 1 μ s. The successive parts of (a) and (b) are "snapshots" of the amplitude profiles measured in successive 1- μ s intervals. The transmitted pulse contains three full cycles of rf at center frequency plus a few cycles of ringing due to the transducer. The received pulse should also last approximately 1 μ s. The 1- μ s sampling intervals in the receiver were preset and, therefore, the received pulse may fall into two 1- μ s windows. Further, the transmitted pulses travel different distances to the receiver elements and the time-delay differences between on-axis and far off-axis elements are in the neighborhood of 3 μ s. Thus the received signals will exist at the receiving array in three successive 1- μ s windows, which is what we observe in transmission through oil [Fig. 8(a)].

The received amplitude profiles propagated through breast ID#66R are shown in Fig. 8(b). This figure indicates temporal spread of multipath by the order of 1 μ s. Signals primarily exist within the 3- μ s period (range gates 84.2, 85.2, and 86.2 μ s) as expected, but also extend into the following 1- μ s period (87.2 μ s). Later profiles have insignificant energies. In addition, the amplitude profile in the 84.2- μ s range gate is significantly less jagged than the later profiles. This also indicates a temporal spread of waveforms and subbeams.

4. Wavefront amplitude distribution

To more accurately assess the extent of multipath development with time, we separately measured wavefront amplitude distributions from different range gates. The wavefront

model introduced in Sec. II cannot be used directly because of the different responses of oil and tissue at different range gates. Instead, the unaberrated amplitude profile $A_o(x)$ is estimated by smoothing the jagged profile with a moving window. $a(n)$ is then calculated as for the narrow-band case. The length of the window is seven elements. The selected amplitude profiles were those that had significant energy. The dashed curves in Fig. 8(b) are the smoothed profiles.

Figure 9 shows histograms of $a(n)$ obtained from four premenopausal-fatty and postmenopausal women (eight breasts) at 3 MHz using the wideband waveform. Figure 9(a) is obtained from the first range gate that received significant energy. Figure 9(b), (c), and (d), are obtained from the next three range gates. The sample means are 1.02, 1.03, 1.02, and 0.99, respectively. The standard deviations are 0.38, 0.39, 0.44, and 0.48. The dashed curves are Rayleigh distributions with means chosen as the sample means. The histograms progressively change from (a) to (d) toward Rayleigh, which indicates that long multipath delays do contribute to progressive amplitude distortion in time.

Because different procedures were used in calculating $a(n)$ for the narrow-band and wideband cases, one possible explanation for the difference in the histograms of Fig. 9 and Fig. 6 may be procedural. As a test, we used the wideband procedure also on the narrow-band measurements. Figure 10 shows histograms of $a(n)$ obtained from the same subjects as Fig. 9 at 3 MHz using the narrow-band waveform. Figure 10(a) is obtained by the moving window procedure and Fig. 10(b) by using the wavefront model introduced in Sec. II. In both cases, the experimental distributions approximately follow the Rayleigh distribution. Small differences between the tails and the heads of Fig. 10(a) and (b) do exist, but they are much too small to account for the large difference between Fig. 9(a) and (b) and Fig. 10(b). Hence the latter difference is not due to the different amplitude processing procedures.

In conclusion, experimental histograms of narrow-band measurements reported in this paper did not differ significantly from the results of wideband measurements. The implications for pulse echo are reserved for Sec. IV.

D. Wavefront amplitude distribution versus frequency

The wavefront amplitude distribution obtained at 3 MHz is Rayleigh, which indicates that the speckle pattern is fully developed at this frequency and, therefore, should not change at higher frequencies. Figure 11 shows the histogram obtained at 4 MHz from four women (eight breasts). As expected the experimental distribution remains close to Rayleigh (dashed). The mean amplitude value is 0.89 and the standard deviation is 0.52. The mean value of the Rayleigh is chosen as the sample mean.

The incident wave is likely to be stronger at lower frequencies and, therefore, the amplitude distribution may have Rician characteristics. However, lower frequencies are unlikely to be used for breast imaging. These measurements, therefore, imply that wavefront deaberration algorithms should be designed for use with Rayleigh wavefront-amplitude distortion.

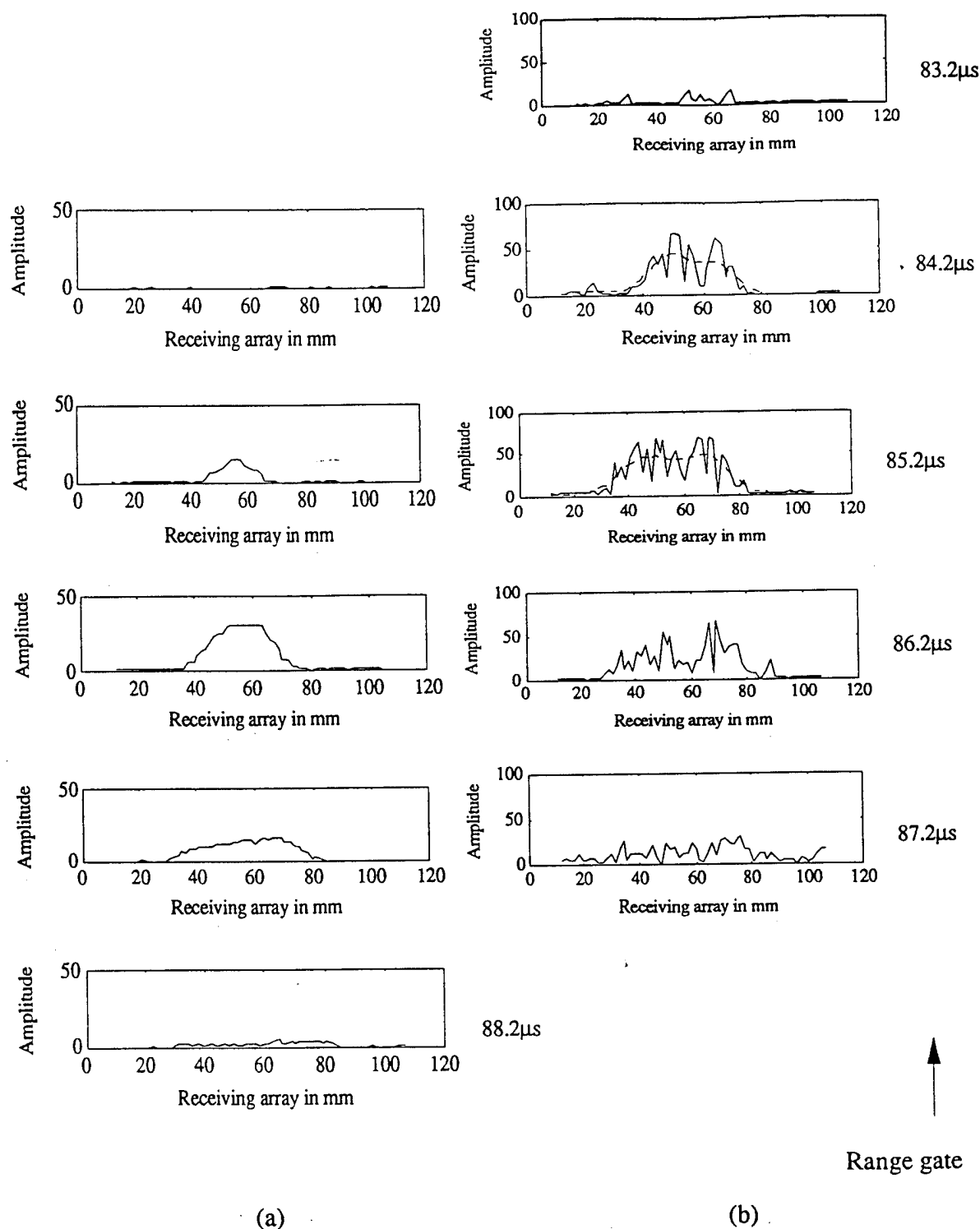


FIG. 8. Received amplitude profiles through oil and breast ID#66R. The receiving aperture is 9.6 cm. The transmitted pulse length is $1 \mu\text{s}$. The receiving windows are activated for $1 \mu\text{s}$ at the range gate indicated. (a) Oil. Relatively smooth amplitude profiles. (b) Breast. The amplitude profiles are severely distorted.

IV. DISCUSSION

A. Implications for pulse echo scanning

1. Transmission versus echo

While the experimental data were obtained from a transmission experiment, they are also pertinent for echo scanning in the breast. This is because the source was 1.5 mm or 3λ at

3 MHz. Its beam, therefore, emulated the narrow insonified region of an $f/3$ narrowbeam echo scanner, which is typical of ultrasound mammography probes.

2. Multipath

Long multipath delays of more than $2 \mu\text{s}$ are evident in the wideband measurements (Fig. 9). This implies that echo wavefronts returned from successive ranges will be distorted

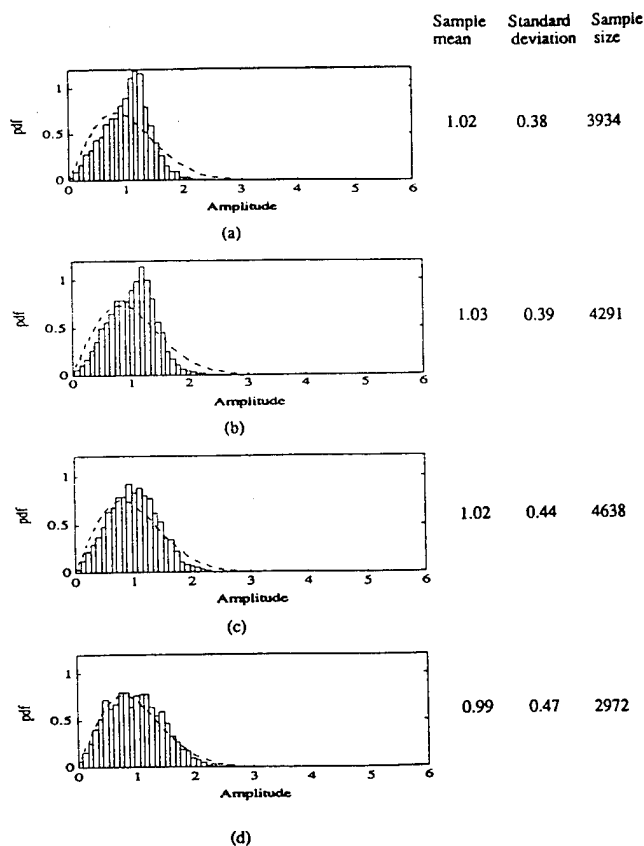


FIG. 9. Histograms of wavefront amplitude obtained from four premenopausal-fatty and postmenopausal women (eight breasts) at 3 MHz from four successive 1- μ s receiving windows using the wideband (1 MHz) waveform. The dashed curve is Rayleigh distribution with mean value chosen as the sample mean. The standard deviations are therefore 0.53, 0.54, 0.53, and 0.52. Sample means, standard deviations, and sample sizes are listed above.

by delays from previous ranges. The wideband histogram evidence offered in this paper shows that the pdfs are close to Rayleigh, i.e., the distribution is the same as for the fully developed scatter field. Thus in pulse echo imaging the wavefront distortion will have common statistics at all ranges except for the first few ranges. Therefore, the deaberation conclusion regarding wavefront-amplitude distribution (last paragraph in Sec. III C) obtained from the transmission experiments is relevant for echo ultrasound.

B. Effect of element size on 1-D amplitude measurement

Each transducer element consists of six equally spaced subelements which are electrically connected. The width (azimuth) of each subelement is 0.183 mm and the center to center spacing is 0.249 mm, which is about $\lambda/2$ at the 3 MHz operating frequency. Its height (elevation) is 10 mm. As a result, each measured wavefront sample at the receiving array is the complex sum of six wavefront samples in the array axis (azimuth) and the integral of the field over 10 mm in elevation. The elevation integration is typical of 1-D arrays and therefore does not affect our conclusions for 1-D scanning systems. The converse is true for 2-D arrays. The azimuth analysis follows.

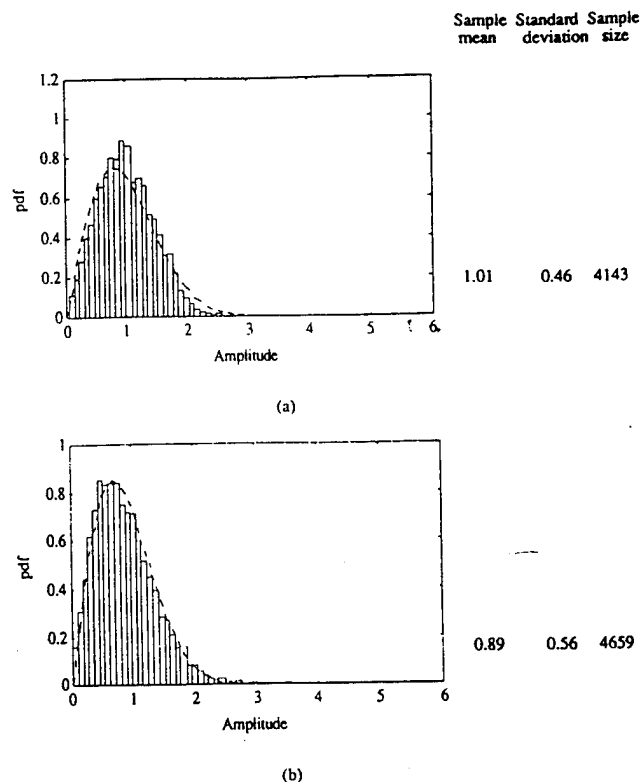


FIG. 10. Histograms of wavefront amplitude at 3 MHz using narrow-band waveform obtained from the four women as in Fig. 9. Dashed curves are Rayleigh with mean values chosen as the sample means. (a) Using smoothing technique. (b) Using wavefront model introduced in Sec. II.

Some unknown amount of distortion can be attributed to the coherent sum of six subelement samples. With finer sampling, we would anticipate more accurate measurements. A measure of the increase in the mean square amplitude distortion caused by subelement summation is found by considering a wavefront $1 + a \exp(jkxu_o)$, which is formed from the sum of two plane waves (implying array focus at the source distance) of relative amplitude a whose arrival directions are spaced by $u_o = \sin \theta_o$, where $k = 2\pi/\lambda$ and θ_o is the angular separation of the two plane waves. The modulus is $\sqrt{1 + a^2 + 2a \cos(kxu_o)}$. The mean square measurement error (MSE) can be found by

(i) Calculating the average amplitude measured at the

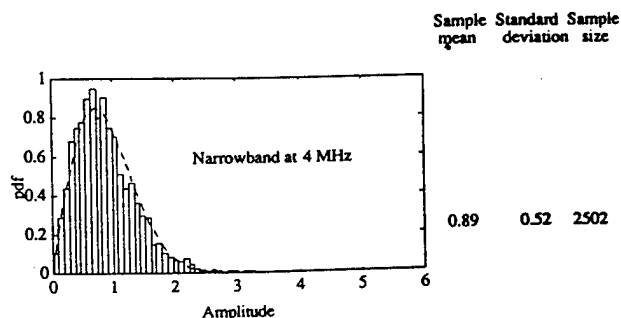


FIG. 11. Histogram of wavefront amplitude at 4 MHz using narrow-band waveform obtained from the four women as in Fig. 9. The dashed curve is Rayleigh. The mean value is chosen as the sample mean and standard deviation is 0.47.

TABLE II. Effect of noise on amplitude measurement.

Histograms	Narrowband 3 MHz			Wideband 3 MHz				NB 4 MHz
	Fig. 6(a)	Fig. 6(b)	Fig. 6(c)	Fig. 9(a)	Fig. 9(b)	Fig. 9(c)	Fig. 9(d)	Fig. 11
Average SNR (dB)	21.4	25.8	24.8	20.4	20.4	18.2	12.3	19.0
Amplitude standard deviation	0.54	0.57	0.51	0.38	0.39	0.44	0.47	0.52
Noise standard deviation	0.075	0.032	0.035	0.070	0.062	0.092	0.175	0.036
Noise-free standard deviation	0.53	0.569	0.509	0.373	0.385	0.430	0.436	0.519

n th element after taking the coherent sum of the field samples at each element

$$e_v = \frac{1}{6} \left| \sum_{m=0}^{m=5} \{1 + a \exp[jk(6n+m)du_o]\} \right|,$$

where m is the subelement position index and d is the inter-subelement spacing which is $\lambda/2$ at 3 MHz.

(ii) Calculating the field at each of the $6n+m$ subelements

$$e_s = \sqrt{1 + a^2 + 2a \cos[k(6n+m)du_o]},$$

where $n=1,2,\dots,64$ and $m=0,1,\dots,5$.

$$(iii) \text{ MSE} = \frac{1}{64 \times 6} \sum_{n=1}^{n=64} \sum_{m=0}^{m=6} (e_s - e_v)^2. \quad (3)$$

The measurement error grows with u_o and a . Typical large values are 0.1 and 0.6 rad, respectively, for which MSE, normalized to the square of the mean amplitude, is 0.038. (The values of u_o and a were estimated from arrival angles observed in our experiment and from peak to valley ratios in the amplitude profiles.) Therefore, the measured normalized amplitude variance would differ by about 0.038 if the wavefront were samples at $\lambda/2$ spacing. This is about 8% of the measured standard deviations. Therefore, the histograms given in this paper would not change significantly if the field were samples at $\lambda/2$ spacing.

C. Effect of noise on amplitude measurement

Analysis shows that noise does not have a significant effect upon the histograms. Let the amplitude profile in tissue $A_t(x) = A_s(x) + N(x)$ consist of signal amplitude plus the system noise that contaminates the measurement. The subscript t denotes tissue, s signal. The profile in oil $A_o(x)$ is unperturbed by noise because the SNR in oil is 30 dB. The normalized profile in the central region of $A_t(x)$ is $a(x) = [A_s + N(x)]/A_o(x) = a_s(x) + n(x)$ and its variance is $\sigma_a^2 = \sigma_{a_s}^2 + \sigma_n^2$. σ_a^2 is the measured value given in the second column of each histogram. σ_n^2 was estimated from the mea-

surements at the left and right ends of the aperture where the signal was negligibly small. Therefore the noise-free variance is estimated by $\sigma_{a_s}^2 = \sigma_a^2 - \sigma_n^2$.

Table II, row 2, lists the measured average SNRs, row 3 the amplitude standard deviations, row 4 the estimated noise standard deviations, and row 5 the estimated noise-free standard deviations. From comparison of rows 3 and 5, it is evident that the histograms would not change significantly if the system were free of noise.

D. Implication for 2-D array

Our measurements were made with a 1-D array having a typical elevation dimension of 10 mm. As shown in Sec. IV B, the results are generally relevant to 1-D echo scanning. However, the spatial sampling in elevation (10 mm is 40 samples spaced by $\lambda/2$) is too coarse to apply them to 2-D, in which there is growing interest in the research and industrial communities. 2-D arrays generally sample more finely in elevation so as to be able to measure the field more accurately. The conclusion is that measurements need to be made with a 2-D aperture.

E. Contact measurements versus liquid path measurements

To ensure good contact between transducers and breast for the purpose of reducing refraction at skin surface, we selected 15 women with large breasts which almost filled the entire reservoir. Furthermore, the ROI was chosen from the region close to the chest wall where the breast cross section is the largest and the contact is good. The transmitters used were selected from the middle elements of the transmitting array to ensure close to normal incidence of the ultrasonic rays at the skin surface. Thus we believe that refraction at the skin surface is reduced to a minimum and our measurement results are close to contact measurements.

F. Effect of propagation distance

The propagation distance in the *in vivo* experiment was approximately 12 cm of tissue. Wavefront amplitude distortion would be less severe at lesser propagation distance. This

is because the energy scattered from the coherent beam increases with depth, causing the wavefront amplitude distribution to evolve from Rician to Rayleigh. It is important that this matter be evaluated experimentally because adaptive correction of phase aberration alone will suffice when the amplitude distortion is small. Only experimentation will provide the needed information about useful penetration depth with existing algorithms.

V. SUMMARY

Wavefront measurements show that wavefront amplitude distributions are close to Rayleigh at 3 and 4 MHz which indicates that strong scattering and/or refraction are the dominant wavefront distortion sources in the large breast. The incident wave is scattered after it propagates through 12 cm of breast tissue and the scattered and/or refracted fields dominate the received field. This phenomenon is fully developed at 3 and 4 MHz and it should not change at higher frequencies, which are of greater interest in ultrasound mammography. The incident wave may reappear at lower frequencies and the wavefront amplitude distribution may have Rician characteristics. It would be interesting to verify this in future experiments. However, lower frequencies are not likely to be used in the breast and, therefore, this matter is only of academic interest.

Wideband measurements show that long multipath delays of more than 2 μ s exist and that they contribute to some extent to wavefront amplitude distortion in more distant ranges. The implication to pulse echo imaging is that these long multipath delays will produce image distortion.

The phase aberration compensation algorithms that have been developed for weak scattering are not powerful enough when significant wavefront amplitude distortion is present. Because amplitude distortion increases with depth, it is important to measure distortion versus depth. For depths at which amplitude distortion in strong scattering and refractive media is too severe, alternative deaberration methods have to be found.

ACKNOWLEDGMENTS

The authors wish to express sincere appreciation to all anonymous volunteers who have participated in this study and to the Commonwealth of Pennsylvania, Interspec, Inc., an ultrasound imaging firm in Ambler, Pa., NSF (BCS92-09680) and U.S. Army Medical Research & Development Command (DAMD 17-93-J-3014) for their funding of the work. Invaluable consultation was freely offered by Dr. Kai Thomenius, Director of Research of Interspec. The authors appreciate the clinical guidance and help of Dr. Ronald Arenson, Chairman of the Dept. of Radiology of the University of California at San Francisco (then Associate Chairman of the Dept. of Radiology of HUP). The heart of the electronic

system, a Vingmed SM-20, was donated by Interspec and the two linear arrays were provided by Dr. Clyde Oakley, Tetrad Corp. (then Manager of R&D of Echo Ultrasound, Lewistown, Pa, a division of Interspec). We are very grateful for the equipment contributions. Special thanks to Dr. Richard J. Pauls for his hardware design and construction of the experimental system used in the paper. The authors appreciate the administrative help of Bruce Carey, research coordinator, of the Dept. of Radiology of HUP.

- ¹ M. Moshfeghi and R. C. Waag, "In vivo and in vitro ultrasound beam distortion measurements of a large aperture and a conventional aperture focused transducer," *Ultrasound Med. Biol.* 5, 415-428 (1988).
- ² F. S. Foster and J. W. Hunt, "Transmission of ultrasound beams through human tissue—focussing and attenuation studies," *Ultrasound Med. Biol.* 3, 257-268 (1979).
- ³ G. E. Trahey, P. D. Freiburger, L. F. Nock, and D. C. Sullivan, "In vivo measurements of ultrasonic beam distortion in the breast," *Ultrason. Imag.* 13, 71-90, (1991).
- ⁴ P. D. Freiburger, D. C. Sullivan, B. H. LeBlanc, S. W. Smith, and G. E. Trahey, "Two dimensional ultrasonic beam distortion in the breast: in vivo measurements and effects," *Ultrason. Imag.* 14, 398-414 (1992).
- ⁵ B. D. Steinberg and Q. Zhu, "Lateral resolution in the breast as a function of transducer size," *Ultrason. Imag.* (to be published, 1993).
- ⁶ Q. Zhu and B. D. Steinberg, "Large-transducer measurements of wavefront distortion in the female breast," *Ultrason. Imag.* 14, 276-299 (1992).
- ⁷ Q. Zhu and B. D. Steinberg, "Wavefront amplitude distortion and image sidelobe levels—Part I: Theory and computer simulation," *IEEE Trans. Ultrason. Ferroelec. Freq. Control* 40, 747-753 (1993).
- ⁸ Q. Zhu, B. D. Steinberg, and R. Arenson, "Wavefront amplitude distortion and image sidelobe levels—Part II: In vivo experiments," *IEEE Trans. Ultrason. Ferroelec. Freq. Control* 40, 754-761 (1993).
- ⁹ J. W. Goodman, *Statistical Properties of Laser Speckle Patterns*, edited by J. C. Dainty Topics in Applied Physics (Springer-Verlag, Berlin, 1984).
- ¹⁰ B. D. Steinberg, "Radar imaging from a distorted array: The radio camera algorithm and experiments," *IEEE Trans. Antennas Propag.* AP-29(5), 740-748 (1981).
- ¹¹ E. H. Attia, "Phase synchronizing large antenna arrays using the spatial correlation properties of radar clutter," Ph.D. dissertation, Univ. of Pennsylvania, Philadelphia, PA (1984).
- ¹² S. W. Flax and M. O'Donnell, "Phase aberration correction using signals from point reflectors and diffuse scatterers: Basic principles," *IEEE Trans. Ultrason. Ferroelec. Freq. Control* 35, 758-767 (1988).
- ¹³ E. H. Attia and B. D. Steinberg, "Self-cohering large antenna arrays using the spatial correlation properties of radar clutter," *IEEE Trans. Antennas Propag.* AP-37 (1), 30-38 (1989).
- ¹⁴ L. Nock, G. E. Trahey, and S. W. Smith, "Phase aberration correction in medical ultrasound using speckle brightness as a quality factor," *J. Acoust. Soc. Am.* 85, 1819-1833 (1989).
- ¹⁵ G. E. Trahey, D. Zhao, J. A. Miglin, and S. W. Smith, "Experimental results with a real-time adaptive ultrasonic imaging system for viewing through distorting media," *IEEE Trans. Ultrason. Ferroelec. Freq. Control* 37, 418-427 (1990).
- ¹⁶ B. D. Steinberg and H. Subbaram, *Microwave Imaging Techniques* (Wiley, New York, 1991), Chaps. 8 and 9.
- ¹⁷ M. Fink, "Time reversal of ultrasonic fields—part I: Basic principles," *IEEE Trans. Ultrason. Ferroelec. Freq. Control* 39, 555-566 (1992).
- ¹⁸ B. D. Steinberg, "A discussion of two wavefront aberration correction procedures," *Ultrason. Imag.* 14, 387-397 (1992).
- ¹⁹ M. O'Donnell and S. W. Flax, "Phase aberration measurements in medical ultrasound: Human studies," *Ultrason. Imag.* 10, 1-11 (1988).
- ²⁰ A. R. Selfridge, "Approximate material properties in isotropic materials," *IEEE Trans. Sonic Ultrason.* SU-32(3), 381-394 (1985).

Correction of Multipath Interference Using CLEAN and Spatial Location Diversity

Qing Zhu, Radiology Department and Valley Forge Research Center
 Bernard D. Steinberg, Valley Forge Research Center, Electrical Engineering Department
 University of Pennsylvania, PA 19104

1. INTRODUCTION

Previous studies indicate that ultrasonic wavefront distortion inside the female breast falls into two categories, incoherent scattering and coherent multipath. Scattering reduces target strength, broadens image lobe and lowers the image contrast while refraction creates coherent multipath interference that produces false targets in the image. Time-delay type compensation algorithms are useful to minimize scattered energy and to improve image contrast to a large extent (15 dB) [1]. Further improvement of contrast resolution requires compensation algorithms that can remove false targets. Multipath interference is a much more difficult problem than scattering. Because it is not a stationary, stochastic process, two distinct steps are required to deaberrate refraction-contaminated image. It is first necessary to recognize which target is the true target and which is the false one caused by interference. In Section 2 we demonstrate that when a cluster of true and false targets is imaged from several different array locations the true target remains in position and changes very little in size and shape. The images of false targets, on the other hand, are highly sensitive to the direction from which they are viewed. Therefore, they change sufficiently in location, size and shape to classify them as false. In this way the recognition problem is solved. The second key problem is the elimination of the multipath arrivals. In Section 3, we show that coherent clean technique can be used as a tool to solve the second problem.

2. RECOGNITION OF TRUE TARGETS

A. Diversity Principle

We have found that geometric techniques may be able to separate nonisotropic from isotropic scattered energy. Fig.1 illustrates the case where a single source and 1-D reception are used for descriptive convenience. The same principle is applicable to a multiple source distribution and 2-D configuration. A source radiates into a scattering and refractive medium and its radiation field is received by a receiving aperture. The source image obtained from any aperture is the superposition of the image lobe, image artifacts caused by coherent interference and an incoherent scatter spectrum. The location and shape of the image lobe generally remains

the same when viewed from different apertures, such as the left and right halves of the aperture, while the locations, sizes and shapes of the image artifacts are likely to change because the fields intercepted by different subapertures encounter refractive bodies with different orientations, curvatures and sizes. The incoherent spectrum is statistically the same in each subaperture image. Therefore, the locations and shapes of the large lobes in different subaperture images can be used to distinguish the image lobe from image artifacts. We found experimentally that 2-D large subarray diversity images are in general useful for identification while 1-D subarray images fail to provide identification most of the time because of incomplete distortion information.

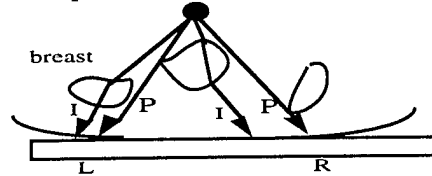


Fig.1 Illustration of diversity. P refers primary field and I interference field. The interference fields change with propagation path.

B. 2-D Experiments

To develop an understanding of deaberration, our studies have concentrated on one-way propagation measurements and corrections of point source fields. The 2-D measurement system and procedure were described in [2]. Briefly, a breast specimen was placed between hemispherical source and receiving array. The 2-D array consisted of a 92-mm 1-D linear array translated 46 mm perpendicular to its axis to form a synthetic 2-D array 92 mm x 46 mm. Element pitch in the receiving transducer was 0.72 mm and a reflecting mask reduced the receiving elevation to 1.44 mm. Frequency was 3.7 MHz. Bandwidth was 2 MHz. Waveforms were measured at each element, from which 2-D wavefronts were reconstructed as functions of time. 3-D image data were calculated by (1) Fourier decomposition of the temporal waveforms at each (x,y) position in the aperture, (2) calculation of a complex CW 2-D image at each Fourier frequency in the focal plane by using the angular spectrum technique, and (3) summation of the 2-D images to form the 3-D transient image.

C. In Vitro Example

Fig. 2 shows an example of single-frequency diversity images. Part (a) is the -20 dB contour plot of 2-D water path image. It is the system diffraction pattern at that contour level. Part (b) is the -20 dB contour plot of the 2-D image of a 4 cm tissue path (brs006) obtained from the entire aperture (92 mm by 46 mm), and (c) is the -20 dB contour of the same image after applying time-delay correction. The improvement is significant because of partial removal of scattered energy. Large multipath lobes remain and decrease image contrast. (d)-(g) are obtained from four subapertures after applying time-delay correction. The real target remains in the same location. False targets move and change size and shapes when viewed from the different subapertures. For example, the lobe with -13 strength located at (4.3 mm, 2.9 mm) in (c) does not appear in (d), therefore it is a false target and should be removed.

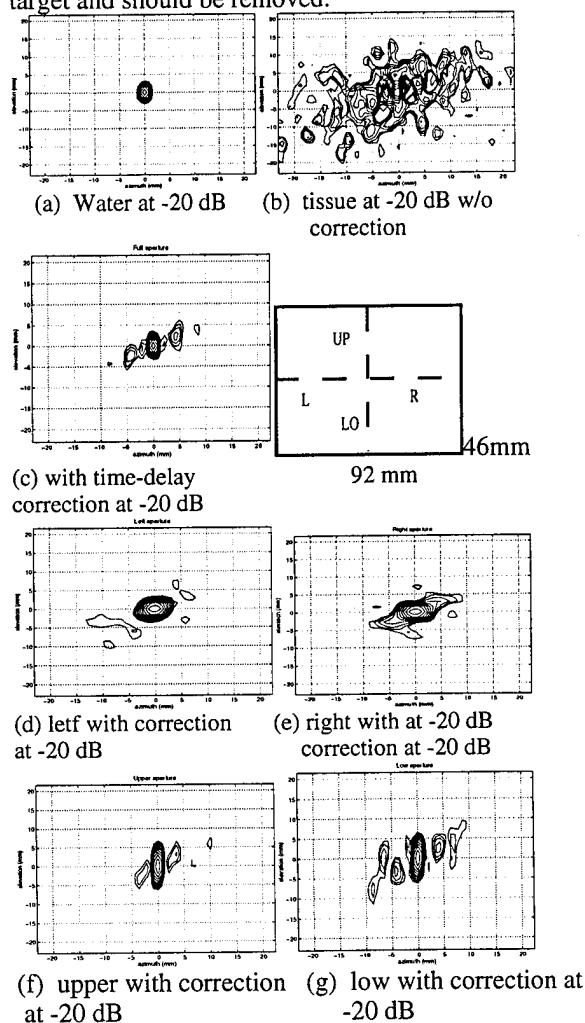


Fig.2 Quadruple spatial diversity discloses false targets. Images are obtained at central frequency. Contour maps are at -20 dB level. Real target remains

in place in subarray images while multipath target changes location, size and shape. (a) Contour map of water path image. (b) Contour map of full-aperture tissue image (brs006) at -20 dB. (c) Contour map of the full-aperture image brs006 at -20 dB after time-delay correction. (d) Image from left half of array. 46x 46 mm. (e) From right half. (f) From upper half (23x92mm). (g) From low half. Point source remains in center in all images. Shape change is due to the change of aperture size.

3. COHERENT CLEAN

A. CLEAN

CLEAN is a nonlinear deconvolution procedure originated in radio astronomy in the 1960s [3], extended to radar by Tsao and Steinberg [4] and applied to ultrasound by Cohen (1992) [5]. The simplest CLEAN procedure is described as following. The diffraction pattern $f(u)$ is shown upper left in Fig.3. The procedure begins with the original dirty image $A_0(u)$ (Fig.3a). The strongest source is found and its complex amplitude a_0 and coordinates u_0 are measured. An image of that source is found by convolving the radiation pattern with a δ -function of strength a_0 located at u_0 . Some fraction of this image is subtracted from $A_0(u)$. The result of this first iteration is a new image, $A_1(u)$, from which all energy from the strongest source has been removed, including its sidelobe energy (Fig.3b). The process continues until the subtraction procedure produces images with negative values or increases energy in the residual image. The result at this stage is a list of detected sources. The next step is to calculate a CLEAN beam that has the resolving power of $f(u)$ but without its sidelobe distortion. The final image is the convolution of the CLEAN beam and each of the detected sources (Fig.3c).

However, the CLEAN procedure cannot be directly applied to an image that is contaminated by image artifacts, because CLEAN will pick up true targets as well as false targets. A clever use of CLEAN is the following.

Step 1 (descattering): Apply time-delay type descattering algorithms upon each diversity image and original image to reduce the scattering induced distortion upon images. This descattering procedure strengthens targets (see Fig. 2(b) and (c)) and improves the performance of CLEAN by providing better target subtraction and consequently exposing more weak targets.

Step 2 (coherent CLEAN): Clean each diversity image and the full aperture image using the approximate system diffraction patterns of the corresponding subarray and the full array.

The result is a set of lists of targets (real and false). Each list is a CLEANed result of each diversity image.

Step 3 (location diversity): Select targets which appear on all lists by using location or neighborhood matching procedures. These targets are considered as true targets.

Step 4 (image reconstruction): Reconstruct a full aperture image from the true targets.

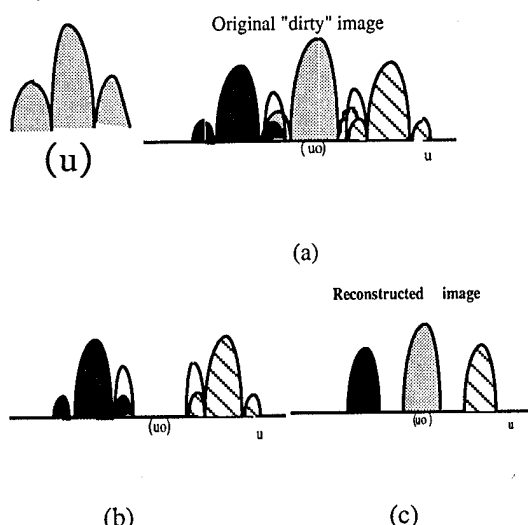


Fig. 3. Illustration of the clean procedure. (a) "Dirty image" of three point targets is the envelope of the coherent sum of the three images. (b) After the first iteration of the clean procedure. The strongest target is subtracted out as well as its sidelobes. Final result of cancellation process is a list of targets (strengths and locations) $A_i \delta(u - u_i)$. (c) Final reconstructed image $= \sum_i A_i \delta(u - u_i) * f(u)$.

The above CLEAN procedure was done at each frequency except for Step 1 which was done in time domain before the Fourier decomposition. The 3-D transient image was obtained by summation of the 2-D CLEANed images at all discrete frequencies obtained from Step 4.

Also, CLEAN is *modified* to change the diffraction pattern $f(u)$ to produce better subtraction result at each iteration. We call this modified CLEAN procedure MCLEAN in the following text. MCLEAN differs from CLEAN in step 3.

B. Experimental Results

Fig. 4 is the CLEANed image of Fig. 2(c) at -30 dB contour after step 2. CLEAN has picked up 30 false targets in addition to the true target. After location diversity, all false targets

are identified. Table I gives the identification result of this example. Each triple represents the x and y locations of the target in mm in full-aperture image identified by CLEAN, and corresponding matching result in bold letter. For example, the first triple indicates that the target located at (0.0 0.0) appeared in four subapertures and therefore can be identified as true target. The 2-D neighborhood distance used

for matching is calculated as $R \sqrt{\left(\frac{\lambda}{L_1}\right)^2 + \left(\frac{\lambda}{L_2}\right)^2}$,

where aperture dimensions L_1 and L_2 are 46.08 mm and 92.16 mm, R is the focussing distance and λ is the wavelength of each discrete frequency. No misclassification occurs in this frequency. The peak of the noise floor after CLEAN is 23.4 dB lower than the peak value before CLEAN. Since the original peak artifact to peak target ratio is -13.0 dB, the dynamic range has been improved by 10.4 dB using MCLEAN. MCLEAN has been repeated on all 39 discrete frequencies. Two misclassifications occur in two CW images. In one case, a false target was identified as true and in another true was identified as false. However, these cases happen in CW images obtained from the low and/or high frequency ends where the signal to noise ratio is low. Fig. 5(a) is the MCLEANed wideband sample image, after peak detection of the 3-D transient image, at -30 dB level. Fig. 5(b) is the wideband water path image at -30 dB for comparison. The false target which appeared at one frequency does not contribute much to the final wideband image because of its low strength. The true target, which was identified as false, was removed at step 4 before the summation to form the 3-D wideband image. The result is the 0.01 dB reduction of the true target strength compared with its strength before MCLEAN. The peak of the wideband noise floor after MCLEAN is -25.1 dB lower than the peak value of the true target before MCLEAN. Since the peak artifact to peak target ratio in wideband image before MCLEAN is -14.5 dB, the dynamic range has been improved by 10.6 dB by MCLEAN.

The average location of the true target in all frequencies in this example is (0.0 mm, 0.0 mm) with (0.73 mm, 0.82 mm) or $d = 1.1$ mm perturbation, which is well within the weighted neighborhood distance

$$\frac{\sum (\lambda_i R \sqrt{(\frac{\lambda_i}{L_1})^2 + (\frac{\lambda_i}{L_2})^2})}{\sum \lambda_i} = 7.9 \text{ mm over all}$$

frequencies. This implies that spatial diversity is an effective method for identification of true target.

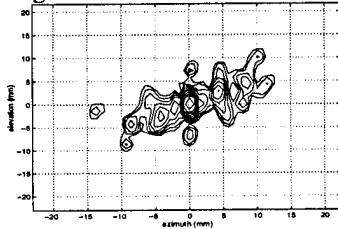


Fig. 4. Reconstructed image of Fig. 2(c) at -30 dB level after step 2 coherent CLEAN.

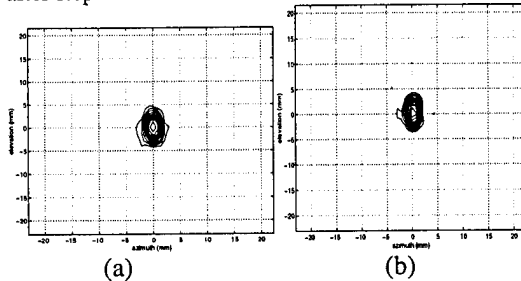


Fig. 5. (a) -30 dB contour of 3-D transient MCLEANed image of brs006 after peak detection. (b) -30 dB contour of 3-D transient water path image after peak detection.

Table I. Locations of the targets and results of spatial matching

(0.0, 0.0, 4),	(4.3, 2.9, 3),	(-4.3, -2.9, 3),
(-2.2, -1.4, 2),	(2.2, 0.0, 2),	(-5.0, -4.3, 0),
(-4.3, -1.4, 0),	(8.6, 4.3, 1),	(5.0, -1.4, 0),
(7.9, 0.0, 2),	(-8.6, -4.3, 0),	(3.6, 1.4, 1),
(-6.5, 0.0, 1),	(-0.7, 2.9, 0),	(4.3, 7.2, 0),
(1.4, 2.9, 0),	(-5.8, 1.4, 0),	(7.2, 5.8, 0),
(11.5, 4.3, 0),	(-2.2, 1.4, 1),	(-7.2, -1.4, 0),
(9.4, 8.6, 0),	(10.1, 10.1, 0),	(-13.7, -1.4, 0),
(0.0, -7.2, 0),	(0.0, 7.2, 0),	(5.8, -2.9, 1),
(10.8, 2.9, 0),	(-9.4, -8.6, 0),	(0.0, -4.3, 0),
(-2.2, -4.3, 0),		

The bold number in each triple is the matching result.

The statistics of the performance of MCLEAN upon 7 samples with well-defined multipath artifacts are given in Table II. The data are self explanatory.

4. DISCUSSION/CONCLUSION

2-D spatial diversity images are useful for identification of true target vs. refractive artifacts. Cohere CLEAN in conjunction with diversity is a useful tool to reconstruct artifact-free high resolution images. The preliminary results with 7 in vitro samples show 7.3 dB

dynamic range improvement with negligible target strength change.

The diffraction pattern used in this report was only modified by varying the focusing speed to match the distorted mainlobe as well as refractive lobes to obtain better subtraction in step 2. The dynamic range can be further improved if the diffraction pattern is modified by perturbing higher order focusing terms to improve the subtraction. This is a subject of for future study.

Table II. Statistics of MCLEAN of 7 breast samples

Target strength reduction (dB)	0.06 (std. 0.06)
Dynamic range improvement (dB)	7.3 (std. 1.92)
Location stability of true target (mm)	1.7 mm (std. 2.9)
Misclassification:	
True as false	4.0% (std. 3.9%)
False as true	11.0% (std. 12.7%)

ACKNOWLEDGMENTS

The *in vitro* measurements were done with the collaboration of Ms. Laura M. Hinkelman and Prof. Robert C. Waag, Departments of Electrical Engineering and Radiology, University of Rochester, Rochester. Invaluable comments were given by Dr. Kai Thomenius, Director of Research, Interspec, Inc., Ambler, PA., a division of ATL. Funding was provided by the Army (DAMD 17-93-J-3014 and DAMD 17-94-J-4133) and NSF (BCS92-09680).

REFERENCE

- [1] Q. Zhu, B. D. Steinberg, "Modelling and Correction of Incoherent Wavefront Distortion," submitted to International Journal of Imaging Systems and Technology (Sept. 1995).
- [2] L. M. Hinkelman, D-L. Liu, and R. C. Waag, Q. Zhu, and B.D. Steinberg, "Measurement and Correction of Ultrasonic Pulse Distortion Produced by the Human Breast", J. Acoust. Soc. Am. 97(3), 1958-1969 (1995).
- [3] Hojbom, J. A., "Aperture Synthesis with Non-Regular Distribution of Interferometer Baselines," Astron. Astrophys. Suppl., Vol. 15, pp. 417-426, 1974.
- [4] Tsao, J. and B.D. Steinberg, "Reduction of Sidelobe and Speckle Artifacts in Microwave Imaging: The Clean Technique," IEEE Trans. Antennas and Prop., Vol. 36, No. 4, April 1988, pp. 543- 556.
- [5] Cohen, N., "Practical real-time deconvolution and image enhancement of medical ultrasound," Biological Image Processing and 3D Microscopy, ed. by R. Acharya, C. Cogswell and D. Goldgof, SPIE, Bellingham WA 1992.

UP-VFRC-1-95

February 1995

SCATTERING FROM A MULTIPLE RANDOM PHASE SCREEN MODEL OF A RANDOM INHOMOGENEOUS MEDIUM*

Bernard D. Steinberg
Valley Forge Research Center
The Moore School of Electrical Engineering
University of Pennsylvania
Philadelphia PA 19014
steinber@pender.ee.upenn.edu

ABSTRACT

The decrease in image target contrast due to scattering of ultrasound energy by an inhomogeneous body is calculated and tested. The analysis is in terms of measurable parameters of the medium (thickness, phase or time-delay variance and correlation length) and parameters of the scanning equipment (frequency and array size). The propagation medium is modeled as a sequence of thin, random phase screens and the number of screens is related to the sample thickness and to the size of the scattering bodies.

It is found that (1) scattering produces a halo, centered on each target, with diameter ($2-6^\circ$ at 3 MHz) proportional to wavelength, (2) target contrast within the halo, defined as target to clutter power ratio (TCR), increases linearly with 2-D array area, is inversely proportional to tissue sample thickness and time delay variance per unit distance in the tissue and decreases quadratically with correlation distance and frequency and (3) multiple scattering plays no significant role.

Several elements of the theory are tested against experimental data. Although the amount of relevant data is small the theory checks well against what does exist.

PACS numbers: 43.80.Cs, 43.80.Ev, 43.80.Vj

GLOSSARY OF TERMS

L	array size
$\lambda, f, \omega = 2\pi f$	wavelength, frequency, angular frequency
λ/L	lateral resolution
σ_ϕ^2	phase variance per screen

* Submitted to JASA. Principally supported by grants from NSF (BCS92-09680) and the Army (DAMD17-93-J-3014).

σ_t^2	time delay variance per screen
x_0	e^{-1} correlation distance of tissue
$\Delta u_s = \lambda/\pi x_0$	half-power width of the scatter spectrum:
$a \approx \pi x_0$	typical scatterer size
TCR	target to clutter power ratio within halo
TDR	target dynamic range within halo
D	propagation path length or tissue thickness
$N \approx D/a$	number of screens
$\sigma_{\phi m}^2, \sigma_{\tau m}^2$	measured phase, time delay variance in tissue
D_m	tissue thickness in which $\sigma_{\phi m}^2$ or $\sigma_{\tau m}^2$ are measured

INTRODUCTION

Wavefronts distort when ultrasound propagates through an inhomogeneous medium, lowering target contrast in the image and introducing image artifacts¹⁻⁹. Isotropic scattering reduces the contrast. The artifacts are discrete multipath arrivals that look like targets⁹. The motivation for most studies of this topic is aberration correction for large aperture, 2-D high resolution imaging. This paper deals with isotropic scattering only. Discrete multipath will be dealt with later. The paper presents a theory of the effect of scattering upon important image quality parameters such as target to clutter power ratio (TCR) and lateral resolution. Several elements of the theory are tested against experimental data.

The main findings are:

- When target strength is stronger than background scattering, the principal scattering mechanism is primary (i.e., simple, single or nonmultiple) scattering.
- Scattering produces a halo in the image centered on each scatter source or target. It's width is the order of 2-6 deg at 3 MHz and is proportional to wavelength.
- TCR within the halo is linear with 2-D array area, inversely proportional to time delay variance per unit distance and propagation path length and decreases as the square of the frequency and correlation distance. The formula is
$$TCR \approx \frac{L^2}{D\omega^2(\pi x_{0m})^2(\sigma_{\tau m}^2/D_m)}$$
- Target dynamic range is about an order of magnitude smaller than TCR.

§1 models the inhomogeneous medium as a cascade of thin, random phase screens and the incident radiation from the target as a plane wave. In §2 the scattered power P_{scat} per screen

is calculated as a function of the phase variance per screen, and also the ratio of P_{scat} to the power P_{pw} of the emergent plane wave. We also calculate the angular width of the scatter field. From these we determine the TCR in the target image and how the lateral and contrast resolution or target dynamic range are affected by the scatter. The target is the source of the plane wave and the clutter is the scatter or background energy. In §3 we calculate the effective number of screens making up a large body and show how to combine the multiple scattering effects between the many screens. We then calculate the quantities above for the entire propagation medium. §4 discusses related topics. Summary and Observations is §5.

1. THE MODEL

When a point target or source is imaged through a weakly scattering medium (small scattering coefficient) the scattered energy creates a background field that clusters about the target image and decreases its contrast with the background and therefore its visibility. It is the same phenomenon that produces the halo around stars and the ring around the moon that one often sees on humid nights. The ultrasound halo is found to be about 2-6 deg wide at 3 MHz centered about the target. Its effect is minimal with small transducers whose beams are comparable to or larger than the halo. But with narrow beamwidth, high resolution arrays the scattered energy can materially reduce target contrast. The calculations use only measurable or known quantities. The scattered energy is variously called scatter or clutter. The diminution in TCR in the image is calculated as well as the angular width of the scatter field and the effects upon lateral and contrast resolution (or target dynamic range) of the imaging system. The procedure divides the medium into thin slices, calculates the relevant statistical properties per slice and then recombines the slices.

A unit amplitude plane wave from an impulsive source propagates from the left in the positive z direction through a random inhomogeneous medium, defined by a uniform, isotropic distribution of scatterers, located in the x, z plane (Figure 1a)[†]. Each slice is treated as a thin, random phase screen with independent scattering occurring in each screen. Each screen is infinite in length (x axis). Its thickness (z axis) is the order of the scale of the compressibility and density variations of the medium, denoted a in the paper. Each screen is defined by a zero-mean, Gaussian random phase shift process $\phi(x, z)$ with phase variance σ_ϕ^2 . $\phi(x, z)$ is the phase delay at frequency f within the signal spectrum through a thin vertical slice perpendicular to the direction of propagation. The propagation delay $\tau(x, z)$ is related to the phase delay by $\phi(x, z) = \omega\tau(x, z)$, $\omega = 2\pi f$. The variation in $\tau(x, z)$ may be attributed to the local medium perturbations, as modeled in the phase screen detail of Figure 1b. The scale of the perturbations is denoted a .

[†] Although the analysis is based upon a plane wave source, the results are also applicable in the focal plane of a focused system close to the focal point. See §4.1.

The time delay variance per slice $\sigma_t^2 = \sigma_\phi^2/\omega^2$. The correlation function of the phase $R(x) = \sigma_\phi^2 \rho(x)$ is modeled as an exponential with correlation distance x_0 . x_0 is related to scatterer size a by $a = \pi x_0$ (§2.5).

Tissue parameters σ_ϕ^2 and x_0 are obtained from measured data. x_0 is the value of x for which $\rho = e^{-1}$. Measurements of variations of arrival time across wavefronts disclose σ_ϕ^2 . Measurements are usually made through tissue thickness $D > a$, \Rightarrow number of slices $N > 1$. The phase variance through N slices is $\sigma_{\phi,N}^2$ and the relation to the single-slice variance is $\sigma_{\phi,N}^2 = N\sigma_\phi^2$ because of the assumed independence of the phase from screen to screen (§3.5). The measured value of x_0 is not a first-order function of N .

2. SCATTERING FROM A RANDOM PHASE SCREEN

The far-field radiation $f(u)$ from a single, infinite screen (Figure 1b) contains an emergent plane wave $f_{pw}(u)$ plus the scattered field $f_{scat}(u)$. The plane wave is reduced in amplitude to account for the energy in the scattered wave as it passes through the screen. $f(u)$ is the Fourier transform of $\phi(x)$, in units of the reduced angular variable $u = \sin\theta$:

$$\begin{aligned} f(u) &= \int e^{j\phi(x)} e^{jkxu} dx \\ &= f_{pw}(u) + f_{scat}(u) \end{aligned} \quad (1)$$

$k = 2\pi/\lambda$ is the wavenumber and $\phi(x)$ is the random phase shift previously described. $f(u)$ is decomposed into the sum of a plane wave $f_{pw}(u) = A\delta(u)$ emerging from the screen and a scattered wave $f_{scat}(u)$. The amplitude of the plane wave is A .

2.1 The emergent plane wave

To calculate $f_{pw}(u)$, $f(u)$ is expanded in a power series and its expectation $E[\cdot]$ taken.

$$f(u) = \int (1 + j\phi - \phi^2/2 - j\phi^3/3! + \phi^4/4! \dots) e^{jkxu} dx \quad (2)$$

The first term is the incident plane wave. The remainder are the scattered terms. Their mean values (expectations, spatial dc) add (subtract) coherently to (from) the incident plane wave and the total establishes the amplitude A of the emergent plane wave. Thus

$$f_{pw}(u) = Ef(u) = \int (1 + E[j\phi - \phi^2/2 - j\phi^3/3! + \phi^4/4! \dots]) e^{jkxu} dx = \int A e^{jkxu} dx \quad (3)$$

$$\begin{aligned} A &= 1 + E[j\phi - \phi^2/2 - j\phi^3/3! + \phi^4/4! \dots] \\ &= 1 + E[\sum_{n=1} j^n \phi^n / n!] \\ &= 1 - \sigma_\phi^2/2! + 3\sigma_\phi^4/4! - 5\sigma_\phi^6/6! + 7\sigma_\phi^8/8! \dots \end{aligned} \quad (4)$$

because the assumed pdf is Gaussian (all odd moments are zero).

The power P_{pw} in the emergent plane wave is proportional to A^2 . Ignoring the proportionality factor, $P_{pw} = A^2$ is plotted in Figure 2 (small circles) for a range of values of σ_ϕ^2 .

2.2 Energy in the scattered field

No loss to absorption is yet included in the model^{††}. (When loss is included (§3.6), the conclusions are found to be unaltered.) Consequently the energy in the scattered field $P_{scat} = 1 - A^2$, which is plotted (as stars) in Figure 2, is the difference between the incident (unit) power and P_{pw} . Lastly, the ratio P_{scat}/P_{pw} , is plotted as plus signs. The fields have equal energies at $\sigma_\phi^2 = 0.7$ and the ratio rises to 1.7 at $\sigma_\phi^2 = 1$. Large values of σ_ϕ^2 severely degrade the quality of ultrasound images. From the theory of radiation pattern distortion caused by random phase errors^{#, 11} σ_ϕ^2 must fall in the neighborhood of 10^{-2} or less for reasonably acceptable beam quality. Thus practical interest lies to the extreme left of Figure 2, which implies a very weak scattering process in which most of the energy passes through each screen unscattered.

2.3 Angular width of the scattered field

The scattered field is the difference between (2) and (3):

$$\begin{aligned} f_{scat}(u) &= \int [j(\phi - E\phi) - (\phi^2 - E\phi^2)/2 - j(\phi^3 - E\phi^3)/3! + (\phi^4 - E\phi^4)/4! \dots] e^{jkxu} dx \\ &= \int [\sum_{n=1} j^n(\phi^n - E\phi^n)/n!] e^{jkxu} dx \\ &= \int [1 - A + \sum_{n=1} j^n\phi^n/n!] e^{jkxu} dx \end{aligned} \quad (5)$$

$f_{scat}(u)$ is a function of the random process $\phi(x)$ and therefore is also a random process. Its power $P_{scat} = 1 - A^2$. Its angular width is found from its angular power density spectrum $S(u)$. $S(u)$ is proportional to the expectation of the square magnitude of the scattered field, $E|f_{scat}(u)|^2$, which in turn can be obtained from the Fourier transform $F\{\cdot\}$ of the correlation function calculated from the measured radiation field, i.e., $S(u) = F\{R(x)\}$.

Wavefront correlation experiments performed in *in vivo* breast¹² have measured the normalized correlation function $\rho(x) = R(x)/R(0)$. From these data the correlation function is found to approximate a decaying exponential (Figure 3). Hence we model

^{††} Absorption is added later in §3.6, where it is found that its inclusion does not materially alter the conclusions of §2.2.

[#] Average sidelobe powerlevel relative to main lobe = $ASL = \sigma_\phi^2/N_e$ where N_e is the no. of array elements¹¹. Specifying -40 dB for the required ASL and assuming the order of 100 array elements, $\sigma_\phi^2 \approx 10^{-2}$. This formula has been checked repeatedly in adaptive beamforming experiments in radar beginning in the early 1980s¹⁶.

$$\rho(x) = \exp(-x/x_0) \quad (6)$$

and call x_0 the e^{-1} correlation distance^{##}. $x_0 = 1.8, 3.3$ and 3.3 mm for average correlation curves of three groups of asymptomatic women: premenopausal dense breasts, premenopausal fatty and postmenopausal. The number of correlation functions averaged were 35, 52 and 76. Other reported measurements are in the same neighborhood^{6,10}. The Figure 3 curves and the body of data from which they come¹² were obtained over long, 12-cm paths, which corresponds to many correlation distances or several phase screens (§3.1). Hence it is possible that the correlation evidence leading to (6) is not representative of a single screen. This is checked in §3.5 where it is shown that the angular spectral width estimated from these data and (6) is representative of a single screen. The result indicates that single scattering dominates, which means that the total scattering spectrum observed out of each of the phase screens approximates a first-order spectrum. This further implies that correlation measurements made from any thickness of tissue disclose x_0 .

Based on (6) the unnormalized correlation function and the angular power spectrum are

$$R(x) \approx \sigma_\phi^2 \exp(-x/x_0) \quad (7)$$

$$S(u) \approx \frac{\sigma_\phi^2 x_0}{1 + (kux_0)^2} \quad (8)$$

and the half-power width of the scatter power spectrum is

$$\Delta u \approx 2/kx_0 \approx \lambda/\pi x_0 \quad (9)$$

which, for a frequency of 3 MHz ($\lambda = 0.5$ mm) and for the values of x_0 given above for the mean correlation functions of premenopausal-dense and premenopausal-fatty/postmenopausal breasts, is 0.089 and 0.048 rad or 2.7 and 5.1 deg. Allowing about one standard deviation additional spreads about the means the predicted halo width Δu increases to 2-6 deg at 3 MHz and is inversely proportional to frequency.

2.4 Estimate from breast samples

An independent prediction of halo width can be made from the size of subcutaneous fat globules in breast tissue. Fat globules have random sizes, orientations and radii of curvature.

^{##} As distinct from the FWHM measure of correlation distance. The relation between the two for the exponential correlation model (6) is $x_{FWHM} = 1.38x_0$.

The scale is predominantly in the 5 to 15 mm range. Each globule is a likely candidate for scattering of ultrasound waves, as seen in a radiologist's schematic of a breast section (Figure 4)¹³.

Referring back to Figure 1b, the distance between scatterers or density hills shown there is nominally a . Scattered energy from subcutaneous fat should lie largely in the Fourier angular interval $\Delta u_F \approx \lambda/a$, $5 < a < 15$ mm, which at 3 MHz is 0.033-0.1 rad or 1.9 to 5.7 deg. The fact that this interval is substantially identical to the calculated halo width of 2-6 deg from correlation data (§2.3) suggests that subcutaneous fat is one of the contributors to the scattered field.

2.5 Exponential coefficient vs. frequency

Time delay variations should be independent of frequency because they result directly from local tissue density variations. Frequency dependence manifests itself in the phase variance where $\sigma_\phi^2 = \omega^2 \sigma_\tau^2$. Consequently, the phase variance should grow as the square of the frequency. Theory also predicts that x_0 and the scatterer size a are related by $a = \pi x_0$ by equating the two calculations of scatter spectrum width, $\Delta u \approx \lambda/\pi x_0$ (9) and $\Delta u_F \approx \lambda/a$ (§2.4). But a is independent of frequency. Therefore the correlation function should be independent of frequency, which agrees with the 3 and 4 MHz comparison shown in Figure 3.

2.6 Point source image

When the composite field $f(u) = f_{pw}(u) + f_{scat}(u)$ is imaged, whether by spherical lens or transducer (Figure 5), the image (in one dimension) in the focal plane contains the point source and the apparent source distribution of the scattered field, each convolved with the diffraction pattern of the lens or transducer. The target is reduced in amplitude to A and it images as the diffraction pattern of the transducer, with half-power width λ/L . The angular clutter spectrum is depicted in the figure as a continuum, which is not a realistic portrayal because it is a Fourier transform of the random phase-perturbation process $\phi(x)$; hence it too is a random process with peaks and valleys. No instantaneous sample function is so smooth. For simplicity the clutter amplitude spectrum is drawn as a smooth function, which may be interpreted as the sq. rt. of the angular clutter power spectrum $S(u)$. The half-power width is $\lambda/\pi x_0$. The clutter power is $1-A^2$. After convolution with the transducer diffraction pattern the half-power width of the clutter spectrum equals the rms sum of $\lambda/\pi x_0$ and λ/L :

$$\Delta u_s = [\lambda/\pi x_0]^2 + (\lambda/L)^2]^{1/2} = \lambda/\pi x_0 \oplus \lambda/L \quad (10)$$

Figure 6 pictures other images. Part a is the image without the phase screen. The unit-amplitude plane-wave image is spread to the diffraction pattern. It consists of a main lobe of

width λ/L plus sidelobes. L is the size of the aperture. The image with the screen is part *b*; it is the same as the image in Figure 5. Its width is $\approx \lambda/\pi x_0$ for high resolution imaging, for then $L \gg \pi x_0$. It is also possible for the opposite condition to hold, i.e., $\pi x_0 > L$, which occurs when the nominal scatterer size exceeds the aperture size of the imaging system. In this case the "scatterer" is a "large" surface (relative to the transducer) such as a wedge which refracts the incident wave and bends the beam. The image is then displaced from its original orientation (in the u -axis) by the refraction angle u_r . Part *c* depicts the case of wedge refraction plus weak scattering. A realistic "wedge" would have rounded rather than planar facets which would change the focal length of the beam and therefore defocus the image (*d*). For the pure scattering problem addressed in this paper we ignore refraction and select $\Delta u_s \approx \lambda/\pi x_0$.

2.7 Resolution

It is evident that lateral resolution is unaffected by the scatter field; it remains the width λ/L of the mainlobe of the diffraction pattern of the aperture *unless the scattered energy obscures the main image lobe*¹⁴. When this happens lateral resolution and contrast vanish. This phenomenon is a direct consequence of increasing the path length (§3.4 and eq.(13)).

2.8 Target to clutter power ratio

Figure 6 is an angular amplitude spectrum. While the scatter spectrum is pictured as a smooth continuum, any sample spectrum is itself a random function with peaks and valleys because the spectrum is the Fourier transform of the random phase-screen process. The target can be discerned so long as it well exceeds the peaks of the scatter spectrum. The measure of target detectability is the target contrast or target to clutter power ratio TCR, which can be estimated for a square 2-D array of size L as follows.

The target and the clutter fields spread in two dimensions as they propagate (Figure 7a). Approximate the angular power spectrum by the sum of two right circular cylinders (part b), pictured in cross section as rectangles in part c. The first cylinder is the target spectrum. Its power A^2 spreads over a circle of diameter λ/L . Its height, therefore, is $(AL/\lambda)^2(4/\pi)$. The second spectrum is the clutter region or halo $S(u)$ induced by the target. Its area is $1-A^2$ and its width is $\lambda/\pi x_0$. Its height is $(1-A^2)(\pi x_0/\lambda)^2(4/\pi)$. Hence the target to clutter power ratio within the halo is

$$\text{TCR} = \frac{A^2 L^2}{(1-A^2)(\pi x_0)^2} \approx \frac{L^2}{\sigma_\phi^2 (\pi x_0)^2} = \frac{L^2}{\omega^2 \sigma_r^2 (\pi x_0)^2} \quad (11)$$

where the approximation $\Rightarrow A \approx 1$ and $1-A^2 \approx \sigma_\phi^2$. Eq.(11) shows that TCR for a single, thin screen is quadratic with 2-D transducer size (linear with area) and inversely proportional to the

time-delay variance of the screen and the square of the frequency and the correlation distance. The frequency dependence of TCR enters only through $\sigma_\tau^2 = \omega^2 \sigma_\tau^2$, because the density and compressibility variations in the tissue induce time delay variations that are independent of frequency (§2.5).

2.9 Target dynamic range

From TCR (11) we can determine the smallest target that can be detected in the interference background and hence the target dynamic range (TDR), which is the ratio of the largest to the smallest detectable target. Eq. (11) is the ratio of the target intensity to the average intensity of the clutter field within the halo. Because the field develops as a bandlimited, noise-like random process, upward deviations of 10 dB from the mean are not unlikely (order of 1% occurrence frequency)¹⁵. Hence other targets within the halo that are 10 dB greater than the mean clutter intensity will not be discernible amidst the high peaks in the clutter spectrum. At least a few more dB are required for unambiguous single-look target detection, although with multiple looks 10 dB is sufficient. Thus suitable contrast between the target image and the clutter background within the halo requires a minimum TCR of about 10 dB. In other words, TDR within the halo is about an order of magnitude smaller than TCR.

3. MULTIPLE ADJACENT SCREENS

The input to the first screen is the unit amplitude plane wave shown in Figure 1. The emergent plane wave plus the scattered field (5) is the input to the second screen, the output of which is the input to the third screen, etc., as shown in Figure 8. The emergent radiation is pictured there as angular (Fourier) spectra with the u-axis parallel to each screen.

3.1 Screen thickness and number of screens

The number of screens N is the propagation depth D of a target divided by the screen thickness. The infinitely-thin screen model calls for as small a thickness as other considerations allow. Because of the assumed independence of the phase distribution from screen to screen, screen thickness can be no smaller than scatterer size a . This is also reasonable on physical grounds, for otherwise the scale of the scattering structure would be altered by choice of screen dimension. For these reasons the nominal scatterer size is taken as the lower bound on screen thickness. Thus, for a propagation depth D of 6 cm and a nominal scatter size $a \approx 1$ cm, the number of screens $N \approx 6$.

3.2 Output angular spectrum

The clutter build-up is illustrated in Figure 8. Its angular spectrum is derived as the output of a cascade of N linear filters, each with angular impulse response $h_n(u)$, $n = 1, 2, \dots, N$. The first screen has impulse response $h_1(u) = A_1\delta(u) + s_1(u)$, which is the total spectrum out of the first screen. $A_1\delta(u)$ is a Dirac δ -function of amplitude A_1 (power A_1^2) located at the origin in the angular spectrum. $s_1(u)$ is a continuous scatter spectrum of power $1-A_1^2 \approx \sigma_\phi^2$, the phase variance of the screen. The total power is unity, as it must be, because no losses have yet been assumed. The width of $s_1(u)$ is $\Delta u \approx \lambda/\pi x_0$ (9).

Screen 2 has impulse response $h_2(u) = A_2\delta(u) + s_2(u)$. Its angular spectrum is $h_1(u)*h_2(u)$, where $*$ denotes convolution. It consists of three parts; a plane wave of amplitude A_1A_2 , the sum of two primary scatter spectra, $A_2s_1(u) + A_1s_2(u)$, and a secondary scatter field $s_1(u) * s_2(u)$. The first primary scatter spectrum arises from the $s_1(u)$ passing unchanged in shape through the screen but reduced in amplitude by A_2 , the plane-wave voltage gain of screen 2; the second is the scattering $A_1s_2(u)$ of the plane wave incident upon screen 2. The power in the primary scatter spectrum is $A_2^2(1-A_1^2) + A_1^2(1-A_2^2)$. The power in the second order scatter spectrum is $(1-A_1^2)(1-A_2^2)$. The total power in the emergent field is again unity ($A_1^2A_2^2 + A_2^2[1-A_1^2] + A_1^2[1-A_2^2] + [1-A_1^2][1-A_2^2] = 1$).

The angular spectrum from screen 3 is $h_1(u)*h_2(u)*h_3(u)$. It consists of a plane wave $A_1A_2A_3\delta(u)$, a primary scatter field $A_3[A_2s_1(u) + A_1s_2(u)] + A_1A_2s_3(u)$, a secondary field $[A_2s_1(u) + A_1s_2(u)] * s_3(u) + A_3[s_1(u) * s_2(u)]$ and a tertiary scatter field $s_1(u) * s_2(u) * s_3(u)$. The primary scatter power is $A_3^2A_2^2(1-A_1^2) + A_3^2A_1^2(1-A_2^2) + A_1^2A_2^2(1-A_3^2)$. The secondary scatter power is $A_2^2(1-A_1^2)(1-A_3^2) + A_1^2(1-A_2^2)(1-A_3^2) + A_3^2(1-A_2^2)(1-A_1^2)$ and the tertiary scatter power is $(1-A_1^2)(1-A_2^2)(1-A_3^2)$.

After N screens the angular spectrum is the N -fold convolution $h_1(u)*h_2(u)*\dots*h_N(u)$. It contains a δ -function representing the emergent plane wave. Its amplitude is $A_1A_2\dots A_N$ which we will call A^N , where A is the geometric mean of the A_i . This is the target. All other components of the output spectrum add to create the signal-induced clutter spectrum.

The power spectrum of the output primary clutter field in Figure 8 is the sum of the primary power spectra and similarly for the higher order scattered fields. Fortunately this complicated picture can be simplified considerably.

3.3 Output power spectra

Schema of cross sections of the target spectrum and the first three scatter spectra are illustrated in Figure 9. The output target power $P_T = [\prod_{i=1}^N A_i]^2 = A^{2N}$. The target power is spread in both dimensions over the diffraction pattern of the transducer. The bulk of the power is in the main lobe. Its beamwidth is λ/L and its angular cross section is $(\pi/4)(\lambda/L)^2$. Within the

beam the power density is $\sim \frac{4A^{2N}}{\pi(\lambda/L)^2}$. Its spectrum is shown schematically in the upper part of Figure 9.

The $s_i(u)$ are independent spectra because they are derived from independent sample functions of the random phase-delay process defining the inhomogeneous medium. They are continuous, noise-like terms with zero means and their powers add. The same is true for convolutional terms such as $s_i(u) * s_j(u)$, $s_i(u) * s_j(u) * s_k(u)$, etc. What is pertinent for each such term is its width and its power and to a much lesser extent its shape. All $s_i(u)$ have the same nominal width, power and shape. Therefore we identify all $s_i(u)$ with a generic first order random scatter spectrum $s(u)$, all $s_i(u) * s_j(u)$ with a generic second order scatter spectrum $s(u) * s(u)$, and so forth. The half-power width of $s(u)$ is $\lambda/\pi x_0$. Variances add under convolution. Therefore the width of $s(u) * s(u)$ is $\sqrt{2}\lambda/\pi x_0$. The widths of higher order convolutions are $\sqrt{3}\lambda/\pi x_0$, $\sqrt{4}\lambda/\pi x_0$, etc. Areas multiply under convolution. The power in $s(u)$ is $1-A^2$, in $s(u) * s(u)$ it is $(1-A^2)^2$, etc. One $s(u)$ term arises from the first screen, two $s(u)$ terms weighted by A from the second, three $A^2 s(u)$ terms from the third, and so forth. Finally, N $s(u)$ terms emerge from the final screen with a weight of A^{N-1} . The power in each term is $(1-A^2)A^{2(N-1)}$. Because the N $s(u)$ terms are independent, their powers add. Therefore the power in the first order scatter spectrum $P_{C1} = N(1-A^2)A^{2(N-1)}$.

Similarly the power in the second order spectrum $P_{C2} = \binom{N}{2}(1-A^2)^2 A^{2(N-2)}$. $P_{C2} \ll P_{C1}$ because A must be close to unity to achieve adequate TCR for useful imaging. For the third order $P_{C3} = \binom{N}{3}(1-A^2)^3 A^{2(N-3)} \ll P_{C2}$, and so on.

The power density is estimated in the same way as was done for the target. The power in the first order scatter field P_{C1} is spread over the scattering angle of $s(u)$, which is $\lambda/\pi x_0$, within which the power density is $P_{C1}/(\lambda/\pi x_0)^2(\pi/4)$, and similarly for the higher order scatter fields. The power in each successive scatter order decreases by the factor $(1-A^2)$. Because A is close to unity, this ensures that the first order scatter field dominates.

3.4 Target to clutter power ratio

Combining the terms above, the target to clutter power ratio for N screens is

$$TCR = \frac{L^2 A^{2N}}{(\pi x_0)^2 \sum_{n=1}^N \binom{N}{n} (1-A^2)^n A^{2(N-n)}} \quad (12)$$

Eq.12 can be simplified considerably. Figure 10 plots TCR vs. $\sigma_\phi^2 \approx 1-A^2$ within the "clutter" region for $L = 25$ mm, $\pi x_0 = 10$ mm and $N = 6$, the number used in the earlier example. The minimum useful TCR must be larger than 10 dB because the target dynamic range is about 10 dB smaller than TCR (§2.9). Thus the maximum phase variance per screen is about 0.01 sq rad for unambiguous detection. Thus, only very small phase variance per screen can be tolerated for otherwise the target rapidly gets lost in the background as σ_ϕ^2 grows. Therefore we can assume $\sigma_\phi^2 \approx 10^{-2}$ and $A^2 \approx 1 - \sigma_\phi^2$. Next, $Na \approx D$ and $a \approx \pi x_0$. Also $\sigma_\phi^2 = \omega^2 \sigma_\tau^2$. Therefore (12) becomes

$$\begin{aligned} TCR &= \frac{L^2}{(\pi x_0)^2 \sum_{n=1}^N \binom{N}{n} \left(\frac{\sigma_\phi^2}{A^2} \right)^n} = \frac{L^2}{(\pi x_0)^2 \left(\left(\frac{\sigma_\phi^2}{A^2} \right) - 1 \right)^N} \\ &\approx \frac{L^2}{(\pi x_0)^2 N \sigma_\phi^2} \approx \frac{L^2}{\pi x_0 D \omega^2 \sigma_\tau^2} \end{aligned} \quad (13)$$

Not surprisingly (13) has the same form as (11), the single screen TCR, because of the dominance of the primary scatter field. In essence both are weak scattering solutions.

Eq.13 predicts that TCR is inversely proportional to propagation distance. *In vitro* TCR measurements were made at the Univ. of Rochester laboratory of Prof. Robert Waag from five samples of different thicknesses of excised, frozen and defrosted breast tissue used in Ref.10. For each measurement, a tissue sample was fixed in a holder within a water tank. Propagation was one-way from a pulsed 3.75 MHz hemispherical (virtual point-) source, through the water and tissue path, to a 1-D linear array in which waveforms were recorded at each element. The array was mounted in a computer-controlled 2-D positioner and moved along the orthogonal axis so as to form a 92x46 sq mm, 2-D synthetic array. Waveforms measured at each element position of the synthetic 2-D array were imaged. Figure 11 shows a 1-D maximum-projection cut through such an image. TCR measurements were made from such cuts. The central lobe is the image of the source. Clustered around it are discrete multipath arrivals from the source. They image as false targets. The broad clutter background is the isotropic scatter field. TCR is the squared reciprocal of the estimated clutter level at the origin. The 9 TCR data points are shown on the log-log plot of Figure 12a. Each point is the average of measurements made from a minimum of 6 cuts. The straight line drawn in the figure has the predicted slope of -1. With the exception of one point - the outlier at 30 mm depth - the data approximate the predicted behavior.

3.5 Relations between single and multiple screen parameters

Correlation distance: A significant amount of multiple scattering is precluded because σ_ϕ^2 has to be small ($\sim 10^{-2}$ sq rad) for successful imaging. This dominance of the primary scatter field means that the spectral width does not increase with propagation path length. Consequently, x_0 is a function of scatterer size only and not the thickness of the propagation medium in which it is measured. Experimental data support this conclusion. Measured halo widths from different thicknesses of a single *in vitro* breast sample used in Ref.10 are plotted in Figure 12b. The angular width is constant over a thickness range from 15 to 40 mm. Thus correlation measurements made in a given type of tissue at one depth are pertinent for any other depth.

Phase variance: σ_ϕ^2 in (13) is the phase variance of a single screen. A measurement in tissue, however, is never across a single screen and therefore the relation of measured phase variance data to σ_ϕ^2 must be determined. We can view the sequence of screens in the multi-screen model as a cascade of linear filters each with phase delay $\phi_i(x)$ or time delay $\tau_i(x)$. The phase (and time) delays add across a group of such circuits. Thus a phase measurement across N screens yields $\phi_1(x) + \phi_2(x) + \phi_3(x) + \dots = \sum_{i=1}^N \phi_i(x)$ and because of the assumed independence and common statistics of the $\phi_i(x)$ the variance is $N\sigma_\phi^2$, which accounts for the factor of N in (13).

3.6 Absorption

To incorporate absorption in the model, an exponential loss $\exp(-\alpha z)$ is appended such that the total field through each screen of thickness a is attenuated by the factor $\exp(-\alpha a)$ where α is assumed independent of position. The gain of the i th screen to the plane-wave component of the field changes from A_i to $A_i' = A_i \exp(-\alpha a)$. Output target power $P_T = [\prod_{i=1}^N A_i]^2 = A^{2N}$ (§3.3) changes to $[\prod_{i=1}^N A_i']^2 = A^{2N} \exp(-2N\alpha a)$.

The clutter is modified similarly. All scatter field terms in §3.2, calculated for a lossless model, are attenuated by the factor $\exp(-\alpha a)$. The first order spectrum $P_{C1} = N(1-A^2)A^{2(N-1)}$ changes to $N(1-A^2)e^{-2\alpha a}A^{2(N-1)}e^{-2(N-1)\alpha a} = N(1-A^2)A^{2(N-1)}e^{-2N\alpha a}$. Target to clutter ratio remains unchanged for the primary scatter spectrum, and similarly for the higher order spectra.

The same is true for the ratio $P_{\text{scat}}/P_{\text{pw}}$; absorption does not affect the balance between the scattered and plane wave components. Further, the argument holds at every frequency and therefore frequency selective absorption, which alters the spectrum of a deeply propagating wideband pulse, does not affect the ratio of the scattered to the plane wave energy.

Also unaffected by absorption are the relative strengths of the components of the scattered field that arise from different depths. This is because all components, whether plane wave or scattered field, are attenuated identically by the time they reach the skin. To illustrate this phenomenon, consider primary scattering arising from the n th screen, which means at a

depth of na . The plane wave component that initiates this field is attenuated by absorption, as it travels through $n-1$ screens toward the skin surface, by the factor $A^{2(n-1)}e^{-2\alpha a(n-1)}$. In the n th screen the scattered field $s(u)$ is attenuated by the factor $e^{-2\alpha a}$. As this field propagates to the skin surface it suffers additional attenuation in the remaining $N-n$ layers by the factor $A^{2(N-n)}e^{-2(N-n)\alpha a}$. The emergent scattered field is the product $\{A^{2(n-1)}e^{-2\alpha a(n-1)}\}\{s(u)e^{-2\alpha a}\}\{A^{2(N-n)}e^{-2(N-n)\alpha a}\} = A^{2(n-1+N-n)}e^{-2\alpha a(n-1+1+N-n)}s(u) = A^{2(N-1)}e^{-2N\alpha a}s(u)$, which is independent of n . In other words all scattered fields arising from the same target reach the surface with the same strength. Consequently the scattered field measured at the surface is a composite of the scattering all along the path from target to surface.

3.7 Parameters obtained from measurements

Finally, we rewrite (13) in terms of measurable parameters. Assume that measurements of correlation distance and time delay variance are made across a body of length $D_m \gg a$, where a is the nominal thickness of a phase screen. Call the measurements x_{om} and σ_{tm}^2 . The parameters needed for analysis are the single-screen values x_o and σ_ϕ^2 or σ_τ^2 . Both can be obtained from the measured data. As discussed above (§3.5) $x_o = x_{om}$ because of the dominance of primary scattering. The single screen phase variance σ_ϕ^2 is calculated from $\sigma_\phi^2 = \sigma_{\phi m}^2/N_m$, as shown in §3.5, and $\sigma_\phi^2 = \omega^2\sigma_\tau^2$. N_m is the number of screens or scatterer sizes a in D_m . $\therefore \sigma_\phi^2 \approx a\sigma_{\phi m}^2/D_m$ is the single screen phase variance. Eq.(13) can then be rewritten as a function of the known parameters of the imaging system (ω, L), the propagation depth during imaging (D), the measured tissue parameters ($x_{om}, \sigma_{\phi m}^2$ or σ_{tm}^2) and the propagation depth during measurement (D_m):

$$TCR \approx \frac{L^2}{N\sigma_\phi^2(\pi x_o)^2} \approx \frac{L^2}{D(\pi x_o)^2(\sigma_{\phi m}^2/D_m)} \approx \frac{L^2}{D\omega^2(\pi x_{om})^2(\sigma_{tm}^2/D_m)} \quad (14)$$

where the last approximation uses $a \approx \pi x_{om}$ and $\sigma_{\phi m}^2 = \omega^2\sigma_{tm}^2$. The right-hand expression is the most generally useful form.

The numerator parameter and first two denominator parameters are design parameters. The next two denominator parameters are measured properties of the tissue. The last is the length of the tissue sample in which tissue parameter measurements are made. Thus, time delay variance and correlation distance are the primary tissue measurements required for prediction of TCR in a purely scattering medium.

3.8 Limit to resolution

In §2.7, the lateral resolution was found to remain λ/L , the width of the diffraction pattern, and unaffected by the scatter field *so long as the scattered energy does not obscure the*

main image lobe. When detection vanishes so do lateral and contrast resolution, as was observed in 12-cm path-length observations reported in Refs.7 and 8.

4. OTHER RELATED TOPICS

4.1 Near field

The theoretical development of the scatter field used a plane wave or far-field model whereas ultrasonic imaging instruments are focused in the near field. There are two separate matters here. First, the physics of scattering has nothing to do with the focal properties of the measuring instrument and hence is unrelated to whether or not the instrument is focused. Second, the scatter spectrum from which spectral width was calculated extends only a few beamwidths from the focus and hence is satisfactorily approximated by the far-field Fourier transform calculation of the scattered field in (1). Thus the plane wave model is acceptable.

4.2 Two-way propagation

The model deals with both point source radiation propagating one-way to a receiving array and to the two-way problem of an isolated point target when illuminated by an arbitrary transmitter. It does not cover the arbitrary target distribution with arbitrary insonification. In principle the method can be extended to any source/target/transmitter configuration and in this paper two practical and easily describable cases are given.

One case is the well-focused transmitter. Only the target is illuminated with full strength. All other targets receive sidelobe illumination. Therefore the scatter level from the target is higher than the other scattered fields by the sidelobe level of the transmitter. Those fields are not first order competitors to the primary scatter background from the target and in general can be ignored.

In another important case the transmitter focus is degraded by the inhomogeneous medium from λ/L to $\lambda/\pi x_0$, the width of the primary clutter spectrum, where $L \gg x_0$. Now all targets within a 2-D circle of diameter $\lambda/\pi x_0$ are illuminated nearly equally and contribute equally to the clutter background. For the sake of argument, let there be $L/\pi x_0$ targets per diameter (one per beamwidth) of nominally the same size (such as Rayleigh scatterers) so insonified. Then the number of illuminated scatterers in a circle of diameter $L/\pi x_0$, which is $(\pi/4)(L/\pi x_0)^2$, is the factor by which the clutter power increases. The total received clutter power is spread in two dimensions over roughly twice the area (diameter is $\sqrt{2}\lambda/\pi x_0$ because the received spectrum, being the convolution of the scatter-source spectrum on transmit and the medium-induced spectrum on receive, is $\sqrt{2}$ times larger in diameter). The result is a change in TCR by the factor $(8/\pi)(\pi x_0/L)^2$.

A more general case is an arbitrary target distribution $T(u)$ illuminated by a field $f(u)$ from a transmitter radiating through an inhomogeneous medium. Its scatter field is $T(u)f(u)*s(u)$, the convolution of the medium response to the target reradiation. Further, let the target distribution be discrete and described by $T(u) = \sum T_k \delta(u-u_k)$ where the T_k are the amplitudes of targets located at $u=u_k$. The scatter field is $s(u)*f(u)\sum T_k \delta(u-u_k) = s(u)*\sum T_k f_k \delta(u-u_k) = \sum T_k f_k s(u-u_k)$ where $f_k = f(u-u_k)$.

4.3 Limitations of the model

Infinite statistically homogeneous phase screen: This model of spatially stationary statistics is satisfactory for weak scattering in a single, large tissue bed. It fails to account for interfaces between tissue beds across which a sound velocity change takes place. In other words, the model ignores all multiple angular arrivals at the transducer array from a common source which could arise from refraction at an interface or reflection from a strongly reflecting surface. Such arrival wavefronts will interfere in the aperture and appear to the imaging system as multiple sources, each with its own scattering halo.

The model is expected to be realistic in a large, reasonably homogeneous organ such as liver and for the purely scattering component in breast from subcutaneous and intramammary fat that fill much of most breasts. High density tumors and liquid-filled cysts will refract wavefronts and introduce image artifacts. It is hoped that these will submit to modeling at a later time.

Array size: The model is appropriate for arrays that are not too small to perceive the spatial fluctuations in $\phi(x)$, for then a statistical description of the medium is inappropriate, nor so large as to violate spatial stationarity (fluctuation statistics no longer constant across the array). The smaller limit likely occurs when $L \ll a$. In the other extreme the array not only sees a stochastic field of random spatial-density fluctuations but also discrete sub-bodies (cysts, tumors) with different refractive indices. In this case the model given in this paper pertains only to the purely scattered portion of the field, to which it can be applied, but not to the coherent multipath from the discrete bodies.

5. SUMMARY AND OBSERVATIONS

Inhomogeneous tissue removes energy from a wave both by incoherent scattering and coherent refraction and reflection. The incoherent scattered field is studied in this paper. The modeling technique is to slice the tissue body into thin, random phase screens, calculate the properties per screen and combine them. Scattering is produced by random speed fluctuations in tissue, largely due to density and compressibility perturbations. The nominal distance between density hills is identified with scatterer size $a \approx \pi x_0$, where x_0 is the exponential correlation distance. Scattering creates a halo around the target that diminishes the image

contrast. The halo width is $\approx \lambda/a$. The loss in contrast is measured by the target to clutter power ratio, which diminishes with the correlation distance, the propagation length D in the tissue and the time-delay variance per unit distance, and the square of the frequency. Lateral resolution within the halo is unaffected by the scatter field; it remains λ/L . L is the array size. However, detection of weak targets within the halo of a strong target requires that $TCR \gg 1$. When TCR is small, however, detection is not possible and the preservation of the lateral resolution is a meaningless virtue.

The obscuring effect of the halo is not only from its intensity but also from the number of lateral resolution cells in which the clutter can hide targets. This number is the ratio of the halo cross section to the beam cross section, which is $(L/a)^2$. This ratio is independent of wavelength. Scattering occurs at all depths between target and skin surface. The principal scattering mechanism is single or first-order scattering because the energy removed by each scattering hill is small.

The following summarizes comparisons between predictions of the theory and experimental data.

1. Halo width: Based on the size of fat globules the theory predicts 2-6 deg at 3 MHz (§2.4). Calculations from wavefront correlation experiments give the same spectral width (§2.3).
2. e^{-1} correlation distance vs. frequency: The experiment shown in Figure 3 indicates independence, which is what the theory predicts (§2.5).
3. TCR vs. propagation depth: Theory predicts inverse linear dependence. Experiment shown in Figure 12a indicates approximately the same behavior.
4. Halo width vs. propagation depth: Theory predicts independence. Experiments show the same (Figure 12b).

ACKNOWLEDGMENTS

My thanks to Dr. Qing Zhu of the Ultrasound Lab of VFRC, UPenn, who provided the new experimental data and carefully critiqued the paper, to Graduate Student Jodi Schwartz of the same lab who checked the derivations, corrected the equations, improved the figures and pointed out numerous instances of cumbersome writing, and to Dr. Chandra Sehgal of the Radiology Dept. whose final review removed the residual misstatements and ambiguities. Thanks also go to Prof. Robert Waag of the Univ. of Rochester for the use of the ultrasound facility and to Ms. Laura Hinkelman for her willing cooperation in the taking of the data.

REFERENCES

1. R.A.Muller and A.Buffington, "Real-Time Correction of Atmospherically Degraded Telescope Images through Image Sharpening," J.Opt. Soc. Am., **64**(9) 1200-1210 (September 1974).

2. J.P.Hamaker, J.D.Sullivan and J.E.Noordam, "Image Sharpness, Fourier Optics, and Redundant-Spacing Interferometry," J. Opt. Soc.Am., **67**(8) 1122-1123 (August 1977).
3. M.O'Donnell and S.W. Flax, "Phase Aberration Correction using Signals from Point Reflectors and Diffuse Scatterers: Measurements," IEEE Trans. Ultrason. Ferroelec. Freq. Cont., **35**(6):768-774, Nov. 1988.
4. L. Nock, G.E. Trahey, S.W. Smith, "Phase Aberration Correction in Medical Ultrasound Using Speckle Brightness as a Quality Factor," J. Acoust. Soc. Am., **85**(5) 1819-1833 (1989).
5. C.Prada, F.Wu and M.Fink , "The iterative time reversal mirror: A solution to self-focusing in the pulse mode," J.Acoust.Soc.Am. **90**(2), Pt.1, pp. 1119-1129, Aug.1991.
6. Sumino, Y. and Waag, R. C., "Measurements of Ultrasonic Pulse Arrival Time Differences Produced by Abdominal Wall Specimens," J. Acoust. Soc. Am. **90**(6) 2924-2930 (1991).
7. Q. Zhu and B.D.Steinberg, "Large-Transducer Measurements of Wavefront Distortion in the Female Breast," Ultrasonic Imaging, **14**: 276-299 (1992).
8. Zhu, Q., Steinberg, B. D.and Arenson R., "Wavefront Amplitude Distortion and Image Sidelobe Levels - Part II: In Vivo Experiments", IEEE Trans. Ultrason. Ferroelec. Freq. Cont.**40**(6) 754-762 (Nov. 1993).
9. Q. Zhu and B. D. Steinberg, "Modeling, Measurement and Correction of Wavefront Distortion produced by Breast Specimens," IEEE Int'l Symp. Ultrason. Ferroelec. Freq. Cont., Cannes, Nov. 1994.
10. L. M. Hinkelman, D-L. Liu, Q. Zhu, B.D. Steinberg, and R. C. Waag, "Measurement and Correction of Ultrasonic Pulse Distortion Produced by the Human Breast", JASA, in press.
11. B.D.Steinberg, Principles of Antenna and Array System Design, John Wiley and Sons, New York, 1976.
12. Zhu, Q. and Steinberg, B. D., "In vivo measurement of correlation length of female breast," submitted to JASA Nov. 92, accepted subject to revision.
13. A.Castro and R.Gomberg, Le Sein: Mammographie. Echographie. Numerization. Galactographie, Arnette, 2 rue Casimir Delavigne, 75006 Paris, 1989.
14. B.D.Steinberg and Q.Zhu, "Lateral Resolution in the Breast as a Function of Transducer Size," UP-VFRC-22-92, Valley Forge Res. Cntr., UPenn., Phila. PA, 1992.
15. Any text on statistical communications or radar theory, e.g., M. Schwartz, Information Transmission, Modulation and Noise, McGraw Hill, New York, 1970.
16. B.D.Steinberg, "Radar imaging from a distorted array: The radio camera algorithm and experiments," IEEE Trans. Ant. Propag., **AP-29**(5), 740-748 (Sept. 1981)

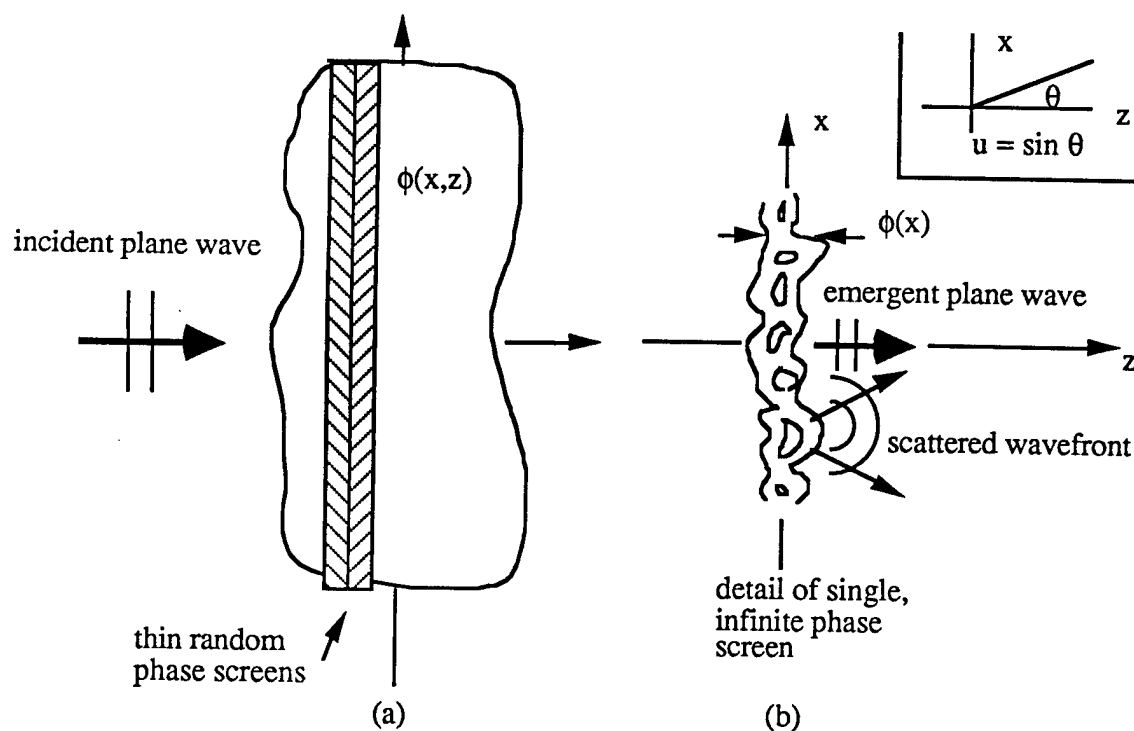


Figure 1. (a) Random, statistically homogeneous medium modeled as sequence of adjacent random phase screens. (b) Detail of single, infinite screen showing density variations (contours) as cause of local perturbations of time delay through screen. Some of the energy of the plane wave incident upon the screen emerges as a plane wave. The remainder is scattered. Shown is the scattered wavefront from one scattering center in the screen.

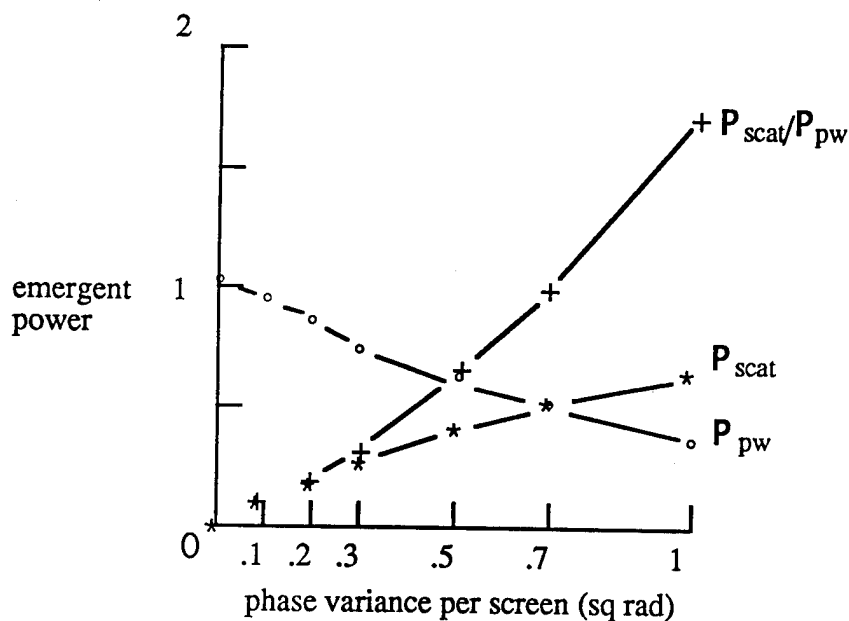


Figure 2. Emergent energy vs phase variance $\sigma_\phi^2 = (2pfs_t)^2$. Single phase screen. $P_{pw} = A^2$ = plane wave power, $P_{scat} = 1 - A^2$ = scattered power, P_{scat}/P_{pw} = ratio of scattered to plane wave powers.

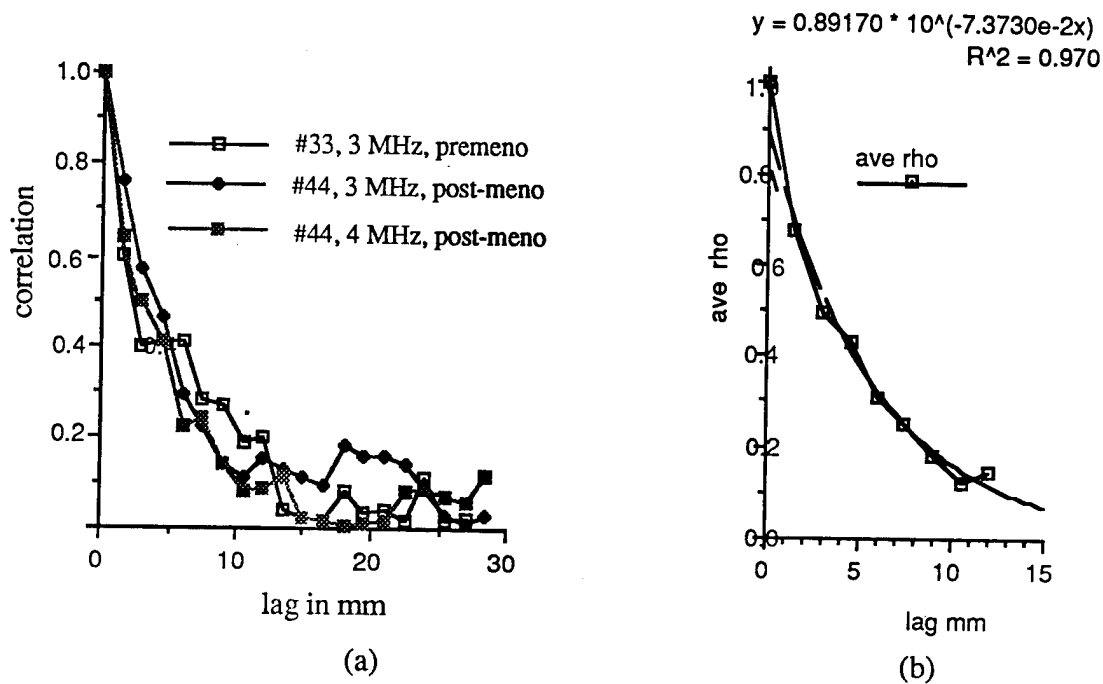


Figure 3. (a) Point source correlation functions of 12-cm thickness *in vivo* breasts measured 2.5-3 cm from chest wall. Data from Ref 1. (b) Average of the three curves of (a) and exponential fit.

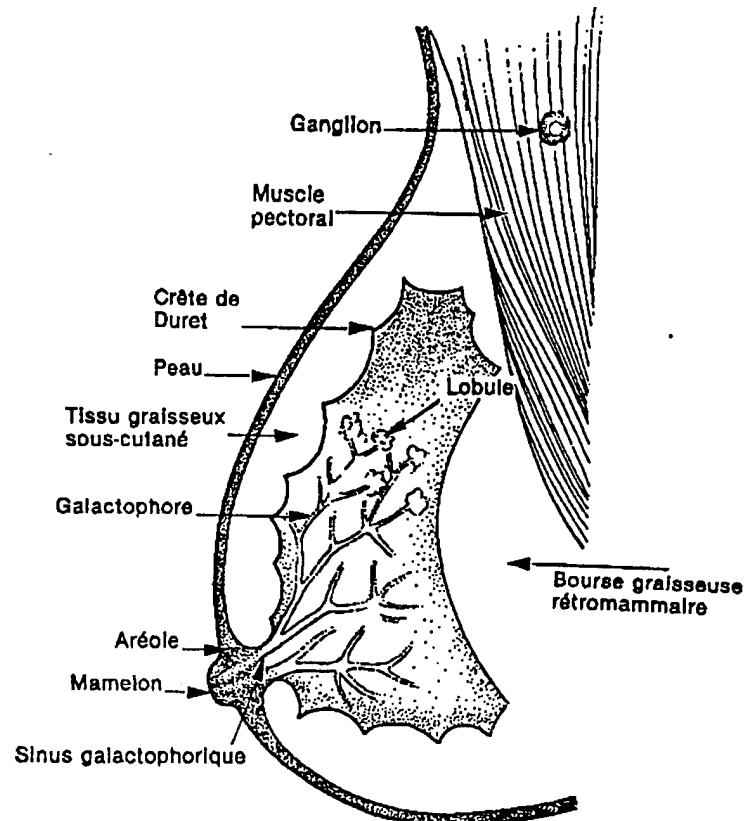


Figure 4. Schematic of breast section. From Ref. 13.

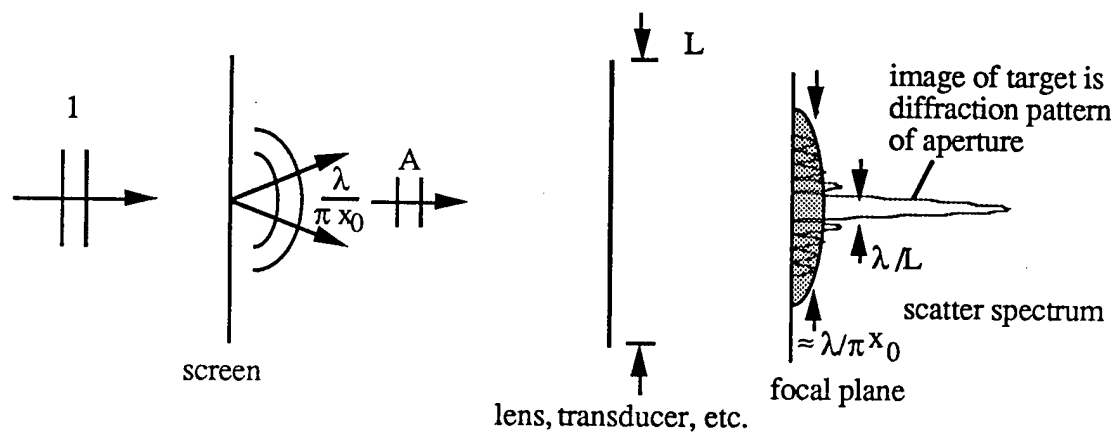


Figure 5. Image contains diffraction pattern of aperture (image of emergent plane wave) and angular spectrum of the scatter field.

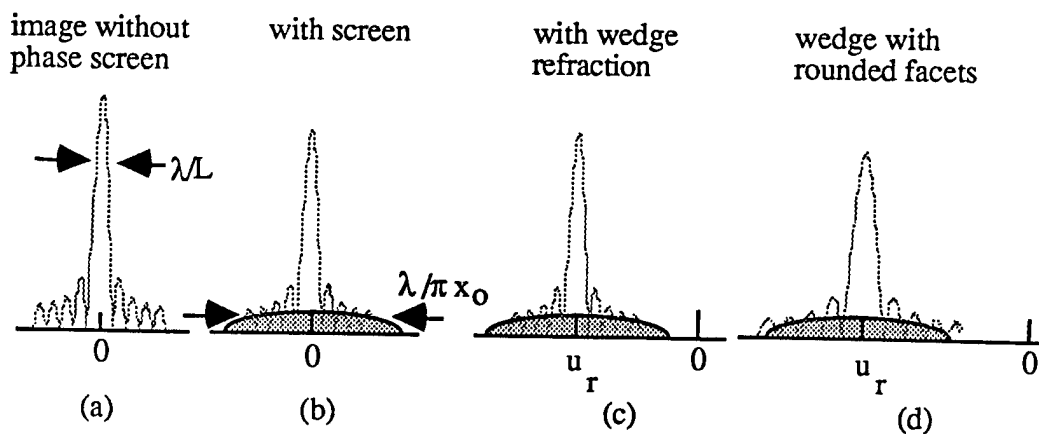


Figure 6. Image of point source is diffraction pattern of imaging aperture. (a) Without phase screen. (b) Scatter spectrum caused by phase screen. Image power reduced. (c) Linear-wedge refraction plus weak scattering. Image displaced through angle u_r . (d) Wedge with rounded facets defocuses image.

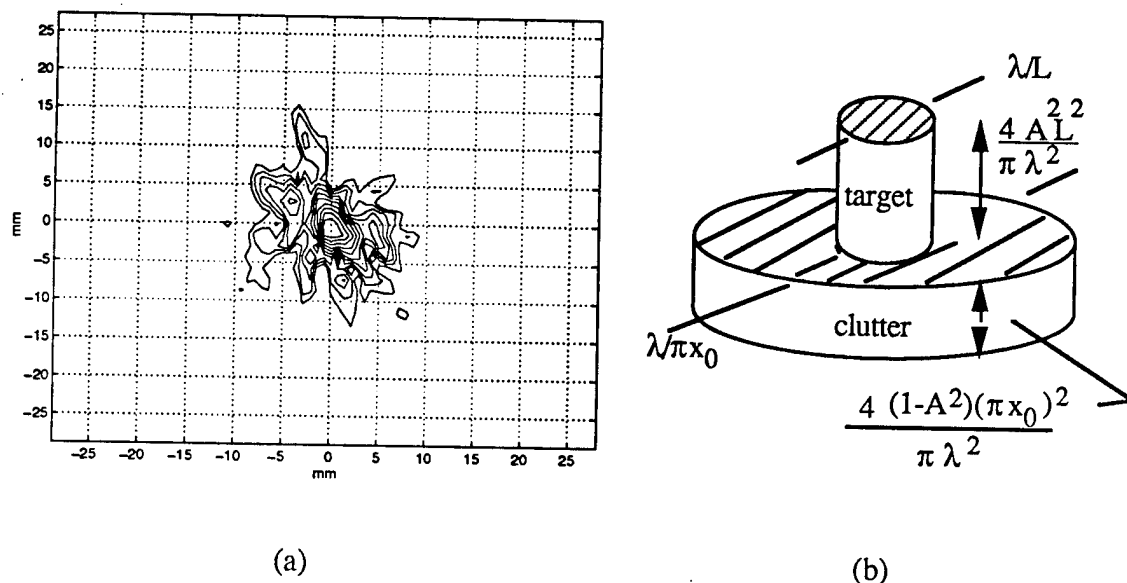


Figure 7. Angular target and clutter spectra. (a) Contour plot of point target (center contours) plus widely dispersed scattered field and discrete multipath. The coordinates are azimuth and elevation. *In vitro* breast sample (brs006) is 4-cm thick. 3.75 MHz. 92 mm x 46 mm array. Outer contour -15 dB. Data from experiment reported in Ref. 10. (b) Approximate target and clutter spectra showing heights and widths.

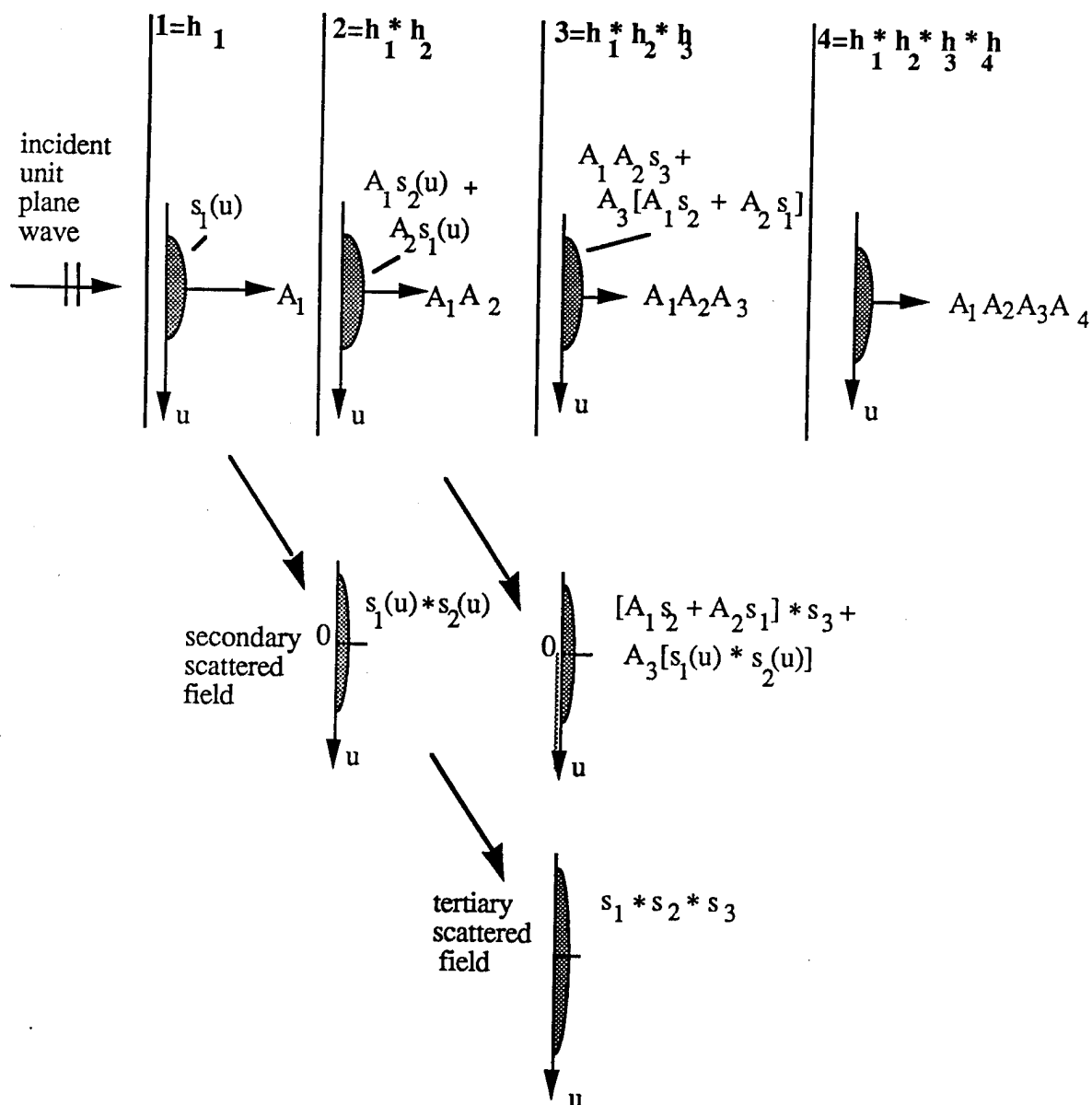


Figure 8. Build-up of the multiple-screen angular output spectrum.

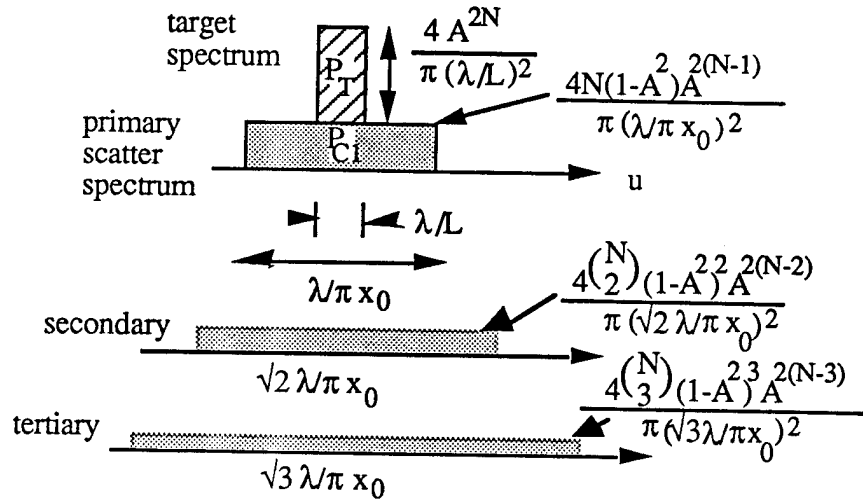


Figure 9. Cross sections of approximate target and clutter spectra after N screens. 2-D array.

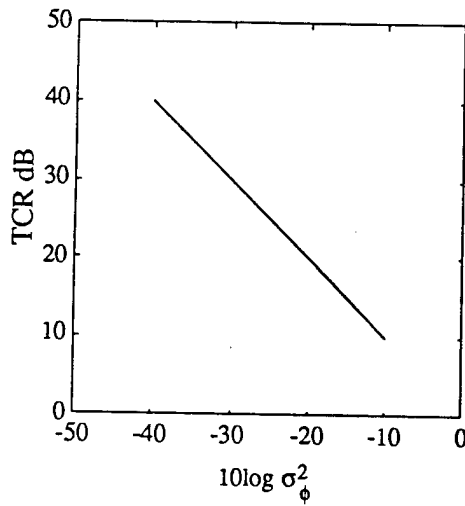


Figure 10. Ratio of point target intensity in image to clutter background induced by scattering. σ_ϕ^2 is the phase variance per screen. 6 screens, 25 mm array size, 10 mm scatterer size. Plot of (13).

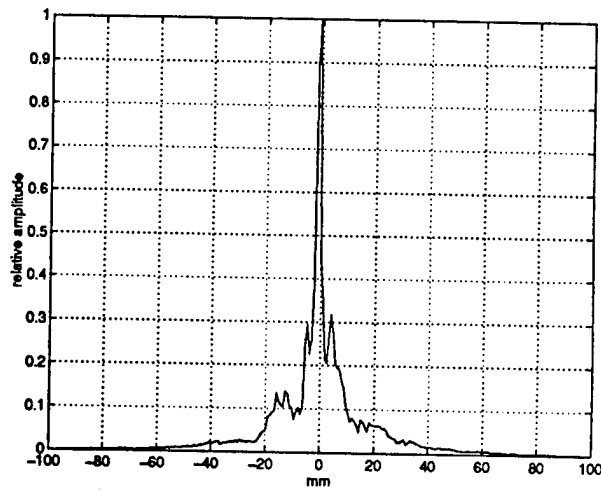
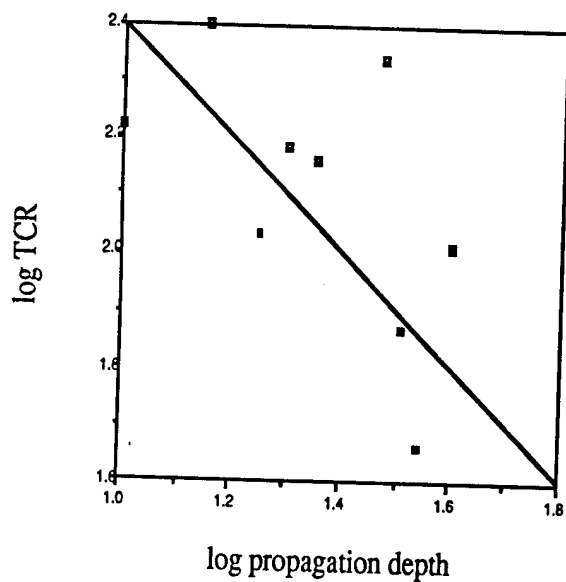
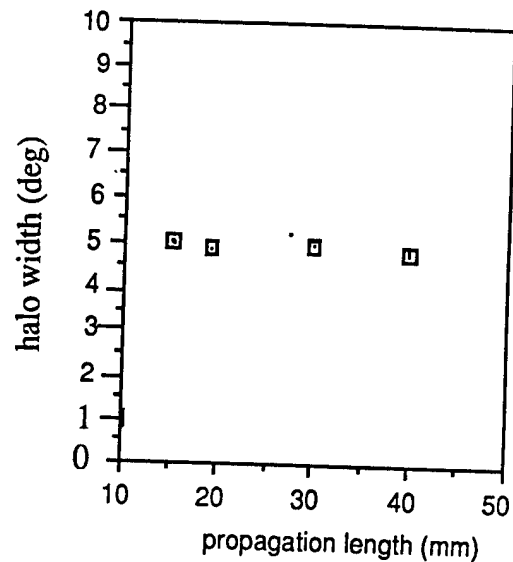


Figure 11. 1-D cut at -25 deg through single-source image of Figure 7a. System noise level ≈ -35 dB. Cut is through region with minimum multiple arrivals. Central lobe is target image. Adjacent lobes are multipath, probably refraction induced. Low, broad background is isotropic scattering. TCR and halo width are estimated from the scatter background.



(a)



(b)

Figure 12. (a) TCR and (b) halo width (deg) vs. thickness of *in vitro* breast samples. TCR shows approximate inverse linear dependence (solid line) with path length. Halo width shows independence.